INSIGHTS INTO THE MOLECULAR MECHANISMS INVOLVED IN THE EFFECTIVE THERAPEUTIC POTENTIALITIES OF NATURAL AND SYNTHETIC COMPOUNDS AGAINST BREAST CANCER

THESIS SUBMITTED
FOR
THE DEGREE OF
DOCTOR OF PHILOSOPHY
IN
SCIENCE
BY

NOYEL GHOSH

REGISTRATION No.: SLSBT1107119

INDEX No.: 71/19/Life Sc./26

2023

DEPARTMENT OF LIFE SCIENCE AND BIOTECHNOLOGY

JADAVPUR UNIVERSITY

Dedicated to My

Loving Parents

CERTIFICATE FROM THE SUPERVISOR(S)

This is to certify that the thesis entitled "**Insights into the molecular mechanisms involved in the effective therapeutic potentialities of natural and synthetic compounds against breast cancer**" Submitted by Smt. **Noyel Ghosh** who got her name registered on **5th September, 2019** for the award of Ph. D. (Science) Degree of Jadavpur University, is absolutely based upon his own work under the supervision of **Prof. Parames Chandra Sil** and that neither this thesis nor any part of it has been submitted for either any degree / diploma or any other academic award anywhere before.

....

Parames Chandra Sil

16.10.2023

....

(Signature of the Supervisor(s) date with official seal)

Prof. Parames C. Sil
Division of Molecular Medicine
BOSE INSTITUTE
P-1/12, CIT Scheme VII M
Kolkata-700 054

Acknowledgement

I express my profound gratitude for the invaluable contributions that have shaped the culmination of my thesis, conveying utmost respect, sincere gratitude, and unbounded elation.

I extend my sincere gratitude to Prof. Parames C. Sil for granting me the opportunity to collaborate with his esteemed group and for guiding me throughout my doctoral journey, motivating me to stay resolute in accomplishing my objective and propelling me forward with invaluable scientific contributions.

This occasion allows me to extend my gratitude to Prof. Nikhil Ranjan Pramanik and Dr. Joydeep Das, whose efforts greatly eased the difficulty of my task by providing valuable scientific guidance, adept problem-solving skills, and clear explanation of complex concepts.

I would like to extend my appreciation to the distinguished faculty members of Bose Institute and Jadavpur University, specifically Prof. Suman K. Banik and Prof. Parimal Karmakar, whose guidance and support have greatly enhanced my educational journey.

I articulate my sincere recognition to my fellow authors, particularly Sumit da, Mousumi di, Abhishek, Samhita, Sushweta di, Ankita di and Sharmistha, for their noteworthy contributions to the multiple projects I have undertaken during this duration. Furthermore, I extend my gratitude to all the members of my laboratory for their extensive support in the routine laboratory work.

Throughout this period, I am grateful for the support received from the technicians at our prestigious institution in operating the different instruments.

I would like to express my heartfelt appreciation to my mother for the countless sacrifices she has made on my behalf, as her unwavering prayers have given me the strength to overcome obstacles and become the person I am today. I am highly indebted to Dr. Sanjay Madhavan, whose unwavering support has been a constant source of gratitude.

I express gratitude to the divine being for providing me with the necessary grace to undertake these research works.

CANDIDATE: **NOYEL GHOSH** INDEX No: **71/19/Life Sc./26**

TITLE: "Insights into the molecular mechanisms involved in the effective therapeutic potentialities of natural and synthetic compounds against breast cancer"

Abstract

In recent times, breast cancer has been a continuous reason for mortality and morbidity among the current female population. Several breakthrough researches in the field of cancer therapeutics have led to enormous advancements in current therapeutic strategies which cumulatively have made disease prognosis better day by day. Still, from a clinical viewpoint, breast cancer therapeutics remain confined to the usage of chemotherapy, radiotherapy, hormone replacement therapy, surgical resection, or a combination of any two or three modalities of these. Such practices, even though remain effective in killing cancer cells, often generate collateral systemic damage to healthy body cells or completely remain unresponsive due to the emergence of resistance. To avoid such treatment-related anomalies, we have focused on studying the anticancer effectivities of certain synthetic metallic compounds and a selective natural compound, chrysin which are safe to be used in vivo when used within the recommended dosage.

Chapter 1 outlines a brief discussion related to general concepts associated with breast carcinoma, present modalities of therapeutic strategies, their limitation, and hence, describing emerging objectives of present studies in this thesis.

Chapter 2 outlines detailed experimental methodological protocols performed during the overall studies.

Chapter 3 describes molecular aspects of anticancer efficacies exhibited by dipicolinic acid passivated 1-allyl imidazole substituted oxidovanadium complex (IV), i.e., VOL, against breast carcinoma in contrast to known metallodrug cisplatin both *in vitro* and *in vivo*.

Chapter 4 describes the utility of another variability of dipicolinic acid passivated oxidovanadium complex (IV) with 1-methylimidazole substitution (OVMI) against triple-negative breast carcinoma and secondary pulmonary metastasis as an alternative option against side effect-causing conventional metallodrug usage both *in vitro* and *in vivo*. The anticancer efficacy of OVMI has been enlightened from the viewpoint of molecular mechanistic approaches.

Chapter 5 describes the folic acid-guided targeted delivery of chrysin and its pH-dependent release from polyacrylic acid-coated mesoporous silica nanocarrier specifically to breast cancer cells limiting chances of off-target toxicity caused by conventional chemotherapy. Additionally, this chapter highlights molecular aspects of enhanced antineoplastic effectivity of chrysin delivered through silica nanocarrier.

Noyel Ghosh.
16/10/2023.

Signature of the candidate

Paramas Chandra Sil
16.10.2023

Signature & seal of supervisor

Prof. Parames C. Sil
Division of Molecular Medicine
BOSE INSTITUTE
P-1/12, CIT Scheme VII M
Kolkata-700 054

Contents

Chapter 3: Oxidative Stress-mediated *in vivo* Anticancer Therapeutic Effectivities of Novel 1-allyimidazole-substituted Oxidovanadium (IV) Complex in Solid Tumor

Chapter 4: Multifaceted Antineoplastic Curative Potency of Novel Water-soluble Methylimidazole-based Oxidovanadium (IV) Complex in Triple Negative Mammary Carcinoma

Chapter 5: Folic Acid-Functionalized pH-responsive Mesoporous Silica Nanocarrier-assisted Enhanced Antineoplastic Efficacy of Chrysin in Breast Cancer Therapy

Chapter 1

General introduction

1.1. General notes on breast cancer

Breast cancer (BC) is one of the prevalent types of malignancy that frequently afflict female population worldwide, displaying an annual rise in its morbidity, thereby posing a significant threat to human well-being. BC is distinguished by its heightened occurrence, elevated fatality rate, extensive heterogeneity, increased likelihood of recurrence, and unfavorable prognosis. Collectively, these factors have contributed to the morbidity and mortality of BC surpassing that of lung cancer in women. In the year 2018, approximately 2 million fresh cases were identified, leading to a distressing 0.6 million fatalities accredited to the ailment (Ferlay et al. 2019). Nearly 281,550 newly reported instances of invasive BC has been reported among women of United States where about 43.6 hundred deaths were expected by 2021 (Society 2020). This scenario necessitates the continuous exploration of all aspects of BC, encompassing tumor gradation and related therapeutic interference.

1.2. Molecular classification of breast cancer

Conventionally, BC has been categorized histologically, but nowadays this grouping has taken a back seat to molecular perspectives. Because, for appropriate therapeutic strategy selection and subsequent prognosis of the disease, molecular approach is far more beneficial. As stated by the World Health Organization (WHO), there are 21 different histological types of BC that are distinct in terms of associated risk index, responsiveness to certain treatment modality, and further treatment outcomes (Sinn and Kreipe 2013). The major BC grouping involves in situ and invasive BC. Invasive one can be further divided into various subtypes, among which infiltrating ductal carcinoma and invasive lobular carcinoma are the major ones (Li et al. 2003, Makki 2015). To determine legitimate therapeutic aptitude, IHC-mediated histological observations act as an initial guide. Primarily, from the view point of clinical significance BC can be categorized into five distinct subtypes (Mueller et al. 2018). They are as follows:

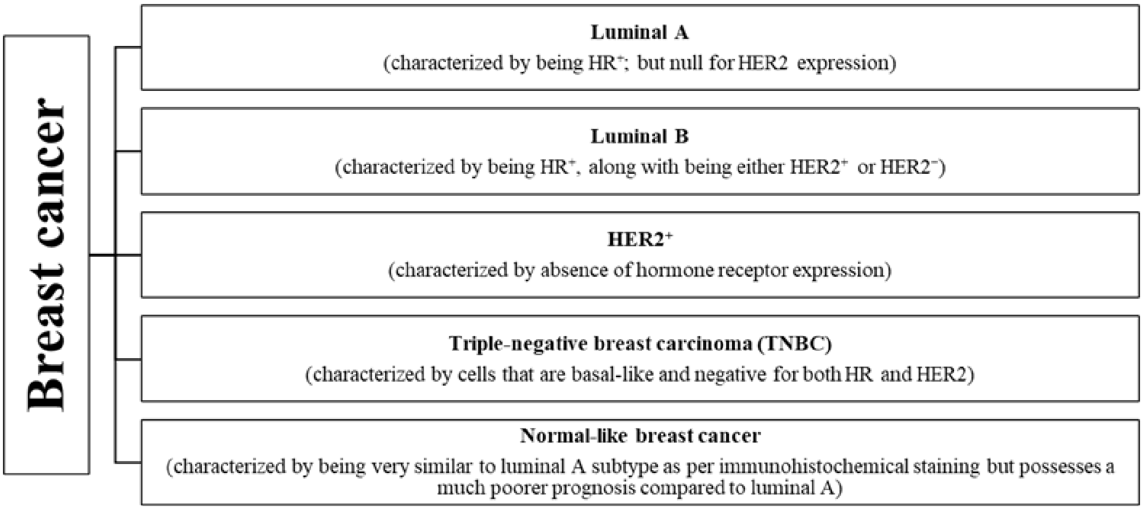

Breast cancer

Luminal A
(characterized by being HR^+; but null for HER2 expression)

Luminal B
(characterized by being HR^+, along with being either $HER2^+$ or $HER2^-$)

$HER2^+$
(characterized by absence of hormone receptor expression)

Triple-negative breast carcinoma (TNBC)
(characterized by cells that are basal-like and negative for both HR and HER2)

Normal-like breast cancer
(characterized by being very similar to luminal A subtype as per immunohistochemical staining but possesses a much poorer prognosis compared to luminal A)

1.2.1. ER $^+$/ PR $^+$ breast cancer

In this subtype of BC more than 1 % of tumor nuclei exhibit positive signal for immunostaining against ER and/or PR. There are two views regarding role of estrogen for initiation and promotion of BC (Allison et al. 2020). According one, ligation on ER stimulates the division and multiplication of mammary cells, leading to increased DNA synthesis. Consequently, this increases the chances of replication errors incorporation, its accumulation due to lack of efficient DNA repair; thus, increasing likelihood of more mutations. Whereas, the second hypothesis posits that genotoxic estrogenic metabolic by-products can impair DNA directly, thereby causing mutations. Nonetheless, it is important to state that a large proportion of women with ER / PR positive BC, often exhibit resistance or acquire resistance during hormone-based therapeutic course. Extent of mutation in estrogen receptor, as well as the intercommunication of ER with HER2 signaling and with other growth factors are frequently implicated in endocrine resistance. Furthermore, estrogen-independent proliferation, heightened sensitivity to low estrogen level, excessive cyclin D1 expression, persistent activation of NF-κB, and diminished expression of ER-α (Szostakowska et al. 2019) are responsible for resistance to hormonal therapy.

1.2.2. HER2$^+$ breast cancer

Nearly 20- 30 % of BC cancer patients show positive immunostaining against HER2 protein. It is a ERBB family protein tyrosine kinase receptor, that is coded by the gene ERBB2. Ligation of growth factors to HER2 plays crucial role in cell growth and further survival. Uplifted expression of HER2 protein in mammary cells results in amplification of its downstream signaling resulting in uncontrolled growth of mammary cells, characteristics of BC (Slamon et al. 1987). The significance of HER2 status as a prognostic factor has also been addressed in case of *in situ* ductal carcinoma (DCIS). It accounts for nearly 20-25 % of all breast cancer cases as detected from population-oriented breast cancer screening studies. In contrast to invasive ones which express approximately only 13 % cases of HER2 positivity, DCIS exhibits higher occurrence of HER2 amplification (34 % cases of total DCISs) (Schick, Ritchie, and Restini 2021). Association of HER2 positivity due to its higher amplification in DCIS, projects unfavorable prognosis of the disease.

1.2.3. Importance of Ki-67 marker

In addition to conventional markers of BC, a proliferation marker known as Ki-67 also holds importance in terms of prognosis. Luminal type A BC with lower expression of Ki-67 has best prognosis post-treatment; whereas, luminal B type BC with high level of Ki-67 shows a bit more aggressiveness and poor comparative prognosis (Schick, Ritchie, and Restini 2021, van Seijen et al. 2019). However, in comparison to luminal types, BCs with increased expression of HER2 in association with elevated Ki-67 expression, possess greater risk index and invasiveness. HER2-enriched cancers tend to grow at a faster pace and may have a more unfavorable prognosis.

1.2.4. Triple negative BC (TNBC)

TNBC is aggressive most BC type with least amount of prognosis among all molecular BC types (Criscitiello et al. 2012). In this context, it is important to state that BRCA1/2 mutation in germplasm, BRCA promoter hypermethylation, a deficient HRR pathway result in defective and inefficient homologous recombination repair (HRR) which strongly characterizes TNBC. Notably, Atchley et al. reported that over 80 % of breast cancers with BRCA mutations are triple negative. Studies have demonstrated that TNBC has a significantly higher risk of recurrence and a worse prognosis after recurrence compared to HR^+ cancers, with an average survival of 1-1.5 years versus 50-60 months, respectively (Atchley et al. 2008). Despite the emergence of targeted therapies as first-line treatments for various cancers, sequential chemotherapy still persists as the primary care for TNBC due to the absence of receptor expression for targeted therapy. Irrespective of the disease's staging, TNBC patients have lower survival rate than the non-TNBC patients having at least positive signal for ER or PR overexpression.

1.3. Breast cancer and oxidative stress

Oxidative stress refers to a state where there is an excessive presence of ROS in comparison to antioxidants (Sies and Jones 2020). This connection underscores the importance of achieving equilibrium between the surplus of ROS and antioxidants. Inline, ROS is a broad-spectrum term that covers reactive byproducts of molecular oxygen and include hydrogen peroxide, hydroxyl radicals, superoxide radicals and singlet oxygen sometimes. Cells are equipped with intricate biochemical and genetic systems to uphold this equilibrium, and it is evident that any disruption to these systems can lead to significant pathophysiological ramifications. Oxygen radicals are incessantly formed within mammalian cells as a direct result of utilizing oxygen for aerobic respiration (Brown and Bicknell 2001). Excessive ROS load inflict harm upon DNA, thereby causing mutations that trigger the development of tumors and sustain their progression. Carcinoma cells often find themselves in a state of perpetual oxidative stress. Neoplasm generate ROS at a higher pace rather than that of the normal cells. Some of the factors that contribute to such increased oxidative burden in BC cells are as follows:

1.3.1. Metabolic alternation

Cancer cells maintains high ROS content intracellularly in contrast to healthy cells, thereby upholding their distinct phenotype. Main source of excess ROS production in cancer cells is none other than altered mitochondrial electron transport chain that is engaged with generation of ATP. Here, mitochondria contribute heightened $O_2^{\bullet -}$ generation in response to modified cellular conditions such as hypoxia and unanchored growth. However, other than mitochondrial source there are nearly 41 catalytic system that contribute to enhanced ROS generation. Among them, membrane-bound NADPH-oxidase (NOX) system that present in innate immune cells such as in neutrophils, macrophages also generate ROS locally with greater potency for bactericidal activities and pathogen killing (Brown et al. 2005). Nowadays, it has been also reported that cancer cells undergoing hyperproliferation or harboring abnormal centrosome can stimulate excess $O_2^{\bullet -}$ production through their altered inherent NOX system. In majority cases, breast cancer cells overexpress an enzyme called thymidine phosphorylase. This enzyme is associated with thymidine metabolism and generates thymine and 2-deoxy-ribose-PO_4, which in turn reduces carbohydrate molecules rapidly resulting in production of ROS in carcinoma cells. Furthermore, oxidative distress in mammary carcinoma may also stem from the metabolism of estrogenic precursors by lactoperoxidase that oxidizes 17β-estradiol through single electron transfer to generate reactive phenoxyl radicals (Sipe Jr et al. 1994). Apart from these, during motility, cancer cells synthesize enhanced hydrogen peroxide molecules by 5-lipoxygenase. Altered protein folding in endoplasmic reticulum (ER), in addition, bestow cancer cells too with excess H_2O_2 (Arnandis et al. 2018).

1.3.2. Insufficient tumor vasculature

A breast tumor rapidly surpasses its blood supply, resulting in a deficiency of glucose and oxygen supplies. BC cells are highly sensitive to such deprivation of glucose that quickly induces oxidative stress, but does not affect instantaneously the non-neoplastic cell populations. Such distinction may result from the fact that glucose deprivation diminishes the intracellular pyruvate reserve in BC cells, preventing the breakdown of endogenous oxygen radicals. BC typically sustain their growth by promoting angiogenesis (Spitz et al. 2000). The blood flow within these newly formed vessels often becomes distorted, leading hypoxia and further reperfusion. Such reperfusion may contribute to excess ROS generation leading to oxidative distress within breast carcinomas.

1.3.3. Non-transformed cell infiltration

Macrophage infiltration in breast tumor is a usual situation. These macrophages at point of infiltration, are capable of ROS overproduction resulting in sub-lethal oxidative distress in BC. Moreover, such tumor-infiltrating macrophages secrete a cytokine named as TNF-α, that too add on cellular oxidative stress related to BC (Kundu, Zhang, and Fulton 1995). Apart from that, fibroblasts represented in tumor microenvironment, get attracted and activated by enhanced ROS, particularly hydrogen peroxide, produced by cancer cells via HIF1α upregulation (Perillo et al. 2020). After being induced, such cancer-associated fibroblasts in turn enables sustained oxidative load in cancer cells via strengthening cellular antioxidant system.

1.3.4. Oxidative stress caused by conventional treatment modalities

Conventional therapeutic measures including chemotherapy with doxorubicin, mitomycin C, etoposide, and cisplatin, along with radiation, photodynamic therapy, and the synthetic hormone-inhibitor such as tamoxifen can potentially increase oxidative stress in BC (Ferlini et al. 1999). For example, doxorubicin-mediated cytotoxicity activates Fenton reaction which ultimately results in excess hydrogen peroxide generation leading to increased oxidative stress and related apoptotic death in BCs.

1.3.5. Genetic perspective of increased oxidative load in breast cancer

overexpression of cellular oncogenes or loss of regulatory effectivity of cellular tumor suppressor genes results in ROS overproduction. Monomeric G-protein Ras, modulates mitochondrial metabolism that results in lowered mitochondrial transmembrane potential and further stimulation of either NOX2 alone or accompanied by NOX4 induction. Activation of NOX4 can also be originated by nuclear translocation of STAT3. Inline, Rac1, another RAS-related oncogene is known to induce NOX1 activation. Apart from G-protein superfamily, anti-apoptotic BCL-2 brings about alternation in mitochondrial activity; whereas MYC, a proto-oncogene can repress PGC-1a and subsequently diminishes mitochondrial biogenesis (Chong et al. 2018, Marcar et al. 2019). Among tumor suppressors, diminished activity of antioxidant genes such as GPX1, SESN1, SOD2 and SESN2 results in TP53 dismissal which in turn evoke ROS overgeneration (Gorrini, Harris, and Mak 2013). Other than genetic modulation, post-translational acetylation of SOD2 can turn on its pro-oxidant activity mode.

Redox-sensitive TRPA1 channel (regulated by upstream NRF2) is overexpressed in cancer cells that activates ERK and PI3K-Akt signaling cascade through stimulation of Ca^{2+} signaling. This enables cancer cells to withstand cellular oxidative distress further by downstream target protein S-glutathionylation (Moloney and Cotter 2018).

1.3.6. Proapoptotic nature of excessive oxidative stress

Cancer cells, in their abnormal redox homeostasis, display a discrepancy in the levels of ROS, which are known to have tumorigenic properties, yet high levels of ROS are detrimental to the cells' viability (Reczek et al. 2017). Tumor cell proliferation is accommodated by increased ROS generation. Thus, these cells are modulated in way so that they are able to withstand excessive ROS burden by shifting cellular equilibrium towards oxidative condition. For such accommodation, neoplastic mammary cells uplift their antioxidant system and evade upper limit ROS withstanding capacity that would otherwise cause cellular senescence, programmed cell death through apoptosis or ferroptosis (Dodson, Castro-Portuguez, and Zhang 2019) (Figure 1).

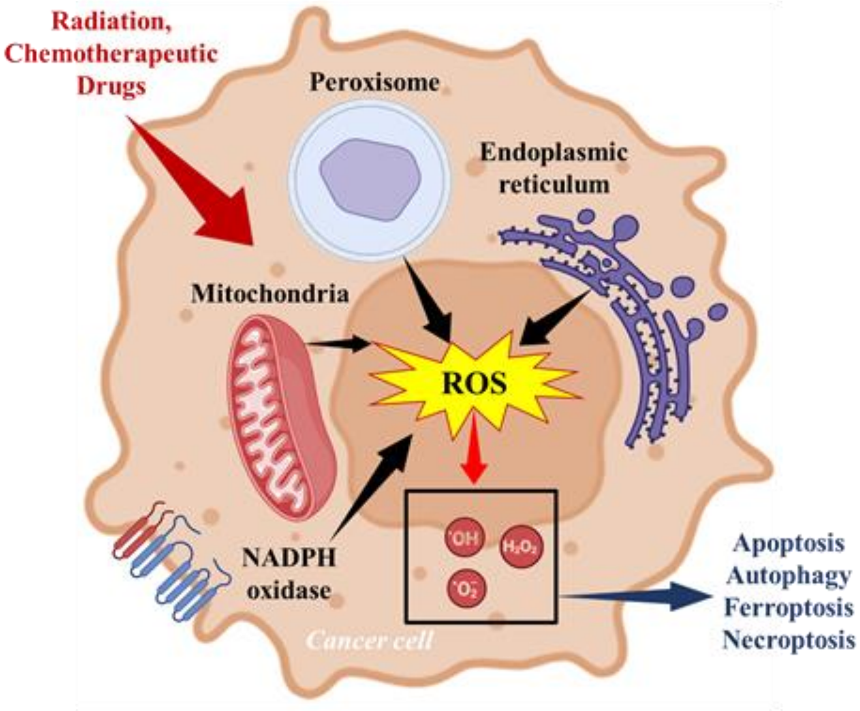

Figure 1: *Source and fate of excessive oxidative stress due to ROS overproduction in BC cells*

While moderate high ROS content acts as tumor promoters, excessive highly ROS burden induced cell killing in tumor cells most preferably by activating apoptosis. During extrinsic apoptosis, formation of death-inducing signaling complex (DISC) is contended by action of cellular FLICE inhibitory protein. Half-life of this protein is reduced by promoting its ubiquitination and subsequent degradation through excess ROS; thus, promoting extrinsic apoptotic death of BC cells. Moreover, excess ROS in cancer cells promotes alternation of mitochondrial permeability by modulating VDAC, ANT and cyclophilin D through oxidating their active site-specific cysteine residues (Perillo et al. 2020). Apart from that, higher ROS expression is known to promote ubiquitin-mediated destruction of anti-apoptotic Bcl-2 protein; that eventually leads to activation of mitochondrial apoptotic cascade in BC cells. In several cases of BCs, ROS is known to alter Bax to Bcl-2 ratio through activation of ER stress (Redza-Dutordoir and Averill-Bates 2016).

Other than apoptosis, autophagic and necroptotic deaths are also promoted in BC cells by excess ROS content. Particularly, hydrogen peroxide-mediated inactivation of ATG4 increases instances of LC3B accompanied formation of autophagosomes. Besides, it also inhibits mTOR1 by ATM-driven oxidative inhibition of AMPK. Both of these incidents promote ROS-driven autophagic death of transformed breast cells. While under moderate oxidative stress, TP53 facilitates tumor cell adaption by expression of antioxidant genes; the same gene acts distinctly under more severe oxidative state by stimulating ROS-mediated cell death. TP53 targets genes including PIG3 and PIG6, that code for mitochondrial proline dehydrogenases (Liu and Xu 2011). The activation of TP53 by higher ROS level, promotes upregulated expressions of BAX, PUMA, and p66Shc, which in turn dysregulate mitochondrial activity and accelerates cytosolic mobilization of cyt C. Furthermore, proapoptotic activation of TP53 declines expression of SOD2 and several NRF2 target genes. Currently, ROS-driven tumor inhibition by altering the activity of TP53 gene has been found to involve an iron-dependent mode of programmed cellular death type called ferroptosis. Excess ROS leads to the oxidation of membrane phospholipid-PUFAs which in turn affects integrity, curvature and respective pore formation in plasma lemma; thereby, inducing cell killing (Dixon and Stockwell 2019). It has been found that optimum intracellular cysteine content and GPX4 activity are essential to prevent ferroptotic death of BC cells. However, ROS-mediated activation of pro-apoptotic TP53 promotes cellular cysteine starvation by repressing cysteine uptake through cysteine/glutamate antiporter. Additionally, ROS-mediated stimulation of p14ARF (a tumor suppressor protein) fosters ferroptosis through TP53 activation and NRF2 repression subsequently (Chen et al. 2017).

1.4. Breast cancer and endoplasmic reticulum stress (ERS)

Three ER resident membrane proteins namely, IRE1, PERK and ATF6 tightly regulate misfolded protein response and subsequent ERS. Under homeostatic condition these proteins recruit an ER chaperone protein known as GRP78/BiP. During ERS, GRP78 releases itself from aforementioned association and assemble with misfolded proteins inside ER. (Chen and Cubillos-Ruiz 2021, Salvagno et al. 2022). In ERα$^+$ BC, estradiol activates UPR through PLC- γ signaling downstream to IP3 receptor channel activation. In ERα$^+$ BC, IRE1-XBP1 signaling gets activated parallel to estrogen signaling where spliced variant of XBP1 (IRE1 substrate) controls nuclear mobilization of NF-κB and contributes toward the anti-estrogenic resistance; thus, creates a positive feedback loop generating estradiol-dependent more cellular proliferation in ERα$^+$ BC (Figure 2). Apart from IRE1α-XBP1 axis, ERS also works through PERK in ERα$^+$ BC. ERα-mediated stimulation of PERK leads to activation of downstream ATF4 and CHOP. Parallelly, PERK activation can promote NF-κB-driven activation and secretion of TNFα to control estrogen-induced apoptosis (Fan and Jordan 2018). Moreover, estrogen is able to speed up ERα$^+$ BC progression by uplifting GRP78 expression which seems to facilitate cell survival in BC by promoting ER stress in all way. Thus, depending upon the duration and intensity of ERS, consequences of the disease vary. HER2$^+$ BC cells has been reported to be sensitive to the compounds that induce UPR mediated ERS.

It has been observed that USP22 effectively restrict the activation of UPR in HER2$^+$ BC by stabilizing ER-resident chaperone HSPA5 (Prokakis et al. 2021).

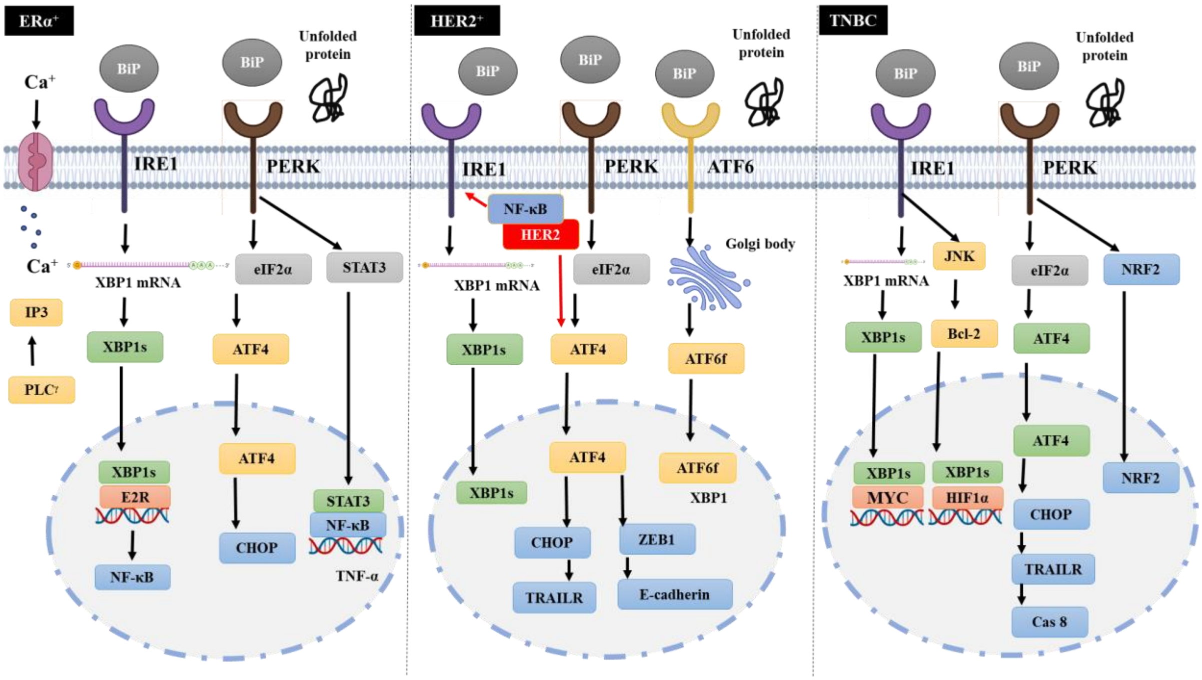

Figure 2: *ER stress in ERα$^+$, HER2$^+$ and TNBC breast carcinoma types*

Furthermore, UPR activation can contradict with the trastuzumab-mediated PI3K/AKT signaling inhibition in HER2$^+$ BC. Thus, selectively targeting molecules of ERS, along with application of anti-HER2 therapeutics may offer valuable therapeutic advantages in relevant disease management. TNBC being negative for colloquial hormone receptor markers, lacks specific targeted therapies and remain unresponsive to hormone therapy. In contrast to ER$^+$ BC, spliced product of XBP1 interacts with HIF-1α to assemble in a complex through the recruitment of RNA polymerase II in TNBC (Chen et al. 2014). Here, c-MYC acts as the activator for IRE1α-mediated XBP1 splicing. PERK-eIF2α pathway in TNBC acts to stimulate autophagy and involved in redox control. Under long-term ERS, caspase-8 and Noxa mediate apoptosis in TNBC. Inline, another chaperone called ER-oxidoreductase 1α (ERO1α), known to control protein folding oxidatively, also has been reported to be upregulated in TNBC and contributes to the poor survival of TNBC patients (Lee et al. 2018). ERO1α has been implicated to angiogenesis promotion too in TNBC through stimulating VEGF-mediated signaling. Moreover, ERO1α has been noted to enable enhanced expression of PD-L1 to facilitate immune escape of TNBC cells. Never the less, ROS-induced ERS in TNBC results from inhibition of IGF-1R signaling that can activate JNK signaling and CHOP parallelly to fine-tune initiation, promotion and maintenance of TNBC (Zhou et al. 2019) (Figure 2).

1.5. Breast cancer and cell cycle arrest

Cancer cells circumvent several cell cycle checkpoints and reorganize tumor-suppressor gene-mediated safeguarding to speed up uncontrolled cellular proliferation despite of being aneuploids and harboring several anomalies. Such rearrangement in cellular repertoire takes place through diverse genetic changes as well as profound epigenetic modulations involving epigenetic readers, writers and erasers. Post-translational modifications also sometimes involve to mitigate tumor suppressor gene activities. Distinct BC subtypes exhibit specific dependencies upon cell cycle pattern and consequently, modulate molecular repertoire of cell cycle checkpoints. In luminal A-type ER^+ BC, neoplastic cell mostly depends on the estrogen-driven stimulation to facilitate cell cycle progression in an uncontrolled manner. Ligation of estrogen with its cognate receptor results in activation of CCND1 gene (responsible for expression of cyclin D1). Increased cyclin D1 expression speeds up heterodimerization of cyclin D-CDK4/6 complex formation. Amplification of CCND1 sequences is also very common in luminal BC subtypes. Furthermore, ER^+ BCs display overexpression of estrogen receptors to sustain estrogen-dependent increased cellular remodeling (Thu et al. 2018). Additionally, oncogenic mutations in PIK3CA are highly implicated in one-third instances of BC; specifically in luminal types and in $HER2^+$ ones. This gene encodes P110α, the catalytic subunit of PI3K; thus, excessively stimulated PIK3CA promotes cell cycle progression via mitogenic overstimulation of AKT/mTOR signaling. Unlike other BC subtypes, ER^+ BC usually harbors fully functional Rb- and p53- mediated tumor suppression system rendering comparatively higher genomic stability (Bower et al. 2017). Amplification of CDK4 gene is specifically frequent in $HER2^+$ BC. Additionally, this subtype exhibits prevalent gain-of-function mutations of proto-oncogenes such as PIK3CA, PTEN etc. and loss-of-function mutation of TP53. Apart from, amplification in ERBB2 gene, copy gain of CCND1 is also frequent in $HER2^+$ BC (Thu et al. 2018). On contrary, loss-of-function mutation of RB1 or its deletions results in compromised regulation of Rb/E2F/CDK4/6 cascade. Moreover, BRCA1, a DNA damage response gene, is often found to be mutated in this BC subtype. Aneuploidy is highly frequent in TNBC subtypes with persistent loss-of-function mutation of TP53 gene. Increased instances of copy umber gain of CCNE1 DNA are highly prevalent in TNBCs along with inhibitory mutation of PTEN gene activity. Studies have reported that due to higher genomic instability and variability TNBC subtype often suffers from increased expression of genes related to spindle assembly checkpoint during mitotic division. This includes TTK, MAD2, BUB1, AURKB etc (Bower et al. 2017).

1.6. Breast cancer and apoptosis

Apoptosis is a self-governing procedure that encompasses the initiation, and regulation of a broad spectrum of genes, resulting in programmed cellular death. This process is crucial for the elimination of undesirable cells and for upholding a steady internal milieu. The execution of apoptosis can occur through either a caspase-mediated or a caspase-individualistic manner. The caspase-mediated pathway can be categorized into the extrinsic pathway and the intrinsic pathway. Caspases comprise catalytic proteins that act as cysteine proteases. According to their involvement in respective cellular processes, they can be segregated into two subfamilies, namely the apoptotic and inflammatory subfamily (Yuan et al. 2022). Among eighteen known mammalian caspases, caspases 2, 3, 6, 7, 8, 9, and 10 are classified to be apoptotic ones: caspase 2 participates in several cell death cascades, while caspases 3, 6, and 7 function as end-stage executioners. In contrast, caspases 8 and 10 are indispensable in the extrinsic pathway, and caspase 9 selectively participate in the intrinsic pathway. Induction of extrinsic mode of apoptosis is facilitated by the activation of caspases through the interaction between cell surface bound death receptor and their cognate ligand. Members of TNFR superfamily are chiefly involved in extrinsic apoptosis. This includes CD120a (commonly known as TNFR1), APO-1/CD95 (commonly called Fas), Weasl (also known as APO-2/death receptor3 duplex), TRAIL-R1 (alternatively known as DR-4), TRAIL-R2 (alternatively known as DR-5), and DR-6 (Pontsho and Lesetja 2015). Initiation of extrinsic apoptosis can be explained with Fas/FasL interaction which crucially synchronizes immune signaling and corresponding pro-apoptotic effects. Fas is present in two forms: membrane-bound form (mFas) and soluble form (sFas). The interaction of FasL with mFas and sFas differs markedly. Upon binding of mFas and FasL lead to death domain (FADD) recruitment and subsequent association with procaspases 10 and 8, resulting in the formation of the DISC, which subsequently activates downstream signaling cascades by cleaving Bid to tBid. tBid in next, activates Bak and Bax on downstream that induce apoptosis and alter permeability of mitochondrial outer membrane. This interaction leads to the formation of the mitochondrial apoptosis-induced channel (MAC) which enables release of cytochrome C into cytosol; thus, merging two different caspase-dependent apoptotic pathways at this point. In the presence of ATP/dATP, cytochrome C interacts with Apaf-1 forming a complex that later matures to form apoptosome. This in turn induces activation procaspase 9 to active caspase 9, subsequently allowing downstream signaling (Yuan et al. 2022). In addition to the extrinsic and intrinsic pathways, caspase-independent pathway of apoptosis too exists. This particular pathway relies on mitochondrial inner membrane bound flavoproteins, termed as apoptosis-inducing factors (AIFs). These AIFs are pro-apoptotic in nature and are effective after they get released into the cytosol due to enhanced mitochondrial permeability or breakdown. Once in the cytoplasm, the AIFs mobilizes inside nucleus and result in chromatin condensation and subsequent fragmentation (Pontsho and Lesetja 2015).

1.7. Vanadium as an anticancer agent

Depending on the fact that metal ions can selectively regulate a wide range of cellular processes, designing and synthesis of metallodrugs was initiated in the field of medicinal chemistry aiming to find cure for ‘difficult to treat’ diseases such as cancer. Till date cancer has been considered as one of the most fatal diseases causing severe mortality over the world. Among several cancer types, incidence of breast cancer is most common among worldwide female population. According to current statistical count, nearly 1.3 million females suffer from mammary carcinoma (Gupta, Shridhar, and Dhillon 2015). In this context, metallodrugs were considered as highly potential anticancer agents from decades. Example of metallodrugs include popular platinum complexes such as cis-$[Pt(NH_3)_2Cl_2]$ and its derivatives oxoplatin and carboplatin which are used as popular chemotherapeutic agents in combination with radiation and other medication in cancer treatment. Interaction between genomic DNA and platinum is essential for exerting cell killing by platinum-based drugs (Wang and Lippard 2005). After initial phase of intensive interest in platinum-based metallodrugs, other potential anticancer metal complexes including gold, palladium, copper, iron-based metallodrugs were also assayed which could follow distinct cell-death mechanisms beyond DNA binding. Despite of being an efficient anticancer mediator, most of the metallodrugs especially, platinum-based drugs, mostly cisplatin exhibits a huge number of adverse effects due to low target selectivity and high off-target toxicity. Thus, introduction of metallodrugs with potent anticancer efficacy and minimal collateral systemic toxicity are of utmost importance in field of cancer therapy. In this regard, though the pharmacological potentials of vanadium as a metallodrug was first exploited in diabetes management, nearly 50 years back vanadium was first implicated in field of cancer research (Kioseoglou et al. 2015). Till then, multiple arrays of vanadium compounds have arisen as prospective therapeutic agents for cancer treatment and management. Vanadium is a well-known first row transitional metal having an electronic configuration of $[Ar]3d^3 4s^2$ with two naturally occurring isotopes, ^{50}V and ^{51}V. Presence of vanadium in abiotic and biotic systems of both marine and terrestrial origins are well established. Among the several elements found on earth, vanadium is the 22nd most abundant one (0.013 % w/w). Human blood plasma contains nearly 200 nM of vanadium and while in tissues, such as kidney, liver and bone, its concentration is approximately 0.3 mg/kg (Ghosh et al. 2022). Vanadium can exist in five different oxidation states, i.e., $V(I^-)$, V(O), V(III), V(IV) and V(V). Among these five, three forms namely, vanadic/V(III), vanadyl/V(IV) and vanadate/ (V). From biological aspects, only two of higher oxidation states of vanadium, i.e., V(IV) and V(V) are of our interest [14] as these two oxidation states of vanadium are capable of forming cationic and anionic complexes within physiological pH (2-8) range. Intracellularly, vanadium exists mostly in tetravalent form, producing vanadyl ion (VO^{2+}) in association with protein. However, only 1% vanadyl ions remain in free unbound state. Besides, pentavalent form of vanadium mostly occurs extracellularly as vanadate ion or (VO_3^-). Based on the chemical structure, anticancer vanadium compounds can be categorized into five groups including binary and tertiary peroxy-vanadates, organometallic vanadocenes, vanadium peroxide-betaine compounds, polyoxovanadate complexes and especially oxidovanadium complexes (Ghosh et al. 2022).

In this regard, the antitumoral efficacy of several vanadium complexes have been explored extensively in various types of cancers. Oxidovanadium derivatives of flavonoids have already been studied to show selective anticancer effectivities in bone cancer *in vitro* (Ghosh et al. 2022). Antitumoral therapeutic studies of vanadocene compounds have also been descripted in hepatic and testicular carcinomas. Alongside, another vanadium compound known as metvan, has been studied extensively for its anticancer activity across several types of cancer cells including multiple myeloma cells, leukemic cells and also solid tumors derived from other vital organs such as ovary, prostate, mammary gland, brain, etc (D'Cruz and Uckun 2002). Additionally, heterocyclic vanadium derivatives those are able to act as Schiff base, have also been studied to exhibit antitumor activity recently against osteosarcoma, mammary carcinoma and colon carcinoma.

Universally, vanadium has been recorded that it inhibits tumor growth by inhibiting uncontrollable tumor cell proliferation and inducing apoptosis. The potentials of vanadium complexes in ROS-RNS-driven apoptosis, involvement in autophagy, cell differentiation and even in anoikis mechanistic procedures or in onco-gene modulation either individually or collectively contribute to the possibility of designating vanado-drugs as potent anticancer agents. Vanadium is able to impede catalytic activities of several transport proteins including sodium-potassium pump, proton/potassium ATPase pump; cargo trafficking proteins such as myosin-ATPase, dynein; phosphorylases such as adenylate kinase, phosphofructokinase etc. Conversely, several enzymes get invigorated by vanadium such as glyceraldehyde-3-PO_4 dehydrogenase, glycogen synthase mitochondrial complex IV, tyrosine phosphorylase etc.

At present, we have studied anticarcinogenic properties of a newly synthesized hydrophilic mononuclear dipicolinic acid passivated 1-methyl- and 1-allyl-imidazole-substituted oxidovanadium (IV) complexes in BC (Ghosh et al. 2022, Biswal et al. 2017). In this context, it is important to notify that along with amphiphilic nature and several pharmacological advantages, dipicolinic acid, present in various natural compounds, is known to stabilize unusual oxidation states of the metals (Jakusch et al. 2003). Besides, pentameric ring structure and potency to intercalate and cleave DNA strands (Keter 2010, Pizarro and Sadler 2009, Reedijk 2003) due to presence of heteroatom nitrogen, imidazole shows significant antioxidant (Smith and Reeves 1987), antimicrobial (Aridoss et al. 2006, Bhandari et al. 2009, Eslami Amirabadi et al. 2019) as well as anticancer (Congiu, Cocco, and Onnis 2008) therapeutic efficacies. For easy interpretation, these compounds have been denoted as VOL and OVMI respectively and their chemical structure has been described in detail in Chapter 3 and 4 respectively.

1.8. Chrysin as an anticancer agent

As discussed in above sections, among several lines of cancer therapeutics, chemotherapy has been chosen as a recurrently used productive modality of cancer treatment till days for both early and late-stage onco-patients. However, chemotherapy comes with a bunch of adverse effects including nausea, vomiting, diarrhea, alopecia, neuropathy, neutropenia, myalgia, and fatigue, that can result in diminished patient compliance. Inline, phytochemicals, that are known to harbor antineoplastic efficacy can be considered as safe option in contrast to chemotherapeutic agents. Phytochemicals, on the basis of their chemical structure can be categorized in to several group; among which flavonoids have widely been acknowledged as a versatile resource for the exploration and development of anticancer agents. Along with possessing cancer cell-killing property, they are biocompatible and non-toxic to non-transformed healthy body cells when used at proper dosage (Naz et al. 2019). Thus, replacing conventional chemotherapy with flavonoid-based treatment will not only be effective against cancer cells, but also will come with lesser probability of adverse effects. Among these flavonoids, chrysin (chemically characterized as 5,7-dihydroxy-2-phenyl-4H-chromene-4-one or briefly, 5,7-dihydroxyflavone) is a naturally occurring compound with a 15-carbon backbone that has shown to exert promising pharmacological properties including antibacterial, antineoplastic, neuroprotective, antiviral, antiasthmatic, anti-inflammatory, hepatoprotective, nephroprotective, cardioprotective, anti-diabetic, antidepressant, anxiolytic, and antiarthritic activities. The natural origins of chrysin is chiefly honey, where the chrysin content can vary from 0.10 mg/kg in honeydew honey to 5.3 mg/kg in forest honey (Ghosh et al. 2023). Other natural sources of chrysin include propolis, with a chrysin content of 28 g/L, as well as various other plant species such as *Pelargonium crispum*, *Passiflora incarnate*, *Oroxylum indicum* etc act as the source of chrysin.

1.8.1. Chrysin in breast cancer

Chrysin pretreatment is potentially cytotoxic to MCF-7 cells where it does so by altering expression of p53 protein expression. Activation of ATM-Chk2 pathway without DNA damage has been noted due to chrysin treatment *in vitro* as well. In a study against T47D cells, its co-sensitization with metformin, has been proven to diminish cyclin D1 and hTERT gene expression to stall cell cycle progression at G_0 / G_1 stage. Moreover, pro-apoptotic as well as antimetastatic role of chrysin was studied in human TNBC cells where it has been observed to repress MMP-10 and Akt signaling (Talebi et al. 2021). When treatments were made on 4T1 cells and respective tumor xenographs, chrysin was found to reduce survival of cancer cells in hypoxic conditions. Additionally, it hindered the activation of STAT3 and reduced the expression of VEGF in these hypoxic cancer cells, effectively putting a halt to the formation of hypoxia-driven angiogenesis, thereby, suppressing and spread of metastatic cancer. Furthermore, chrysin exhibited

TRAIL-mediated apoptotic death of MDA-MB-cells. Additionally, chrysin has been observed to induce apoptosis by promoting the expression of Skp2 and LRP6 while simultaneously downregulating the expression of several metastatic markers sch as MMP-2, MMP-9, fibronectin, and snail in MDA-MB-231 cells (Talebi et al. 2021).

1.9. Cancer nanotherapeutics

Conventional therapeutic approaches for cancer, such as tumor removal surgery, hormone therapy, chemotherapy, radiation, and even immunotherapy, offer limited benefits in terms of cancer treatment (Sengupta and Balla 2018). These strategies often result in collateral damage to vital organs and a decrease in the average survival rates of patients. Hence, the significance of newly developed bioanalytical strategies that facilitate the overall treatment procedure in cancer patients becomes apparent. In this context, the detrimental effects of traditional cancer therapeutics can be effectively bypassed by substituting them with naturally occurring plant-derived polyphenolic anticancer compounds. However, the poor solubility and decreased bioavailability resulting from inadequate absorption and rapid metabolism pose significant challenges in the administration of chrysin for cancer treatment. In this regard, the utilization of nanotechnology is a common strategy that can effectively enhance the bioavailability of hydrophobic natural compounds specifically at the tumor site (Matsumura and Maeda 1986). The effectiveness of a chemotherapeutic drug or any anticancer agent can be improved through the implementation of a smart nano-drug delivery system (nano-DDS) labeled with specific targeting ligands, which enables a precise interaction with tumor cells and facilitates intelligent stimulus-boosted drug unloading performance within the tumor microenvironment. Upon intravenous injection, these circulating nanoparticles can selectively accumulate at the tumor site by exploiting the leaky and permeable vasculature, and their retention is further enhanced by the limited lymphatic drainage, a phenomenon known as the enhanced permeability and retention (EPR) effect (Farokhzad and Langer 2006).

However, the limited ability of nanocarriers to pass through multiple layers of tumor cells is attributed to the elevated interstitial fluid pressure and the dense cell population at the tumor site, resulting in uneven distribution of its cargo. It is anticipated that these challenges can be overcome through the utilization of ligand-labeled nano-formulations, which not only passively accumulate at the tumor site (due to the enhanced permeability and retention effect), but also actively accumulate by modifying the surface with ligand molecules capable of recognizing tumor-specific receptor molecules (Salmaso et al. 2004). In summary, this approach offers enhanced tumor-selectivity and improved delivery of cargo within cells, thus providing a targeted nano-drug delivery system. Consequently, in a targetable nano-drug delivery system, the surface of the nanocarriers' core is often appropriately tailored with targeting moieties such as hormones, aptamers, vitamins, peptides, antibodies, and so on. In addition, an optimal 'intelligent' drug delivery system (DDS) must prevent premature unloading at nonspecific locations and possess the ability to customize therapeutic agents by differentiating between healthy cells and neoplastic cells. Among the various mechanisms for releasing drugs guided by stimuli in nanocarriers, the alteration in pH is the most extensively examined due to the clear presence of a pH gradient in the tumor microenvironment (Zhu and Chen 2015). pH-responsiveness can be achieved by employing substances such as polyacrylic acid and poly methyl acrylate. Among various inorganic nanoparticles, mesoporous silica nanoparticles possess remarkable characteristics of a silica framework that is well-suited for pH-guided drug release at the site of a tumor. The well-organized porous network of mesoporous silica nanoparticles enables controlled loading of therapeutic agents and ensures a consistent release rate. The overall lack of toxicity and chemical stability of mesoporous silica nanoparticles make them highly suitable as biocompatible carriers for therapeutic purposes *in vivo* (Giret, Wong Chi Man, and Carcel 2015). Furthermore, the larger surface area and the ease of modifying the surface using the widely utilized alkoxysilane chemistry establish mesoporous silica nanoparticles as an ideal candidate for intelligent nano drug delivery systems.

1.10. References

Allison, Kimberly H, M Elizabeth H Hammond, Mitchell Dowsett, Shannon E McKernin, Lisa A Carey, Patrick L Fitzgibbons, Daniel F Hayes, Sunil R Lakhani, Mariana Chavez-MacGregor, and Jane Perlmutter. 2020. "Estrogen and progesterone receptor testing in breast cancer: ASCO/CAP guideline update."

Arnandis, Teresa, Pedro Monteiro, Sophie D Adams, Victoria Louise Bridgeman, Vinothini Rajeeve, Emanuela Gadaleta, Jacek Marzec, Claude Chelala, Ilaria Malanchi, and Pedro R Cutillas. 2018. "Oxidative stress in cells with extra centrosomes drives non-cell-autonomous invasion." *Developmental cell* 47 (4):409-424. e9.

Atchley, Deann P, Constance T Albarracin, Adriana Lopez, Vicente Valero, Christopher I Amos, Ana Maria Gonzalez-Angulo, Gabriel N Hortobagyi, and Banu K Arun. 2008. "Clinical and pathologic characteristics of patients with BRCA-positive and BRCA-negative breast cancer." *Journal of Clinical Oncology* 26 (26):4282.

Biswal, Debanjana, Nikhil Ranjan Pramanik, Syamal Chakrabarti, Michael GB Drew, Krishnendu Acharya, and Swarnendu Chandra. 2017. "Syntheses, crystal structures, DFT calculations, protein interaction and anticancer activities of water soluble dipicolinic acid-imidazole based oxidovanadium (iv) complexes." *Dalton Transactions* 46 (47):16682-16702.

Bower, Jacquelyn J, Leah D Vance, Matthew Psioda, Stephanie L Smith-Roe, Dennis A Simpson, Joseph G Ibrahim, Katherine A Hoadley, Charles M Perou, and William K Kaufmann. 2017. "Patterns of cell cycle checkpoint deregulation associated with intrinsic molecular subtypes of human breast cancer cells." *NPJ Breast Cancer* 3 (1):9.

Brown, Nicholas S, and Roy Bicknell. 2001. "Hypoxia and oxidative stress in breast cancer Oxidative stress-its effects on the growth, metastatic potential and response to therapy of breast cancer." *Breast cancer research* 3 (5):1-5.

Brown, NS, EH Streeter, A Jones, AL Harris, and R Bicknell. 2005. "Cooperative stimulation of vascular endothelial growth factor expression by hypoxia and reactive oxygen species: the effect of targeting vascular endothelial growth factor and oxidative stress in an orthotopic xenograft model of bladder carcinoma." *British journal of cancer* 92 (9):1696-1701.

Chen, Delin, Omid Tavana, Bo Chu, Luke Erber, Yue Chen, Richard Baer, and Wei Gu. 2017. "NRF2 Is a Major Target of ARF in p53-Independent Tumor Suppression." *Molecular Cell* 68 (1):224-232.e4. doi: https://doi.org/10.1016/j.molcel.2017.09.009.

Chen, Xi, and Juan R Cubillos-Ruiz. 2021. "Endoplasmic reticulum stress signals in the tumour and its microenvironment." *Nature Reviews Cancer* 21 (2):71-88.

Chen, Xi, Dimitrios Iliopoulos, Qing Zhang, Qianzi Tang, Matthew B Greenblatt, Maria Hatziapostolou, Elgene Lim, Wai Leong Tam, Min Ni, and Yiwen Chen. 2014. "XBP1 promotes triple-negative breast cancer by controlling the HIF1α pathway." *Nature* 508 (7494):103-107.

Chong, Stephen Jun Fei, Jolin Xiao Hui Lai, Jie Qing Eu, Gregory Lucien Bellot, and Shazib Pervaiz. 2018. "Reactive oxygen species and oncoprotein signaling-A dangerous liaison." *Antioxidants & Redox Signaling* 29 (16):1553-1588.

Criscitiello, Carmen, HA Azim Jr, PC Schouten, SC Linn, and Christos Sotiriou. 2012. "Understanding the biology of triple-negative breast cancer." *Annals of oncology* 23:vi13-vi18.

D'Cruz, Osmond J, and Fatih M Uckun. 2002. "Metvan: a novel oxovanadium (IV) complex with broad spectrum anticancer activity." *Expert Opinion on Investigational Drugs* 11 (12):1829-1836.

Dixon, Scott J., and Brent R. Stockwell. 2019. "The Hallmarks of Ferroptosis." *Annual Review of Cancer Biology* 3 (1):35-54. doi: 10.1146/annurev-cancerbio-030518-055844.

Dodson, Matthew, Raul Castro-Portuguez, and Donna D. Zhang. 2019. "NRF2 plays a critical role in mitigating lipid peroxidation and ferroptosis." *Redox Biology* 23:101107. doi: https://doi.org/10.1016/j.redox.2019.101107.

Fan, Ping, and V Craig Jordan. 2018. "How PERK kinase conveys stress signals to nuclear factor-κB to mediate estrogen-induced apoptosis in breast cancer cells?" *Cell Death & Disease* 9 (8).

Farokhzad, Omid C, and Robert Langer. 2006. "Nanomedicine: developing smarter therapeutic and diagnostic modalities." *Advanced drug delivery reviews* 58 (14):1456-1459.

Ferlay, Jacques, Murielle Colombet, Isabelle Soerjomataram, Colin Mathers, Donald M Parkin, Marlon Piñeros, Ariana Znaor, and Freddie Bray. 2019. "Estimating the global cancer incidence and mortality in 2018: GLOBOCAN sources and methods." *International journal of cancer* 144 (8):1941-1953.

Ferlini, C, G Scambia, M Marone, M Distefano, C Gaggini, G Ferrandina, A Fattorossi, G Isola, P Benedetti Panici, and S Mancuso. 1999. "Tamoxifen induces oxidative stress and apoptosis in oestrogen receptor-negative human cancer cell lines." *British journal of cancer* 79 (2):257-263.

Ghosh, Noyel, Sharmistha Chatterjee, Debanjana Biswal, Nikhil Ranjan Pramanik, Syamal Chakrabarti, and Parames C Sil. 2022. "Oxidative stress imposed in vivo anticancer therapeutic efficacy of novel imidazole-based oxidovanadium (IV) complex in solid tumor." *Life Sciences* 301:120606.

Ghosh, Noyel, Mousumi Kundu, Sumit Ghosh, Abhishek Kumar Das, Samhita De, Joydeep Das, and Parames C Sil. 2023. "pH-responsive and targeted delivery of chrysin via folic acid-functionalized mesoporous silica nanocarrier for breast cancer therapy." *International Journal of Pharmaceutics* 631:122555.

Giret, Simon, Michel Wong Chi Man, and Carole Carcel. 2015. "Mesoporous-silica-functionalized nanoparticles for drug delivery." *Chemistry–A European Journal* 21 (40):13850-13865.

Gorrini, Chiara, Isaac S. Harris, and Tak W. Mak. 2013. "Modulation of oxidative stress as an anticancer strategy." *Nature Reviews Drug Discovery* 12 (12):931-947. doi: 10.1038/nrd4002.

Gupta, Addya, K Shridhar, and PK Dhillon. 2015. "A review of breast cancer awareness among women in India: Cancer literate or awareness deficit?" *European Journal of Cancer* 51 (14):2058-2066.

Kioseoglou, Efrosini, Savvas Petanidis, Catherine Gabriel, and Athanasios Salifoglou. 2015. "The chemistry and biology of vanadium compounds in cancer therapeutics." *Coordination Chemistry Reviews* 301:87-105.

Kundu, Namita, Shaozeng Zhang, and Amy M Fulton. 1995. "Sublethal oxidative stress inhibits tumor cell adhesion and enhances experimental metastasis of murine mammary carcinoma." *Clinical & experimental metastasis* 13:16-22.

Lee, Seungeun, Eunhye Lee, EunYi Ko, Mina Ham, Hye Min Lee, Eun-Sook Kim, Minsoo Koh, Hyun Kyung Lim, Joohee Jung, and So Yeon Park. 2018. "Tumor-associated macrophages secrete CCL2 and induce the invasive phenotype of human breast epithelial cells through upregulation of ERO1-α and MMP-9." *Cancer Letters* 437:25-34.

Li, Christopher I, Benjamin O Anderson, Janet R Daling, and Roger E Moe. 2003. "Trends in incidence rates of invasive lobular and ductal breast carcinoma." *Jama* 289 (11):1421-1424.

Liu, Dongping, and Yang Xu. 2011. "p53, oxidative stress, and aging." *Antioxidants & redox signaling* 15 (6):1669-1678.

Makki, Jaafar. 2015. "Diversity of breast carcinoma: histological subtypes and clinical relevance." *Clinical medicine insights: Pathology* 8:CPath. S31563.

Marcar, Lynnette, Kankana Bardhan, Liliana Gheorghiu, Patrick Dinkelborg, Heike Pfäffle, Qi Liu, Meng Wang, Zofia Piotrowska, Lecia V. Sequist, Kerstin Borgmann, Jeffrey E. Settleman, Jeffrey A. Engelman, Aaron N. Hata, and Henning Willers. 2019. "Acquired Resistance of EGFR-Mutated Lung Cancer to Tyrosine Kinase Inhibitor Treatment Promotes PARP Inhibitor Sensitivity." *Cell Reports* 27 (12):3422-3432.e4. doi: https://doi.org/10.1016/j.celrep.2019.05.058.

Matsumura, Yasuhiro, and Hiroshi Maeda. 1986. "A new concept for macromolecular therapeutics in cancer chemotherapy: mechanism of tumoritropic accumulation of proteins and the antitumor agent smancs." *Cancer research* 46 (12_Part_1):6387-6392.

Moloney, Jennifer N., and Thomas G. Cotter. 2018. "ROS signalling in the biology of cancer." *Seminars in Cell & Developmental Biology* 80:50-64. doi: https://doi.org/10.1016/j.semcdb.2017.05.023.

Mueller, Claudius, Amanda Haymond, Justin B Davis, Alexa Williams, and Virginia Espina. 2018. "Protein biomarkers for subtyping breast cancer and implications for future research." *Expert review of proteomics* 15 (2):131-152.

Naz, Saima, Muhammad Imran, Abdur Rauf, Ilkay Erdogan Orhan, Mohammad Ali Shariati, Muhammad Shahbaz, Tahira Batool Qaisrani, Zafar Ali Shah, Sergey Plygun, and Mojtaba Heydari. 2019. "Chrysin: Pharmacological and therapeutic properties." *Life sciences* 235:116797.

Perillo, Bruno, Marzia Di Donato, Antonio Pezone, Erika Di Zazzo, Pia Giovannelli, Giovanni Galasso, Gabriella Castoria, and Antimo Migliaccio. 2020. "ROS in cancer therapy: The bright side of the moon." *Experimental & molecular medicine* 52 (2):192-203.

Pontsho, Moela, and R. Motadi Lesetja. 2015. "Apoptotic Molecular Advances in Breast Cancer Management." In *Cell Death*, edited by M. Ntuli Tobias, Ch. 10. Rijeka: IntechOpen.

Prokakis, Evangelos, Anna Dyas, Regina Grün, Sonja Fritzsche, Upasana Bedi, Zahra B Kazerouni, Robyn L Kosinsky, Steven A Johnsen, and Florian Wegwitz. 2021. "USP22 promotes HER2-driven mammary carcinoma aggressiveness by suppressing the unfolded protein response." *Oncogene* 40 (23):4004-4018.

Reczek, Colleen R., Kıvanç Birsoy, Hyewon Kong, Inmaculada Martínez-Reyes, Tim Wang, Peng Gao, David M. Sabatini, and Navdeep S. Chandel. 2017. "A CRISPR screen identifies a pathway required for paraquat-induced cell death." *Nature Chemical Biology* 13 (12):1274-1279. doi: 10.1038/nchembio.2499.

Redza-Dutordoir, Maureen, and Diana A Averill-Bates. 2016. "Activation of apoptosis signalling pathways by reactive oxygen species." *Biochimica et Biophysica Acta (BBA)-Molecular Cell Research* 1863 (12):2977-2992.

Salmaso, Stefano, Alessandra Semenzato, Paolo Caliceti, Johan Hoebeke, Fabio Sonvico, Catherine Dubernet, and Patrick Couvreur. 2004. "Specific antitumor targetable β-cyclodextrin− poly (ethylene glycol)− folic acid drug delivery bioconjugate." *Bioconjugate chemistry* 15 (5):997-1004.

Salvagno, Camilla, Jessica K Mandula, Paulo C Rodriguez, and Juan R Cubillos-Ruiz. 2022. "Decoding endoplasmic reticulum stress signals in cancer cells and antitumor immunity." *Trends in cancer*.

Schick, Jason, Raquel P Ritchie, and Carolina Restini. 2021. "Breast cancer therapeutics and biomarkers: past, present, and future approaches." *Breast Cancer: Basic and Clinical Research* 15:1178223421995854.

Sengupta, Somoshree, and Vamsi K Balla. 2018. "A review on the use of magnetic fields and ultrasound for non-invasive cancer treatment." *Journal of advanced research* 14:97-111.

Sies, Helmut, and Dean P Jones. 2020. "Reactive oxygen species (ROS) as pleiotropic physiological signalling agents." *Nature reviews Molecular cell biology* 21 (7):363-383.

Sinn, Hans-Peter, and Hans Kreipe. 2013. "A brief overview of the WHO classification of breast tumors, focusing on issues and updates from the 3rd edition." *Breast care* 8 (2):149-154.

Sipe Jr, Herbert J, Sandra J Jordan, Phillip M Hanna, and Ronald P Mason. 1994. "The metabolism of 17β-estradiol by lactoperoxidase: a possible source of oxidative stress in breast cancer." *Carcinogenesis* 15 (11):2637-2643.

Slamon, Dennis J, Gary M Clark, Steven G Wong, Wendy J Levin, Axel Ullrich, and William L McGuire. 1987. "Human breast cancer: correlation of relapse and survival with amplification of the HER-2/neu oncogene." *science* 235 (4785):177-182.

Society, American Cancer. 2020. "How common is breast cancer?" *Breast Cancer Statistics 20190*.

Spitz, Douglas R, Julia E Sim, Lisa A Ridnour, Sandra S Galoforo, and Yong J Lee. 2000. "Glucose deprivation-induced oxidative stress in human tumor cells: a fundamental defect in metabolism?" *Annals of the New York Academy of Sciences* 899 (1):349-362.

Szostakowska, Małgorzata, Alicja Trębińska-Stryjewska, Ewa Anna Grzybowska, and Anna Fabisiewicz. 2019. "Resistance to endocrine therapy in breast cancer: molecular mechanisms and future goals." *Breast Cancer Research and Treatment* 173:489-497.

Talebi, Marjan, Mohsen Talebi, Tahereh Farkhondeh, Jesus Simal-Gandara, Dalia M Kopustinskiene, Jurga Bernatoniene, and Saeed Samarghandian. 2021. "Emerging cellular and molecular mechanisms underlying anticancer indications of chrysin." *Cancer Cell International* 21 (1):1-20.

Thu, K. L., I. Soria-Bretones, T. W. Mak, and D. W. Cescon. 2018. "Targeting the cell cycle in breast cancer: towards the next phase." *Cell Cycle* 17 (15):1871-1885. doi: 10.1080/15384101.2018.1502567.

van Seijen, Maartje, Esther H Lips, Alastair M Thompson, Serena Nik-Zainal, Andrew Futreal, E Shelley Hwang, Ellen Verschuur, Joanna Lane, Jos Jonkers, and Daniel W Rea. 2019. "Ductal carcinoma in situ: to treat or not to treat, that is the question." *British journal of cancer* 121 (4):285-292.

Wang, Dong, and Stephen J Lippard. 2005. "Cellular processing of platinum anticancer drugs." *Nature reviews Drug discovery* 4 (4):307-320.

Yuan, Lie, Yongqing Cai, Liang Zhang, Sijia Liu, Pan Li, and Xiaoli Li. 2022. "Promoting apoptosis, a promising way to treat breast cancer with natural products: A comprehensive review." *Frontiers in Pharmacology* 12:801662.

Zhou, Wenhui, Huan Fang, Qiuju Wu, Xinye Wang, Rong Liu, Fubin Li, Ji Xiao, Lin Yuan, Zhongmei Zhou, and Junying Ma. 2019. "Ilamycin E, a natural product of marine actinomycete, inhibits triple-negative breast cancer partially through ER stress-CHOP-Bcl-2." *International journal of biological sciences* 15 (8):1723.

Zhu, Ying-Jie, and Feng Chen. 2015. "pH-responsive drug-delivery systems." *Chemistry–An Asian Journal* 10 (2):284-305.

Chapter 2

Reagents and methodology

2.1. Utilized reagents

The following reagents/materials were procured from respective companies, listed below in Table 1

Table 1: *List of utilized materials and reagents*

Reagents	Companies
(3-aminopropyl) triethoxysilane (APTES – 99 % extra pure), Chrysin (97 % pure), polyacrylic acid (PAA), lactate dehydrogenase (LDH) leakage assay kit, ethanol, fluorescein isothiocyanate (FITC), dimethyl sulfoxide (DMSO), phosphatase inhibitor cocktail. Protease inhibitor cocktail, coumaric acid, luminol, and cisplatin	Sigma-Aldrich (St. Louis, Missouri, US)
VECTASHILD mounting medium with inbuilt DAPI	Vector Laboratories, Inc. (Mowry Ave, CA 94560)
Gibco fetal bovine serum (FBS), Dulbecco's modified eagle's media (DMEM), trypsin, Bicinchoninic acid (BCA) protein measurement kit, N-acetylcysteine (NAC), ribonuclease, Verso cDNA synthesis kit, DreamTaq Green PCR Master Mix (2X), TRIzol RNA isolation reagent solution and APO-BrdU™ TUNEL assay kit with Alexa Fluor™ 488, PageRuler^{TM} Prestained Protein Ladder	Thermo Fisher Scientific, US.
RPMI-1640 cell culture media, L-glutamine, amphotericin B, gentamycin, penicillin, streptomycin and non-essential amino acids	Hi-media, Maharashtra, India
Sodium hydroxide (NaOH), sodium chloride (NaCl), disodium hydrogen phosphate dihydrate, bovine serum albumin (BSA), tetraethyl orthosilicate (TEOS), 1-(3-dimethylaminopropyl)-3-ethyl carbodiimide hydrochloride (EDC.HCl – 99 % pure), N-hydroxy succinimide (NHS – 97 % pure), 3-(4,5-dimethylthiazol-2-yl)-2,5-diphenyltetrazolium bromide (MTT)	SRL, India
EXPOSE Rabbit specific HRP/DAB detection IHC kit (ab80437); Prestained Protein Ladder – Broad molecular weight (10-245 kDa) (ab116028); Primary antibodies to Calpain 1 – Domain IV (ab39170), E-cadherin (ab76055), p53 (ab1413), eIF-2α-phospho S51 (ab32157), Bcl-2 (ab7973), caspase 8 (ab25901), GRP78 (ab21685), SOD2 (ab13533), TNF-α (ab6671) and TRADD (ab223040); Goat polyclonal secondary antibody to rabbit IgG – H&L (HRP) (ab97051)	Abcam, Cambridge, UK

Primary antibodies to phospho-GSK-3β (#5558), Cyclin D1(#2978), β-actin (#4970), PARP (#9532), phosphor-Akt (#4060), caspase 3 (#9662), caspase 9 (#9508), cytochrome C (#4272), Apaf-1 (#8723), Bax (#2772), VDAC (#4866), MMP-2 (#40994), CHOP (#5554), Ki67 (#12202), vimentin (#5741); Anti-mouse IgG – HRP-linked secondary antibody (#7076)	Cell Signaling Technology, Danvers, MA 01923
MMP-9 (A0289), N-cadherin (A19083), ICAM1 Rabbit polyclonal antibody (A20472)	ABclonal Technology, MA, US
VCAM1 Rabbit monoclonal antibody (A11236)	Neo Scientific, Cambridge, MA
β-actin (BB-AB0024)	Bio Bharti Life Science Pvt. Ltd., Kolkata, India
Alkaline phosphatase (ALP), alanine transferase (ALT), blood urea nitrogen (BUN), and creatinine assay kits.	Span Diagnostics, India

2.2. Methodology

2.2.1. *In vitro* experiments

2.2.1.1. Cell culture

Human triple-negative carcinoma cell line MDA-MB-231 was obtained originally from the American Type Culture Collection (ATCC). Additionally, an immortalized normal kidney epithelial cell line NKE was received as a gift from Prof. Kaushik Biswas. For the *in vivo* experiment, murine triple-negative mammary carcinoma cells 4T1 were cultured which was wisely gifted by Dr. Kuldip Jana. While, MCF-7, NKE, and 4T1 cells were cultured in RPMI-1640 cell culture media, MDA-MB-231 was cultured in DMEM. It is noteworthy that in every case, culture media were supplemented with 10 % FBS along with non-essential amino acids and the required amount of antibiotics as well as anti-fungal agents. Cells were maintained in a humified 5 % CO_2 chamber at 37 °C temperature (Sarkar et al. 2016, Ghosh, Kundu, et al. 2022, Ghosh et al. 2023).

2.2.1.2. Defining cell viability through MTT assay

Cytotoxicity in MCF-7, MDA-MB-231, and NKE cells was determined following basic protocol using MTT reagent (Ghosh et al. 2023). Briefly, cells were seeded at a density of 5×10^3 cells per well in 200 µl 10 % FBS supplemented with cognate growth media. Following maintaining for 24 hours at 37 °C temperature within a humified incubator containing 5 % CO_2 for confluency, cells were treated with cognate compound for 24/48 hours providing unaltered environmental conditions. After completion of treatment hours, media from wells was discarded and MTT solution (100 µl; 0.5 mg/ml) was added to each well. Treated cells within the MTT solution were incubated further for 4 hours at 37 °C temperature within a 5 % CO_2 incubator. Following incubation 100 µl DMSO was added to each well and spectrophotometric absorption reading was taken at 570 nm with the help of a ninety-six-well microplate reader. The viability of a particular cell in response to a particular compound was determined by comparing the absorbance of treated cells to that of control cells. Respectively, by plotting standard curves, IC_{50} values of compounds in particular cell lines were evaluated.

2.2.1.3. Assessment of *in vitro* LDH leakage

After being treated with cognate compounds, MCF-7 / MDA-MB-231 cells were checked for lactate dehydrogenase (LDH) leakage. LDH leakage measurement was taken colorimetrically at 450 nm by following the manufacturer’s protocol (Ghosh et al. 2022, Sadhukhan et al. 2016).

2.2.1.4. Ascertainment of the mode of cell death

To ascertain the mode of cell death, treated cells were either stained with FITC-tagged Annexin-V (Ghosh et al. 2023) or double stained with FITC-Annexin-V and PI following the manufacturer’s protocol (Ghosh, Kundu, et al. 2022). For flow cytometry-based analysis, treated cells suspended in 500 µl of 1X Annexin-V binding assay buffer, were stained with 5 µl of FITC-Annexin-V alone or both for 5 minutes. Following staining cells were subjected to FACS Verse cell sorter either at 530 nm or for both 530 nm and 610 nm. For the confocal microscopic study, a similar staining protocol was followed for cells grown on coverslips and finally was viewed with either a dual filter set for DAPI and FITC or a triple filter set for DAPI, rhodamine, and FITC.

2.2.1.5. Ascertainment of intracellular reactive oxygen species (ROS)

Intracellular ROS content was elucidated following standard DCFHDA staining protocol (Sadhukhan et al. 2016, Ghosh et al. 2023). In general, 2×10^5 numbers of cells after being treated with specific doses of selective compounds, were washed twice in 1X PBS and stained with DCFDA solution at a final concentration of 2 µM. Cells were allowed to incubate in the dark with DCFHDA for 20 minutes at 37 °C so that DCFHDA could react with intracellular ROS to generate green fluorescent DCF. After optimum incubation, cells were washed again 1X PBS and were checked for intracellular ROS content in the flow cytometer (BD Biosciences) using a bandpass filter of 525 nm wavelength. For visual interpretation cells grown on coverslips were allowed to stain with DCFHDA solution after being treated with the cognate compound in a similar fashion followed for flow-cytometer-based study. However, in this case, stained cells were mounted with VECTASHIELD upon glass slides and were studied under a confocal microscope in contrast to DAPI staining.

2.2.1.6. Ascertainment of transmembrane mitochondrial potential (TMP)

Changes in mitochondrial membrane potential were evaluated by JC-1-based fluorescent staining method (Ghosh et al. 2022). Membrane-permeant JC-1 shows potential-dependent accumulation in mitochondria. In monomeric form, it emits green fluorescence emission nearly at 525 nm whereas, its concentration-dependently formed aggregates emit red fluorescence nearly at 590 nm. Consequently, mitochondrial depolarization is indicated by a lowered red-to-green fluorescence intensity ratio. After being treated with cognate compounds as designated concentrations, cells were exposed to JC-1 dye at a final concentration of 5 µM in the dark for half an hour at 37 °C. For flow cytometric evaluation cells were washed in 1X PBS by centrifugation at 300 g for 5 minutes and were examined using a bandpass filter at 525 nm. However, for imaging purposes, stained cells on coverslips were washed twice in 1X PBS, mounted with VERTASHIELD, and finally evaluated under a confocal microscope for red/green fluorescence in contrast to the blue fluorescence of DAPI.

2.2.1.7. Ascertainment of *in vitro* GSSG and GSH content

Following the protocol described elsewhere (Ghosh et al. 2022), quantification of intracellular reduced glutathione (GSH) content was made using Ellman's reagent. Briefly, after being treated with cognate compounds cells were lysed through centrifugation at 12000 rpm for 15 minutes. Resultant whole cell lysates were then added to Ellman's reagent and absorbance was documented at 412 nm resulted due to DTNB reduction. Intracellular GSH content was quantified using a GSH standard curve and values were expressed in µmol per mg of protein.

For glutathione (GSSG) content quantification a standard protocol was followed as described by Hissin and Hilf in 1976 (Hissin and Hilf 1976). Here, cell lysate-treated cells were first mixed with 0.4 M N-ethylmaleimide to prevent GSH oxidation to GSSG, followed by an incubation period of half an hour at room temperature. This mixture was next added with 0.3 M of sodium bisphosphate (Na_2HPO4) and Ellman's reagent and absorbance were recorded again at 412 nm (Sadhukhan et al. 2016).

2.2.1.8. Ascertainment of *in vitro* lipid peroxidation

The extent of intracellular lipid peroxidation gives an idea about the oxidative status of the treated cells. Hence, MCF-7 / MDA-MB-231 cells were initially treated with cognate anticancer agents at specific doses. Afterward, intracellular lipid peroxidation was evaluated in terms of in term of malonaldehyde (MDA) content. Following the preparation of whole cell lysates of the treated and control cells, 20 %

trichloro acetic acid and 0.67 % thiobarbiturate were added and the mixture was heated for an hour at 100 °C, cooled down at room temperature, and processed through centrifugation to eliminate deposited pellet. In the end, a clear supernatant was used to measure the MDA content spectrophotometrically at 535 nm (Ghosh et al. 2023).

2.2.1.9. Assessment of *in vitro* antioxidant enzyme activities

The intracellular oxidative status of treated and control mammary cancer cells was also viewed by assessing the enzyme activities of two prime antioxidant enzymes; namely, catalase (CAT) and superoxide dismutase (SOD) (Ghosh et al. 2022). For assessing CAT activity method described by (Bonaventura, Schroeder, and Fang 1972) was followed. Shortly, whole cell lysates each containing 5 µg of protein from control and treated cells were initially mixed to 0.0075 M of hydrogen peroxide (2.1 ml) and then reduction in the absorbance was calculated spectrophotometrically at 240 nm over 10 minutes. A unit of CAT activity is the concentration of enzyme required to decrease 1 µmol of hydrogen peroxide within a minute. To assess the SOD activity protocol explained by (Nishikimi, Rao, and Yagi 1972) and later modified by (Kakkar, Das, and Viswanathan 1984), was followed. Whole cell lysates containing 5 µg were mixed with sodium pyrophosphate buffer, nitro blue tetrazolium and phenyl methosulfate initially. Later on, the addition of NADH started the reaction. This mixture was incubated for 1.5 minutes at 30 °C followed by termination of the reaction by the addition of 1 ml of glacial acetic acid. Thereafter the absorbance of the chromogen formed was evaluated spectrophotometrically at 560 nm. A unit of SOD activity is the enzyme concentration required to inhibit chromogen production by 50 % in a minute under similar conditions.

2.2.1.10. Analysis of cell cycle distribution

In a nutshell, 1×10^6 cells/ml were seeded in each petri dish initially for the study. After being 80 % confluent, MCF-7 / MDA-MB-231 cells were treated with desired compounds at specific dose/s for 24 hours. Thereafter the treatment, scraped cells were PBS-washed and were fixed in 70 % ice-cold ethanol by keeping cells for an hour at 4 °C. Any ethanol was decanted and cells were centrifuged in 1X PBS (supplemented with 2 % FBS) for an hour at 4 °C at 850 *g*. Resultant cell pellets were incubated with 50 µl of 100 µg/ml RNase solution for half an hour followed by their staining with 0.2 ml (50 µg/ml) of PI and were afterward analyzed flow cytometrically at 617 nm (Ghosh et al. 2023, Zhang et al. 2018). The distribution of cells in different cell cycle phages was depicted through histograms representing DNA content along the x-axis (in terms of PI fluorescence) versus cell numbers along the y-axis.

2.2.1.11. Assessment of mitochondrial swelling

Intracellular Ca^{2+}-mediated mitochondrial swelling was evaluated following the method described elsewhere (Li, Zhang, and Sun 2018). Briefly, mitochondria were isolated from treated 3×10^6 numbers of TNBC cells employing mitochondria isolation buffer made up of 0.25 M sucrose, 0.01 M HEPES, 0.01 M KCl, 1 mM EDTA, 1.5 mM $MgCl_2$ along with protease inhibitor cocktail supplementation. Isolated mitochondria were resuspended in KCl media (pH 7.4) containing 0.125 M KCl, 0.02 M HEPES, 0.005 M of glutamate and malate each, 0.002 M of rotenone and K_2HPO_4. Thereafter, mitochondrial protein concentration was quantified using a standard BCA assay kit at 562 nm. Now an equal number of mitochondria were transferred from each sample group to estimation cuvettes based on equal protein concentration and the absorbance was recorded at 540 nm.

2.2.1.12. Assessing anti-migratory effect through wound healing assay

The anti-migratory effect of anticancer agents on human TNC cell line MDA-MB-231 was checked through a traditional bidirectional wound healing assay (Sarkar et al. 2016). Cells grown up to 80 % confluency in a 6-well culture plate were subjected to wound-making with the help of a 200 µl sterile pipette tip followed by treatment with the compound of interest at specific predetermined doses. The migratory capability of MDA-MB-231 cells was first imaged by a bright field optical microscope after the 0th hour and 24th hour post-treatment. Afterward, the data from the triplicate well were quantified using Image J software and compared with untreated control cells (Pijuan et al. 2019). The anti-migratory effectivity of the compound of interest was evaluated in terms of the percent of wound area closure with respect to the overall area of spread.

2.2.1.13. Acquirement of cytosolic and mitochondrial fractionations

Cytosolic and mitochondrial subcellular fractionations were obtained by sticking to the procedure described elsewhere with slight modification (Chowdhury et al. 2019, Cox and Emili 2006). Concisely, treated cells were lysed within 250-STMDPS buffer (pH 7.4) and added with protease and phosphatase inhibitor cocktails. Subcellular fractionation cells were lysed following the method described elsewhere with minimal modification. OVMI-treated cells were washed in 1X PBS and then were lysed in protease and phosphatase inhibitor-supplemented 250-STMDPS buffer (50 mM Tris HCl, 250 mM sucrose, 5 mM $MgCl_2$, 1 mM PMSF, 1 mM DTT, 25 µg spermidine). Obtained cell lysates were subjected to centrifugation at 800 *g* for 15 minutes and collected supernatant (sup-I) was centrifuged further at 6000 *g* for 15 minutes. Pellet sedimented after the second centrifugation was resuspended with 5 times volumes of ME buffer containing 15 % glycerol, 1.5 % Triton-X, 0.4 M NaCl, 0.02 M Tris-HCl of pH 7.8 and 0.001 M of DTT and PMSF each. Now, the supernatant (sup-II) was further centrifuged at 100,000 *g* for an hour to analyze the translational expression of cytoplasmic fractionation of cytochrome C by immunoblotting. Lastly, another centrifugation was done after sonication-assisted lysis at 14000 *g* for 15 minutes and the obtained supernatant was used for checking immunoblot expression of mitochondrial proteins such as mitochondrial cytochrome C and VDAC. All centrifugation steps were performed at 4 °C temperature.

2.2.1.14. Whole-cell lysate preparation and protein estimation

For whole-cell lysate preparation, cells were initially with the compound of interest for 24 hours (Ghosh et al. 2023). After being treated cells were washed with 1X PBS resuspended, and were lysed using radio-immunoprecipitation assay (RIPA) buffer solution containing 0.5 % sodium deoxycholate, 0.150 M NaCl, Triton X-100, 50 mM Tris and 0.1 % SDS. During lysis, the buffer was supplemented with 5 mM EDTA, 1 mM of each EGTA and sodium orthovanadate, 10 mM sodium fluoride, 1 mM PMSF, phosphatase, and protease inhibitors (pH 8). Following lysis, the lysate was centrifuged at 12000 rpm for 10 minutes at 4 °C. Supernatant collected after centrifugation was then utilized for protein concentration measurement at 562 nm employing BCA assay kit following the manufacturer’s protocol (Das et al., 2022; Ghosh et al., 2022a).

2.2.1.15. Western-blotting

Samples with equal protein concentration were first resolved through 10-12 % SDS-containing polyacrylamide gel electrophoresis (PAGE) (Sinha et al. 2019, Ghosh, Kundu, et al. 2022). Following electrophoretic mobilization, proteins were separated across the gel were transferred onto PVDF membranes employing a Trans-Blot Turbo Transfer System (Bio-Rad, Hercules, CA, USA). Membranes carrying blotted proteins were then incubated in 5 % BSA (w/v) solution made in Tween 20-added tris buffer saline (TBST) for 45 minutes at 37 °C temperature. Following incubation, proteins on the membrane were allowed to react with the primary antibody of interest (1:10000 dilution) at 4 °C overnight on a rhythmic rocker. The next day, blots were washed thrice in 1X TBST followed by 2 hours of incubation in horseradish peroxidase tagged secondary antibody at room temperature with mild agitation. Thereafter, any extra secondary antibody was washed out using 1X TBST. Lastly, protein bands were visualized on x-ray films by an H_2O_2-dependant enhanced chemiluminescence method employing luminol and coumaric acid. Employment of an anti-β-actin antibody was made as an internal protein loading control.

2.2.1.16. Inhibitor study

The importance of excessive ROS production for mediating anticancer effectivities of the compounds of interests, was checked by pre-treating cells with 5 mM N-acetyl-cysteine (NAC) (Ghosh et al. 2023).

2.2.2. *In vivo* solid tumor model development and study of tumor regression

2.2.2.1. Animal care

For experimental purposes, both Swiss albino mice and female Balb/c mice were reared. Four to six weeks old Swiss Albino mice with an average body weight of 25 grams were obtained (Ghosh et al. 2023, Ghosh et al. 2022). Whereas, female Balb/c mice of four-week-old age and weighing about 23 grams on average were collected for another separate experimental purpose (Ghosh, Kundu, et al. 2022). Animals were obtained from the central animal house of the Bose Institute, Madhyamgram, Kolkata, India. Both strains of mice were acclimatized to the laboratory environment for 2 weeks keeping them in alternative 12-hour light and dark periodic cycles. Mice were cared for with sterile food and water ad libitum. Any further experimental planning and procedure were done by following the rules and regulations of the Institutional Animal Ethics Committee (IAEC), Bose Institute, Kolkata [approval no. IAEC/BI/142/2019 for Swiss Albino mice and IEAC/BI1003/2021 for Balb/c mice], CPCSEA (Committee for Control and Supervision on Experiments on Animals), Ministry of Environment and Forests, New Delhi, India (1796/PO/Ere/S/14/CPCSEA). Following acclimatization mice were prepared for tumor inoculation followed by intravenous treatment with compounds of interest or they were treated with the compounds to be studied for toxicological evaluation (discussed in detail in section 2.5.5.). During the treatment period mice were regularly monitored for their weight and tumor volume (if applicable). After the end of the treatment period, tumor tissues from the tumor-bearing mice were resected and examined for any change in tumor volume and mass in contrast to the control group.

2.2.2.2. Ehrlich ascites carcinoma (EAC) cell-based solid tumor development in Swiss Albino mice

After acclimatization, Swiss Albino mice were injected with nearly 1×10^7 EAC cells suspended in 50 µl of 1X PBS (Kundu et al. 2019). Injections were made intramuscularly in the left flank region of the mice and tumors were allowed to grow. After ten days after tumor inoculation once the tumors attained an average volume of 5-6 cm^3, tumor-bearing mice were segregated randomly into groups according to the requirement of experimental design.

2.2.2.3. 4T1 cell-based solid mammary tumor development in female Balb/c mice

For 4T1 cell inoculation, 1 × 106 number of 4T1 cells suspended within 200 µl of 10 % serum-supplemented antibiotic-free RPMI-1640 media, were injected subcutaneously into mammary fat pad region female Balb/c mice. When the volume of the tumors reached ∼100 mm3, the mice were randomly arranged in several experimental groups for further studies according to the necessity of experimental design (Yang et al. 2020).

2.2.2.4. 4T1 cell-based secondary pulmonary metastasis development in female Balb/c mice

Female Balb/c mice were given hot compression at their tail vein for localized increased blood flow. Next nearly 1 × 10^5 numbers of 4T1 tumor cells suspended in 10 % serum supplemented antibiotic-free RPMI-1640 media were intravenously injected through tail veins in female Balb/c mice (Pillar et al. 2018, Kim et al. 2009).

2.2.2.5. *In vivo* systemic toxicity assessment

To ascertain treatment-based systemic toxicity wild-type mice were treated intravenously with the compounds of interest at doses similar to the treatment doses received by tumor-bearing mice. After being treated with desired compounds at desired doses mice were sacrificed and vital organs such as kidneys, lungs, livers, and hearts were collected and stored in a 10 % formalin solution. Later these were checked for histological evaluation through hematoxylin and eosin (H & E) staining for the presence of any abnormality. Also, blood was collected from each animal via cardiac puncture. Collected whole blood was kept undisturbed at room temperature and allowed to clot for 30 minutes. Then, the removal of the clot and collection of serum as supernatant was made by centrifugation at 2000 *g* for 20 minutes at 4 °C. Isolated serum was stored for further use at -20 °C (Ghosh et al. 2022). Later, this serum was used for quantification of hepatic and renal health-specific serum parameters (respectively alkaline phosphatase and alanine transferase; creatinine and blood urea nitrogen) according to the manufacturer's protocol (Ghosh et al. 2023).

2.2.2.6. Histological assessment

Resected tumor tissues as well as vital organs collected for the studies of *in vivo* systemic toxicity were evaluated for histological abnormalities through H & E staining (Ghosh et al. 2022). Collected tissues were cleared and fixed in 10 % formalin initially. Fixed tissue sections were processed through steps for paraffin embedding followed by micro-sectioning using a microtome. Tissue sections carrying a thickness of nearly 5 µm were then adhered to glass slides. These tissue sections underwent sequential deparaffinization, dehydration, staining, and rehydration and finally were mounted with antifade permanent mounting media DPX. After being dried properly stained tissue sections were evaluated under a bright field light microscope at a magnification of 20X.

2.2.2.7. Biochemical studies from tumor tissues

2.2.2.7.1. Measurement of SOD and CAT activities from tumor tissues

To measure the enzymatic activities of antioxidant enzymes such as SOD and CAT, resected tumor tissues were homogenized in RIPA lysis buffer followed by examining protein concentration using a standard

BCA protein estimation kit. Thereafter, the activities of CAT and SOD were evaluated spectrophotometrically. For measuring SOD activity in tumor tissues from treated and untreated animals, tissue homogenate containing 5 µg protein was added to sodium pyrophosphate buffer, PMT, and NBT. Initiation of the reaction was made possible with the addition of NADH. Then incubation of the reaction mixture was made at 30 °C for 1.5 minutes and terminated thereafter by the addition of 1 ml of glacial acetic acid. Finally, the absorbance was measured at 560 nm. A unit of SOD activity is represented as the enzyme concentration required to prevent chromogen production by 50 % in a minute under standard assay conditions (Ghosh, Chatterjee et al. 2022).

Similarly, tissue homogenate containing 5 µg protein was added to 2.1 ml of 7.5 mM hydrogen peroxide, and then diminishing absorbance was noted spectrophotometrically at 240 nm for about 10 min at 25 °C. A unit of CAT activity is represented to be the amount of enzyme required to decrease 1 µmol of hydrogen peroxide in a minute (Ghosh, Chatterjee et al. 2022).

2.2.2.7.2. Measurement of protein carbonylation in tumor tissues

Extents of lipid peroxidation in tumor tissues resected from experimental mice were measured through a colorimetric method with thiobarbiturate as discussed elsewhere (Ghosh, Chatterjee et al. 2022). Tumor tissue homogenate containing 1 mg protein was mixed with 0.67 % thiobarbiturate and 20 % solution of trichloroacetic acid. After heating the reaction mixture at 100 °C for half an hour the supernatant containing thiobarbiturate reactive substance following centrifugation was measured for absorbance at 532 nm.

2.2.2.8. RNA extraction and reverse transcriptase PCR study in tumor tissue

Transcriptional expressions of genes of interest were determined through reverse transcriptase PCR (Sinha et al. 2019, Ghosh et al. 2022). Tumor tissues resected from treated animals were first homogenized using TRIzol following the manufacturer’s manual. Then total RNA concentration was calculated employing a nanodrop (Hellma Tray Cell Type 105.810). complementary DNA (cDNA) was prepared thereafter from 2 µg of specific RNA using a Thermo Scientific Verso cDNA synthesis kit followed by amplification of the PCR product. Then these PCR products were separated electrophoretically across a 1.5 % agarose gel according to the specific annealing temperature of respective primers.

2.2.2.9. Homogenization & immunoblot analysis from resected tumor tissues

For checking the translational expression of protein from *in vivo* tumor tissue samples, tissues were initially homogenized using Dounce homogenizer in RIPA lysis buffer supplemented with protease and phosphatase inhibitor cocktails (Sinha et al. 2019, Ghosh et al. 2022, Ghosh et al. 2023). Homogenization was done in an ice chamber. Following homogenization, the tissue homogenate was cleared up by centrifugation at 4 °C at 1200x g for 10 minutes. Clear protein-rich supernatant was then checked for total protein concentration colorimetrically at 562 nm using a BCA assay kit. Thereafter, the protein of interest was electrophoretically separated on SDS-PAGE and mobilized on PVDF membrane for western blotting similarly described in section 2.2.1.15.

2.2.2.10. Immunohistochemical analysis from resected tumor tissues

Immunohistochemical expression studies of selective molecules were made upon paraffin-embedded tumor tissue sections (Ghosh et al. 2023). Tissue sections were at first deparaffinized and rehydrated by passing tissue sections from absolute alcohol to water. Next, antigenic epitopes of the protein to be studied were demasked with the help of trypsin solution (0.05 %, pH 7.8). The rest of the steps in the assay were executed following the protocol provided with the IHC assay kit. Briefly, a kit-based H_2O_2 blocking solution was used to block endogenous peroxidase activity to prevent false positive results. Then a protein block was applied on sections for 10 minutes to prevent non-specific antigen-antibody interaction. This step was followed by overnight incubation with primary antibodies of interest at 4 °C. On the next day, after washing away any excess non-bound primary antibody with 1X TBST, incubation with HRP-tagged secondary antibody was executed at 37 °C for half an hour followed by a chromogenic HRP substrate 3, 3′-diaminobenzidine tetrahydrochloride (DAB) application and incubation for another half an hour in moist chamber at 37 °C. Hematoxylin was used to counter-stain the nuclei present in tissue sections and DPX was applied for mounting. Finally, stained tumor tissue sections were examined under a bright field optical microscope at 20X magnification.

2.2.2.11. TUNEL assay upon resected tumor tissue

To evaluate the extent of apoptosis in treated 4T1-derived mammary tumor tissues compared to untreated ones terminal deoxynucleotidyl transferase-mediated dUTP nick-end labeling (TUNEL) assay was performed (Chowdhury et al. 2016, Lespagnol et al. 2008). Paraffin-embedded tissue sections were deparaffinized and rehydrated through the down-gradation of ethyl alcohol. Following rehydration in distilled water tissue sections were incubated at 37 °C for an hour in the dark with 0.05 ml of DNA labelling dye. Post-incubation, tissue sections were rinsed in kit-based rinse buffer followed by another incubation for half an hour in the dark with antibody staining buffer containing Alexa Fluor. Following rinsing for removal of any extra antibody, tissue sections were counterstained with kit-based RNase/PI staining buffer and were maintained in the dark to avoid photobleaching. Thereafter, stained sections were mounted in DPX with a cover slide and were viewed under a confocal microscope with green and red filters.

2.2.3. Nanoparticle formulation and subsequent studies

2.2.3.1. Fabrication of aminated $mSiO_2$

Following the method described elsewhere, $mSiO_2$ synthesis was done (Kundu et al. 2020, Xiao et al. 2014). In short, a gram of CTAB and 0.28 gm of sodium hydroxide were dissolved in 480 ml of ultrapure distilled water with vigorous stirring at 8 °C. Then, 6.7 ml of TEOS was drop-wisely added to the previous solution when it became transparent. To obtain amine functionalized $mSiO_2$, 1 ml of APTES was added to the solution and was kept in stirring condition for 5 hours. Next, removal of the surfactant was done by refluxing the synthesized product with a mixture of 500 ml ethanol and 6 ml concentrated HCl for 24 hours at 78 °C. Lastly, to obtain the end product synthesized nano-composites were washed with absolute ethanol through centrifugation at 6000 rpm for 10 minutes followed by oven-drying.

2.2.3.2. Chrysin entrapment into aminated- $mSiO_2$ pores (Chr- $mSiO_2$)

For chrysin loading, a dispersed solution of amine-functionalized $mSiO_2$ was added to the DMSO solution of chrysin at a ratio of one to two parts and was kept in stirring condition using a magnetic stirrer at 400 rpm for 24 hours at room temperature. At this point, drug loading content (DLC) and drug entrapment efficiency (DEE) of Chr- $mSiO_2$ were calculated through UV-vis spectroscopy at 315 nm. DLC and DEE were calculated according to the equation described below (Kundu et al. 2019):

$$\text{DLC (\%)} = \frac{mass\ of\ chrysin\ loaded\ within\ nanoparticle}{total\ mass\ of\ nanoparticle} \times 100$$

$$\text{DEE (\%)} = \frac{mass\ of\ chrysin\ loaded\ within\ nanoparticle}{mass\ of\ chrysin\ used\ during\ drug\ entrapment} \times 100$$

2.2.3.3. PAA addition upon Chr-$mSiO_2$ (Chr- $mSiO_2$@PAA)

To synthesize Chr- $mSiO_2$@PAA, suspension of Chr- $mSiO_2$ was added to PAA solution in a 1:1 weight ratio and was kept under stirring condition at 400 rpm using a magnetic stirrer at 100 °C for 2 hours (Peng et al. 2013, Xiao et al. 2014).

2.2.3.4. Tagging of FA to Chr-$mSiO_2$@PAA (Chr-$mSiO_2$@PAA/FA)

For the synthesis of Chr-$mSiO_2$@PAA/FA, first, the free carboxyl groups of PAA at Chr-$mSiO_2$@PAA surface were activated by stirring along with EDC and NHS for 3 hours at 400 rpm. Finally, FA (dissolved in DMSO) was added to the reaction mixture in a 2:1 weight ratio to activated Chr-mSiO_2@PAA and further stirred for 24 hours to formulate Chr- mSiO_2@PAA/FA (Ghosh et al. 2023).

2.2.3.5. Preparation of fluorescent mSiO_2

To check FA receptor-oriented enhanced chrysin nanoconjugate uptake, Chr-mSiO_2 and Chr-mSiO_2@FA were mixed with ethanolic solution of FITC and were kept stirring for 24 hours at 400 rpm in dark to obtain Chr-mSiO_2@FITC and Chr-mSiO_2@FA/FITC respectively (Hakeem et al. 2016, Zhai et al. 2012).

2.2.3.6. Characterization of synthesized nano-conjugates

The size of the nanoparticle was measured using a transmission electron microscope (Tecnai G2 TF-20-200 KV). Morphology and the structure of the synthesized nanoconjugates were validated by scanning electron microscope (JSM7600F, JEOL, Japan). To clarify the successful loading of chrysin and further addition of PAA and FA, a series of experiments were performed including analysis of Fourier-transform infrared (FTIR) spectra of the samples at each step of modification using KBr pellets, analysis of UV-vis spectra of the nanocomposites via Shimadzu spectrophotometer, measurement of hydrodynamic size and zeta potential of the synthesized nanoconjugates in aqueous suspension through dynamic light scattering (DLS) employing Delsa™ Nano C particle size analyzer (Beckman Coulter, Brea, CA, USA) (Ghosh et al. 2023).

2.2.3.7. *In vitro* biocompatibility testing of nanoconjugates

2.2.3.7.1. Hemolytic assay

Hemolytic studies on synthesized nanocomposites were made following the protocol described elsewhere (Chen et al. 2019). Initially, 2 ml of collected human blood in K_2-EDTA was centrifuged at 500 x *g* for five minutes to obtain the pellet and discard the plasma supernatant. The volume of plasma was replaced then by 0.15 M NaCl solution followed by further centrifugation at 500 x g for five minutes more. This time supernatant was also discarded and replaced by an equal volume of PBS of pH 7.4. Such solution was further diluted 50 times using 1X PBS. Next, 0.1 ml of each of mSiO_2 and mSiO_2@PAA/FA solutions at five distinct concentrations (0.5, 1.0, 2.0, 4.0, 8.0, 10.0 mg/ml) were added to 1.9 ml of diluted RBC solution to get final mSiO_2 and mSiO_2@PAA/FA solutions of 0.025, 0.05, 0.1, 0.2, 0.4 and 0.5 mg/ml concentrations. The solutions were kept under agitation at 100 rpm for one hour at 37 °C followed by centrifugation at 500 x *g* for five minutes. Finally, supernatants were analyzed spectrophotometrically at 541 nm. 0.1 ml of each 20 % triton-X-100 solution and 1X PBS (pH 7.4) were employed as positive and negative controls respectively. Lastly, the percentage of hemolysis was calculated according to the equation stated below:

$$\text{\% of Hemolysis} = \frac{mass\ of\ chrysin\ loaded\ within\ nanoparticle}{mass\ of\ chrysin\ used\ during\ drug\ entrapment} \times 100$$

2.2.3.7.2. Protein adsorption assay

Adsorption of protein onto the surface of synthesized nanocomposites was measured by examining surface adsorption of BSA (Chen et al. 2019). 100 ml of 0.6 mg/ml BSA solution was prepared initially, of which 5 ml BSA solution was added to 5 ml of 2 mg/ml PBS suspension of $mSiO_2$, $mSiO_2$@PAA and $mSiO_2$@PAA/FA. Sample mixtures were kept stirring at 135 rpm for four hours at 37 °C. Following stirring clear solutions from the upper solution part was collected and further BSA concentrations were measured using a BCA kit at 562 nm. The adsorbed amount of BSA for each sample was then quantified following the equation stated below.

$$\text{BSA adsorption} = \frac{(initial\ concentration\ of\ BSA - BSA\ concentration\ of\ samples \times volume\ off\ sample\ solution}{total\ mass\ of\ nanoparticlemass\ of\ nanoparticle\ added}$$

2.2.3.8. pH-responsive behavior of formulated nanoconjugate

To validate the pH-oriented release behavior of chrysin from synthesized nanocomposites, release media of three distinct pHs were prepared using PBS (154 mM) of three distinct pH (pH 7.4, pH 6.0, and pH 5.0). To analyze the *in vitro* pH-responsive release of chrysin from Chr-$mSiO_2$ and Chr-$mSiO_2$@PAA, PBS was supplemented with 0.1 % Tween 80 to maintain the sink condition for chrysin dissolution in release media (Lungare, Hallam, and Badhan 2016). 2 mg of chrysin containing $mSiO_2$ were dispersed into 2 ml of release medium which were sonicated throughout the experimental time and was maintained at 100 rpm in a stirring condition at 37 °C. Sample were transferred at prefixed time intervals and the volume was replaced with an equal volume of pre-warmed release medium (Lungare, Hallam, and Badhan 2016). The amount of released chrysin in the original buffer solution was determined spectrophotometrically at 315 nm on specific time spots within a 0-48 hours period. The percentage of drug release was calculated as described below (Jabbari et al. 2018):

$$\text{\% of drug release} = \frac{masamount\ of\ drug\ in\ release\ medium\ at\ time\ t}{amount\ of\ drug\ loaded\ within\ nanoparticle} \times 100$$

2.2.3.9. Confirming FA-guided targeted intracellular uptake of nanoconjugates via microscopic fluorescence imaging

70% confluent MCF-7 cells were incubated for 3 hours with equivalent concentrations of Chr-$mSiO_2$@FITC and Chr-$mSiO_2$@FITC/FA. Following 1X PBS wash treated cells were pelleted down by centrifugation at 6000 rpm for 5 minutes. Cell pellets were then analyzed through a flow cytometer at 520 nm. Parallelly, cells grown on coverslips were treated similarly after which coverslips were placed upon glass slides coated with antifade mounting media called VECTASHIELD (Ghosh et al. 2023). These were then checked under confocal laser scanning microscopes using filters for DAPI and FITC.

2.2.3.10. Resolution of the intracellular release of chrysin

Intracellular release of chrysin was evaluated by treating MCF-7 cells with the equivalent dose of free chrysin, Chr-mSiO_2@PAA, and Chr-mSiO_2@PAA/FA for 24 hours. Treated cells were lysed to collect supernatants through centrifugation at 6000 rpm for 5 minutes and were examined spectrophotometrically for the amount of released chrysin at 315 nm. The release pattern of chrysin was similarly studied on NKE cells as well (Sarkar et al. 2016, Ghosh et al. 2023, Kundu et al. 2020).

2.2.3.11. Study of *in vivo* nanoparticle-mediated chrysin accumulation in tumor tissue

High-pressure liquid chromatography (HPLC) was applied on tumor tissue homogenates acquired from different treatment groups of mice (Kundu et al. 2020, Ghosh et al. 2023). To perform the study, EAC-induced tumor-bearing mice were bunched into three groups namely, group-I (receiving free chrysin solution at 10 mg per kg body weight intravenously), group-II (treated with intravenous Chr-mSiO_2@PAA solution at a dose of 60.60 mg per kg body weight) and lastly, group-III (treated with 74 mg per kg body weight of Chr-mSiO_2@PAA/FA solution intravenously). Twenty-four hours post-treatment mice were sacrificed and tumors were resected. 100 mg of tumor tissue from each experimental mice was homogenized within a mixture of 75 % ethanol and 0.05 % DMSO. Obtained homogenates were centrifuged at 4 °C at 10000 rpm for 15 min. The liquid portion of the supernatant was dried in a nitrogen evaporator followed by the dissolution of the rest in methanol to prepare methanolic tumor tissue extract. Methanolic extract (20 µl) from experimental mice was injected into a C18 column of 250 × 4.5 mm in dimension at an optimized flow rate of 1 ml per minute using acetonitrile and methanol (65:35) mixture solution as a solvent system. Lastly, HPLC detection was made on 315 nm spectrophotometrically. For calculating the amount of chrysin in tissue sample solutions, a standard curve was prepared using a standard methanolic solution of chrysin preparation and calibration at five different concentrations (3, 5, 15, 30, and 50 µg per ml).

2.2.4. Statistical analysis

Every experiment conducted in this study has been replicated independently on at least three separate occasions to ensure reliable and accurate interpretation of the results. The average value of the experimental data is presented along with the standard deviation to provide a comprehensive representation. The variation observed among the different test groups was assessed using a statistical method known as one-way analysis of variance (one-way ANOVA). In cases where the results deviated significantly from the central tendency, the statistical significance between the test groups was examined through the use of Tukey's post hoc test. It was determined that values deviate from the central tendency when the P value exceeds the threshold of 0.05.

2.3. References

Bonaventura, Joseph, WA Schroeder, and Suen Fang. 1972. "Human erythrocyte catalase: an improved method of isolation and a reevaluation of reported properties." Archives of biochemistry and biophysics 150 (2):606-617.

Chen, Chao, Wen Tang, Dawei Jiang, Guoliang Yang, Xiaoli Wang, Lina Zhou, Weian Zhang, and Ping Wang. 2019. "Hyaluronic acid conjugated polydopamine functionalized mesoporous silica nanoparticles for synergistic targeted chemo-photothermal therapy." Nanoscale 11 (22):11012-11024.

Chowdhury, Sayantani, Sumit Ghosh, Abhishek Kumar Das, and Parames C Sil. 2019. "Ferulic acid protects hyperglycemia-induced kidney damage by regulating oxidative insult, inflammation and autophagy." Frontiers in Pharmacology 10:27.

Chowdhury, Sayantani, Sumit Ghosh, Kahkashan Rashid, and Parames C Sil. 2016. "Deciphering the role of ferulic acid against streptozotocin-induced cellular stress in the cardiac tissue of diabetic rats." Food and Chemical Toxicology 97:187-198.

Cox, Brian, and Andrew Emili. 2006. "Tissue subcellular fractionation and protein extraction for use in mass-spectrometry-based proteomics." Nature protocols 1 (4):1872-1878.

Ghosh, Noyel, Sharmistha Chatterjee, Debanjana Biswal, Nikhil Ranjan Pramanik, Syamal Chakrabarti, and Parames C Sil. 2022. "Oxidative stress imposed in vivo anticancer therapeutic efficacy of novel imidazole-based oxidovanadium (IV) complex in solid tumor." Life Sciences 301:120606.

Ghosh, Noyel, Mousumi Kundu, Sumit Ghosh, Abhishek Kumar Das, Samhita De, Joydeep Das, and Parames C Sil. 2023. "pH-responsive and targeted delivery of chrysin via folic acid-functionalized mesoporous silica nanocarrier for breast cancer therapy." International Journal of Pharmaceutics 631:122555.

Ghosh, Sumit, Mousumi Kundu, Sayanta Dutta, Sushweta Mahalanobish, Noyel Ghosh, Joydeep Das, and Parames C Sil. 2022. "Enhancement of anti-neoplastic effects of cuminaldehyde against breast cancer via mesoporous silica nanoparticle based targeted drug delivery system." Life Sciences 298:120525.

Hakeem, Abdul, Fouzia Zahid, Ruixue Duan, Muhammad Asif, Tianchi Zhang, Zhenyu Zhang, Yong Cheng, Xiaoding Lou, and Fan Xia. 2016. "Cellulose conjugated FITC-labelled mesoporous silica nanoparticles: intracellular accumulation and stimuli responsive doxorubicin release." Nanoscale 8 (9):5089-5097.

Hissin, Paul J, and Russell Hilf. 1976. "A fluorometric method for determination of oxidized and reduced glutathione in tissues." Analytical biochemistry 74 (1):214-226.

Jabbari, Sepideh, Aliyeh Ghamkhari, Yousef Javadzadeh, Roya Salehi, and Soodabeh Davaran. 2018. "Doxorubicin and chrysin combination chemotherapy with novel pH-responsive poly [(lactide-co-glycolic acid)-block-methacrylic acid] nanoparticle." Journal of Drug Delivery Science and Technology 46:129-137.

Kakkar, Poonam, Ballabh Das, and PN Viswanathan. 1984. "A modified spectrophotometric assay of superoxide dismutase."

Kim, Eun Ji, Minjeong Shin, Heesook Park, Ji Eun Hong, Hyun-Kyung Shin, Jongdai Kim, Dae Young Kwon, and Jung Han Yoon Park. 2009. "Oral administration of 3, 3′-diindolylmethane inhibits lung metastasis of 4T1 murine mammary carcinoma cells in BALB/c mice." The Journal of nutrition 139 (12):2373-2379.

Kundu, Mousumi, Sharmistha Chatterjee, Noyel Ghosh, Prasenjit Manna, Joydeep Das, and Parames C Sil. 2020. "Tumor targeted delivery of umbelliferone via a smart mesoporous silica nanoparticles controlled-release drug delivery system for increased anticancer efficiency." Materials Science and Engineering: C 116:111239.

Kundu, Mousumi, Pritam Sadhukhan, Noyel Ghosh, Sharmistha Chatterjee, Prasenjit Manna, Joydeep Das, and Parames C Sil. 2019. "pH-responsive and targeted delivery of curcumin via phenylboronic acid-functionalized ZnO nanoparticles for breast cancer therapy." Journal of advanced research 18:161-172.

Lespagnol, Alexandra, D Duflaut, Chantal Beekman, L Blanc, G Fiucci, Jean-Christophe Marine, M Vidal, Robert Amson, and Adam Telerman. 2008. "Exosome secretion, including the DNA damage-induced p53-dependent secretory pathway, is severely compromised in TSAP6/Steap3-null mice." Cell Death & Differentiation 15 (11):1723-1733.

Li, Wei, Chen Zhang, and Xiulian Sun. 2018. "Mitochondrial Ca2+ retention capacity assay and Ca2+-triggered mitochondrial swelling assay." JoVE (Journal of Visualized Experiments) (135):e56236.

Lungare, Shital, Keith Hallam, and Raj KS Badhan. 2016. "Phytochemical-loaded mesoporous silica nanoparticles for nose-to-brain olfactory drug delivery." International journal of pharmaceutics 513 (1-2):280-293.

Nishikimi, Morimitsu, N Appaji Rao, and Kunio Yagi. 1972. "The occurrence of superoxide anion in the reaction of reduced phenazine methosulfate and molecular oxygen." Biochemical and biophysical research communications 46 (2):849-854.

Peng, Hailong, Ruichen Dong, Shenqi Wang, Zhong Zhang, Mei Luo, Chunqing Bai, Qiang Zhao, Jinhua Li, Lingxin Chen, and Hua Xiong. 2013. "A pH-responsive nano-carrier with mesoporous silica nanoparticles cores and poly (acrylic acid) shell-layers: fabrication, characterization and properties for controlled release of salidroside." International journal of pharmaceutics 446 (1-2):153-159.

Pijuan, J., C. Barceló, D. F. Moreno, O. Maiques, P. Sisó, R. M. Marti, A. Macià, and A. Panosa. 2019. "In vitro Cell Migration, Invasion, and Adhesion Assays: From Cell Imaging to Data Analysis." Front Cell Dev Biol 7:107. doi: 10.3389/fcell.2019.00107.

Pillar, Nir, Avital Luba Polsky, Daphna Weissglas-Volkov, and Noam Shomron. 2018. "Comparison of breast cancer metastasis models reveals a possible mechanism of tumor aggressiveness." Cell Death & Disease 9 (10):1040.

Sadhukhan, Pritam, Sukanya Saha, Krishnendu Sinha, Goutam Brahmachari, and Parames C Sil. 2016. "Selective pro-apoptotic activity of novel 3, 3′-(aryl/alkyl-methylene) bis (2-hydroxynaphthalene-1, 4-dione) derivatives on human cancer cells via the induction reactive oxygen species." PloS one 11 (7):e0158694.

Sarkar, Abhijit, Shatadal Ghosh, Sayantani Chowdhury, Bhawna Pandey, and Parames C Sil. 2016. "Targeted delivery of quercetin loaded mesoporous silica nanoparticles to the breast cancer cells." Biochimica et Biophysica Acta (BBA)-General Subjects 1860 (10):2065-2075.

K. Sinha, S. Chowdhury, S. Banerjee, B. Mandal, M. Mandal, S. Majhi, G. Brahmachari, J. Ghosh, P.C. Sil, Lupeol alters viability of SK-RC-45 (Renal cell carcinoma cell line) by modulating its mitochondrial dynamics, Heliyon 5(8) (2019).

Xiao, J, H Zhai, Y Yao, C Wang, W Jiang, C Zhang, AR Simard, R Zhang, and J Hao. 2014. "Chrysin attenuates experimental autoimmune neuritis by suppressing immuno-inflammatory responses." Neuroscience 262:156-164.

Yang, Liang, Ling Yong, Xiao Zhu, Yaoyao Feng, Yu Fu, Daming Kong, Wei Lu, and Tian-yan Zhou. 2020. "Disease progression model of 4T1 metastatic breast cancer." Journal of pharmacokinetics and pharmacodynamics 47:105-116.

Zhai, Wanyin, Changliang He, Lei Wu, Yue Zhou, Hangrong Chen, Jiang Chang, and Hongfeng Zhang. 2012. "Degradation of hollow mesoporous silica nanoparticles in human umbilical vein endothelial cells." Journal of Biomedical Materials Research Part B: Applied Biomaterials 100 (5):1397-1403.

Zhang, Jing, Li Li, Yueting Peng, Yu Chen, Xiaoying Lv, Shun Li, Xiang Qin, Hong Yang, Chunhui Wu, and Yiyao Liu. 2018. "Surface chemistry induces mitochondria-mediated apoptosis of breast cancer cells via PTEN/PI3K/AKT signaling pathway." Biochimica et Biophysica Acta (BBA)-Molecular Cell Research 1865 (1):172-185.

Chapter 3

Oxidative Stress-mediated In vivo Anticancer Therapeutic Effectivities of Novel 1-allyimidazole-substituted Oxidovanadium (IV) Complex in Solid Tumor

3.1. Introduction

In this current investigation, we have extensively examined the anticarcinogenic effects of a newly developed water-soluble oxidovanadium complex. This complex features ‘vanadium’ as the central atom, which exists in the IV oxidative state. The water solubility of the compound is achieved through the inclusion of dipicolinic acid, while its anticarcinogenic properties are attained through the incorporation of a mononuclear imidazole group. In this group, the first nitrogen atom has been substituted with an allyl group. For easy interpretation, this compound can be chemically represented as $VOLB_2$ where H_2L = dipicolinic acid and B = 1-allyl imidazole (Figure 1).

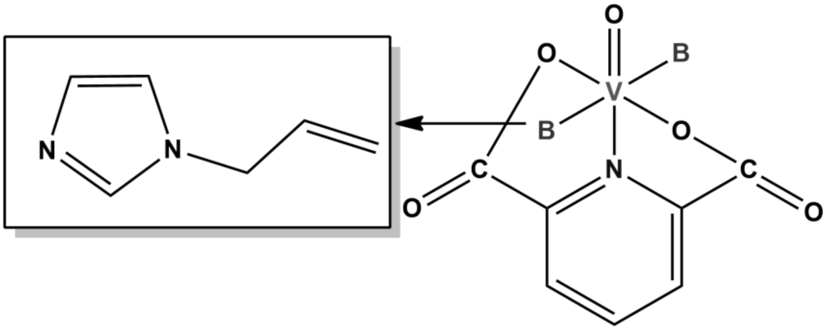

Figure 1: *Chemical structure of mononuclear dipicolinic acid-1-allyl imidazole-based oxidovanadium (IV) complex, referred to as VOL*

In the present investigation, the compound has been designated as VOL. The previous research endeavor of our collaborator has already elucidated the anticancer properties of VOL in the human hepatocellular carcinoma cell line Hep3B. Bearing in mind the findings from that study, we have now examined the efficacy of VOL as an anticancer agent in the progesterone receptor-positive human breast cancer cell line MCF-7, in comparison to the platinum-based drug cisplatin, which is widely recognized for its anticancer properties, using *in vitro* experiments. VOL has been observed to induce cytotoxicity in a dose-dependent manner in the MCF-7 cell line, primarily through the generation of intracellular oxidative stress and modification of the mitochondrial membrane potential. Once identified as highly effective, such as cisplatin, in laboratory settings, further investigations were conducted in Swiss Albino mice. These experiments revealed that VOL exhibits a dose-dependent anticancer effect, accompanied by the induction of oxidative stress. Notably, VOL treatment has been shown to induce both mitochondrial and extra-mitochondrial apoptosis in tumor tissue, leading to a more potent anticancer effect. Moreover, *in vivo* treatment with VOL was found to be well-tolerated, as evidenced by a noticeable reduction in tumor size, absence of significant body weight loss, and absence of nephrotoxicity and hepatotoxicity.

3.2. Utilized reagents

The necessary reagents and chemicals for conducting this study have been acquired from reputable scientific manufacturing companies, as mentioned in section 2.1. A mononuclear dipicolinic acid-1-allyl imidazole-based oxidovanadium (IV) complex, referred to as VOL, was successfully synthesized by Biswal et al. and generously provided for experimental use by Professor Nikhil Ranjan Pramanik (Biswas et al, 2017).

3.3. Methods

3.3.1. Cell culture

In the current study, the anticancer effect of the concerned compound was checked on human PR$^+$ breast cancer cell line MCF-7 and one normal cell line, human normal kidney epithelial cell line NKE. Maintenance of the cells has been done according to the protocol described in section 2.2.1.1.

3.3.1. Study of VOL-induced *in vitro* cytotoxicity

The measurement of VOL-mediated cytotoxicity was conducted using the fundamental MTT assessment method, as outlined in section 2.2.1.2. Within this study, various doses of VOL ranging from zero to 40 μg/ml were examined on both MCF-7 and NKE cell types.

3.3.2. Dosage for *in vitro* treatment

In contradistinction to the well-established platinum metallodrug cisplatin, the cytotoxicity of VOL was assessed. The MTT assay was performed on both MCF-7 cells and NKE cells. Furthermore, a variety of additional *in vitro* experiments were conducted on both MCF-7 and NKE cells, using their corresponding LC_{50} doses.

3.3.3. Determination of *in vitro* LDH activity

The quantification of LDH release *in vitro* was conducted by subjecting the cells to VOL with LC_{50} doses following the methodology outlined in section 2.2.1.3.

3.3.4. Analysis of VOL-induced *in vitro* apoptosis

Flow-cytometric analysis of cell death modality has been studied on both MCF-7 and NKE cells after being treated with respective LC_{50} doses of VOL and cisplatin for 48 hours through FITC-Annexin-V staining according to the protocol described in section 2.2.1.4.

3.3.5. Determination of intracellular ROS production

Detection of intracellular ROS was carried out employing fluorescent H_2DCFDA dye following the method described by Cossarizza et al (Cossarizza et al. 2009). In brief, MCF-7 and NKE cells after being treated with optimum cytotoxic doses of VOL and cisplatin were checked for flow cytometry basis analysis according to the protocol described in section 2.2.1.5.

3.3.6. Analysis of treatment-induced changes in transmembrane mitochondrial potential (TMP)

The determination of TMP in both MCF-7 and NKE cells was performed after treatment with VOL and cisplatin for 48 hours. This was done after the cells were stained with JC-1 dye, as detailed in the earlier section 2.2.1.6. In this study, flow cytometric analysis was solely employed to examine the alteration in TMP resulting from treatment at a specific dosage.

3.3.7. Estimation of *in vitro* GSH to GSSG ratio

To find out *in vitro* GSH to GSSG ratio, GSH, and GSSG content after treatment with respective LC_{50} doses of VOL and cisplatin for 48 hours were evaluated separately following the protocol described earlier in section 2.2.1.7. The study was done both in MCF-7 and NKE cells.

3.3.8. Quantification of *in vitro* lipid peroxidation

To authenticate the modulation of cellular oxidative status through treatment, the measurement of lipid peroxidation in terms of MDA content was conducted after 48 hours of treatment with VOL and cisplatin in both MCF-7 and NKE cells. This measurement was carried out following the aforementioned protocol outlined in section 2.2.1.8.

3.3.9. Determination of *in vitro* antioxidant enzyme activities

Enzymatic activities of antioxidant enzymes, catalase (CAT), and superoxide dismutase (SOD) were checked in both NKE and MCF-7 cell lines after treatment with respective LC_{50} doses of VOL and cisplatin for 48 hours. The activity of CAT and SOD were estimated spectrophotometrically obeying the protocols demonstrated previously in section 2.2.1.9.

3.3.10. Determining effect *in vitro* ROS inhibition

Both cell types (MCF-7 and NKE) were treated at 80 % confluency with an LC_{50} dose of VOL (20.83 μg/ml) alone and with 5 mM NAC. Later on, treated cells were checked for cytotoxicity via MTT assay and for oxidative status of cells by evaluating flow cytometric intracellular ROS content, intracellular GSH/GSSG ratio, enzymatic activities of SOD and CAT.

3.3.11. *In vivo* antitumorigenic activities of VOL in Swiss Albino mice

A total of thirty-six male Swiss Albino mice were obtained and were maintained under laboratory conditions following the guidelines outlined in section 2.2.2.1. To induce the growth of EAC-induced solid tumors, eighteen mice were selected at random and administered with EAC cells intramuscularly, as described in section 2.2.2.3., in the left flanks. Subsequently, the tumors were allowed to reach a certain volume over 10 days, following which the mice were intravenously injected with VOL treatment doses. The grouping of the mice was carried out as detailed below in Scheme 1. The remaining eighteen mice were not injected with EAC cells and were instead kept for toxicological studies.

Group I – tumor-bearing mice treated intravenously with 0.9 % saline water

Group II – tumor-bearing mice treated intravenously with VOL (10 mg per kg body weight)

Group III – tumor-bearing mice treated intravenously with VOL (20 mg per kg body weight)

The treatment was sustained for fourteen days. The mice were subjected to continuous monitoring to discern any alterations in body mass, tumor size, and general vitality. After the culmination of the entire treatment span, the mice were sacrificed and the excised tumors were physically appraised concerning their mass. To determine the tumor volume, the subsequent equation was employed. Additionally, the excised tumor tissues as well as the spleens underwent further histological evaluation.

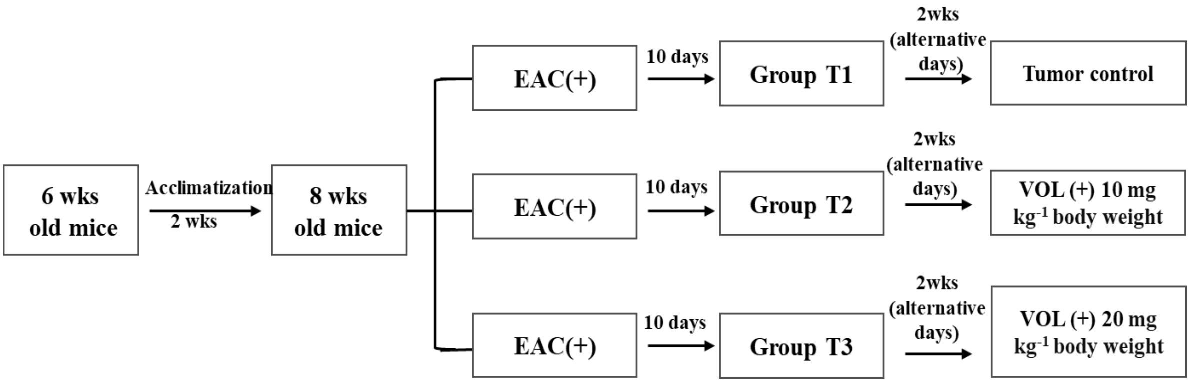

Scheme 1: *Schematic work plan for EAC-mediated solid tumor induction and further treatment with VOL injection in Swiss Albino mice.*

3.3.12. Determination of SOD and CAT activities in resected VOL-treated tumor tissues

The enzymatic activities of catalase (CAT) and superoxide dismutase (SOD) were quantified in tumor tissues that were surgically removed from experimental Group-I-III, as outlined in section 2.2.2.7.1.

3.3.13. Determination of lipid peroxidation in resected VOL-treated tumor tissues

The measurement of lipid peroxidation extent in tissue homogenate derived from resected tumor tissues of groups I to III was conducted as previously explained in section 2.2.2.7.2.

3.3.14. Extraction of RNA and reverse transcriptase PCR from resected tumor tissues

Resected tumor tissues were assessed for the transcriptional expression of specific genes that pertain to the present investigation. These genes are enumerated in Table 1 hereunder. To confirm the VOL-mediated alteration at the tissue level, homogenates of the resected tumor tissues were subjected to RNA isolation. Subsequently, the RNA was converted into cDNA, and alterations in expression levels were examined using agarose gel electrophoresis. A comprehensive outline of this methodology can be found in Chapter 2, specifically under section 2.2.2.8.

Table 1: Sequence, amplicon size, and annealing temperature of primers used for RT-PCR analysis of specific genes.

Gene Name	Primer sequence (5’-3’)	Annealing Temperature (^{0}C)	Amplicon size (bp)
CAT	**FP:** *CACACTCACACACACTCATACA* **RP:** *CACACTCACACACACTCATACA*	50	178
TNF-α	**FP:** *TCTCAGAATGAGGCTGGATAAG* **RP:** *CCCGGCCTTCCAAATAAATAC*	55	188
IL-1β	**FP:** *GAGTGTGGATCCCAAGCAATA* **RP:** *TCCTGACCACTGTTGTTTCC*	45	174
IL-6	**FP:** *GATAAGCTGGAGTCACAGAAGG* **RP:** *TTCTGACCACAGTGAGGAATG*	58.7	163
MCP-1	**FP:** *GAAGGAATGGGTCCAGACATAC* **RP:** *CACTCCTACAGAAGTGCTTGAG*	55	190

GAPDH	**FP:** *GGAGAAACCTGCCAAGTATGA* **RP:** *CCAGGAAATGAGCTTGACAAAG*	50	193

3.3.15. Protein quantification and immunoblotting of excised neoplastic tumor tissues

To investigate the impact of VOL on the translational expression of relevant genes, the resected tumor tissues were initially homogenized and subjected to total protein estimation using the methodology described in section 2.2.2.9. Subsequently, the tumor tissue samples were assessed using the SDS-PAGE technique, followed by western blotting, as outlined in section 2.2.2.9. The translational expression of proteins was examined by employing primary antibodies targeting SOD2 (ab13533), Bcl-2 (ab7973), Bax (#2772), Bid (#2002), cytochrome C (#4272), Apaf-1 (#8723), caspase 9 (#9508), caspase 8 (ab25901), caspase 3 (#9662), TNF-α (ab6671), and TRADD (ab223040), with β-actin (#4970) serving as the internal loading control.

3.3.16. Immunohistochemical studies of resected tumor tissues

Resected tumor tissues were evaluated for immunohistochemical expression of caspase 9 (#9508), caspase 8 (ab25901), and caspase 3 ((#9662) using DAB-substrate assisted method as discussed in section 2.2.2.10. in detail.

3.3.17. Experimental set-up for *in vivo* toxicological evaluation

To investigate the systemic toxicity induced by VOL, a total of eighteen Swiss Albino mice with wild-type phenotypes were divided into three groups. These mice were administered VOL via intravenous injection for fourteen days, as described in the following manner:

Group IV – wildtype mice treated intravenously with 0.9 % saline

Group V - wildtype mice treated intravenously with 10 mg per kg body weight of VOL

Group VI - wildtype mice treated intravenously with 20 mg per kg body weight of VOL

These animals were analyzed for any alteration in their fur pigmentation, physical mass, and other relevant factors. After undergoing treatment, mice were subjected to blood extraction via cardiac puncture. Additionally, essential organs including the liver and kidneys were obtained and histologically assessed.

3.3.18. Analysis of toxicological serum parameters

Following the serum isolation procedure as described in section 2.2.2.5, the serum levels of ALP, ALT, BUN, and creatinine were examined.

3.3.19. Physical analysis of splenic profile

To evaluate the decrease in EAC-induced splenomegaly mediated by VOL, an examination of splenic parameters was conducted on mice belonging to groups I-IV.

3.3.20. H & E staining

Resected tumor tissues, spleens collected from tumor-bearing mice, and vital organs (liver & kidney) collected from mice from groups IV-VI were stained with H & E following the steps discussed in section 2.2.2.6. Slides carrying stained tissue sections were evaluated histologically under a light microscope at 20 X magnification.

3.3.21. Statistical analysis

The data has been presented in the form of mean ± standard deviation (SD) after conducting a minimum of three independent experiments. The statistical analysis employed ANOVA and to compare the mean values among the different groups, Tukey's post-hoc test was conducted. A P-value less than 0.05 was deemed to have statistical significance in this particular study.

3.4. Results and Discussions

3.4.1. VOL is differentially cytotoxic to MCF-7 cells at a dose comparable to that of cisplatin

When subjected to the MTT assay, the cytotoxic effect of VOL on MCF-7 cells exhibited a dose-dependent relationship within the range of 0-40 µg/ml (Figure 2A). The LC_{50} dose of VOL in MCF-7 cells was determined to be 20.825 µg/ml based on calculations from the standard curve. In the case of NKE cells, the LC_{50} value of VOL was approximately five times higher at 104.723 µg/ml (Figure 2A). Furthermore, to assess the extent of cytotoxicity, the cytotoxic nature of VOL was compared to that of the well-known platinum drug cisplatin. The LC_{50} dose of cisplatin in MCF-7 cells was recorded as 21.136 µg/ml, whereas in NKE cells it was 24.616 µg/ml (Figure 2B). Furthermore, the cytotoxic patterns of VOL and cisplatin in both MCF-7 and NKE cells as obtained from the MTT assay were validated by assessing the amount of LDH leakage from each cell type (Figure 2C). In MCF-7 cells, treatment of VOL and cisplatin both caused significant amounts of LDH leakage, i.e., 82.909 U/L and 81.099 U/L respectively. However, the non-cancerous NKE cells were found to be less sensitive to VOL treatment as it caused LDH leakage in negligible amount with respect to untreated NKE cells; however, cisplatin was potent enough to cause significant damage to NKE cells as it triggered significantly higher LDH leakage (76.211 U/L) than that of the non-treated ones. Thus, unlike cisplatin, VOL was found to be distinctively toxic to MCF-7 cancer cells showing no remarkable toxicity for normal NKE cells.

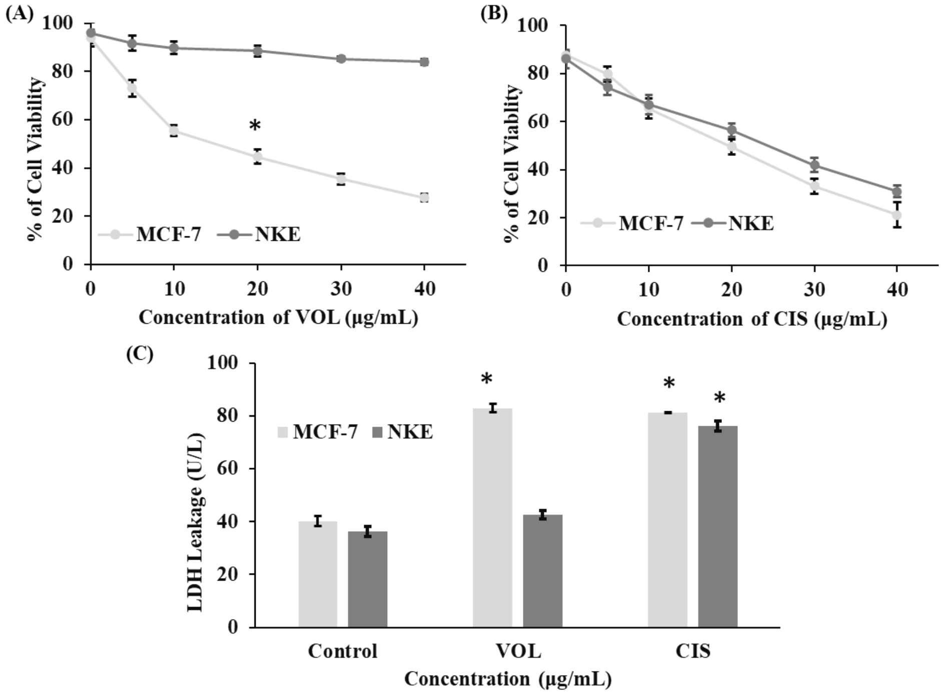

Figure 2: Cytotoxic effect of VOL in MCF-7 cells in comparison with known anticancer agent cisplatin: *Dose-dependent cytotoxicity of (A) VOL and (B) cisplatin in MCF-7 and NKE cell lines through a range of 0-40 µg/ml concentration detected through MTT assay. (C) Comparison of VOL (20.83 µg/ml) and cisplatin (21.13 µg/ml)-mediated LDH leakage in MCF-7 and NKE cells. All the data are representatives of three independent experiments. "*" represents a significant difference from the control group (P* < 0.05).*

3.4.2. VOL induces dose-dependent apoptosis to MCF-7 cells

The FITC-Annexin-V-mediated flow cytometric assay was conducted to comprehend the characteristics of cellular demise caused by VOL. As illustrated in Figure 3, the existence of cells in the fourth quadrants of the scatter plots signifies cells that exhibit a positive response to Annexin-V labeling. Cells exhibiting this staining pattern demonstrate the presence of phosphatidylserine residues on the outer surface of the cell membrane, which is indicative of apoptotic cells. Consequently, the compound VOL induces apoptosis in MCF-7 cells, with 46.99 % of the cells undergoing apoptosis at the respective LC_{50} dose. Similarly, like VOL, cisplatin also exhibits sufficient efficacy in inducing apoptotic cell death in human breast cancer cells MCF-7, with 46.50 % of the cells undergoing apoptosis at its LC_{50} dose. However, in contrast to VOL, which has minimal apoptotic effects on normal NKE cells (with only 7.84 % apoptotic cell population), cisplatin induces significant apoptosis (with 41.34 % apoptotic cells) even in the NKE cell population.

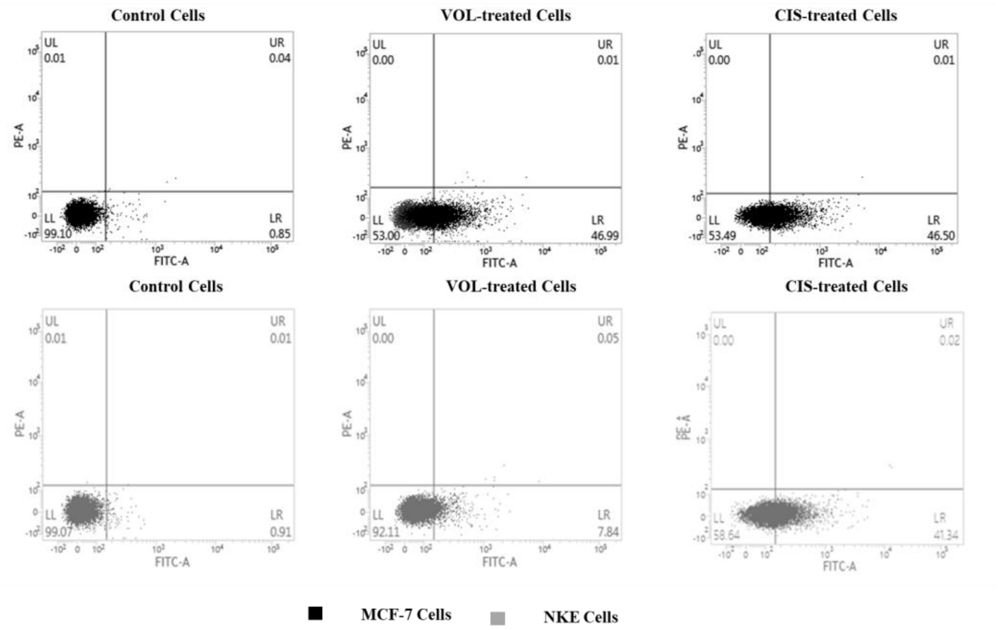

Figure 3: ***Detection of VOL and cisplatin-induced apoptosis in both MCF-7 and NKE cell lines:*** *MCF-7 and NKE cells pretreated with desired compounds (20.83 µg/mL of VOL and 21.12 µg/mL of cisplatin) were subjected to Annexin-V-FITC staining and subsequent flowcytometric study. Here, a dual parameter dot plot has been prepared where the x-axis represents the logarithmic fluorescence of FITC-tagged Annexin V. Apoptotic cell deaths are indicated in (A) MCF-7 cells and (B) NKE cells.*

3.4.3. VOL treatment imposed oxidative stress significantly in MCF-7 cells

In both physiological and pathological states, reactive oxygen species (ROS) play crucial roles in initiating apoptosis. Consequently, alterations in intracellular ROS production were assessed via flow cytometry using fluorescent DCFDA dye after the treatment. An elevation in green fluorescence was detected in MCF-7 cells treated with VOL, in contrast to untreated cells and VOL-treated normal NKE cells. Conversely, the induction of ROS was significantly higher in cisplatin-treated MCF-7 cells as well as NKE cells (Figure 4A-4B). This observation suggests a distinct augmentation of intracellular ROS in response to VOL treatment. Elevated intracellular ROS levels serve as a hallmark of global cellular oxidative stress (Park, Lee, and Choi 2011). To verify the state of oxidative stress in cells, various cellular antioxidant markers were examined. These markers included the activities of antioxidant enzymes SOD and CAT, the extent of lipid peroxidation (MDA), and the ratio of GSH to GSSG, among others (see Figure 4C-4F). Both cisplatin and VOL exposure had a significant detrimental effect on the antioxidant activities of CAT and SOD in MCF-7 cells. Exposure to these compounds also led to a significant decrease in GSH levels and an increase in GSSG levels in MCF-7 cells. In NKE cells, exposure to cisplatin resulted in a much lower GSH to GSSG ratio, whereas VOL-treated NKE cells maintained a normal physiological range of this ratio. Furthermore, VOL treatment greatly increased the amount of MDA in MCF-7 cells, but not in the non-cancerous cells. This indicates that VOL-induced oxidative stress is specific to MCF-7 cells.

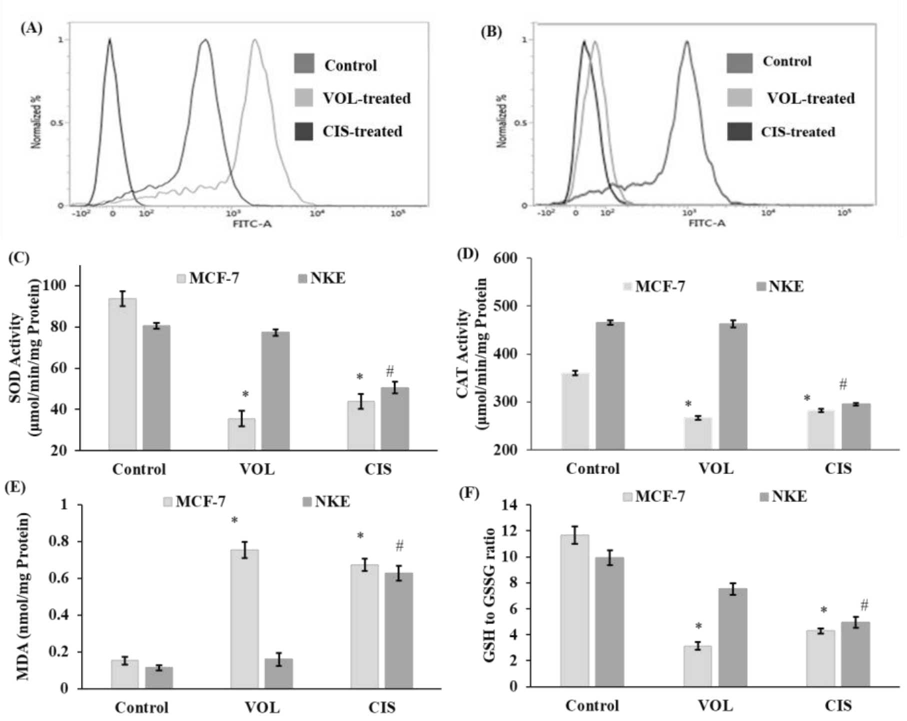

Figure 4: Determination of oxidative status of MCF-7 and NKE cells upon VOL and cisplatin treatment: *VOL-mediated differential ROS production in contrast to cisplatin treatment in (A) MCF-7 cells and (B) NKE cells. whereas, cisplatin-mediated enhanced oxidative stress is prominent in both MCF-7 and NKE cells. VOL and cisplatin-mediated changes in (C) SOD, (D) CAT activities, (E) MDA content & (F) GSH: GSSG ratio in cancerous MCF-7 and non-cancerous NKE cells. Each column is represented as mean ±SD, n = 6. "*" represents the significant difference with respect to control MCF-7; whereas, ''#" represents the significant difference with respect to the Control NKE cells. (P* < 0.05). Each data is representative of three independent experiments.*

3.4.4. VOL treatment selectively induces changes to TMP in MCF-7 cells

The induction of apoptosis and heightened cellular ROS are frequently associated with an augmented permeability and dysfunction of the mitochondria (Ghosh and Sil 2021). Consequently, we sought to investigate any potential alterations in the mitochondrial membrane potential of MCF-7 cells following treatment with cisplatin and VOL. Upon staining with JC-1 and subsequent flow cytometric analysis, an increase in green fluorescence accompanied by a simultaneous decrease in red fluorescence is indicative of a decline in the transmembrane potential (TMP). Notably, cisplatin exhibited the ability to diminish the mitochondrial membrane potential in both MCF-7 cells and NKE cells (Figure 5A-5B). Whereas, a reduction in transmembrane potential (TMP) was selectively induced by VOL in MCF-7 cells. The change in TMP induced by VOL was negligible in the treated NKE cells. This observation also suggests that mitochondrial dysfunction may play a crucial role in the apoptotic death of breast cancer cells.

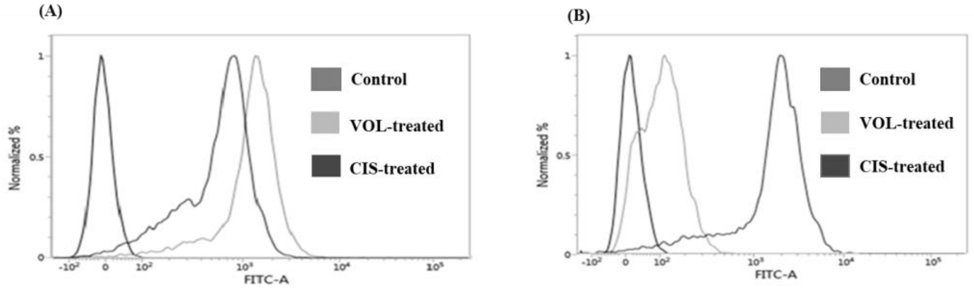

Figure 5: ***Detection of VOL and cisplatin-imposed TMP induction:*** *Effect of 20.83 µg/ml of VOL and 21.13 µg/ml of cisplatin treatment upon changes in mitochondrial membrane potential of (A) MCF-7 cells and (B) NKE cells respectively represented by the monomeric green fluorescence of the JC-1 dye. All data are representative of three independent experiments.*

3.4.5. NAC modulates VOL-mediated cell death

From the aforementioned observations, we harbored a sense of curiosity regarding the impact of reactive oxygen species (ROS) on the overall efficacy of VOL-induced cell death. To appease our curiosity, we employed NAC, a well-known ROS inhibitor. Upon treating MCF-7 cells with NAC in conjunction with an LC_{50} dose of VOL, we observed a significant reduction in intracellular ROS levels compared to cells treated solely with an LC_{50} dose of VOL (Figure 6A). Furthermore, pretreatment with NAC exhibited a remarkable ability to greatly mitigate the effect of VOL on the enzymatic activities of intracellular catalase (CAT) and superoxide dismutase (SOD) (Figure 6B-6C). NAC pretreatment, surprisingly, exhibited a notable decrease in VOL-induced cell death in MCF-7 cells (Figure 7A). The decrease in apoptotic cell death caused by VOL, as a result of NAC pre-treatment, was confirmed through flow cytometric sorting analysis of FITC-Annexin-V-stained control and treated MCF-7 cells (Figure 7B). These findings indicate that ROS plays a crucial role in the VOL-mediated anticancer effectiveness in inducing cell death in MCF-7 breast cancer cells.

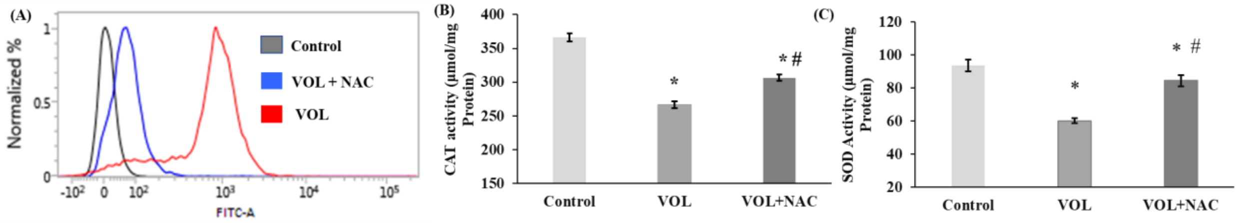

Figure 6: ***NAC reverses VOL induced ROS:*** (*A) Flowcytometric histogram showing comparative intracellular ROS content in MCF-7 cells treated with LC$_{50}$ dose of VOL alone and with 5mM NAC. Effect on (B) CAT & (C) SOD activities of MCF-7 cells upon exposure to VOL alone and in combination with 5mM NAC. Data are represented as mean ± SD, (n = 6) from three independent experiments. "*" & ''#" represent significant differences in contrast to normal control cells and VOL-treated cells (P^* & $P^{\#} < 0.05$).*

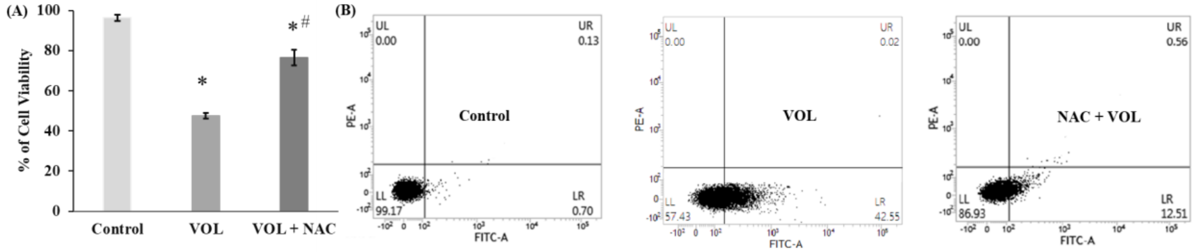

Figure 7: ***NAC reverses VOL-induced subsequent cell death and apoptosis:*** (*A) Bar diagram showing the percentage of viability of MCF-7 cells treated with LC$_{50}$ dose of VOL alone and with 5mM NAC. Each column is represented as mean ± SD, n = 6. "*" and ''#" respectively represent the significant with respect to the normal control and VOL-treated cells (P^* & $P^{\#} < 0.05$). Data are representatives of three independent studies. (B) Effect of exposure of 20.83 µg/ml VOL alone and in combination with 5mM NAC on cellular apoptosis in MCF-7 cells.*

3.4.6. VOL-induced tumor reduction study *in vivo*

EAC-derived solid tumors obtained from sacrificed experimental mice were assessed for their masses and dimensions. The average tumor mass and size of each experimental cohort (Groups I, II, and III) were graphed to facilitate visual comprehension of the changes.

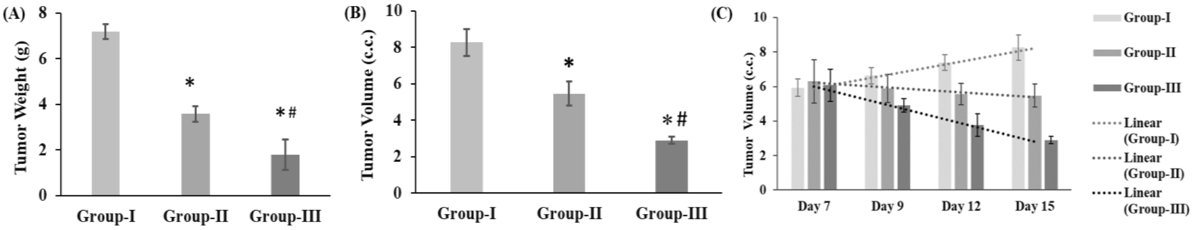

Figure 8: ***VOL-induced reduction in tumor mass and volume:*** *Dose-dependent reduction in (A) tumor mass (expressed in gram), (B) tumor volumes (expressed in cubic centimeters) upon VOL administration. (C) Relative changes in tumor volume (expressed in cubic centimeters) over 15 experimental days. Each column is represented as mean ± SD, n = 6. "*" & ''#" respectively represent the significant difference with respect to Group-I & Group-II. (P^* & $P^\#$ < 0.05).*

It was observed that VOL significantly reduced tumor magnitude, both in terms of mass and volume, in the treated cohorts (Figure 8A-8B), when compared to the untreated cohort (Group I), where the tumors had grown significantly substantial sizes throughout treatment (Figure 8C). Moreover, the outcomes demonstrated a dosage-dependent relationship, with a more pronounced anti-tumorigenic effect observed at higher doses (specifically in group III, where mice were administered VOL at a concentration of 20 mg per kg of body weight).

3.4.7. VOL treatment repairs disrupted tumor tissue architecture

VOL has been found to decrease multinucleated cells, distorted tumor tissue architecture and total number of nuclei in resected tumor tissues dose dependently (Figure 9A).

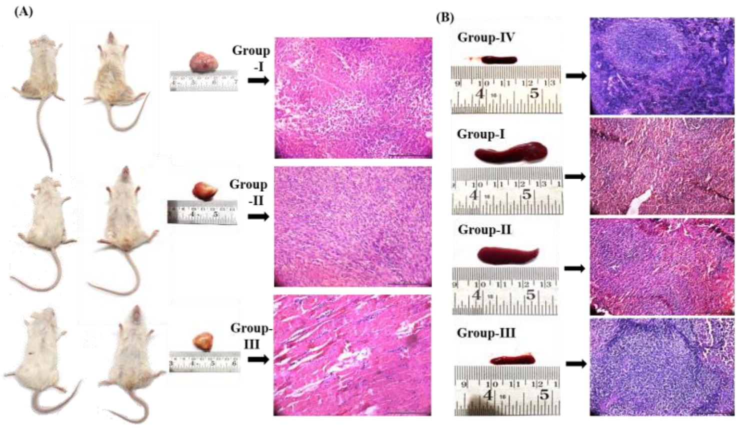

Figure 9: ***VOL-induced reduction in tumor load:*** *(A) Representative photographs of dorsal and ventral views of tumor-bearing mice, respective dissected tumor tissues, and their histological*

appearance with H & E staining. All data are representative of experiments repeated three times. (B) Representative photographs of dissected spleens from experimental mice of Group I-IV and their respective H & E-stained histological sections (at 20X magnification).

3.4.8. VOL treatment reduces EAC-induced splenomegaly in Swiss Albino mice

The evaluation of splenic size and weight was conducted as a means to identify inflammatory markers *in vivo*, which were induced by the incorporation of EAC (Queiroz et al. 2004). It was observed that the administration of VOL resulted in a reduction of splenomegaly in the treated animals of Groups II and III, in comparison to the untreated control group (Group I) (Figure 9B). These findings suggest that VOL treatment did not elicit significant toxicity in the overall physiological well-being of the animals; instead, it demonstrated efficacy in mitigating the extent of splenomegaly in the treated animals of Group II and III, thereby indicating an overall decrease in cancer burden in the tumor-bearing animals that received treatment. To substantiate these findings, histological analysis of H & E-stained splenic tissue sections from experimental animals of groups I-IV was performed, yielding consistent results as previously observed.

3.4.9. VOL altered *in vivo* redox parameters in tumor tissue

The investigation focused on the examination of antioxidant enzymes, specifically SOD and CAT, within tumor tissues (Figure 10A-10B).

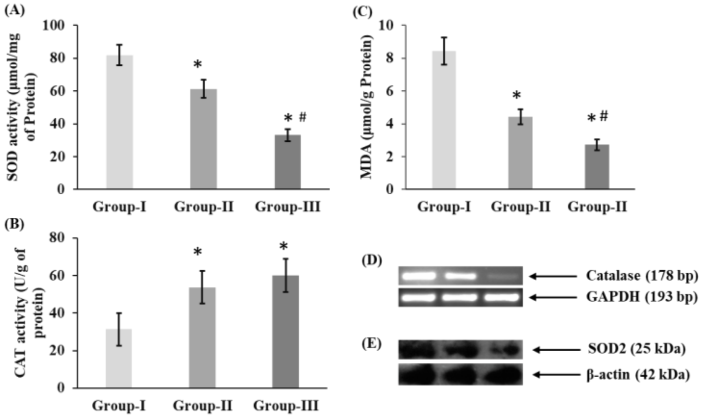

Figure 10: Changes of in vivo tumor tissue antioxidant parameters after VOL application: *(A) SOD and (B) CAT activities in tumor tissues of respective experimental groups. (C) represents the MDA levels in tumor tissue after being treated with 10 mg/kg and 20 mg/kg doses of VOL (expressed in terms of µmol/g of protein). (D) & (E) respectively represent expressions of CAT and SOD2 in tumor tissue.*

Expression of CAT was assessed through RT-PCR; whereas, SOD2 expression was studied by western blot analysis. The data shown here are representatives of three individual experiments. Each column has been plotted as mean ± SD, n = 6. "" represents the significant difference with respect to Group I; whereas, ''#" represents the significant difference with respect to Group II. (P* < 0.05).*

This examination was conducted using tumor tissue homogenates obtained from the corresponding experimental animals. The purpose was to determine if the observed *in vivo* outcomes aligned with the findings of the *in vitro* assays. CAT, a phase II detoxification enzyme of great significance, plays a crucial role in safeguarding against cancer cell damage caused by ROS. Similarly, SOD2 or MnSOD functions in a comparable manner. Therefore, in addition to assessing the activities of these two enzymes within the tumor tissue, we also analyzed the respective transcriptional and translational levels of CAT and SOD2 *in vivo* (Figure 10D-10E). It has been determined that the findings from the *in vivo* investigation indeed support the results obtained from the *in vitro* analysis, albeit with certain variations due to the physiological conditions present in the *in vivo* setting. In the group treated with VOL, the antioxidant activities of CAT and SOD2 were observed to decrease in line with their expression levels, in contrast to the tumor control group. Furthermore, an increase in the dose of VOL was found to stimulate lipid peroxidation in tumor tissues as well (Figure 10C). Therefore, it can be deduced that VOL has the potential to disrupt the redox balance in tumor tissue.

3.4.10. VOL altered Bcl-2-family proteins inducing intrinsic apoptotic effect

To examine the protein expressions of different pro-apoptotic and anti-apoptotic molecules in the tumor tissues at the translational level, we analyzed the data obtained from western blotting. The findings of our previous determination of the transmembrane potential (TMP) provided a clue regarding the dysfunctionality of mitochondria. Consequently, we aimed to investigate the translational expression of crucial molecules that are associated with the mitochondria-mediated apoptotic pathway (Figure 11A). In this particular course, it was observed that the administration of VOL had a dose-dependent effect on reducing the Bcl-2/Bax ratio. The decrease in the Bcl-2/Bax ratio is a distinctive characteristic that leads to the activation of intrinsic apoptotic cell death. Additionally, the depletion of TMP is correlated with an increase in mitochondrial permeability, resulting in the release of the mitochondrial protein cytochrome C. Consequently, there was a noticeable translation of cytochrome C. Subsequently, we examined the heightened expression of Apaf-1, which confirmed the formation of the apoptosome. Furthermore, to verify the specific activation of caspase, we assessed the expression levels of cleaved caspase 9 and cleaved caspase 3, both of which exhibited higher levels of expression in tumor tissue treated with 20 mg of VOL (Figure 11A, 11D).

3.4.11. VOL concomitantly induced extra-mitochondrial apoptosis in tumor tissues

As we observed a significant increase in tumor-related inflammatory splenomegaly in mice carrying experimental tumors, we were interested in determining whether there was a corresponding increase in inflammatory signals in tumor tissue treated with VOL. Therefore, we assessed the expression of pro-inflammatory cytokines, such as tumor necrosis factor-α (TNF-α) and interleukins (IL-6, IL-1β), at the transcriptional level (Figure 11B, 11E).

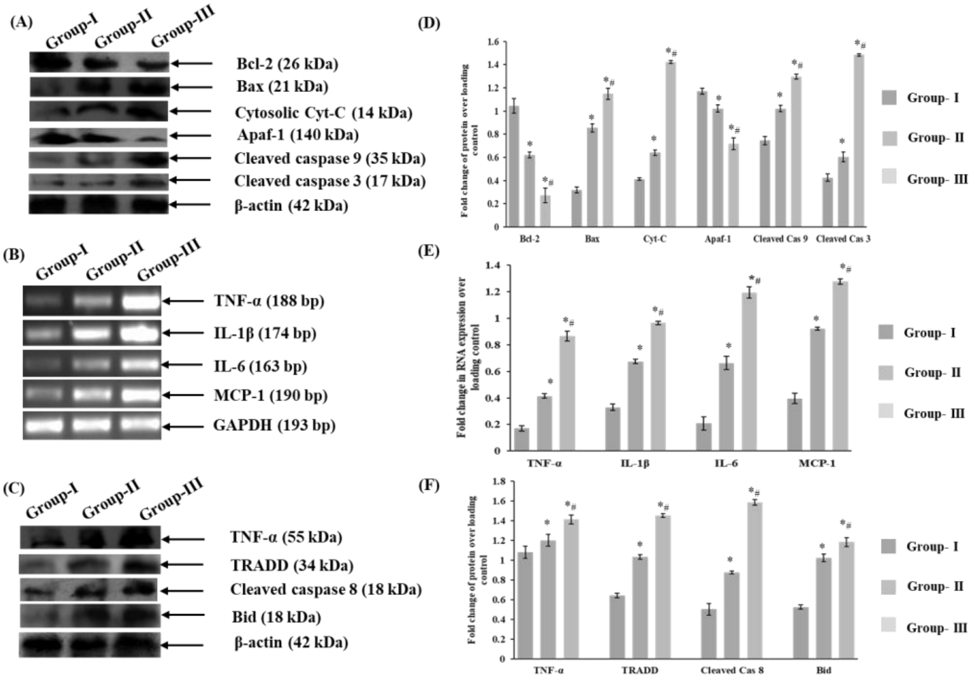

Figure 11: VOL-induced in vivo tumor reduction is related to upregulation of apoptotic and inflammatory markers: *(A) Immunoblot analysis of Bcl-2, Bax, cytosolic Cyt C, apaf-1, cleaved caspase 9 and 3 from tumor tissues homogenates obtained from respective experimental groups. β-actin has been used as the loading control here. (B) Analysis of transcriptional expression of inflammatory markers such as TNF-α, IL-1β, IL-6, and MCP-1 in tumor tissues from all three experimental groups through RT-PCR. GAPDH has been used as a loading control. (C) Immunoblot expression of TNF-α, TRADD, cleaved caspase-8, and Bid (β-actin has been employed as internal loading control) (D-F) Densitometric analysis respective immunoblot and RT-PCR data expressed as the mean ± SD. "*" & "#" respectively represent the significant difference with respect to the Group-I and Group-II.* ($P^* \& P^{\#} < 0.05$).

Inflammatory cytokines are known to stimulate the production of chemokines, leading to the infiltration of leukocytes. In our current investigation, we examined whether there were any changes in the transcriptional expression of monocyte chemo-attractant protein-1 (MCP-1) as a result of VOL treatment. Additionally, we utilized western blotting to analyze the expression of TNF-α in tumor tissues collected from the experimental mice in Groups I-III. Our study revealed that the expression of TNF-α was upregulated at both the transcriptional and translational levels following VOL treatment (Figure 11B-11C). Additionally, based on the analysis of RT-PCR data, it was observed that VOL treatment could enhance the expression of IL-1β, IL-6, and MCP-1 mRNA. In addition to its role in the inflammatory response, TNF-α can also induce apoptosis. Consequently, an investigation was conducted to assess the expression of genes involved in the extrinsic apoptotic pathway mediated by TNF-α (Figure 10C). Consequently, it was found that downstream of TNF-α, the expression of TNFR1-associated death domain protein (TRADD) and cleaved caspase-8 were both elevated (Figure 11C-11F). Furthermore, downstream of this, the increased expression of Bid was sufficient to establish a link between the extrinsic apoptotic pathway mediated by TNF-α and the intrinsic pathway.

3.4.12. VOL induces higher expression of cleaved caspases 9, 8, and 3 in tumor tissue *in vivo* with dose-dependency

To visualize the changes induced by VOL treatment *in vivo*, an immunohistochemical experiment was conducted to examine the expressions and localizations of Caspase-8, 9, and 3 in the tumor tissues of experimental animals (Figure 12A-12C).

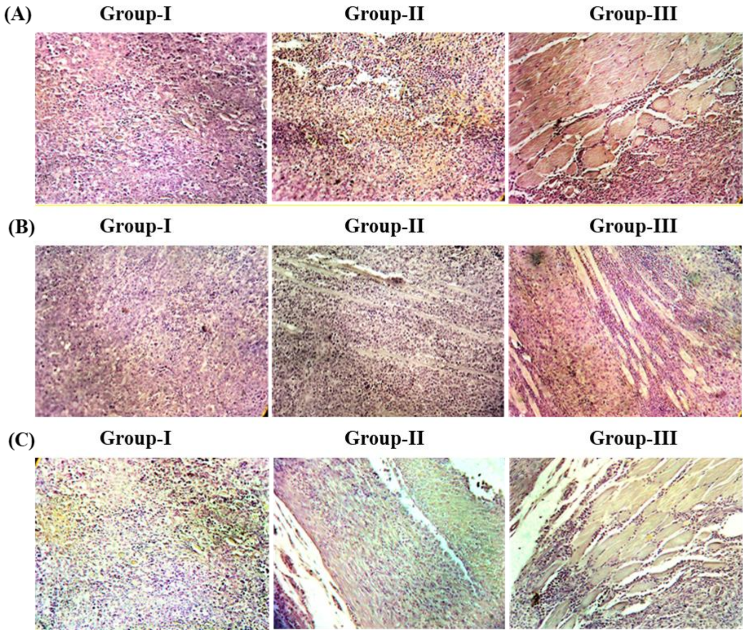

Figure 12: *Immunohistochemical expression of (A) caspase-9, (B) caspase-8, and (C) caspase-3 in resected tumor tissue after being treated with different doses of VOL.*

The degree and intensity of DAB expression were utilized as markers for the expression of the proteins of interest. It was observed that the immunohistochemical results aligned with the findings obtained from western blotting. Furthermore, Caspase-9, caspase-8, and caspase-3 also exhibited increased expression and localization in the tumor tissues obtained from animals in Group III, which were administered a higher dosage in comparison to Group II. As anticipated, the untreated group displayed minimal expressions of these three pro-apoptotic proteins.

3.4.13. VOL is overall non-toxic to healthy body tissues

The mice that received VOL treatment were regularly monitored to observe any alterations in their fur color or change in body weight throughout the treatment period to detect any indications of toxicity resulting from the treatment. Additionally, it was observed that there were no changes in the fur color of the treated animals (Figure 9A). Moreover, in animals belonging to Group III, the tumors visibly diminished in size, while the mice from Groups II, III, IV, V, and VI continued to display normal growth in terms of body weight. This was in contrast to the sporadic increase in body weights observed in mice from Group I. In other words, there was neither a decrease nor a cessation in the growth of the mice (Figure 13).

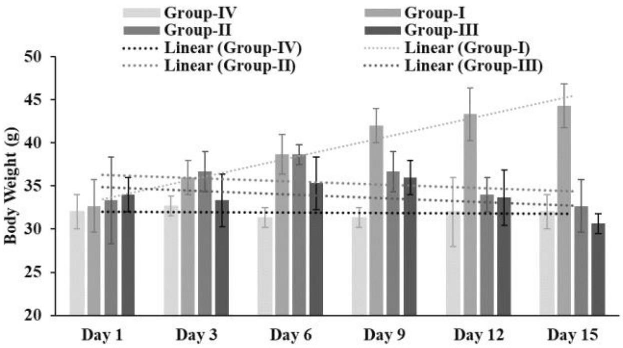

Figure 13: *Changes in body weight of tumor-bearing mice over a treatment period of 15 days*

3.4.14. VOL does not alter *in vivo* liver and kidney parameters significantly

Serum derived from experimental animals, from all six groups were assessed for the levels of crucial liver and kidney health indicators, namely ALT, ALP, BUN, and creatinine (Figure 14A-14D). The findings of the experiments were promising, as they revealed that the administration of VOL in either of the two doses did not cause any substantial toxicity to the animals in groups V and VI. This outcome was further supported by the examination of histopathological sections of liver and kidney tissues stained with hematoxylin and eosin from the respective experimental groups, demonstrating no significant systemic cytotoxicity of our compound candidate VOL (Figure 15). The levels of all four toxicity indicators remained almost similar to those of the healthy control animals in group IV.

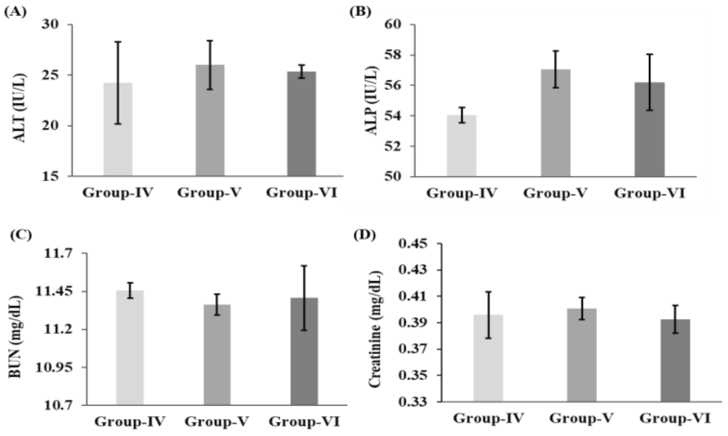

Figure 14: ***In vivo systemic toxicity profile of VOL:*** *(A) Serum ALT level; (B) Serum ALP level; (C) Serum BUN level; (D) Serum creatinine level of experimental mice of Group-IV-VI. Each column is represented as mean ± SD, n = 6.*

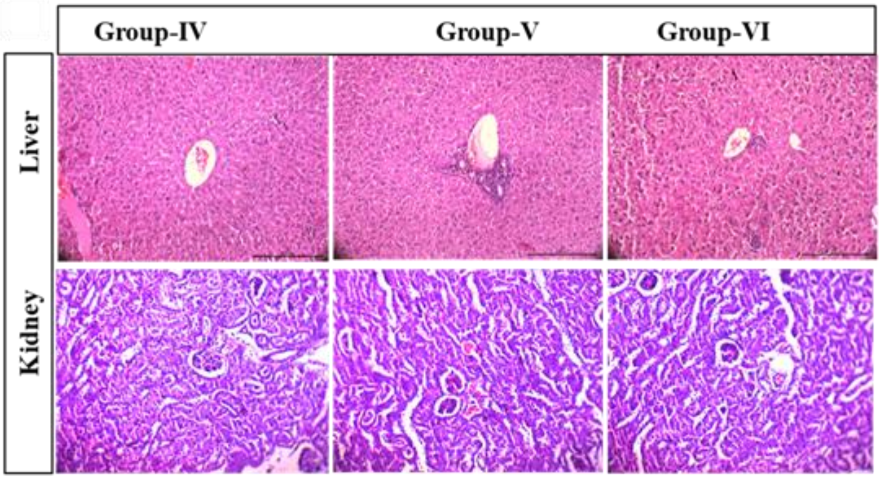

Figure 15: *Histological assessment of representative H & E-stained microscopic sections of renal and hepatic tissues under 20X magnification.*

3.5. Conclusion

The current study showcases the robust anticancer properties of the newly synthesized oxovanadium complex VOL, which have been succinctly outlined in Figure 16. VOL was observed to exhibit dose-dependent cytotoxicity in human breast cancer cells comparable to the anticancer efficacy of cisplatin.

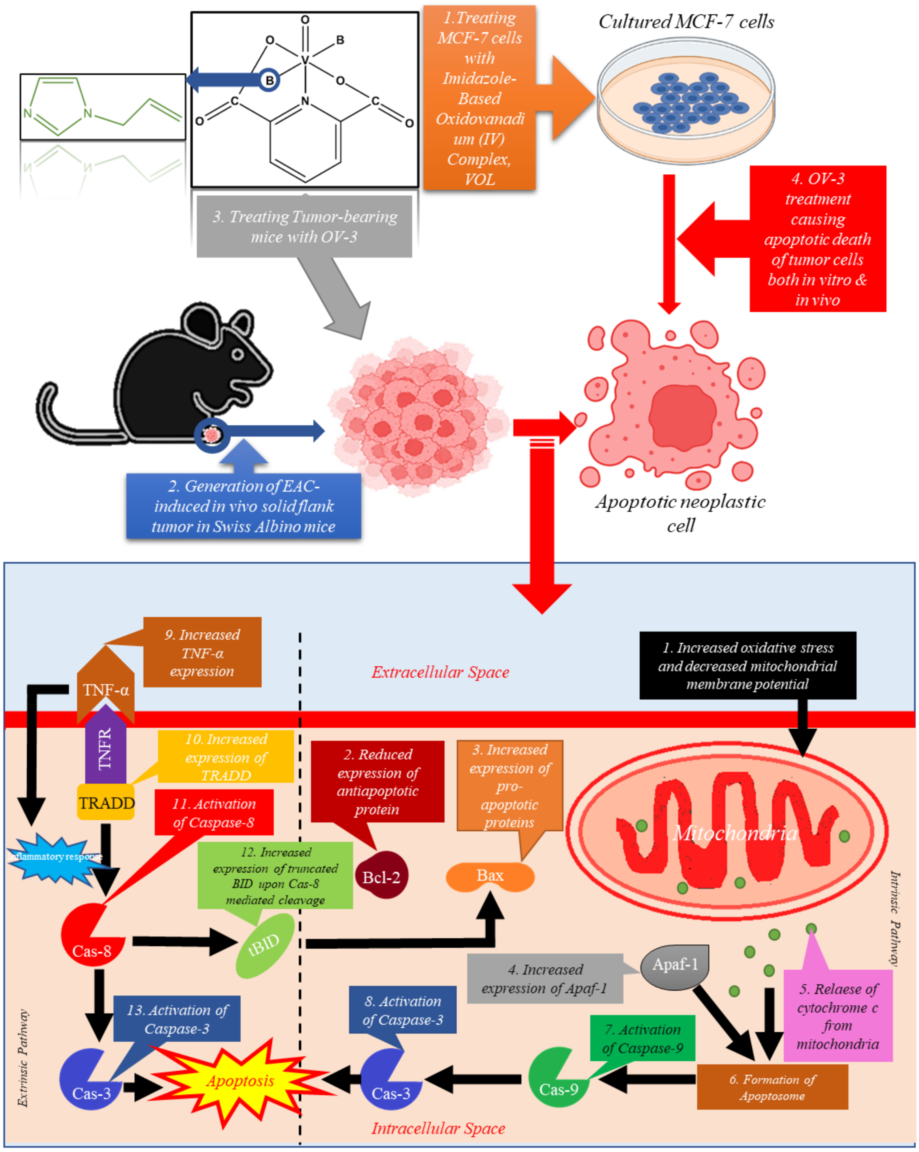

Figure 16: ***Schematic diagram representing the anti-cancer activity of VOL:*** *In vitro (in MCF-7 cells) and in vivo (in Swiss Albino mice) anti-tumor efficacy of novel water-soluble mononuclear dipicolinic acid-imidazole based oxidovanadium (IV) complex VOL.*

The administration of cisplatin is associated with the occurrence of significant adverse effects on healthy tissues in cancer patients due to its non-specific toxicity. In contrast, VOL demonstrated limited toxicity towards normal cells *in vitro*, as confirmed by both MTT and LDH leakage assays. Furthermore, when evaluated *in vivo*, VOL displayed no significant toxicity toward vital organs such as the liver and kidney. The demonstration of normal levels of serum hepatic and renal toxicity markers, as well as the absence of histological abnormalities in liver and kidney sections, provides sufficient evidence to support the claim of minimal off-target toxicity. Despite this minimal off-target toxicity, VOL exhibited potent tumor-suppressing effects, leading to a reduction in tumor volume and mass within a treatment period of only 14 days. Additionally, increasing doses of VOL were found to alleviate the splenomegaly observed in tumor-bearing Swiss Albino mice. Furthermore, an improvement in splenomegaly was observed in Swiss Albino mice along with tumor regression when they were administered increasing doses of VOL. Upon closer examination of its mechanism of action, VOL was found to activate both the intrinsic and extrinsic pathways of programmed cell death. VOL was noted to induce mitochondrial apoptosis by modulating the delicate balance between cellular pro-apoptotic and anti-apoptotic factors. The primary regulator in this process was identified as an augmented intracellular load of ROS and subsequent reduction in mitochondrial potential. The study conducted with NAC elucidates the clear indication of the induction of ROS-dependent apoptosis by VOL. To circumvent the detrimental effects of oxidative stress, tumor cells are known to possess a higher-than-normal level and/or activity of antioxidant enzymes (George and Abrahamse 2020). VOL has been documented to diminish both the activity and level of antioxidant enzymes, both *in vitro* and *in vivo*, thereby augmenting the overall likelihood of intrinsic apoptosis induction. Additionally, VOL has been found to elicit a heightened inflammatory response in tumor tissues, subsequently leading to extra-mitochondrial apoptosis. Furthermore, the *in vivo* immunoblot analysis has revealed the confluence of the extrinsic apoptotic pathway with the intrinsic one, contributing to the enhanced cell-killing ability of VOL. Based on the aforementioned observations, it can be hypothesized that similar to other oxidovanadium complexes, VOL primarily triggers apoptosis through the mechanism of oxidative damage. In this particular context, it is imperative to conduct further analysis on anticancer oxidovanadate compounds such as VOL. However, to briefly summarize, VOL and cisplatin, despite their comparable anticancer and tumor-inducing properties, differ fundamentally in terms of their mode of action. According to numerous existing reports, it is widely recognized that inorganic compounds containing vanadium (IV) can hydroxylate 2’-deoxyguanosine, subsequently leading to DNA breakage mediated by reactive oxygen species (Shi, Jiang, et al. 1996, Shi, Wang, et al. 1996). Furthermore, it has been observed that VOL induces its anticancer effects by first inducing reactive oxygen species, followed by alterations in the oxidative state of cells and an associated increase in mitochondrial permeability. Thus, based on the aforementioned discussion, VOL may serve as a powerful metallodrug for breast cancer treatment, serving as an alternative to platinum-based drugs.

3.6. References

Biswal, Debanjana, Nikhil Ranjan Pramanik, Syamal Chakrabarti, Michael GB Drew, Krishnendu Acharya, and Swarnendu Chandra. 2017. "Syntheses, crystal structures, DFT calculations, protein interaction and anticancer activities of water soluble dipicolinic acid-imidazole based oxidovanadium (iv) complexes." *Dalton Transactions* 46 (47):16682-16702.

Chen, Shang-Hung, and Jang-Yang Chang. 2019. "New insights into mechanisms of cisplatin resistance:

from tumor cell to microenvironment." *International journal of molecular sciences* 20 (17):4136.

Cossarizza, Andrea, Roberta Ferraresi, Leonarda Troiano, Erika Roat, Lara Gibellini, Linda Bertoncelli, Milena Nasi, and Marcello Pinti. 2009. "Simultaneous analysis of reactive oxygen species and reduced glutathione content in living cells by polychromatic flow cytometry." *Nature protocols* 4 (12):1790-1797.

George, Sajan, and Heidi Abrahamse. 2020. "Redox potential of antioxidants in cancer progression and prevention." *Antioxidants* 9 (11):1156.

Ghosh, Noyel, and Parames C Sil. 2021. "Mitochondria and apoptosis." In *Mitochondrial Physiology and Vegetal Molecules*, 127-149. Elsevier.

Marks, Tobin J. 1996. "Metallocene interactions with DNA and DNA-processing enzymes." *Metal Ions in Biological Systems: Volume 33: Probing of Nucleic Acids by Metal Ion Complexes of Small Molecules* 33:53.

Park, Junseong, Jungsul Lee, and Chulhee Choi. 2011. "Mitochondrial network determines intracellular ROS dynamics and sensitivity to oxidative stress through switching inter-mitochondrial messengers." *PloS one* 6 (8):e23211.

Queiroz, Mary LS, MC Valadares, C Bincoletto, and GC Dieamant. 2004. "Ehrlich ascites tumor as a tool in the development of compounds with immunomodulatory properties." *Immunopharmacology and immunotoxicology* 26 (4):511-525.

Shi, Xianglin, Hengguang Jiang, Yan Mao, Jianping Ye, and Umberto Saffiotti. 1996. "Vanadium (IV)-mediated free radical generation and related 2′-deoxyguanosine hydroxylation and DNA damage." *Toxicology* 106 (1-3):27-38.

Shi, Xianglin, Peichang Wang, Hengguang Jiang, Yan Mao, Nadera Ahmed, and Naresh Dalal. 1996. "Vanadium (IV) causes 2'-deoxyguanosine hydroxylation and deoxyribonucleic acid damage via free radical reactions." *Annals of Clinical & Laboratory Science* 26 (1):39-49.

Chapter 4

Multifaceted Antineoplastic Curative Potency of Novel Water-soluble Methylimidazole-based Oxidovanadium (IV) Complex in Triple Negative Mammary Carcinoma

4.1. Introduction

At present, we have studied the anticarcinogenic properties of a newly synthesized hydrophilic mononuclear dipicolinic acid and 1-methyl imidazole-substituted oxidovanadium (IV) complex (Biswal et al. 2017) (Figure 1).

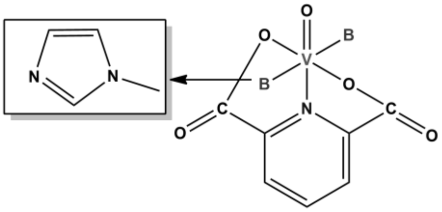

Figure 1: *Chemical structure of synthesized hydrophilic mononuclear dipicolinic acid and 1-methyl imidazole-substituted oxidovanadium (IV) complex, abbreviated as OVMI*

In this context, it is important to note that along with its amphiphilic nature and several pharmacological advantages, dipicolinic acid, present in various natural compounds, is known to stabilize unusual oxidation states of the metals (Jakusch et al. 2003). Besides, pentameric ring structure and potency to intercalate and cleave DNA strands (Keter 2010, Pizarro and Sadler 2009, Reedijk 2003) due to the presence of heteroatom nitrogen, imidazole shows significant antioxidant (Smith and Reeves 1987), antimicrobial (Aridoss et al. 2006, Bhandari et al. 2009, Eslami Amirabadi et al. 2019) as well as anticancer (Congiu, Cocco, and Onnis 2008) therapeutic efficacies. For easy interpretation, the compound has been denoted as OVMI throughout the manuscript. Earlier anticarcinogenic activities of OVMI have been explored *in vitro* using human hepatocellular carcinoma cell Hep3B (Biswal et al. 2017). In our previous work, another compound in this series has also been tested for its both *in vitro* and *in vivo* anti-neoplastic activities in progesterone receptor-positive breast carcinoma (Ghosh et al. 2022). To be consistent with the outcome, currently, we have tried to find out the anti-neoplastic activities of OVMI in human TNBC cells, MDA-MB-231. Additionally, findings are also extrapolated *in vivo* system using 4T1 cell-induced Balb/c TNBC-bearing mice. Also, work has been extended to see the effect of OVMI against 4T1-mediated secondary lung metastasis *in vivo.* Once found to be significantly effective against TNBC cell proliferation and metastasis, we also looked deep into the molecular aspect of its antitumor activities and probable systemic toxicities (if any) associated with female Balb/c mice.

4.2. Utilized reagents

The reagents and chemicals utilized in this research were acquired from esteemed scientific manufacturing corporations, as mentioned in section 2.1. The focus of this study centers around evaluating the effectiveness of the mononuclear dipicolinic acid-1-methyl imidazole-based oxidovanadium (IV) complex (OVMI), which was synthesized by Biswal et al. and generously provided for experimental use by Professor Nikhil Ranjan Pramanik (Biswal et al. 2017).

4.3. Methods

4.3.1. Cell culture

Three different types of cells were introduced, cultivated, and sustained for experimentation in this particular study. Specifically, the cells used were human triple-negative breast epithelial cancer cells MDA-MB-231 (which were originally acquired from ATCC, US), immortalized normal human renal epithelial cells NKE, and murine triple-negative mammary carcinoma cells 4T1 (both of which were generously provided by Prof. Kaushik Biswas). These cells were grown under standard laboratory conditions in DMEM media, as described in section 2.2.1.1 of Chapter 2.

4.3.2. Cytotoxicity assessment

The cytotoxic impacts of OVMI were assessed in both MDA-MB-231 and NKE cells across a range of doses spanning from 0 µg/ml to 50 µg/ml over 24 hours. This evaluation was conducted utilizing the established MTT method, as described in detail in Chapter 2, specifically in section 2.2.1.2. For comparative purposes, cisplatin was employed as the positive control in this investigation.

4.3.3. LDH leakage assessment

Cellular injury induced by OVMI in both MDA-MB-231 and NKE cells was assessed using the LDH leakage assay, as elaborated upon in section 2.2.1.3 of Chapter 2.

4.3.4. Analysis of apoptosis induction by Annexin-V-PI dual staining

After undergoing treatment with three distinct doses of OVMI (0, 10, 20, and 30 µg/mg) over 24 hours, an analysis of apoptosis induction, which was dependent on the administered dose, was conducted using Annexin-V/PI-dual staining as elucidated in section 2.2.1.4. of chapter 2. The assessment was performed utilizing both flow cytometry and confocal laser scanning microscopy.

4.3.5. DCFDA Staining

Following exposure to various doses (0, 10, 20, and 30 µg/mg) of OVMI, MDA-MB-231 cells were subjected to DCFDA staining. Subsequently, the resultant fluorescence was assessed using both flow cytometry and confocal microscopy. A comprehensive methodology outlining the study can be found in section 2.2.1.5. of Chapter 2.

4.3.6. JC1 staining

The alterations in OVMI-induced TMP in MDA-MB-231 cells at different doses (0, 10, 20, and 30 µg/ml) were assessed utilizing JC1 staining. Additionally, the fluorescence intensity of the JC1 monomer as well as the dimer was analyzed using both flow cytometry and confocal microscopy. The application of image-J software enabled the computation of the red-to-green fluorescence intensity ratio of JC1. A comprehensive description of the representative methodology can be found in section 2.2.1.6. of Chapter 2.

4.3.7. Evaluation of mitochondrial swelling

The phenomenon of OVMI-mediated calcium ion-dependent mitochondrial swelling was investigated using the experimental procedure outlined in section 2.2.1.11. of Chapter 2.

4.3.8. Inhibitor study

Cells that underwent pretreatment with NAC were subsequently subjected to treatment with OVMI to assess the impact of inhibiting ROS in MDA-MB-231 cells. The cells were treated in three distinct groups: one with NAC alone, another with OVMI alone, and the last one with NAC + OVMI. The influence of NAC treatment was then assessed in terms of the antineoplastic effectiveness of OVMI. The detailed protocol has been described in section 2.2.1.16. of Chapter 2.

4.3.9. Whole cell protein extraction and immunoblotting

The extraction of total cellular protein and subsequent determination of protein levels was conducted following the procedure outlined in section 2.2.1.14. within Chapter 2. Following the measurement, the proteins of interest were separated and subjected to electrophoresis on an SDS-polyacrylamide gel based on their molecular weight. In this study, primary antibodies targeting Bcl-2 (ab7973), Bax (#2772), Apaf-1 (#8723), cleaved caspase-9 (#9508), cleaved caspase-3 (#9662), PARP (#9532), calpain-1 (ab39170), GRP-78 (ab21685), phosphor-eIF-2α (ab32157), and CHOP (#5554) were employed, and their detection was carried out using secondary antibodies labeled with HRP against both rabbit (ab97051) and mouse (#9508). To ensure equal protein loading, β-actin (BB-AB0024) was utilized as a control. A comprehensive protocol detailing these experimental procedures can be found in section 2.2.1.15. within Chapter 2.

4.3.10. Acquirement of cytosolic and mitochondrial fractionations

Mitochondrial and cytosolic subcellular fractions of MDA-MB-231 cells treated with OVMI were acquired following the methodology elucidated in section 2.2.1.13 of Chapter 2. Primary antibody against cytochrome C (#4272) in both mitochondrial and cytosolic fractions was utilized here, For the cytoplasmic and mitochondrial separations, β-actin (BB-AB0024) and VDAC (#4866) were employed as loading controls, respectively.

4.3.11. Wound healing assay

The anti-migratory properties of OVMI concerning MDA-MB-231 cells were assessed at three distinct dosages over a time frame ranging from 0 to 48 hours. This evaluation was conducted according to the comprehensive protocol outlined in Chapter 2, specifically within section 2.2.1.12. The quantification of data was made feasible through the utilization of the Image-J software.

4.3.12. 4T1 induced *in vivo* breast tumor regression study

Twenty female Balb/c mice, with standard age and body weight, were acclimated and maintained according to the standard protocol outlined in the previous exposition, specifically in chapter 2 within section 2.2.2.1. The experimentation involving animals adhered to the ethical guidelines set forth by the Committee for Control and Supervision on Experiments on Animals (CPCSEA) located in New Delhi, India (1796/PO/Ere/S/14/CPCSEA), and received the necessary approval from the Institutional Animal Ethics Committee (IAEC) of Bose Institute, Kolkata [Approval no. IEAC/BI1003/2021]. The procedure for 4T1-based mammary tumor inoculation was carried out as described in section 2.2.2.3 of Chapter 2. Once the tumor volume reached an approximate size of 100 mm^3, the mice were randomly divided into four groups and the treatment plan was as depicted in Scheme 1.

PT_{NC} : mice treated with 1X PBS (pH 7.4)

PT_{10} : treated at a dose of 10 mg/kg of body weight with OVMI

PT_{20} : treated at a dose of 20 mg/kg of body weight with OVMI

PT_{30} : treated with 30 mg/kg of body weight with OVMI

A total of six injections were administered through the tail vein over a duration of 16 days, ensuring a 72-hour interval between each consecutive injection (Scheme 1). Alterations in body weight were assessed throughout treatment. Upon completion of the treatment, the mice were euthanized, and both tumors and spleens were excised from each animal. On the day of euthanasia, the volume and mass of the tumors were measured, followed by their immersion in formalin solution for subsequent histological examination.

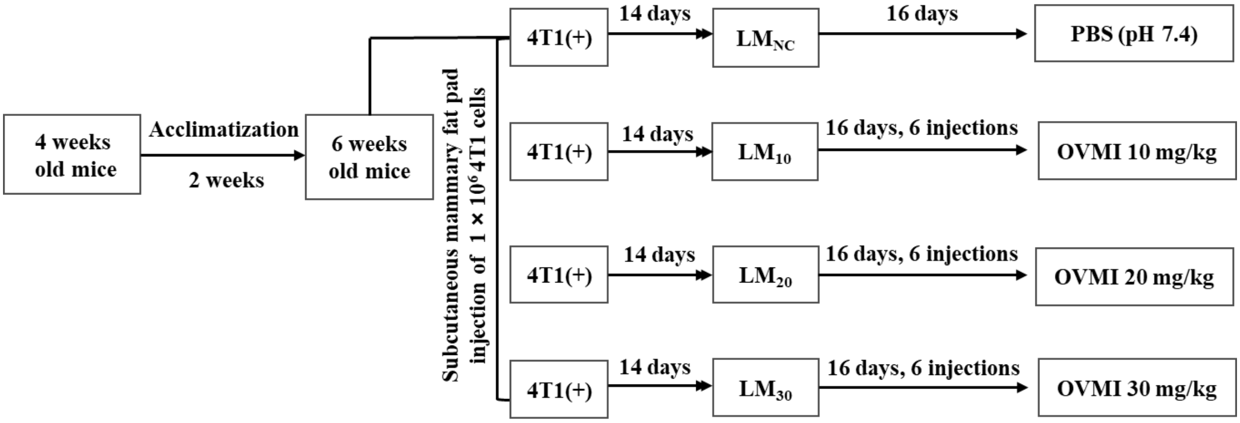

Scheme 1: ***Schematic diagram explaining****: 4T1-induced mammary tumor induction and subsequent treatment plan in female Balb/c mice*

4.3.13. TUNEL assay

The degree of apoptosis in mammary tumor tissues treated with OVMI was assessed by utilizing the TUNEL assay as per the provided protocol guidelines from the manufacturer of the APO-BrdU™ TUNEL Assay Kit, which employed Alexa Fluor™ 488 (A23210, Thermo Fischer). A comprehensive protocol explanation can be found in section 2.2.2.11. of chapter 2. The processed tissue sections were examined using confocal microscopy.

4.3.14. Immunohistochemistry

Immunohistochemical staining was conducted on mammary tumor tissues treated with OVMI. The staining procedure utilized a DAB-based IHC detection kit (ab80437, Abcam, UK). The steps for staining were carried out under the guidelines provided by the manufacturer, as previously described in Chapter 2, section 2.2.2.10. The stained slides were examined under a bright field microscope to assess the relative expression of PARP (#9532), Ki-67 (#12202), N-cadherin (A19083), and E-cadherin (ab76055) using respective primary antibodies.

4.3.15. Study of 4T1-mediated secondary lung metastasis induction and its regression through OVMI treatment

Female Balb/c mice were administered an intravenous injection of 4T1 cells via the tail vein to induce the formation of lung metastases. The detailed procedure for this experiment is described in the section of chapter 2. Fourteen days after the inoculation of the tumor, the mice were divided into four groups to receive OVMI treatment, as outlined below (Scheme 2):

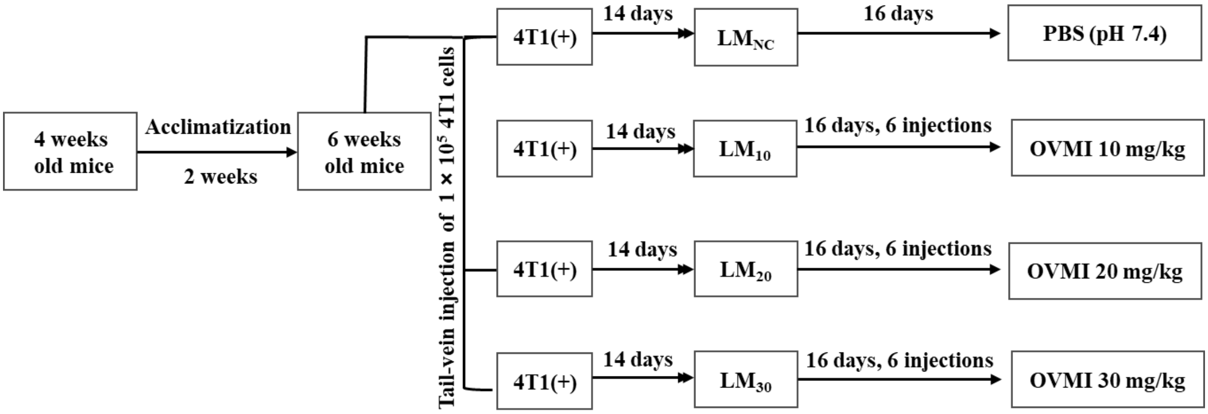

Scheme 2: ***Schematic diagram explaining****: 4T1-mediated secondary pulmonary metastasis induction and subsequent treatment plan in female Balb/c mice*

LM$_{NC}$: These mice were treated with 1X PBS of pH 7.4.

LM$_{10}$: These mice were treated with OVMI at a dose of 10 mg/kg of body weight.

LM$_{20}$: These mice were treated with OVMI at a dose of 20 mg/kg of body weight.

LM$_{30}$: These mice were treated with OVMI at a dose of 30 mg/kg of body weight.

The treatments were administered intravenously through the tail veins for 16 days, with a total of 6 injections administered at intervals of 72 hours (Scheme 2). Following the treatment period, the mice were euthanized and the metastatic lungs were surgically removed and examined for the presence of external micro-metastatic nodules. Additionally, the weight of the resected lungs was also recorded.

4.3.16. *In vivo* western blot analysis from secondary lung metastasis

The translational expression of proteins implicated in metastasis, namely MMP-2 (#40994), MMP-9 (A0289) VCAM-1 (A11236), and ICAM-1 (A20472), was assessed using western blotting. This was achieved by homogenizing lung tissues in RIPA buffer, followed by quantification of protein concentration and subsequent SDS-polyacrylamide gel electrophoresis. A comprehensive protocol for this procedure can be found in the relevant section 2.2.2.9. of Chapter 2.

4.3.17. *In vivo* systemic toxicity assessment

To evaluate the systemic toxicity induced by OVMI, a total of twenty female Balb/c mice without tumors were selected and divided into four different treatment groups in a random manner. These groups were as follows:

ST_{NC} : This group was treated with 1X PBS of pH 7.4.

ST_{10} : The mice in this group were administered a dose of 10 mg/kg OVMI.

ST_{20} : The mice in this group were administered a dose of 20 mg/kg OVMI.

ST_{30} : The mice in this group were administered a dose of 30 mg/kg OVMI.

After a period of experimentation lasting sixteen days, during which OVMI/PBS was administered intravenously six times through the tail veins of the mice, the mice were euthanized. Blood was obtained from each experimental mouse through cardiac puncture, and vital organs such as the lungs, liver, kidneys, and heart were collected for subsequent histological analysis using H & E staining. The collected blood from each mouse was then processed to isolate the serum, followed by the use of a kit to determine the levels of serum ALP, ALT, BUN, and creatinine. A detailed protocol outlining the procedures undertaken in this experiment can be found in section 2.2.2.5 of chapter 2.

4.3.18. Histological assessment

Resected 4T1-induced mammary tumor tissues and isolated cardiac, hepatic, renal, and pulmonary tissues from systemic toxicity experimental studies were processed through H & E staining for histological analyses under a bright field microscope. Detailed protocol of H & E staining has been described in section 2.2.2.6. of Chapter 2.

4.3.19. Statistical analyses

Each set of experimental data has been expressed as the mean value plus or minus the standard deviation (SD) of three separate experiments. These data were then subjected to an analysis of variance (ANOVA) test with a one-factor design. In cases where it was appropriate, a Tukey's post-hoc test was conducted for further evaluation of significance. A significance level of *$P < 0.05$ was deemed as statistically significant.

4.4. Result and Discussion

4.4.1. OVMI inhibited MDA-MB-231 cell proliferation and induced cell death

The cytotoxic impact of OVMI on the proliferation and survival of MDA-MB-231 cells was evaluated using the conventional MTT assay. It was observed that OVMI triggered cell death in MDA-MB-231 cells in a dose-dependent manner. The IC50 value of OVMI against MDA-MB-231 cell proliferation within 24 hours was determined to be 20.04 µg/ml. In contrast, OVMI did not exhibit any toxicity towards nonmalignant NKE cells, even when exposed to similar doses, as evidenced by an IC_{50} value of 118.39 µg/ml (Figure 2A). Furthermore, microscopic examination was conducted on MDA-MB-231 cells treated with OVMI at three distinct doses of 10, 20, and 30 µg/ml. The administration of OVMI was observed to induce notable alterations in the morphology of MDA-MB-231 cells. In addition to experiencing a loss of membrane integrity, the cells exhibited clear indications of apoptotic death, such as the formation of membrane blebs and the presence of apoptotic bodies, as depicted in Figure 2D.

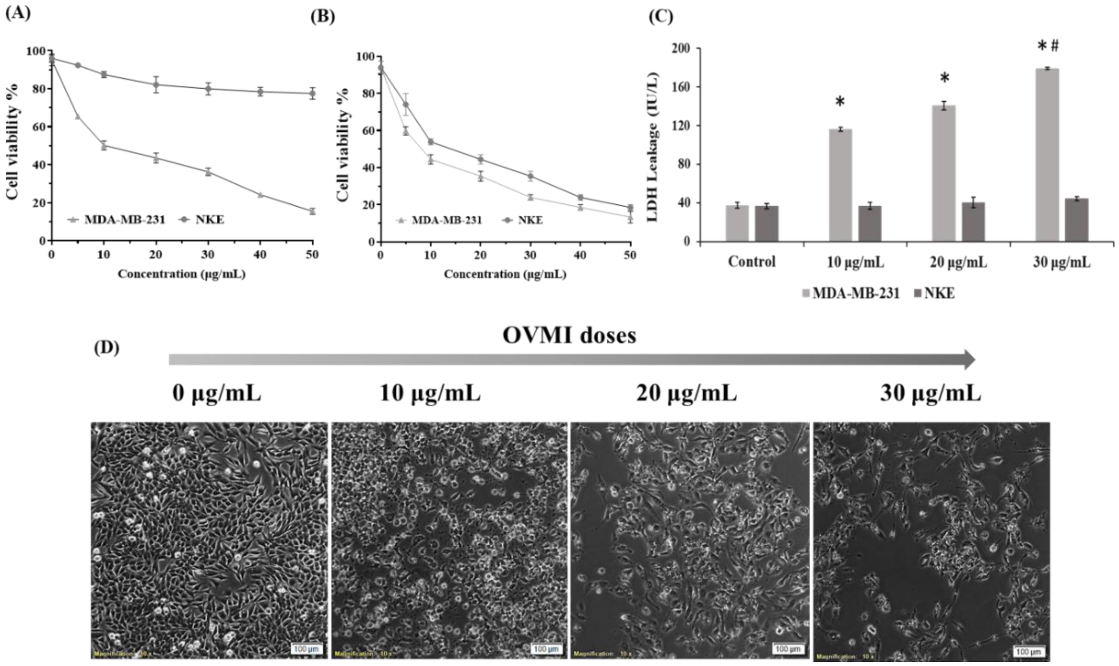

Figure 2: In vitro cytotoxic nature of OVMI in MDA-MB-231 cells: *Dose-dependent detection of cytotoxicity of (A) OVMI and (B) cisplatin in MDA-MB-231 cells and NKE cells in a range of 0-50 µg/mL concentration through MTT assay. Cisplatin taken as a positive control. (C) Determination of dose-dependent leakage of cellular LDH in OVMI-treated MDA-MB-231 cells. (D) Microscopic images of*

MDA-MB-231 cells treated with 0, 10, 20, and 30 μg/mL doses for 24 hrs. All the data are representative of three independent experiments. "" and "#" represent significant difference with respect to zero dose and IC_{50} dose treatment of OVMI ($P^* < 0.05$, $P\# < 0.05$).*

To further confirm the cytotoxic properties of OVMI, an LDH leakage assay was conducted. It was found that the extent of LDH leakage was significantly higher in TNBC cells treated with OVMI. However, when the same range of doses was applied to NKE cells, the leakage was negligible, as illustrated in Figure 2C. Within the same realm of investigation, the half maximal cytotoxic capacity of OVMI is comparable to that of cisplatin demonstrated at a concentration of 15.76 μg/ml in MDA-MB-231 cells (Figure 2B). However, unlike OVMI which displayed negligible toxicity in NKE cells even at a higher dosage of 50 μg/ml, cisplatin was highly cytotoxic to NKE at a minimal concentration of 5 μg/ml (IC_{50} 21.55 μg/mL) (Figure 2B). Consequently, it can be concluded that the synthesized derivative of oxovanadium complex, specifically 1-methylimidazole, exhibited noteworthy cytotoxicity in human TNBC cells at a dosage that did not affect normal epithelial cells, NKE.

4.4.2. OVMI induces apoptosis in MDA-MB-231 cells

To explore, the cell cell-killing modality of OVMI, we employed Annexin-V affinity binding assay along with PI counterstaining. As per standard rules, Annexin-V$^+$ and Annexin-V$^+$/PI$^+$ cells were considered here as early apoptotic and late apoptotic cells respectively constituting the total population of apoptotic cells. When checked through flow-cytometric dot plots, apoptosis was delineated as the principal mode of cell death imposed by OVMI against MDA-MB-231 cells (Figure 3).

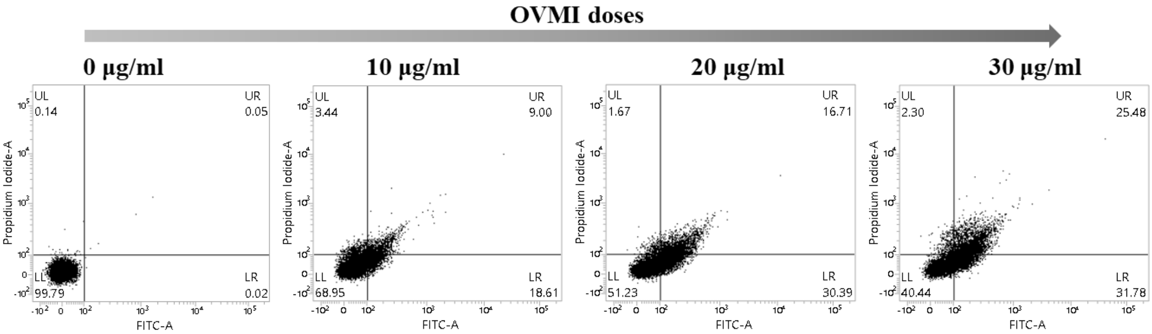

Figure 3: ***OVMI is capable of inducing apoptosis in vitro:*** *Flow cytometric analysis of apoptosis of OVMI-treated MDA-MB-231 cells; represented through dual parameter dot plots (x-axis representing the logarithmic fluorescence of FITC/Annexin V and the y-axis reprsenting that of PI.*

When treated with a lower dose (10 µg/ml), OVMI was found to induce early apoptotic changes in MDA-MB-231 cells (18.61 % were early apoptotic and 9 % were late apoptotic). At IC_{50} concentration, a total of 47.1 % cell population was found to be apoptotic where 30.39 % were early apoptotic and 16.17 % were late apoptotic. At a higher dose (30 µg/ml), it was found that more cells were primed for apoptosis (25.48 % of cells were in late apoptotic out of 57.23 % of total apoptotic MDA-MB-231 cells).

Induction of apoptosis in a dose-dependent manner was also validated through confocal microscopy in this study (Figure 4).

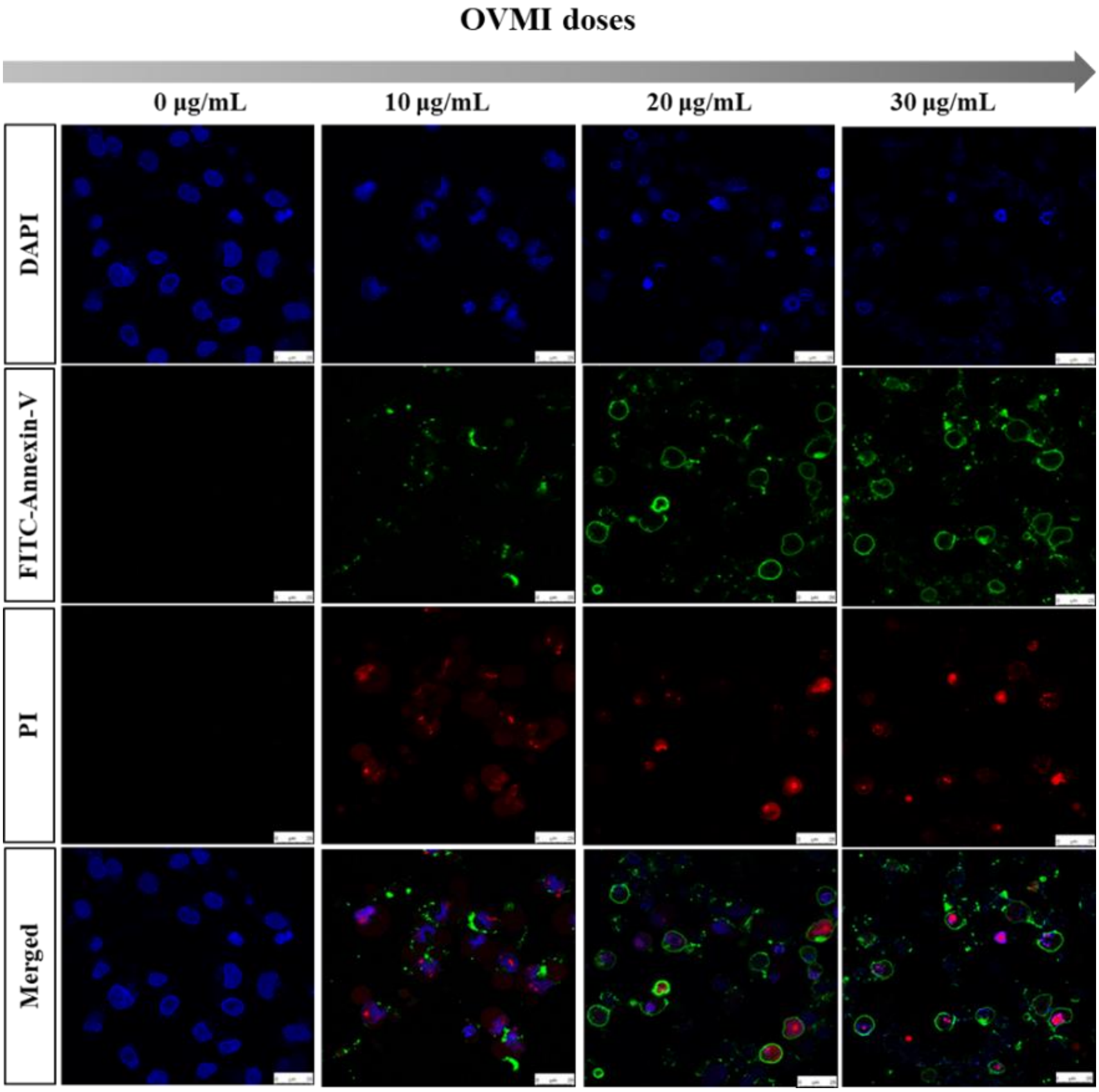

Figure 4: ***OVMI is capable of inducing apoptosis in vitro:*** *Confocal microscopic images of FITC-Annexin-V/PI-stained and OVMI-treated MDA-MB-231 cells. (Scale bar 25 µm).*

4.4.3. OVMI induces Bax to Bcl-2 ratio alternation *in vitro*

After validating apoptosis induction by OVMI treatment, we looked for changes related to apoptosis-related protein machinery at the molecular level. Two key proteins of the Bcl-2 family, i.e., Bax and Bcl-2 itself are known to be modulated during the time of apoptosis induction (Qian et al. 2022). Hence, OVMI-mediated modulation of the Bax to Bcl-2 ratio was quantified after analysis of their translational expressions. OVMI was found to uplift Bax/Bcl-2 ratio dose-dependently by downregulating Bcl-2 expression very significantly providing a molecular hallmark of apoptotic death (Figure 5A & 5B).

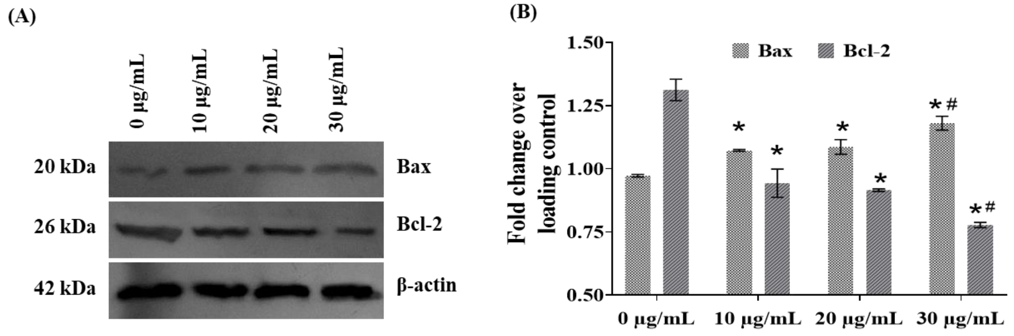

Figure 5: ***OVMI induces Bax to Bcl-2 ratio alternation in vitro:*** *(A) Immunoblot analyses of Bax and Bcl-2, where β-actin has been employed as a loading control. Blots are representatives of three individual experiments. (B) Densitometric analysis of the respective immunoblots. "*" and "#" represent significant difference with respect to zero dose and* IC_{50} *dose treatment of OVMI (P* < 0.05, P# < 0.05).*

4.4.4. OVMI disrupts mitochondrial membrane potential

The alteration of the Bax to Bcl-2 ratio frequently results in compromised mitochondrial membrane potential (Kuwana and Newmeyer 2003). Consequently, we investigated whether OVMI was associated with the induction of changes to the mitochondrial membrane potential. To assess this, MDA-MB-231 cells treated with OVMI were subjected to JC-1 staining. Following staining, the cells were evaluated using flow cytometry to determine any alterations in the green fluorescence emitted by JC-1 monomers (Figure 6A). Additionally, confocal microscopy was employed for further analysis (Figure 6C). Our results demonstrated that OVMI treatment led to a decrease in the red-to-green ratio of fluorescence emitted by JC-1 monomers and dimers, respectively (Figure 6B). Therefore, it can be concluded that OVMI has the potential to induce a significant decline in mitochondrial membrane potential in treated MDA-MB-231 cells. Loss of mitochondrial membrane potential often is related to loss of mitochondrial membrane integrity that may lead to the release of mitochondrial cytochrome C (cyt C) into cytosol; thereby, initiating an intrinsic apoptotic cascade within the cell (Ghosh and Sil 2021).

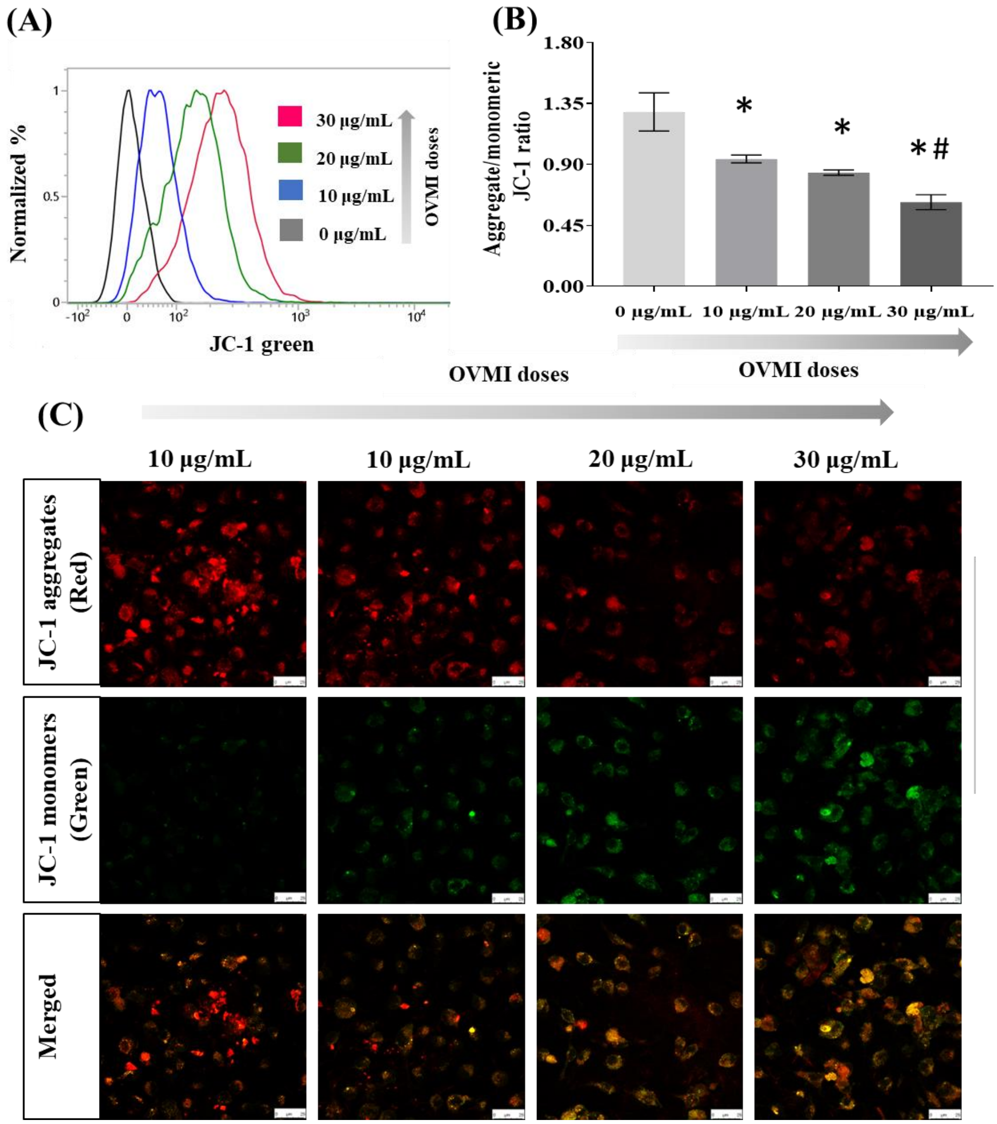

***Figure 6:* OVMI induces apoptosis in vitro through disrupting mitochondrial membrane potential:** *(A) Confocal fluorescence micrographs of OVMI-treated MDA-MB-231 cells depicting changes in mitochondrial membrane potential through JC-1 staining under the red and green filter. (Scale bar 25 µm). (B) Determination of changes in transmembrane mitochondrial potential by calculating fluorescence intensity ratio of JC1 aggregates to JC1 monomer. "*" represents significant difference with respect to zero dose and* IC_{50} *dose treatment of OVMI (P* < 0.05, P# < 0.05). (C) Flow cytometry-assisted detection of changes of mitochondrial membrane potential in OVMI-treated MDA-Mb-231 cells, corresponding to changes in fluorescence intensity of monomeric JC-1.*

Thus, to confirm cytoplasmic mobilization of cyt C, its mitochondrial as well as cytoplasmic protein expressions were checked through western blotting. In mitochondrial subcellular fraction, translational expression of cyt C was found to be gradually decreasing with an increase in OVMI dosage (Figure 7A & 7C); whereas, an opposite trend was noticed for cytosolic cyt C expression in MDA-MB-231 cells, treated with OVMI (Figure 7B & 7D). Parallelly, translational expressions of molecules of the intrinsic apoptotic cascade, i.e., Apaf-1, cleaved caspase 9, and caspase 3 were also evaluated. OVMI was able to increase translational expressions of these proteins in MDA-MB-231 cells followed by cleavage of PARP, emphasizing its ability for DNA degradation (Figure 7B & 7D)

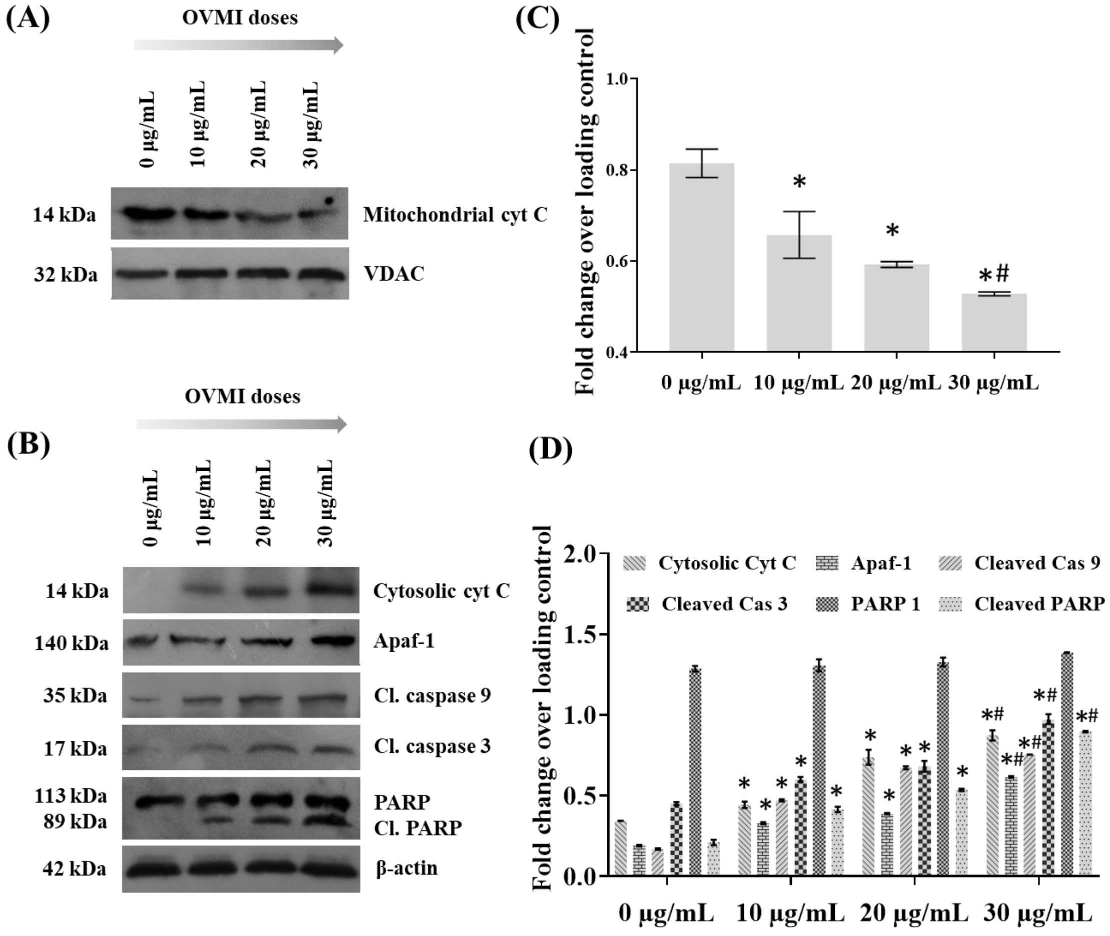

Figure 7: Effect of OVMI treatment on translation expression of molecules related to mitochondrial apoptosis pathway: *(A) Immunoblot analyses of mitochondrial cyt C where VDAC has been utilized as an internal loading control. (B) Immunoblot analyses of cytosolic cyt C, Apaf-1, cleaved caspase-9, cleaved caspase-3, and PARP-1 to rule out the occurrence of intrinsic apoptosis in vitro. Here, β-actin has been used as the loading control. (C-D) Densitometric analyses of respective immunoblots. "*" and "#" represent significant difference with respect to zero dose and* IC_{50} *treatment dose of OVMI (P* < 0.05, P# < 0.05).*

4.4.5. Excessive cellular ROS drives cytotoxic ability of OVMI

Excessive cellular ROS and mitochondrial cyt C release are frequently correlated with the onset of apoptosis (Ghosh et al. 2022). In continuation of previous experiments, we were keen to know whether OVMI-mediated cell killing is ROS-driven or not. Thus, OVMI-treated MDA-MB-231 cells were stained with DCFDA to check the amount of intracellular ROS generation in response to OVMI treatment. Extents of green fluorescence emitted by fluorescent DCF in MDA-MB-231 cell (treated with different doses of OVMI, i.e., 0, 10.20, and 30 µg/ml) was then compared flow-cytometrically and also through confocal microscopy (Figure 8A-8B).

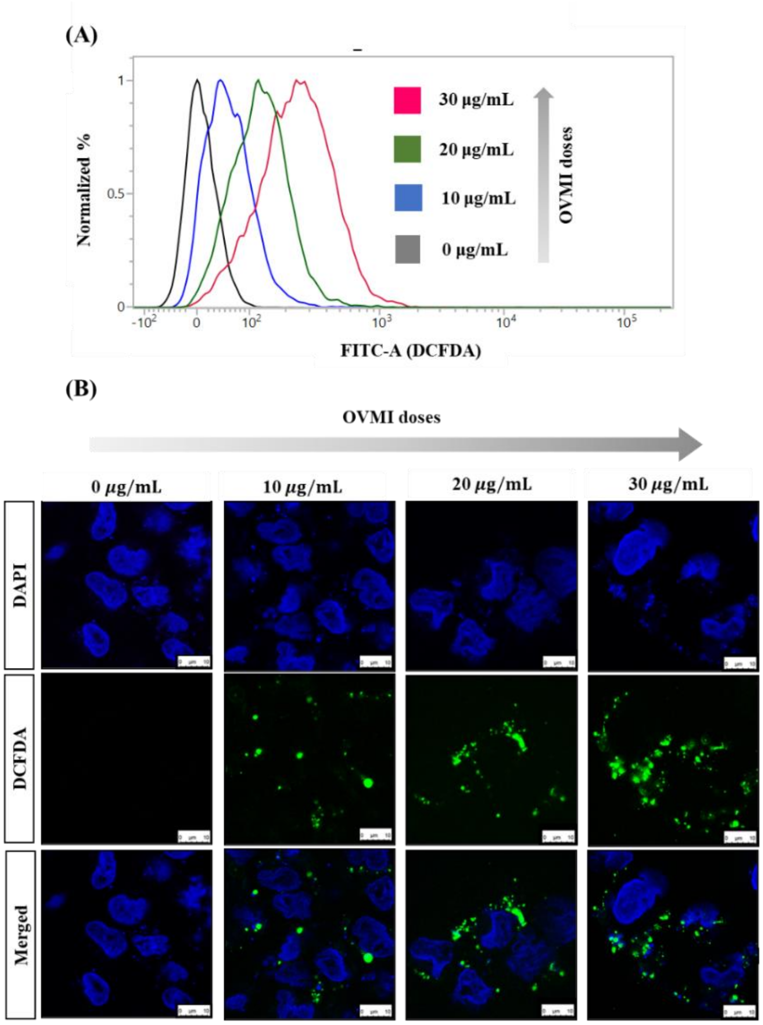

Figure 8: OVMI works through inducing excessive ROS production in MDA-MB-231 cells: *(A) Flow cytometric study of intracellular ROS generation through DCFDA staining in response to dose-dependent OVMI treatment. (B) Confocal microscopic imaging of DCFDA-stained, OVMI-treated MDA-MB-231 cells (scale bar 10 µm).*

Treatment with 10 µg/mL of OVMI was noticed to elicit of significant extent of ROS overproduction in MDA-MB-231 cells. Moreover, ROS generation in MDA-MB-231 was found to be dose-dependent. When MDA-MB-231 cells were subjected to NAC pretreatment along with OVMI exposure, cells were noted to experience significantly lower ROS production (Figure 9A). Moreover, scavenging excess ROS production was overserved to reduce OVMI-mediated overall cell death percentage (Figure 9B). When checked through Annexin-V/PI affinity binding assay, a similar outcome was obtained; i.e., NAC pretreatment was found to reduce apoptotic cell counts from 56.29 % (treated with 30 µg/ml OVMI alone) to 18.26 %. Such results indicate inhibition can severely damage the cell-killing ability of OVMI in MDA-MB-231 cells (Figure 9C).

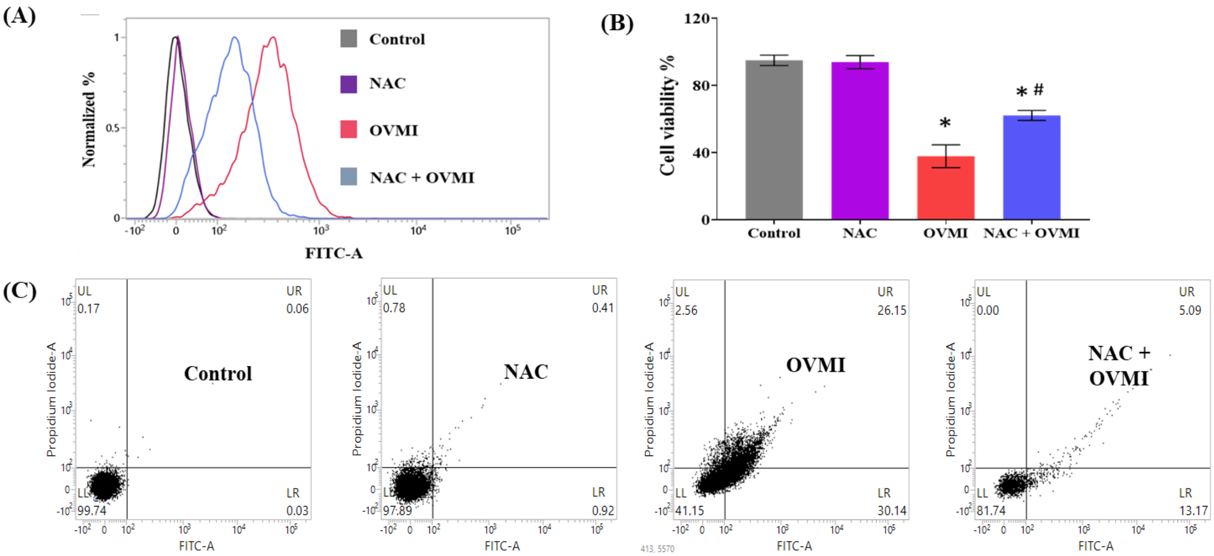

Figure 9: ***Effect of NAC pretreatment on OVMI-treatment outcome:*** *(A) Flow cytometric histogram showing changes in intracellular ROS content upon NAC pretreatment. (B) Effect of NAC pretreatment upon cell viability percentage of OVMI-treated MDA-MB-231 cells. (C) Effect of NAC-pretreatment upon OVMI-mediated apoptosis of MDA-MB-231 cells.*

When translational expressions of chief apoptotic molecules were checked, it was observed that NAC-mediated inhibition of ROS overproduction, reduced Bax and cleaved caspase 3 expression in OVMI-treated MDA-MB-23 cells along with comparatively higher Bcl-2 expression (Figure 10A-10B). However, it must be noted that NAC + OVMI treatment cannot completely reverse OVMI-mediated cytotoxicity in MDA-MB-231. Hence, it can be speculated that beyond ROS overload there must be some other mechanism/s involved to drive proapoptotic property of OVMI.

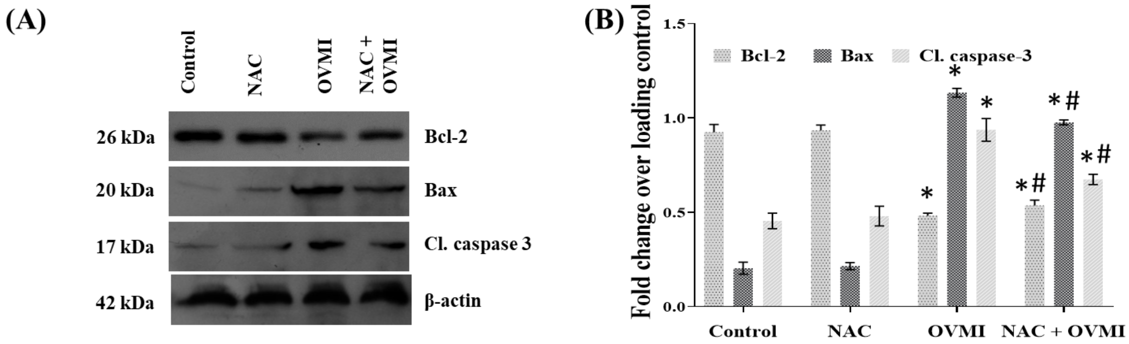

Figure 10: *(A) Immunoblot analysis of Bcl-2, Bax, and cleaved caspase 3 upon NAC pretreatment. (B) Densitometric analysis of the NAC pretreatment immunoblots. All data are representatives of three individual experiments where "*" and "#" represent significant differences with respect to control and OVMI-treated groups, respectively, (P* < 0.05, P# < 0.05).*

4.4.6. OVMI treatment sensitizes MDA-MB-231 cells towards ER stress with CHOP upregulation

Following the elucidation of OVMI-mediated apoptotic death induction in MDA-MB-231 cells via ROS-mediated mitochondrial cascade, we again questioned the involvement of another probable signaling pathway that may act in association with ROS generation. Inline, we studied the effect of OVMI treatment on mitochondrial health again through mitochondrial swelling assay. From this study, it was noticed that apart from changes to mitochondrial membrane potential, OVMI could induce Ca^{2+}-mediated mitochondrial swelling in MDA-MB-231 cells (Figure 11A). To ensure, whether such excessive mitochondrial swelling has resulted from faulty Ca^{2+} homeostasis, translational expression of calpain 1 (a major protein involved in Ca^{2+} homeostasis) (Storr et al. 2011) was checked through western blotting and found to be elevated due to OVMI treatment (Figure 11B-11C). Now, it is noteworthy that the endoplasmic reticulum (ER) is known to be the center of maintaining cellular Ca^{2+} homeostasis (Papp et al. 2020). Hence, in the current study, the effect of OVMI treatment on ER health *in vitro* was evaluated. In this context, it is important to remember that excessive ROS production and imbalance of ER-protein folding are linked often, subsequently which may result in ER stress provoking unfolded protein response (UPR) cascade providing an opportunity for proper folding of proteins. However, when the defect cannot be resolved, UPR can signal cell death decisions upstream and irrespective of the mitochondrial gateway of death (Bravo et al. 2013). Thus, we looked for changes in the translational expression of molecules related to the UPR cascade. Here also, enhanced translational expressions of GRP78, phosphorylated eIF-2α, and CHOP in a dose-dependent fashion were visible in OVMI-treated MDA-MB-231 cells (Figure 11B-11C). CHOP upregulation is also known to be associated with Bcl-2 downregulation (Li et al. 2019) which corresponds to immunoblot expression of Bcl-2 represented in Figure 5A.

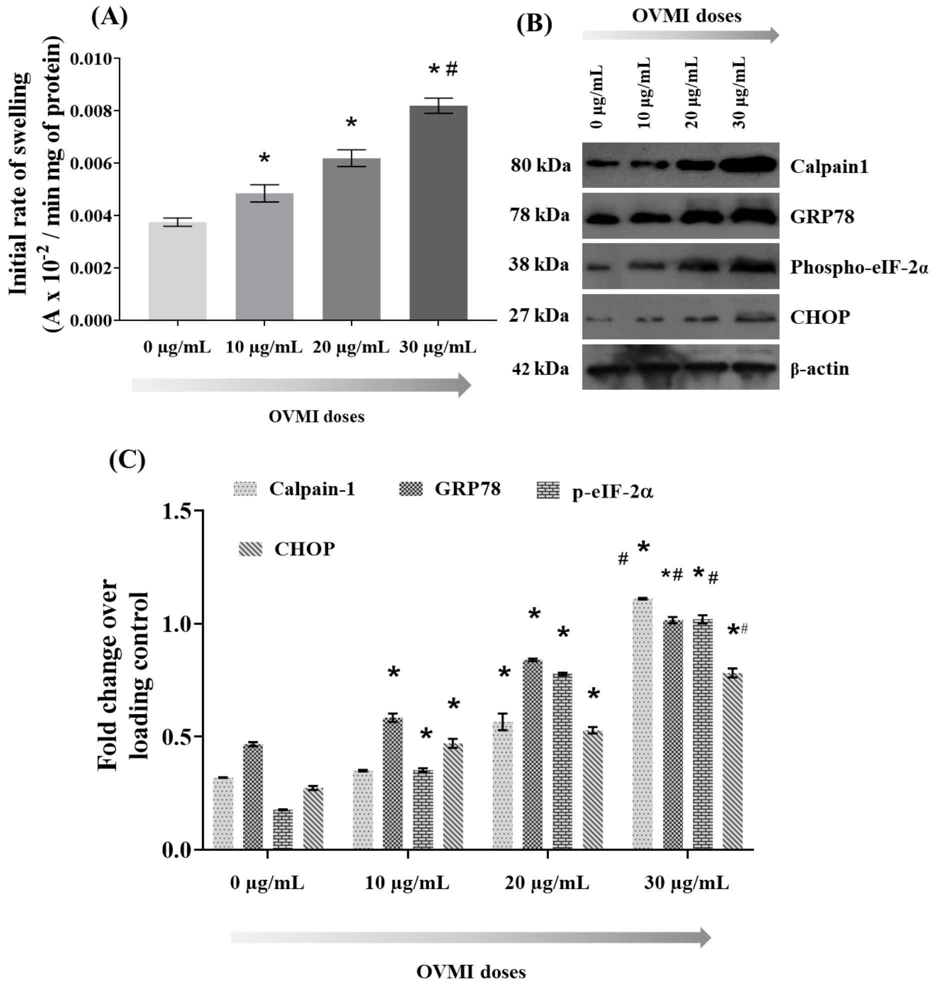

Figure 11:   OVMI exerting in vitro ER stress in MDA-MB-231: *(A) Mitochondrial swelling of OVMI-treated MDA-MB-231 cells with dose dependency. (B) Immunoblot expression of proteins involved in ER stress pathway. (C) Densitometric analyses of translational expression of calpain-1, GRP78, phosphor-eIF-2α, and CHOP. "*" and "#" represent significant differences with respect to zero treatment dose and* IC_{50} *dose of OVMI respectively (P* < 0.05, P# < 0.05).*

4.4.7. OVMI induces *in vitro* retardation of TNBC cell migration

Apart from that, MDA-MB-231 cells are known to be highly metastatic with their eminent migratory nature. Hence, we also inspected about anti-migratory roles of OVMI (if any). Thus, a bidirectional wound-healing assay was performed in MDA-MB-231 cells (Figure 12A). It has been observed that in the control group of cells, gradually almost filled up wound space after 24 hours (wound representing 14.57 ± 2.53 % of total area) whereas, OVMI is effective in inhibiting migration of MDA-MB-231 cells dose-dependently. Even at a dose as low as 10 µg/ml, OVMI is effective in stalling cell migration significantly by representing a wound area accounting for 45.80 ± 14.35 % of the total area (Figure 12B). After 24 hours, the wound area percentage was higher at the highest experimental dose, i.e., 30 μg/mL, accounting for 93.15 ± 4.12 %. This undoubtedly correlates with antimigratory properties imposed by OVMI (Figure 12B). Even after 48 hours of treatment, OVMI was potent enough to prevent the migration of MDA-MB-231 cells on a 2D plane in a dose-dependent manner (Figure 12B).

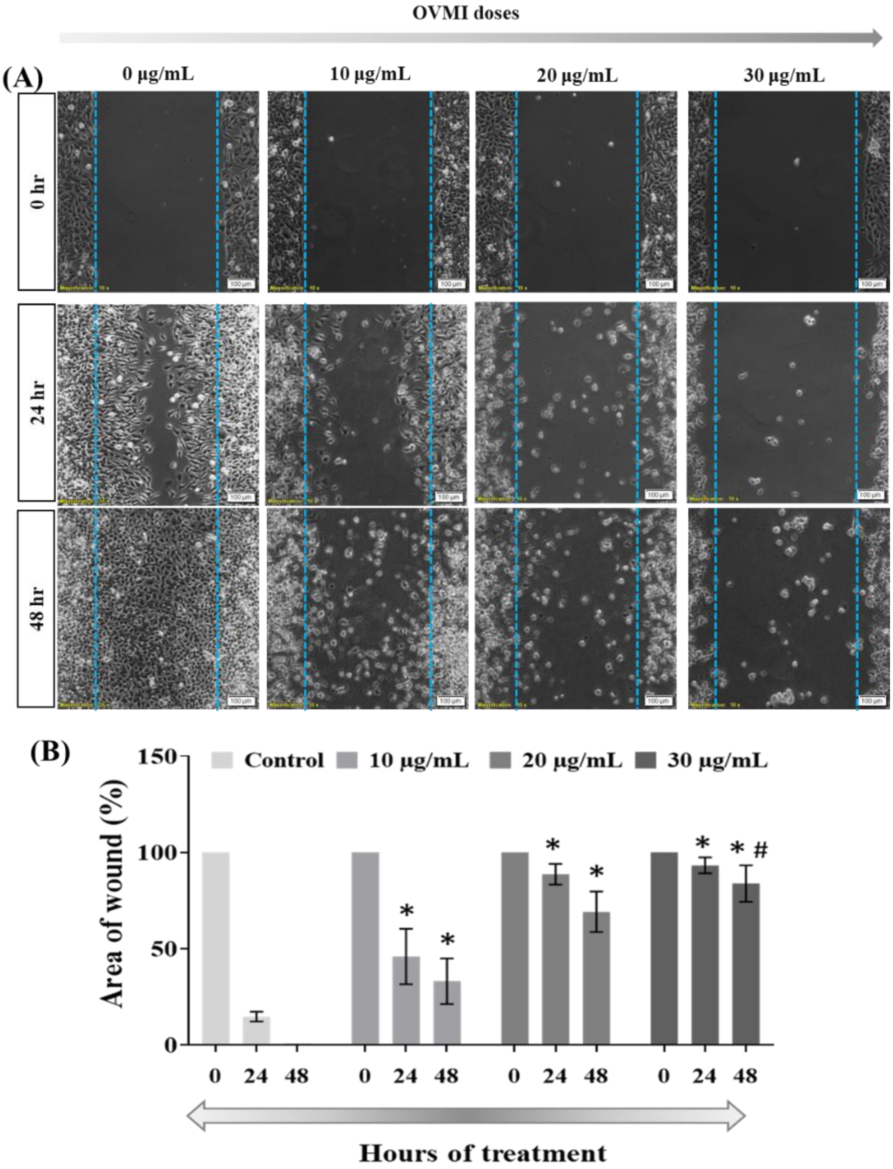

Figure 12: ***OVMI exerting in vitro anti-migratory effect on MDA-MB-231 cells:*** *(A) Bright-field microscopic images of bidirectional wound healing in MDA-MB-231 cells after being treated with OVMI at three successive doses for 24 and 48 hrs. (B) Anti-migratory effect of OVMI expressed in form of a percentage of wound area healed.*

For evaluating the effect of OVMI on migratory properties of MDA-MB-231 cells, we further performed immunoblot analysis of proteins related to epithelial-to-mesenchymal transition (EMT) of cancer cells, such as E-cadherin, N-cadherin, and vimentin. OVMI treatment declined translational expression of mesenchymal marker N-cadherin and vimentin (Figure 13A-13B). In this context, it is important to state that E-cadherin which seems to be one of the most significant epithelial markers, has also been checked through immunoblot analysis. Expression of E-cadherin, even in control MDA-MB-231 cells, was not very prominent, probably due to mutated and hypermethylated promoter region of the gene responsible for coding E-cadherin, specific to this cell line (Chao, Shepard, and Wells 2010, Eslami Amirabadi et al. 2019). However, no significant change in the translational expression of E-cadherin upon OVMI treatment was noted (Figure 13A-13B). These findings discussed so far, clearly showed that apart from the apoptotic impact on TNBC cells, OVMI is capable of imposing potent *in vitro* anti-migratory effects

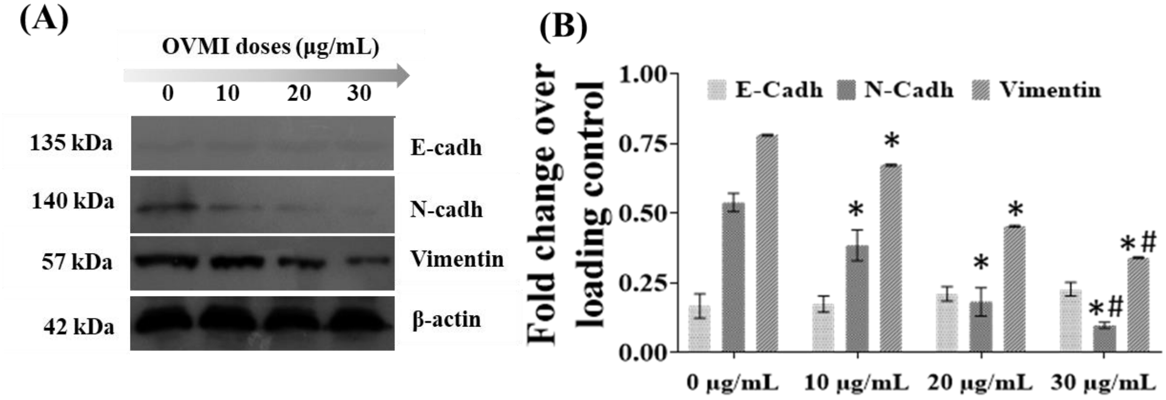

Figure 13: ***Effect of OVMI on EMT markers in vitro:*** *(A) Immunoblot analyses of protein involved in epithelial-mesenchymal transition of OVMI-treated MDA-MB-231 cells. β-actin had been employed here as the internal loading control. (B) Densitometric analyses of immunoblots of E-cadherin, N-cadherin, and vimentin. All data are representatives of three separate experiments; where "*" and "#" represent significant differences with respect to zero treatment dose and* IC_{50} *dose of OVMI respectively,* ($P^* < 0.05$, $P\# < 0.05$).

4.4.8. Antitumorigenic effects of OVMI on 4T1-induced mammary tumors in female Balb/c mice

Furthermore, for validating the anticancer effect of OVMI, a synergistic *in vivo* mice model was built by injecting 4T1 cells in mammary fat pad regions of immune-competent female Balb/c mice. Tumors grew in size till the day of sacrifice in the group containing untreated tumor-bearing mice. However, the group of mice that received OVMI intravenously at a concentration of 10 mg/kg body weight, exhibited a significant reduction in tumor volume along with the time of the entire treatment period.

Reductions in tumor weight and volume were highest among the animals of group PT_{30} (Figure 14C-14D). In this context, we have found a dose-dependent reduction in tumor size upon OVMI treatment. Moreover, tumor tissues were examined histologically along with their morphological evaluation (Figure 14A).

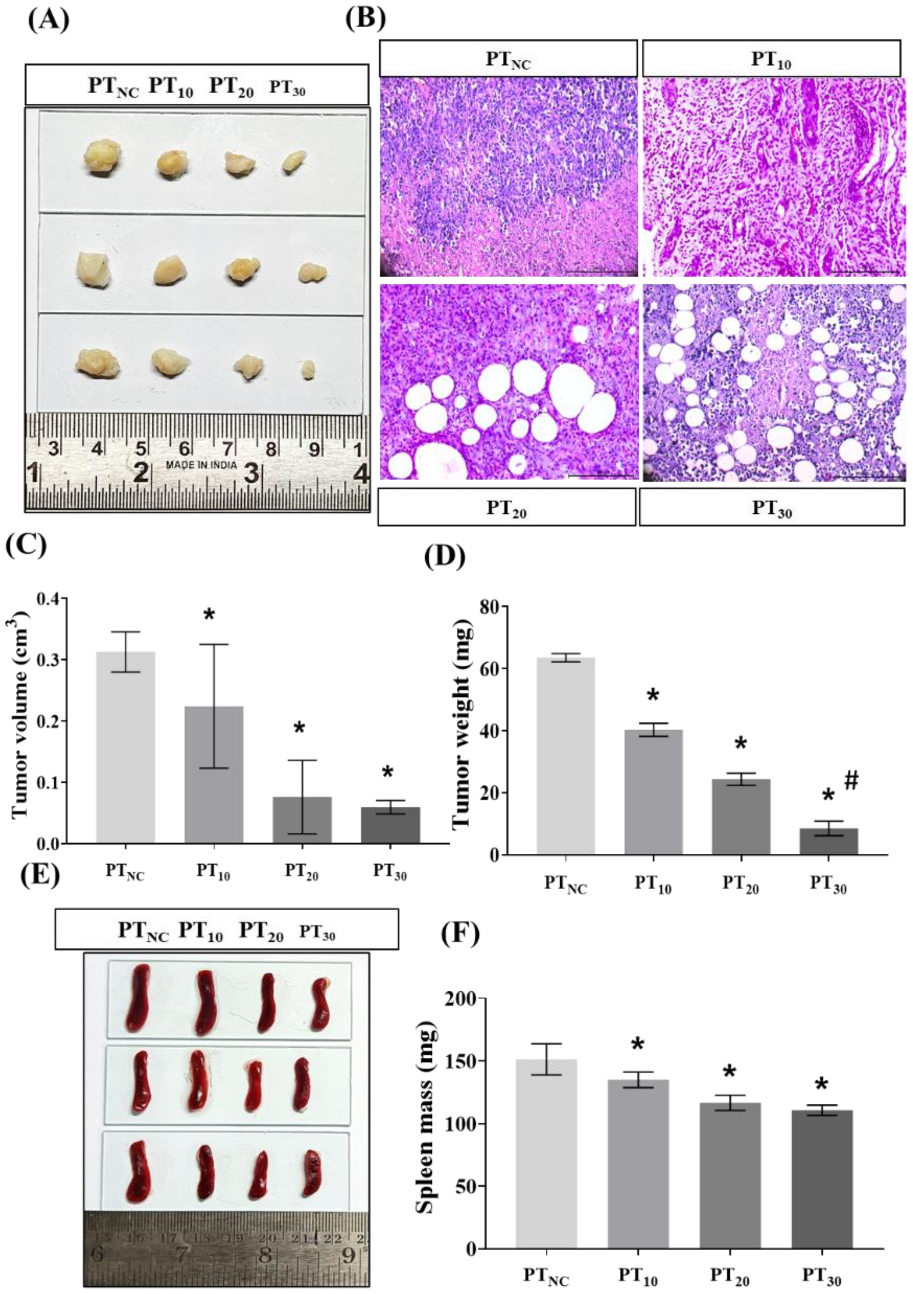

Figure 14: ***In vivo anti-tumorigenic activity of OVMI:*** *(A) Representative photographs of resected tumor tissues showing an overall reduction in tumor size. (B) Representative micrograph of H & E-*

stained tissue sections of mammary tumor tissues from female Balb/c mice. Overall reduction in (C) tumor volume and (D) tumor mass after OVMI treatment. Changes in splenic profile exhibited (E) representative photographs of spleens collected from tumor-bearing OVMI-treated mice and (F) changes in splenic mass after being treated with OVMI. "" and "#" represent significant differences with respect to control and OVMI (IC_{50})-treated groups respectively, ($P^* < 0.05$, $P\# < 0.05$).*

Microscopic observations of H & E-stained tumor tissue sections revealed restoration of better tissue architecture and reduced number of multinucleated cells upon OVMI treatment (Figure 14B). 4T1 carcinoma cells are capable of inducing a leukemoid reaction to the spleen resulting in the occurrence of splenomegaly (Chen and Ross 2012). This is probably because 4T1 cells are capable of inducing a leukemoid reaction to the spleen resulting in the occurrence of splenomegaly. Notably, signs of splenomegaly were also reduced in treated mice may be due to an overall reduction in tumor load (Figure 14E-14F.

4.4.9. OVMI induced apoptosis and reduced EMT markers in primary mammary tumor

As recorded from earlier *in vitro* observations, we wanted to know whether OVMI follows a similar mechanism of apoptosis induction *in vivo* as well. So, tissue sections of mammary tumors were subjected to TUNEL assay to validate the *in vivo* proapoptotic nature of OVMI.

Indications of DNA fragmentation by nicking, specific to late apoptosis were observed to be significantly higher in treated groups with respect to the PT_{NC} group. Furthermore, an increase in OVMI dosage was found to increase the TUNEL-positive apoptotic index *in vivo* dose-dependently (Figure 15A). Additionally, immunohistochemical expressions of PARP1 and Ki67 were studied in resected breast tumor tissues (Figure 15B). It was quite prominent that OVMI treatment was highly effective in increasing PARP1 expression *in vivo* along with a significant reduction in expression of proliferation marker Ki67 (Tuninetti et al. 2023, Chopra et al. 2020).

Apart from apoptotic and proliferation markers, *in vivo, the* anti-migratory effect of OVMI was evaluated immunohistochemically in the resected mammary tumors. Evaluation of EMT markers such as E-cadherin and N-cadherin were examined here (Tuninetti et al. 2023) (Figure 16). Tissue-specific reduction in immunohistochemical expression of N-cadherin and enhancement of that of the E-cadherin in a dose-dependent manner signifies migratory effectivity of OVMI *in vivo.*

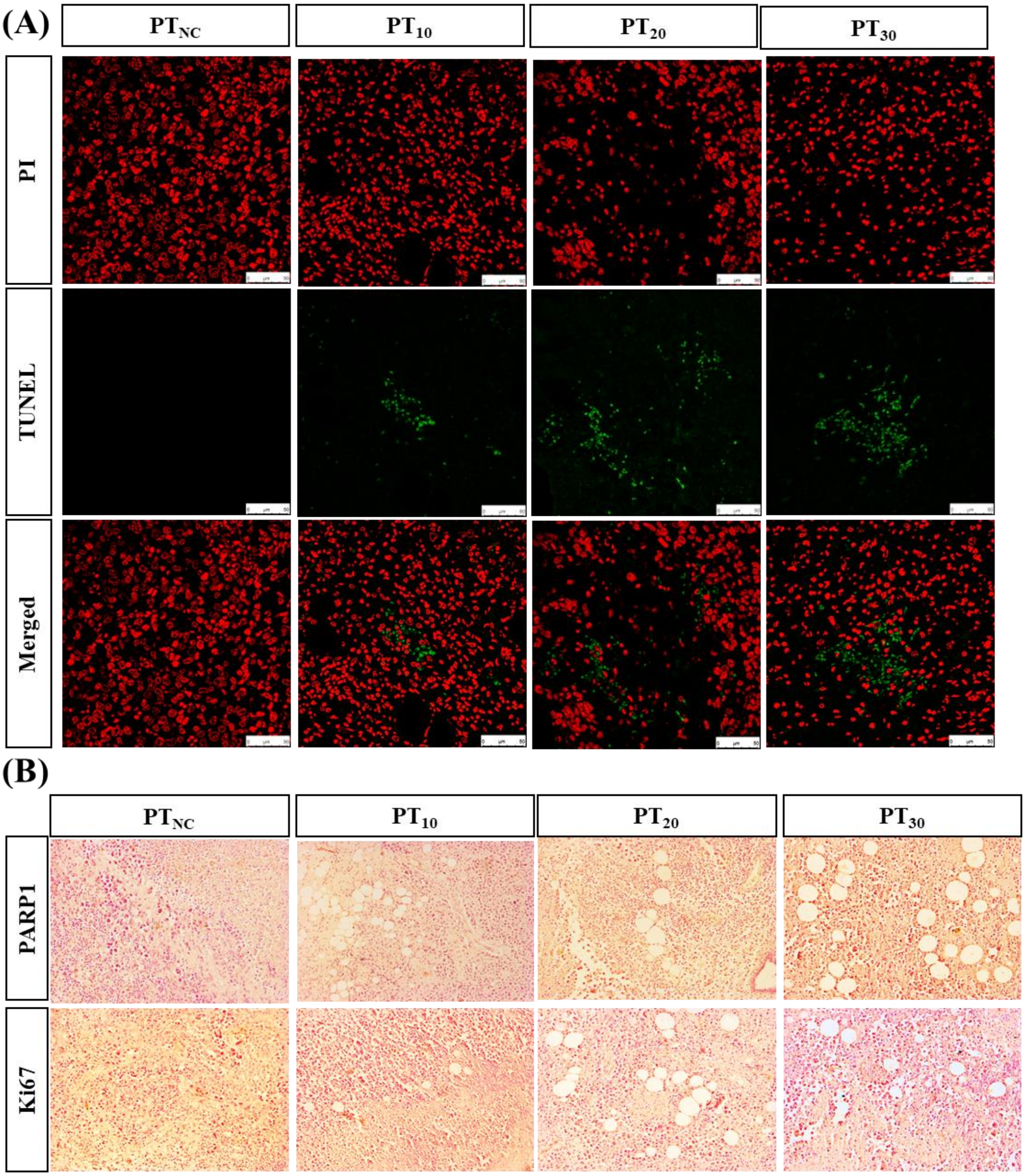

Figure 15: ***OVMI is capable of exerting apoptosis in vivo:*** *(A) Confocal micrographs depicting TUNEL-positive apoptotic tissue section of mammary tumor tissue of female Balc/c mice (Scale bar 50 µm). (B) In vivo apoptotic and anti-proliferative effectivities of OVMI on resected mammary tumor tissues (from group* PT_{NC} *to* PT_{30}*) through microscopic evaluation (20X magnification) of immunohistochemical expression of PARP-1 and Ki67.*

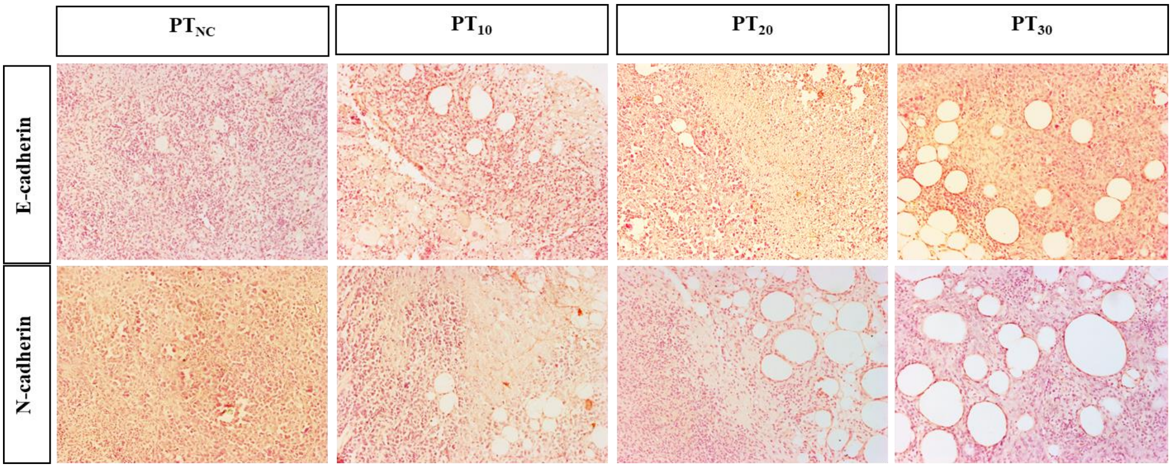

Figure 16: ***Anti-migratory effect of OVMI through immunohistochemical expressions of EMT markers in mammary tumor tissue:*** *(A) Immunohistochemical expression of E-cadherin and N-cadherin in vivo in resected primary mammary tumor tissues captured by bright field microscope (20X magnification).*

4.4.10. OVMI reduces 4T1-induced secondary lung metastasis in female Balb/c mice

The effect of OVMI was evaluated on female Balb/c mice having 4T1-induced secondary pulmonary metastasis (Figure 17A). OVMI treatment has been found to reduce the number of external metastatic pulmonary nodule-count dose-dependently. Also, there was a significant reduction in the weight of lungs in OVMI-treated mice in comparison to untreated ones, emphasizing its altogether antitumorigenic and antimetastatic roles *in vivo* (Figure 17B-17C). To get a deeper insight into the effect of OVMI treatment against 4T1-induced secondary lung metastasis, the translational expressions of molecules significant in this respect were studied. In this regard, it is noteworthy that both MMP-2 and MMP-9 belong to zinc-based endopeptidases which through the destruction of extracellular matrix proteins play key roles in tumor invasion, metastasis, and angiogenesis (Somiari et al. 2006, Coussens and Werb 1996, Duffy et al. 2000). Here, we have found that translational expression of MMP-2 and MMP-9 were higher in the lungs of mice where 4T1-induced metastasis was left untreated; whereas, such upliftment was reduced by the intravenous administration of OVMI (Figure 17D-17E). Another two molecules, ICAM-1 and VCAM-1 have been checked also as they are known to be associated with the endothelial adhesion of cancer cells resulting in the induction of metastasis and promotion of tumor invasiveness (Carlos and Harlan 1994, Coskun et al. 2006, Polychronidis et al. 2003). OVMI treatment was potent enough to reduce VCAM-1 dose-dependently though ICAM-1 expression was found not to be significantly responsive to OVMI treatment in a dose-dependent manner (Figure 17D-17E).

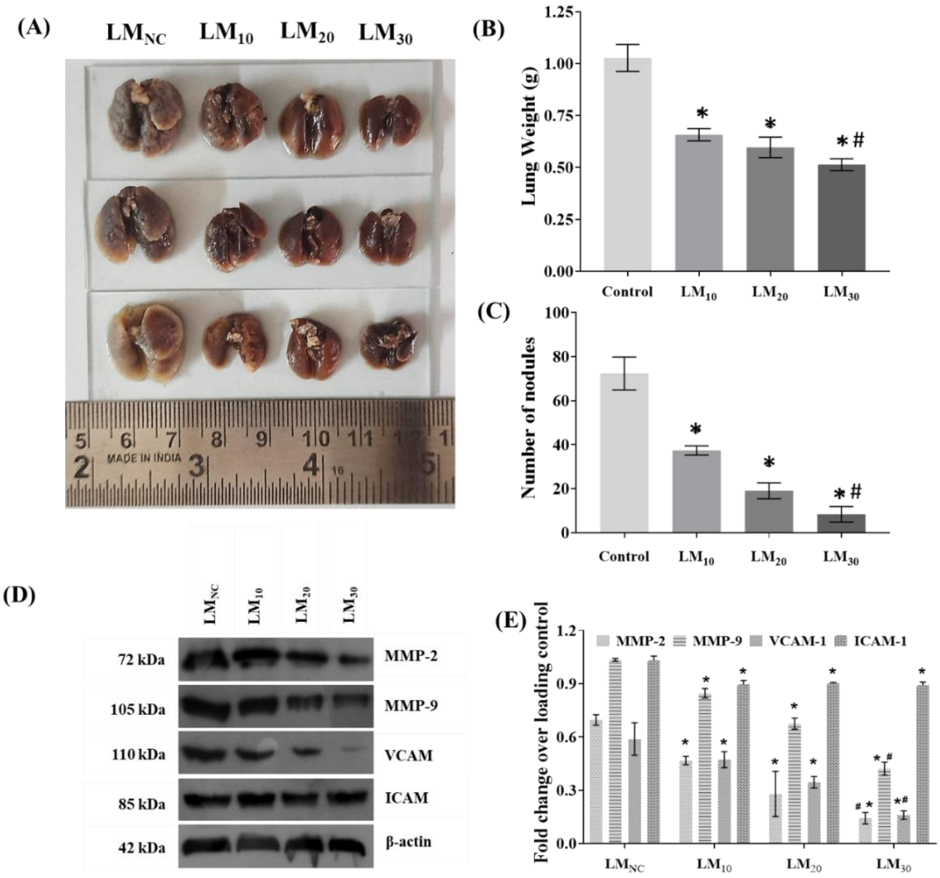

Figure 17: ***Anti-metastatic effect of OVMI treatment on secondary lung metastasis in vivo:*** *Determination of capability of OVMI for the reduction of 4T1- induced secondary pulmonary metastasis by (B) representative photographs of lungs resected from female Balb/c mice showing a reduction in secondary pulmonary metastasis, (C) reduced pulmonary weight, and (D) reduced number of external nodules on the surface metastatic lungs. "*" represents significant differences with respect to the LMNC group and "#" represent significant difference with respect to the LM20 group (P* < 0.05, P# < 0.05). (E) Immunoblot analysis of metastatic parameters in untreated and OVMI-treated female Balb/c metastatic lung tissues. (F) Densitometric analysis of MMP-2, MMP-9, VCAM-1, and ICAM-1 in metastatic lung tissues. "*" represents significant differences with respect to the LMNC group and "#" represent significant difference with respect to the LM20 group (P* < 0.05, P# < 0.05).*

4.4.11. OVMI is non-toxic to vital organs

Ideally, a successful anticancer agent must be able to kill neoplasm without causing any harm to normal healthy body cells. For that anticancer agent must be biocompatible to the *in vivo system.* Hence, we checked serum hepatic and renal parameters such as ALP, ALT, BUN, and creatinine (Figure 18A-18D).

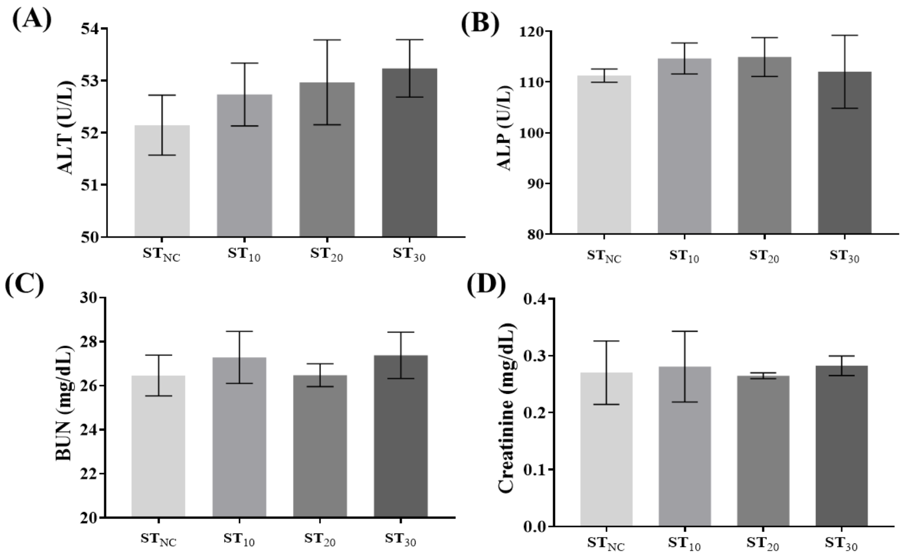

Figure 18: ***OVMI is safe to use in vivo:*** *Analysis of systemic toxicity by assessing serum (A) ALT, (B) ALP, (C) BUN, and (D) Creatinine in different experimental groups of mice. Data are represented by mean ± SD (n = 3).*

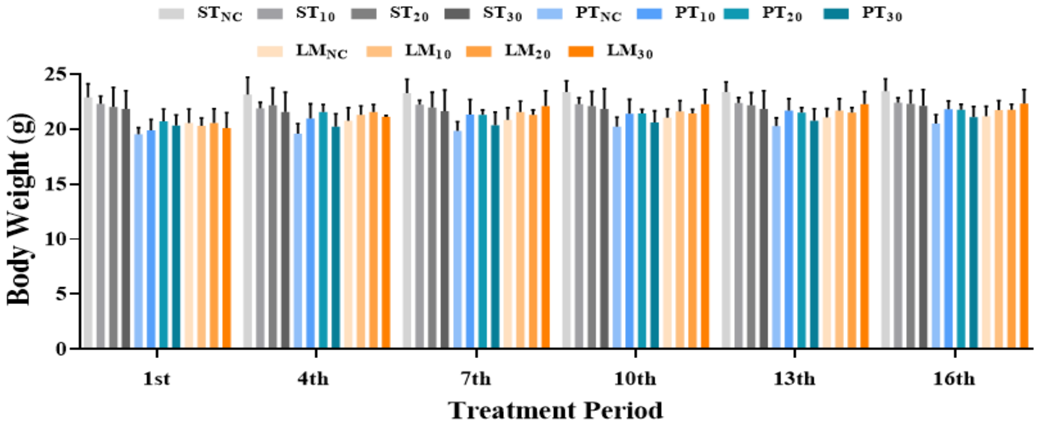

Figure 19: *Body weight of female Balb/c mice over the treatment period*

No toxic increase in these parameters was noted in response to OVMI treatment. Additionally, H & E-stained hepatic, cardiac, renal, and pulmonary tissue sections were histologically assessed with no sign of abnormality (Figure 19).

Besides, we looked for any treatment-induced abnormal change in body weight in all sets of experimental mice (Figure 20). However, no significant abnormality was noted. Thus, OVMI can be said to be safe and biocompatible in murine system when treated within the aforementioned experimental doses.

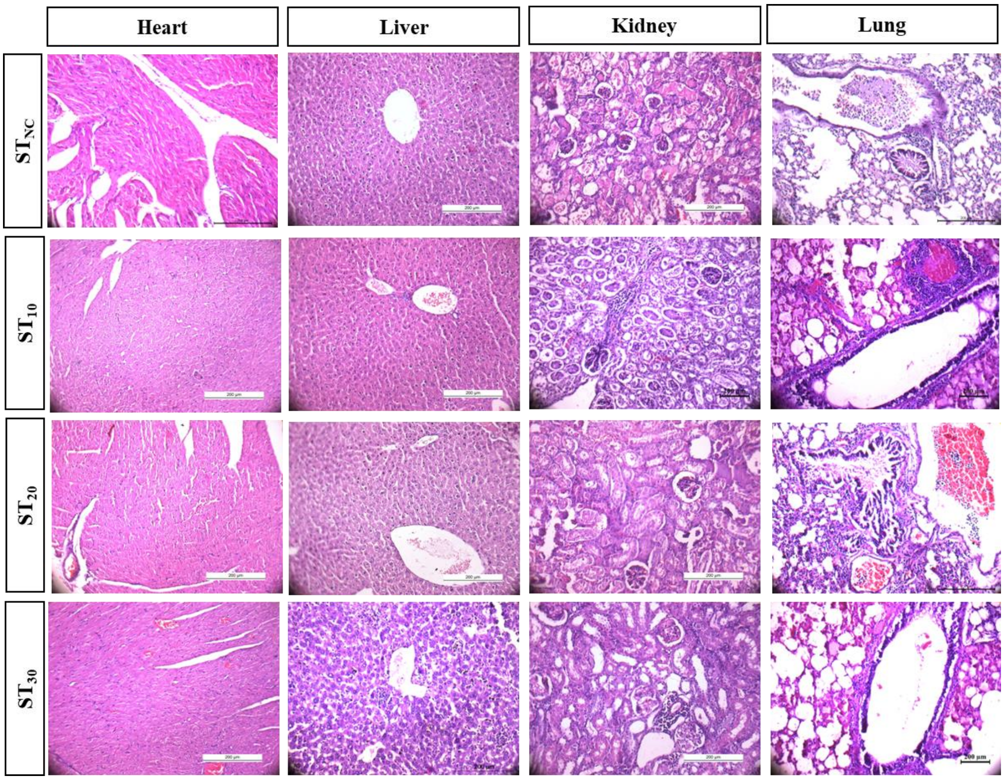

Figure 20: ***OVMI is non-toxic to vital organs****:Histological assessment of H & E-stained microsections of murine heart, liver, kidney, and lung from different experimental groups with bright field microscopy under 20X magnification.*

4.5. Conclusion

Despite significant advancements in clinical research over the past few decades, breast cancer remains the leading cause of cancer-related deaths in women. The effectiveness of chemotherapeutic management using conventional anticancer agents such as doxorubicin, cisplatin, and tamoxifen is severely compromised due to their significant off-target adverse effects on healthy noncancerous cells (Aggarwal et al. 2021). Consequently, the pursuit of novel therapeutic options continues. In this context, we have selected a small synthetic molecule, OVMI, which has been extensively studied for its ability to selectively eliminate cancer cells while minimally affecting normal cells (Figure 21). OVMI has demonstrated the ability to cause a 50% reduction in the population of MDA-MB-231 cells when administered at a concentration of 20.04 µg/mL. Notably, this effect does not pose a risk to the normal epithelial NKE cells within the same concentration range, distinguishing OVMI from the cell-killing mechanism employed by the metallodrug cisplatin. Additionally, studies conducted *in vivo* have confirmed the safety and biocompatibility of OVMI in female Balb/c mice. This current investigation aims to validate the apoptosis-inducing nature of OVMI in a dose-dependent manner, specifically by evaluating its impact on the expression ratio of Bax to Bcl-2 proteins *in vitro*. Furthermore, OVMI has been observed to generate elevated levels of intracellular ROS and subsequently diminish the mitochondrial transmembrane potential, thereby initiating the intrinsic apoptotic cascade in MDA-MB-231 cells.

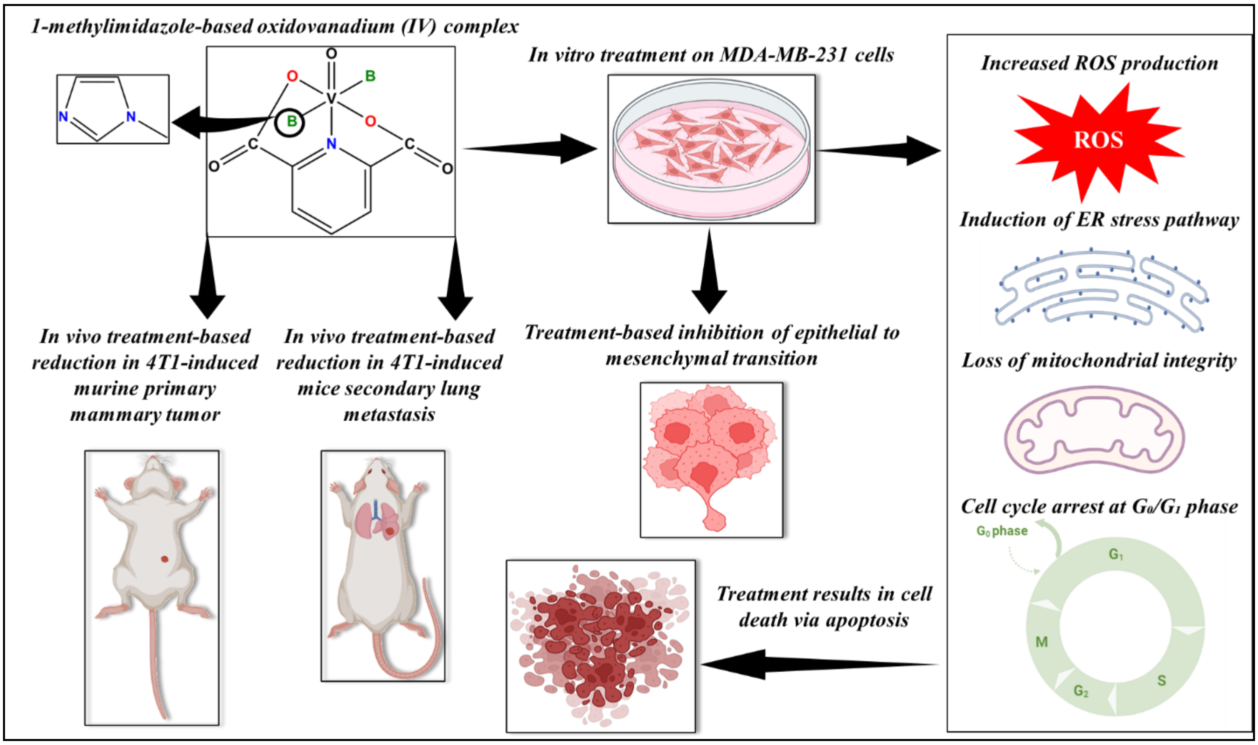

Figure 21: *Schematic representation of antineoplastic effect of OVMI*

However, it is important to note that the ability of OVMI to induce cell death appears to only be partially attributed to the ROS-mediated mitochondrial apoptosis mechanism. Moreover, OVMI can enhance ER stress-induced UPR in MDA-MB-231 cells, which ultimately primes the cells for CHOP-mediated apoptosis. However, it is crucial to address another clinical aspect of TNBC cells, which is their significant metastatic potential. Through the use of OVMI treatment at higher concentrations, researchers have discovered its effectiveness in inhibiting the migration of MDA-MB-231 cells across bidirectional wounds on culture plates. This treatment also leads to a reduction in the translational expression of metastatic markers such as vimentin and N-cadherin *in vitro*. Furthermore, *in vivo* studies have demonstrated that OVMI can decrease the number of pulmonary nodules induced by 4T1 cells, along with a concurrent decrease in the translational expression of specific metastatic markers. As a result, signs of secondary lung metastasis of 4T1 cells in female Balb/c mice are significantly reduced. OVMI has the potential to not only reduce the size and volume of primary mammary tumors but also to decrease cancer cell proliferation and the presence of EMT markers. Additionally, OVMI can enhance the expression of apoptotic markers in 4T1-induced mammary tumors. It is important to note that TBNC is a complex disease that manifests as a multimodal condition, often characterized by heightened drug efflux, severe chemoresistance, and a propensity for aggressive metastasis. Consequently, patients with TBNC often have a poor prognosis. Therefore, there is a need for chemicals that can target multiple signaling pathways involved in carcinogenesis, while minimizing harm to vital organs and circumventing chemoresistance. In this context, OVMI emerges as a promising chemotherapeutic agent for future clinical investigations, as it possesses the versatility and the ability to exert cytotoxic, antiproliferative, and antimetastatic effects on TNBC in various ways.

4.6. References

Aggarwal, Sadhna, Sumit Singh Verma, Sumit Aggarwal, and Subash Chandra Gupta. 2021. "Drug repurposing for breast cancer therapy: Old weapon for new battle." Seminars in cancer biology.

Aridoss, G, S Balasubramanian, P Parthiban, and S Kabilan. 2006. "Synthesis and in vitro microbiological evaluation of imidazo (4, 5-b) pyridinylethoxypiperidones." European journal of medicinal chemistry 41 (2):268-275.

Bhandari, Kalpana, Nagarapu Srinivas, GB Shiva Keshava, and Praveen K Shukla. 2009. "Tetrahydronaphthyl azole oxime ethers: the conformationally rigid analogues of oxiconazole as antibacterials." European journal of medicinal chemistry 44 (1):437-447.

Biswal, Debanjana, Nikhil Ranjan Pramanik, Syamal Chakrabarti, Michael GB Drew, Krishnendu Acharya, and Swarnendu Chandra. 2017. "Syntheses, crystal structures, DFT calculations, protein interaction and anticancer activities of water soluble dipicolinic acid-imidazole based oxidovanadium (iv) complexes." Dalton Transactions 46 (47):16682-16702.

Bravo, R., V. Parra, D. Gatica, A. E. Rodriguez, N. Torrealba, F. Paredes, Z. V. Wang, A. Zorzano, J. A. Hill, E. Jaimovich, A. F. Quest, and S. Lavandero. 2013. "Endoplasmic reticulum and the unfolded protein response: dynamics and metabolic integration." Int Rev Cell Mol Biol 301:215-90. doi: 10.1016/b978-0-12-407704-1.00005-1.

Carlos, Timothy M, and John M Harlan. 1994. "Leukocyte-endothelial adhesion molecules."

Chao, Y. L., C. R. Shepard, and A. Wells. 2010. "Breast carcinoma cells re-express E-cadherin during mesenchymal to epithelial reverting transition." Mol Cancer 9:179. doi: 10.1186/1476-4598-9-179.

Chen, Qiuyan, and A Catharine Ross. 2012. "All-trans-retinoic acid and the glycolipid α-galactosylceramide combined reduce breast tumor growth and lung metastasis in a 4T1 murine breast tumor model." Nutrition and cancer 64 (8):1219-1227.

Chopra, Neha, Holly Tovey, Alex Pearson, Ros Cutts, Christy Toms, Paula Proszek, Michael Hubank, Mitch Dowsett, Andrew Dodson, and Frances Daley. 2020. "Homologous recombination DNA repair deficiency and PARP inhibition activity in primary triple negative breast cancer." Nature communications 11 (1):2662.

Congiu, Cenzo, Maria Teresa Cocco, and Valentina Onnis. 2008. "Design, synthesis, and in vitro antitumor activity of new 1, 4-diarylimidazole-2-ones and their 2-thione analogues." Bioorganic & medicinal chemistry letters 18 (3):989-993.

Coskun, Ugur, Banu Sancak, Ilker Sen, Neslihan Bukan, Muge Aydın Tufan, Özlem Gülbahar, and Sinan Sozen. 2006. "Serum P-selectin, soluble vascular cell adhesion molecule-I (s-VCAM-I) and soluble intercellular adhesion molecule-I (s-ICAM-I) levels in bladder carcinoma patients with different stages." International immunopharmacology 6 (4):672-677.

Coussens, Lisa M, and Zena Werb. 1996. "Matrix metal loproteinases and the development of cancer." Chemistry & biology 3 (11):895-904.

Duffy, Michael J, Teresa M Maguire, Arnold Hill, Enda McDermott, and Niall O'Higgins. 2000. "Metalloproteinases: role in breast carcinogenesis, invasion and metastasis." Breast cancer research 2 (4):1-6.

Eslami Amirabadi, H., M. Tuerlings, A. Hollestelle, S. SahebAli, R. Luttge, C. C. van Donkelaar, J. W. M. Martens, and J. M. J. den Toonder. 2019. "Characterizing the invasion of different breast cancer cell lines with distinct E-cadherin status in 3D using a microfluidic system." Biomedical Microdevices 21 (4):101. doi: 10.1007/s10544-019-0450-5.

Ghosh, Noyel, Sharmistha Chatterjee, Debanjana Biswal, Nikhil Ranjan Pramanik, Syamal Chakrabarti, and Parames C Sil. 2022. "Oxidative stress imposed in vivo anticancer therapeutic efficacy of novel imidazole-based oxidovanadium (IV) complex in solid tumor." Life Sciences 301:120606.

Ghosh, Noyel, Mousumi Kundu, Sumit Ghosh, Abhishek Kumar Das, Samhita De, Joydeep Das, and Parames C Sil. 2023. "pH-responsive and targeted delivery of chrysin via folic acid-functionalized mesoporous silica nanocarrier for breast cancer therapy." International Journal of Pharmaceutics 631:122555.

Ghosh, Noyel, and Parames C. Sil. 2021. "Chapter 5 - Mitochondria and apoptosis." In Mitochondrial Physiology and Vegetal Molecules, edited by Marcos Roberto de Oliveira, 127-149. Academic Press.

Jakusch, Tamás, Wenzheng Jin, Luqin Yang, Tamás Kiss, and Debbie C Crans. 2003. "Vanadium (IV/V) speciation of pyridine-2, 6-dicarboxylic acid and 4-hydroxy-pyridine-2, 6-dicarboxylic acid complexes: potentiometry, EPR spectroscopy and comparison across oxidation states." Journal of inorganic biochemistry 95 (1):1-13.

Keter, Frankline Kiplangat. 2010. Palladium, platinum and gold complexes: a synthetic approach towards the discovery of anticancer agents: University of Johannesburg (South Africa).

Kuwana, T., and D. D. Newmeyer. 2003. "Bcl-2-family proteins and the role of mitochondria in apoptosis." Curr Opin Cell Biol 15 (6):691-9. doi: 10.1016/j.ceb.2003.10.004.

Papp, B., S. Launay, P. Gélébart, A. Arbabian, A. Enyedi, J. P. Brouland, E. D. Carosella, and H. Adle-Biassette. 2020. "Endoplasmic Reticulum Calcium Pumps and Tumor Cell Differentiation." Int J Mol Sci 21 (9). doi: 10.3390/ijms21093351.

Pizarro, Ana M, and Peter J Sadler. 2009. "Unusual DNA binding modes for metal anticancer complexes." Biochimie 91 (10):1198-1211.

Polychronidis, Alexandros C, Alexandra K Tsaroucha, Sofoklis P Samolis, Sotirios K Botaitis, Sebachedin S Perente, and Constantinos E Simopoulos. 2003. "Serum levels of intercellular adhesion molecule-1 correlate with advanced and metastatic disease and poor prognosis in gastric cancer." Folia Medica 45 (1):20-24.

Qian, S., Z. Wei, W. Yang, J. Huang, Y. Yang, and J. Wang. 2022. "The role of BCL-2 family proteins in regulating apoptosis and cancer therapy." Front Oncol 12:985363. doi: 10.3389/fonc.2022.985363.

Reedijk, Jan. 2003. "New clues for platinum antitumor chemistry: kinetically controlled metal binding to DNA." Proceedings of the National Academy of Sciences 100 (7):3611-3616.

Simpson, Peter V, Nima Maheshkumar Desai, Ilaria Casari, Massimiliano Massi, and Marco Falasca. 2019. "Metal-based antitumor compounds: Beyond cisplatin." Future Medicinal Chemistry 11 (2):119-135.

Smith, Robert C, and Jeri C Reeves. 1987. "Antioxidant properties of 2-imidazolones and 2-imidazolthiones." Biochemical pharmacology 36 (9):1457-1460.

Somiari, Stella B, Richard I Somiari, Caroline M Heckman, Cara H Olsen, Rick M Jordan, Stephen J Russell, and Craig D Shriver. 2006. "Circulating MMP2 and MMP9 in breast cancer—potential role in classification of patients into low risk, high risk, benign disease and breast cancer categories." International journal of cancer 119 (6):1403-1411.

Storr, Sarah J, Neil O Carragher, Margaret C Frame, Tim Parr, and Stewart G Martin. 2011. "The calpain system and cancer." Nature Reviews Cancer 11 (5):364-374.

Tuninetti, Valentina, Eleonora Ghisoni, Sandro Pignata, Elisa Picardo, Francesco Raspagliesi, Claudia Andreetta, Elena Maldi, Grazia Artioli, Serafina Mammoliti, and Lucia Zanchi. 2023. "Ki67 as a Predictor of Response to PARP Inhibitors in Platinum Sensitive BRCA Wild Type Ovarian Cancer: The MITO 37 Retrospective Study." Cancers 15 (4):1032.

Chapter 5

Folic Acid-Functionalized pH-responsive Mesoporous Silica Nanocarrier-assisted Enhanced Antineoplastic Efficacy of Chrysin in Breast Cancer Therapy

5.1. Introduction

Standard cancer therapeutics include surgical resection of tumor mass, hormonal inhibition, chemotherapy and radiation; altogether which only offer limited benefits in cancer treatment leading to collateral damage to vital organs and decreased post-treatment average patient survival (Sengupta and Balla, 2018). Such disparity calls for the significance of advanced and thoughtful strategies leading to minimal off-target toxicity. In this context, naturally-occurring flavonoid-phytochemicals attract our attention as prospective anticancer agents. Among several other flavonoids, 5,7-dihydroxyflavone (Figure 1), also known as chrysin, is an attractive option. However, inadequate absorption- and rapid metabolism-driven poor bioavailability and insufficient water solubility are the current major challenges for chrysin to be considered in cancer therapeutics (Walle et al., 2001).

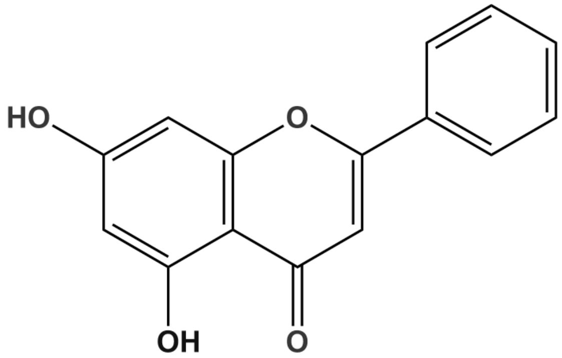

Figure 1: *Chemical structure of chrysin (5,7-dihydroxyflavone)*

In line, bioavailability and subsequent efficacy of chrysin can be uplifted by packing it inside tumor cell-specific ligand-labeled smart nanocarrier which will be capable of stimulus-responsive drug unloading at tumor microenvironment (Wang, Lu, et al. 2021, Sun et al. 2022). Such tumor-specificity can be achieved easily by functionalizing nanocarrier surface through cognate ligand mounting (Deshayes et al., 2013). Additionally, premature and unnecessary off-target unloading of the therapeutic agents can be accomplished by modulating nanocarrier for stimuli-driven drug release (Garcia-Bennett, Nees, and Fadeel 2011, Salinas et al. 2018, Wang, Zhang, et al. 2021). Among several stimuli-guided drug release mechanisms, change in pH is the most studied one, as tumor microenvironment is known possess a sharp pH-gradient (Kundu et al. 2019). By acknowledging modulation procedures, here, we have formulated a mesoporous silica nanoparticle ($mSiO_2$)-based nanocarrier for chrysin where polyacrylic acid (PAA) coating has provided a superior 'molecular gate'-like effect to deliver its cargo following the change in pH. Further, tumor-selectivity has been achieved through folic acid (FA) fabrication. In this regard, it is important to state that $mSiO_2$ has been selected due to its phenomenal features of silica scaffold which is suitable for pH-guided controlled release of drug at tumor site following a steady state kinetics (Salinas et al. 2018, Giret, Wong Chi Man, and Carcel 2015, Lu et al. 2010). In addition to nanohybrid formulation, we have studied enhanced cellular uptake and consequent increased bioavailability, anticancer effectivity of chrysin both *in vitro* and *in vivo.* Study was extended to find out possible molecular mechanisms responsible for chrysin nanocarrier-driven cell killing in MCF-7 cells and further validated in Ehrlich Ascites Carcinoma (EAC) cell-induced solid tumors in Swiss Albino mice.

5.2. Utilized reagents

Required chemicals were procured from eminent chemical and biochemical companies as stated in Chapter-2 under section 2.1.

5.3. Methods

5.3.1. Formulation of amine (-NH_2)-functionalized mSiO_2

Chemical formulation of mSiO_2 was done by chemical combination of CTAB, NaOH and TEOS. Further amine functionalization with addition of APTES was done as discussed section 2.2.3.1 of Chapter 2.

5.3.2. Chrysin entrapment inside aminated mSiO_2 and formulation of Chr-mSiO_2

Chrysin was ensnared inside the pore of mSiO_2 in 2:1 feed ratio as described in Chapter-2 under section 2.2.3.2. followed by calculation of respective percentage of DLC and DEE.

5.3.3. PAA addition upon Chr-mSiO_2 (Chr-mSiO_2@PAA)

Chr-mSiO_2 and PAA in 1:1 mass ratio, were combined to prepare Chr-mSiO_2@PAA as described in chapter-2 under section 2.2.3.3.

5.3.4. Preparation of Chr-mSiO_2@PAA/FA through FA labelling

Chr-mSiO_2@PAA was added to FA in 2:1 weight ratio to formulate Chr-mSiO_2@PAA/FA as discussed in Chapter-2 under section 2.2.3.4.

5.3.5. Preparation of fluorescent mSiO_2 nanoconjugates

According to the method described in chapter-2 under section 2.2.3.5, Chr-mSiO_2@FITC and Chr-mSiO_2@FA/FITC were prepared through conjugation of FITC with Chr-mSiO_2 and Chr-mSiO_2@PAA respectively.

5.3.6. Characterization of nanoconjugates

Synthesized nanoconjugates were characterized at each step by FTIR spectra, specific UV absorption spectra, DLS and zeta potential analyses. TEM and SEM were performed to as represented in detail in chapter-2 under section 2.2.3.6.

5.3.7. Hemolytic capability of nanoconjugates

Changes in nanoconjugate-induced hemolysis, at each step from bare $mSiO_2$ up to the final modification, were assessed according the protocol discussed in chapter-2 under section 2.2.3.7.

5.3.8. Protein adsorption on surface of nanoconjugates

Adsorption of protein on the surface of prepared nanoconjugates was measured spectrophotometrically using BSA as discussed in chapter-2 under section 2.2.3.8.

5.3.9. Stimuli-responsive release profile of chrysin

Here, we have studied pH-dependent release of chrysin from $mSiO_2$ nanoconjugates through mounting PAA. Study of chrysin release due to pH-sensitivity was done at different pH-conditions (pH 7.4, pH 6.0 and pH 5.0) following the protocol described in chapter-2 under section 2.2.3.10.

5.3.10. Cell culture

Seeding, culture and respective maintenances of MCF-7 and NKE cells were done according to the standard protocol mentioned in chapter-2 under section 2.2.1.1.

5.3.11. *In vitro* cellular uptake of nanoconjugates and release of chrysin

After treatment with Chr-$mSiO_2$@FITC and Chr-$mSiO_2$@FITC/FA, FA-guided uptake of $mSiO_2$ nanoconjugates in MCF-7 cells were checked flowcytometrically at 520 nm and were validated through confocal scanning laser microscopy as per the protocol mentioned in chapter-2 under section 2.2.3.9. For studying intracellular release of chrysin from nanohybrids, both MCF-7 cells and NKE, both cells were treated and finally spectrophotometric reading was taken at 315 nm (discussed in the section 2.2.3.10.).

5.3.12. Cytotoxic effect of synthesized chrysin nanoconjugates

Standard MTT assay was carried out on both MCF-7 and NKE cells following the protocol described in chapter-2 under section 2.2.1.2. Treatments were made with free chrysin, Chr-$mSiO_2$@PAA, Chr-

$mSiO_2$@PAA/FA and $mSiO_2$@PAA/FA for 24 hours in a range of five doses from 5 µg/ml to 40 µg/ml of free chrysin and corresponding equivalent concentrations of chrysin-loaded nanoconjugates.

5.3.13. Determination of mode of cell death

Chrysin nanoconjugates-mediated mode of cell death in MCF-7 cells, was checked by Annexin V/FITC staining followed by flowcytometric and confocal microscopic analysis as stated in chapter-2 under section 2.2.1.4.

5.3.14. Intracellular cumulative ROS generation

Intracellular ROS content in MCF-7 cells, following the treatment with LC_{50} doses of free chrysin, Chr-$mSiO_2$@PAA and Chr-$mSiO_2$@PAA/FA was made using DCFH-DA staining as stated in chapter-2 under section 2.2.1.5. Results were evaluated through flowcytometry and confocal microscopy.

5.3.15. *In vitro* mitochondrial membrane potential detection

Following the treatment with nano-chrysin-formulations, mitochondrial membrane potential was determined according to the protocol described in chapter-2 under the section 2.2.1.6. using JC-1 dye followed by flow cytometric analysis using BD FACS Verse flow cytometer.

5.3.16. Detection of *in vitro* oxidative status

Changes in oxidative status of MCF-7 cells after being treated with free chrysin, Chr-$mSiO_2$@PAA and Chr-$mSiO_2$@PAA/FA, was investigated by evaluating intracellular GSH and GSSG content; extent of intracellular lipid peroxidation; quantifying catalytic activities of antioxidant enzymes, such as, SOD and CAT as discussed in sections 2.2.1.7., 2.2.1.8. and 2.2.1.9.

5.3.17. Cell cycle distribution analysis

Cultured MCF-7 cells were analyzed flow cytometrically for cell cycle distribution after being treated with free chrysin and Chr-$mSiO_2$@PAA/FA. PI was used to stain for this assessment. Detailed protocol has been discussed in chapter-2 under section 2.2.1.10.

5.3.18. Whole cell protein extraction & immuno-blotting

MCF-7 cells, treated with LC_{50} dose of free chrysin and corresponding equivalent doses of Chr-$mSiO_2$@PAA and Chr-$mSiO_2$@PAA/FA, were lysed in 1X RIPA lysis buffer followed by quantification of total protein concentration in cell lysates as per the protocol discussed earlier in chapter-2 under section 2.2.1.14. Cell lysate from each experimental group were then compared for translational expression of certain selective proteins using primary antibodies against GSK-3β, cyclin D1, p-Akt, cytochrome C, Apaf-1, Bax, Bcl-2, cleaved caspase 9 and cleaved caspase 3 through immune blotting as explained in chapter-2 under section 2.2.1.15. β-actin was used as internal loading control.

5.3.19. Inhibitor study

Effect of NAC-based ROS inhibition was studied in Chr-mSiO$_2$@PAA/FA-treated MCF-7 cells as discussed in chapter-2 under the section 2.2.1.16. Following ROS inhibition, cells were checked for intracellular ROS content, cell viability % through MTT assay, extent of apoptosis through Annexin-V staining and protein-level expression study of Bcl-2 to Bax ratio and cleaved caspase-3 via immunoblotting.

5.3.20. Study of tumor regression study in EAC-induced tumor-bearing Swiss Albino mice

Thirty Swiss Albino mice (4-6 weeks old and weighing 23-25 gm) were received from central animal house of Bose Institute, Kolkata, India, were acclimatized and maintained in laboratory condition according to the standard guidelines explained in chapter-2 under the section 2.2.2.1. Ten days after EAC-induced tumor inoculation (following the standard protocol explained previously in chapter 2 under the section 2.2.2.2.), twenty-four tumor-bearing mice were segregated randomly in four groups (namely, T1, T2, T3 and T4), each group carrying a total of six animals. Mice receiving no EAC injection were designated to group-T0. Twenty-four tumor-bearing mice bunched in four groups (T1-T4) received tail-vein injection for two consecutive weeks on alternative days as follows:

T0 – control mice without tumor

T1– treated with intravenous PBS of pH 7.4 (tumor control)

T2 – treated with intravenous chrysin solution (10 mg per kg body weight)

T3– treated with intravenous Chr-mSiO$_2$@PAA solution (60.60 mg per kg body weight)

T4 – treated with intravenous Chr-mSiO$_2$@PAA/FA solution (74 mg per kg body weight)

Mice were evaluated for any changes in body weight and tumor volume on day-to-day basis throughout the entire treatment period. Tumor volume was measured by following equation: Tumor Volume = [(tumor length) x (tumor width)^2] / 2

Later, upon the completion of entire treatment period, mice were sacrificed by cervical dislocation and precautions were taken to reduce pain and suffering of the animals. Tumors from each group (T1-T4) were collected and studied for spot weight and volume calculation. Further, spleen from tumor-bearing mice were collected to evaluate tumor-responsive splenomegaly and any changes related to the same.

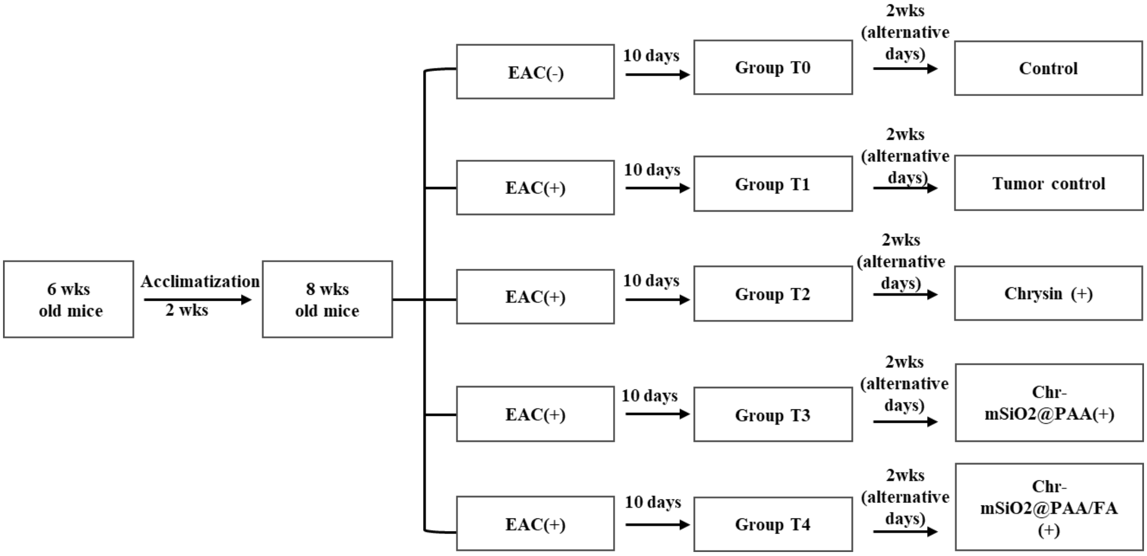

Scheme 1: *Schematic work plan for EAC-mediated solid tumor induction in Swiss Albino mice and further treatment with chrysin-nanohybrids.*

5.3.21. Assessment of chrysin uptake in tumor tissue through HPLC performance

Efficacy of nanoencapsulation of chrysin and its further medication in terms of increased tumor-tissue specificity was evaluated through assessing chrysin uptake in tumor tissues of treated mice. HPLC was performed for estimation of chrysin uptake in tumor tissues following the protocol discussed in chapter-2 under the section 2.2.3.11.

5.3.22. Immunohistochemical study of *in vivo* proapoptotic behavior of chrysin nanohybrid

Immunohistochemical expressions of caspase-9 and caspase-3 were evaluated on resected tumor tissue sections using IHC assay kit (Abcam, ab80437) following manufacturer’s guidelines are described under the section 2.2.2.10. in chapter-2.

5.3.23. Systemic toxicity assessment

To examine nanoconjugate induced systemic toxicity, twelve wildtype Swiss Albino mice were divided into four groups (S1-S4). These mice were subjected to treatment schedule of fourteen days as follows:

S1 – control group of mice receiving 1X PBS (pH 7.4) intravenously.

S2 – mice treated with free chrysin intravenously (10 mg kg-1 body weight).

S3 - mice receiving intravenous Chr-mSiO2@PAAtreatment (60.60 mg kg-1 body weight).

S4 - mice receiving intravenous Chr-mSiO2@PAA/FA treatment (74 mg kg-1 body weight).

After completion of entire treatment, mice were sacrificed. Blood and serum were collected for checking hepatic and renal heath parameters such as ALP, ALT, BUN and creatine, following the protocol described in section 2.2.2.5. Additionally, vital organs such as lung, liver, kidney and heart were resected out to check any treatment-induced sign of tissue-specific histological abnormality.

5.3.24. Histological assessment

Resected tumor and splenic tissues from tumor-bearing mice as well as tissues of vital organs from systemic toxicity experimental groups were evaluated histologically as described in chapter-2 under the section 2.2.2.6.

5.3.25. Statistical analysis

Statistical analyses were carried out as described under the section 2.2.4. in chapter-2.

5.4. Results and Discussion

5.4.1. Characteristic properties of Chr-mSiO$_2$ nano-formulations

Schematic description of Chr-mSiO$_2$@PAA/FA formulation has been depicted in Figure 2.

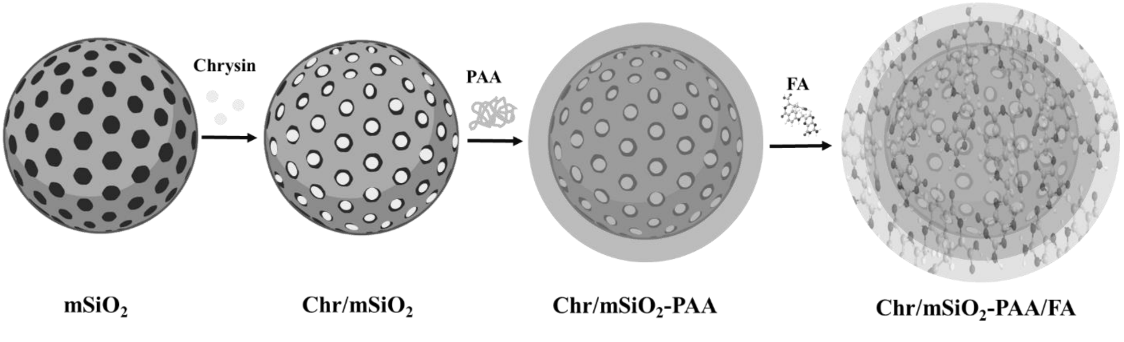

Figure 2: *Schematic representation of step-by-step formulation and modification of mSiO$_2$ -based chrysin nanohybrids.*

In short, synthesized $mSiO_2$ was amine ($-NH_2$) functionalized initially, followed by chrysin entrapping into the pores of aminated mesoporous nanoparticles. Amine functionalization provided positive charge to the bare $mSiO_2$ nanoparticles that was anticipated to ease the loading process of negatively charged flavonoid, chrysin, inside $mSiO_2$ pores. Unexpected drug leakage was diminished by providing a coating of PAA on the surface of Chr-$mSiO_2$ nanoconjugates. Finally, Chr-$mSiO_2$@PAA/FA was formulated by labelling FA on the PAA-coated nanoconjugate to achieve FA-specific tumor targeting. Actual size and the overall morphology of synthesized nanoconjugates were investigated by performing TEM and SEM. TEM image reveals well-defined porous and almost spherical morphology of bare $mSiO_2$ with an average diameter of 34.167 nm (Figure 3A & 3D).

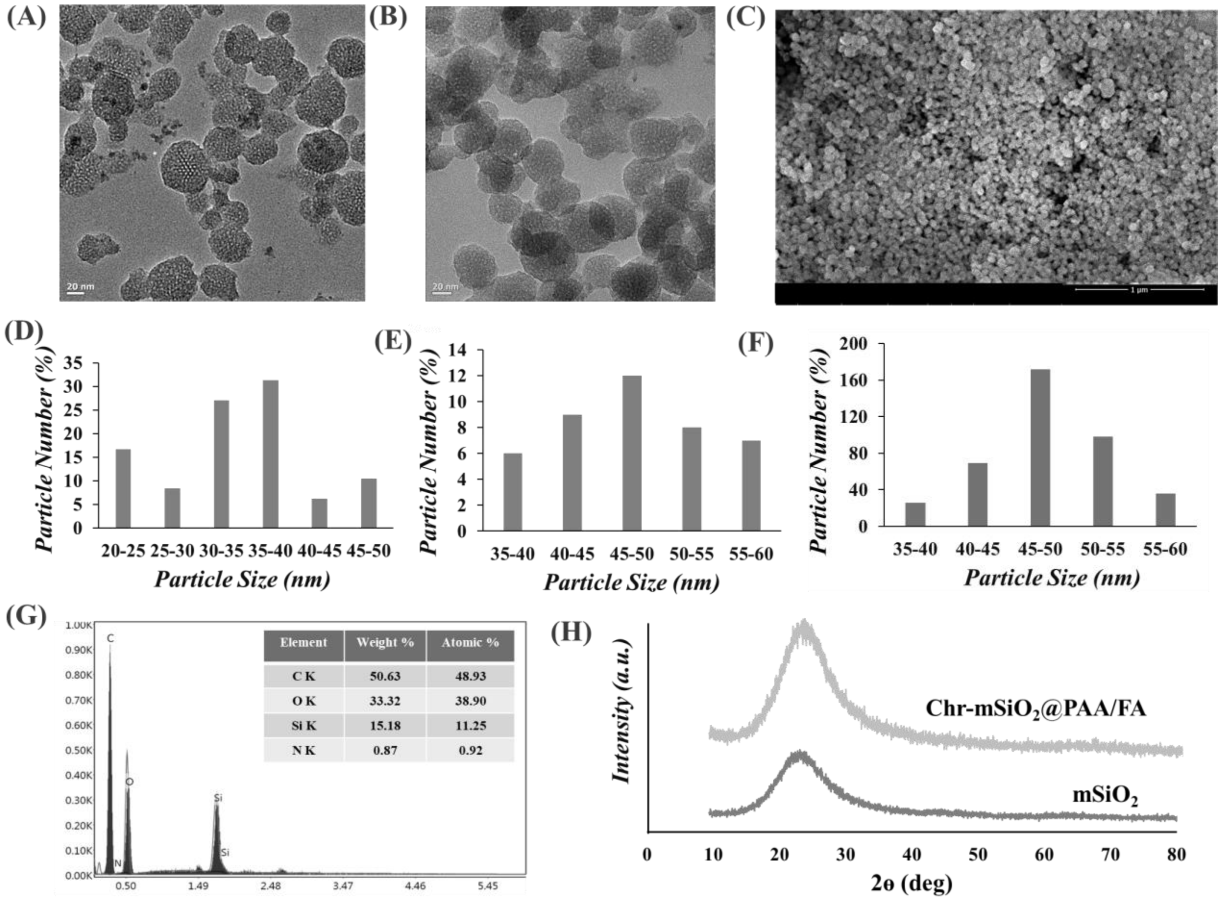

Element	Weight %	Atomic %
C K	50.63	48.93
O K	33.32	38.90
Si K	15.18	11.25
N K	0.87	0.92

Figure 3:* *Characterization of chrysin-nanohybrid by TEM, SEM, EDX, XRD: *Representative TEM photographs of (A) bare* $mSiO_2$ *and (B) Chr-*$mSiO_2$*@PAA/FA. (C) SEM photograph of Chr-*$mSiO_2$*@PAA/FA. Diameter-wise particle distribution of (C) bare* $mSiO_2$ *(TEM), (D) Chr-*$mSiO_2$*-PAA/FA (TEM) and of (E) Chr-*$mSiO_2$*-PAA/FA (SEM). (F) EDX analysis of Chr-*$mSiO_2$*@PAA/FA. (G) XRD graphs of bare* $mSiO_2$ *and final chrysin nanoconjugate Chr-*$mSiO_2$*@PAA/FA.*

Finally obtained Chr-mSiO_2@PAA/FA exhibited almost similar nearly-spherical morphology as that of the bare mSiO_2 but differed in an increase in particle size to an average diameter of 47.619 nm and blurry pores (Figure 3B & 3E). These suggest the presence of PAA and FA layers around. Corresponding SEM image of Chr-mSiO_2@PAA/FA also validates the same (Figure 3C & 3F). The EDX analysis was performed to ensure chemical nature of final nanocomposite, Chr-mSiO_2@PAA/FA and was found to contain C, N, O and Si (Figure 3G). The X-ray diffraction spectral patterns of bare mSiO_2 and final Chr-mSiO_2@PAA/FA were investigated too. In both cases, no distinctive crystalline peak was found and broad peaks at 2ɵ values in between 20° to 30° were found that specify amorphous natures of both mSiO_2 and Chr-mSiO_2@PAA/FA (Figure 3H)

FTIR spectra were collected at each step of nanoconjugate modification to validate successful loading of chrysin and subsequent addition of PAA and FA (Figure 4).

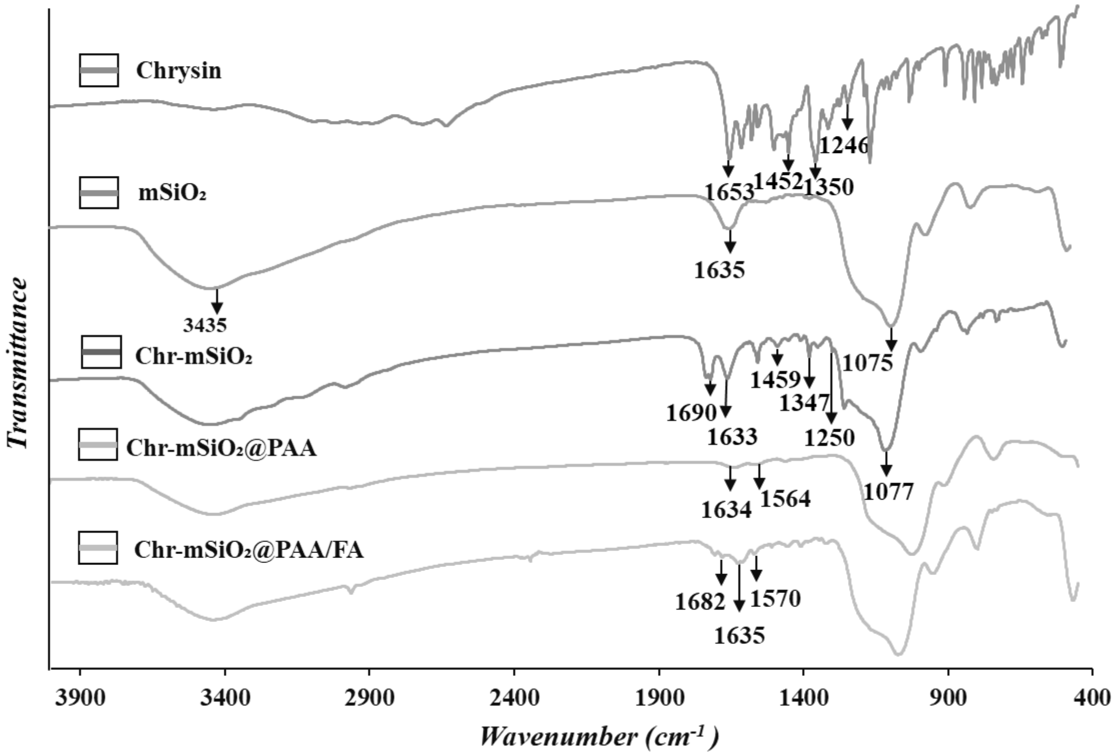

Figure 4: ***Characterization of chrysin-nanohybrids by FTIR spectra analysis:*** *FTIR spectra of free chrysin, Chr-mSiO_2, Chr-mSiO_2@PAA, Chr-mSiO_2@PAA/FA*

A spectral peak at 1075 cm^{-1} specific to Si-O stretching bond vibration in bare mSiO_2 shows successful formulation of mesoporous silica nanoparticle. Additional peaks at 1635 cm^{-1} and 3435 cm^{-1} are due to respectively bending and stretching vibrations of N-H bond which demonstrates successful $-NH_2$ functionalization of $mSiO_2$ (Kundu et al., 2020). Additionally, a series of peaks from 1653 cm^{-1} to 1245 cm^{-1} region in FTIR spectrum of chrysin, are also visible in the FTIR spectrum of Chr-$mSiO_2$, indicating successful loading of chrysin. Presence of two new peaks at 1634 cm^{-1} and 1564 cm^{-1} in the FTIR spectrum of Chr-$mSiO_2$@PAA, reveals presence of respectively C=O stretching vibration and N-H bending vibrations of amide linkage. FTIR spectrum of Chr-$mSiO_2$@PAA/FA, similarly, shows peaks at 1682 cm^{-1}, 1635 cm^{-1} and 1570 cm^{-1} assigning stretching vibrations of carboxylic acid group of lastly added FA along with C=O stretching vibration and N-H bending vibration of amide bond respectively

Nano-formulations were also characterized by their specific UV-vis absorption spectra (Figure 5A).

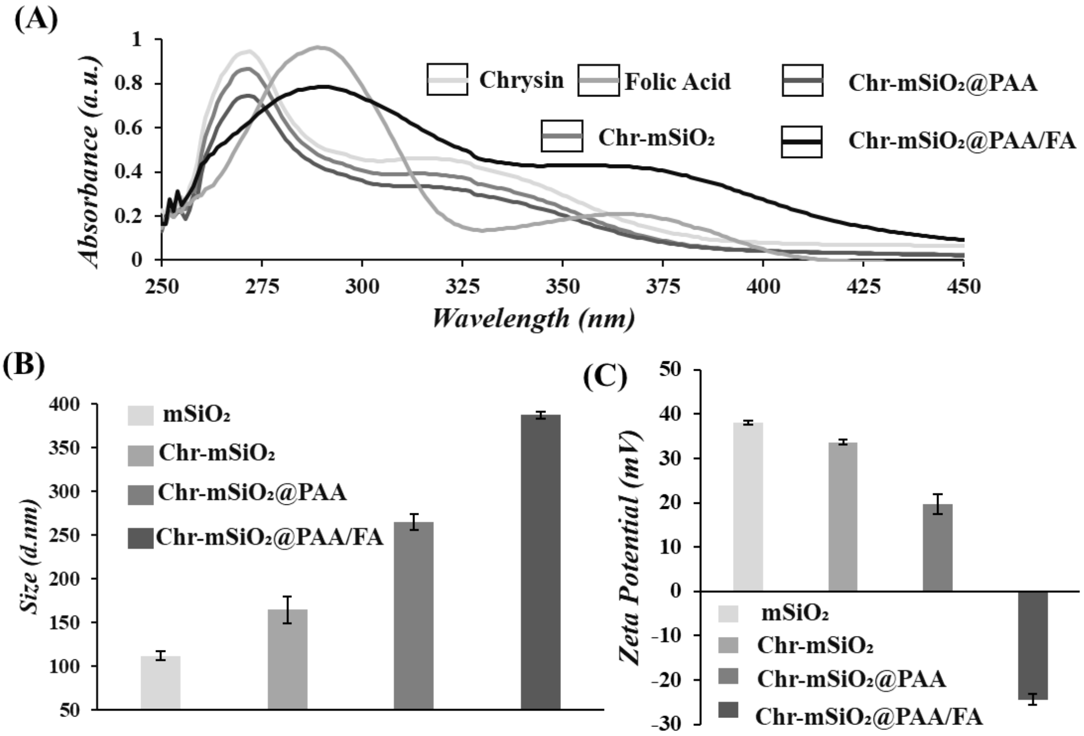

Figure 5: ***Characterization of chrysin nano-hybrids by*** *analyzing (A) UV-VIS spectra, (B) hydrodynamic sizes through DLS and (C) zeta potentials.*

No absorption spectrum was obtained in a wavelength range of 250-400 nm for $mSiO_2$ and aminated $mSiO_2$ (data not shown). Two characteristics absorption peaks of pure chrysin were obtained; strong one at 272 nm (created due to $\pi - \pi^*$ transition in benzoyl system) and another weak one at 315 nm (due to absorbance of cinnamoyl system) (Zeng et al., 2003). The absorbance peak at 315 nm was considered as characteristic peak for chrysin for any UV-based detection throughout the study. Successful chrysin entrapment was validated further as both of these characteristic peaks were present in UV-spectrum of Chr-mSiO$_2$. As the capping agent PAA didn't exhibit any absorption spectrum in aforementioned UV-vis range, Chr-mSiO$_2$@PAA had no distinct absorption spectrum distinct from that of the Chr-mSiO$_2$. However, significantly reduced absorption intensity of Chr-mSiO$_2$@PAA with respect to that of the Chr-mSiO$_2$, signifies satisfactory PAA-coating around Chr-mSiO$_2$. Targeting molecule FA itself exhibits a distinct absorption peak at 289 nm due to $\pi - \pi^*$ transition of pterin ring which can be noticed at 290 nm in the absorbance spectrum of Chr-mSiO$_2$@PAA/FA. Nevertheless, another absorbance peak of free FA at 364 nm is also evident in UV-vis spectrum of Chr-mSiO$_2$@PAA/FA.

Hydrodynamic sizes of synthesized nanoconjugates were determined through DLS (Figure 5B). Average hydrodynamic size of bare mSiO$_2$ was recorded to be 111.85 ± 5.303 nm; whereas, that of the Chr-mSiO$_2$, Chr-mSiO$_2$@PAA and Chr-mSiO$_2$@PAA/FA were found to be respectively 164.35 ± 15.485 nm, 264.90 ± 8.768 nm and 387.45 ± 4.030 nm. Successive increase in average hydrodynamic diameter related to sequential modification steps, validates successful nano-modulation of bare mSiO$_2$. In this regard, it is important to state that hydrodynamic sizes of nanoconjugates significantly differ from actual sizes measured by TEM due to the formation of aqueous layer surrounding the nanoparticles during DLS study.

Finally, nanoconjugates were studied through their characteristic zeta potential values at each of modification (Figure 5C). Zeta potential of aminated mSiO$_2$ was highly positive (38.30 ± 0.707 mV) which modulated only to a little extent (33.60 ± 0.565 mV) after chrysin entrapping and a little probable adsorption. After fabrication of negatively charged PAA onto Chr-mSiO$_2$, average surface charge of Chr-mSiO$_2$@PAA was a way more negative (19.65 ± 2.333 mV). Lastly, FA addition to the carboxyl group of PAA through amide bonding were expected to leave the carboxylic group of FA free on Chr-mSiO$_2$@PAA/FA surface leading to a highly negative average zeta potential (-24.40 ± 1.272 mV) of Chr-mSiO$_2$@PAA/FA.

5.4.2. Biocompatibility and stability assessment of chrysin-nanocarrier

An ideal nanocarrier must be highly biocompatible in order to minimalize unwanted adverse effect. Hence, hemocompatibility of the final nanocarrier, mSiO$_2$@PAA/FA was checked by hemolysis assay (Figure 6A). It has been found to be highly hemocompatible (exhibiting 7.34 % hemolytic activity), even at a concentration of 500 μg/ml in contrast to initial bare mSiO$_2$ (exhibiting 32.75 % hemolytic activity). Lowered hemolytic activity of mSiO$_2$@PAA/FA may be due to the shielding effect on the surface silanol groups of naked mSiO$_2$ by PAA-FA layering as it prevents interaction of silanol groups to the RBC membrane, rendering RBC membrane less disturbed and damaged.

Besides, study of protein adsorption is also of great worth as it explains possibility of nanoparticle clumping within bloodstream. Result from BSA adsorption study (Figure 6B), illustrates that PAA and FA modification on $mSiO_2$ has reduced BSA adsorption. In contrast to BSA adsorption on bare $mSiO_2$ (18.83 wt %), PAA coating and FA labelling has been shown to lower the same in $mSiO_2$@PAA and $mSiO_2$@PAA/FA to 10.7 wt % and 18.83 wt % respectively. Such decrease in BSA adsorption not only ensures stability of circulating nano-conjugate but also prolongs blood circulation time of the synthesized nanocarrier.

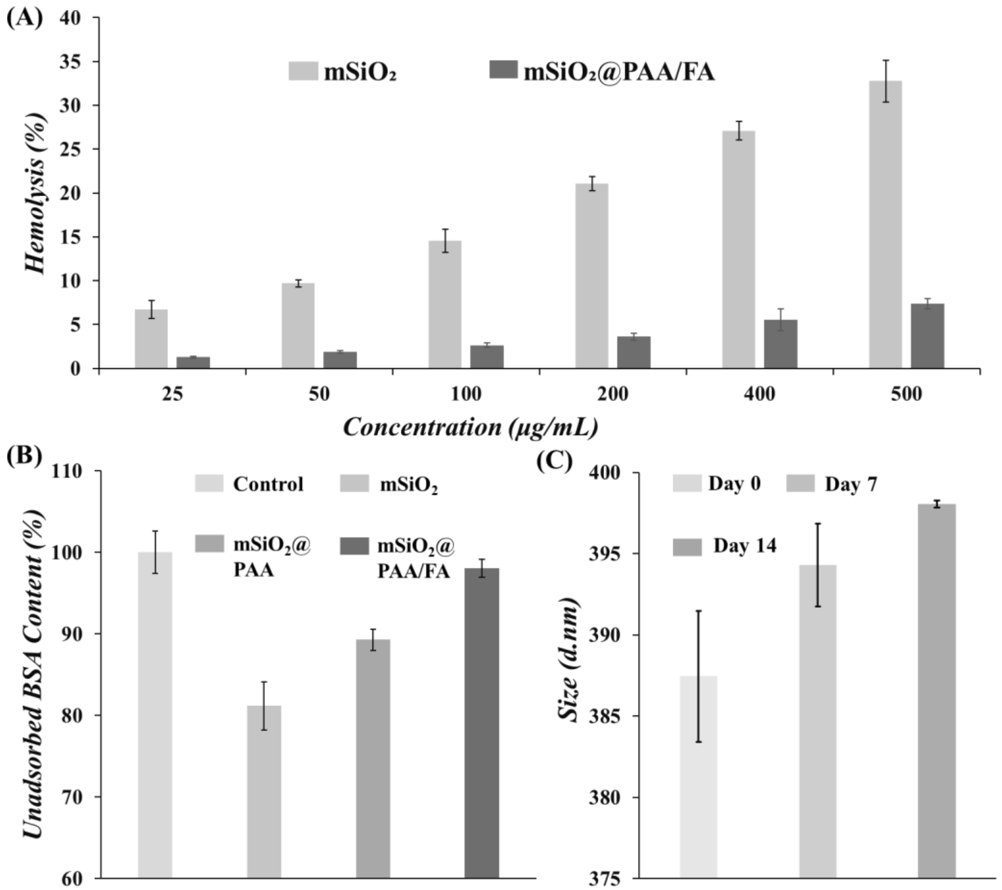

Figure 6: ***Assessment of in vitro stability and biocompatibility of chrysin nanoconjugate.*** *(A) Hemolysis at different concentrations of $mSiO_2$ and $mSiO_2$@PAA/FA. (B) Unadsorbed amount of BSA of $mSiO_2$, $mSiO_2$@PAA and $mSiO_2$@PAA/FA. Data are represented as mean ± SD (n = 3). (C) Hydrodynamic size (d.nm) of Chr-$mSiO_2$@PAA/FA on 0^{th}, 7^{th} and 14^{th} day after synthesis.*

Stability of the nanoconjugates was evaluated by checking whether the synthesized nanoformulations swell due to prolonged suspension in aqueous media or not. Thus, the final nanohybrid, Chr-$mSiO_2$@PAA/FA was suspended in 1X PBS (pH 7.4) supplemented with 10 % FBS in order to mimic condition similar to human plasma and was further examined with DLS for respective average hydrodynamic diameters on 7th and 14th day post-incubation. Comprehensive result mentioned in Table 1 and Figure 6C, suggests no significant change in hydrodynamic diameter of Chr-mSiO$_2$@PAA/FA over two weeks. Moreover, the lower PDI values indicate homogeneous size distribution and stability of the final nanohybrid within the circulating blood-stream.

Chr-mSiO$_2$@PAA/FA	**Day 0**		**Day 7**		**Day 14**	
	Size	**PDI**	**Size**	**PDI**	**Size**	**PDI**
Average (d.nm)	387.45	0.461	394.30	0.391	398.05	0.543
SD (± d.nm)	4.030	0.169	2.545	0.070	0.212	0.148

Table 1: *Time dependent changes in hydrodynamic sizes and corresponding PDI values of Chr-mSiO$_2$@PAA/FA*

5.4.3. PAA-coating mediated pH & time-responsive steady release of chrysin

In order to explore advantage of PAA capping, release patterns of chrysin in cell-free system were noted from Chr-mSiO$_2$ and Chr-mSiO$_2$@PAA over a period of 48 hours. Chrysin release from the Chr-mSiO$_2$ has been found to be pH-independent (Figure 7A).

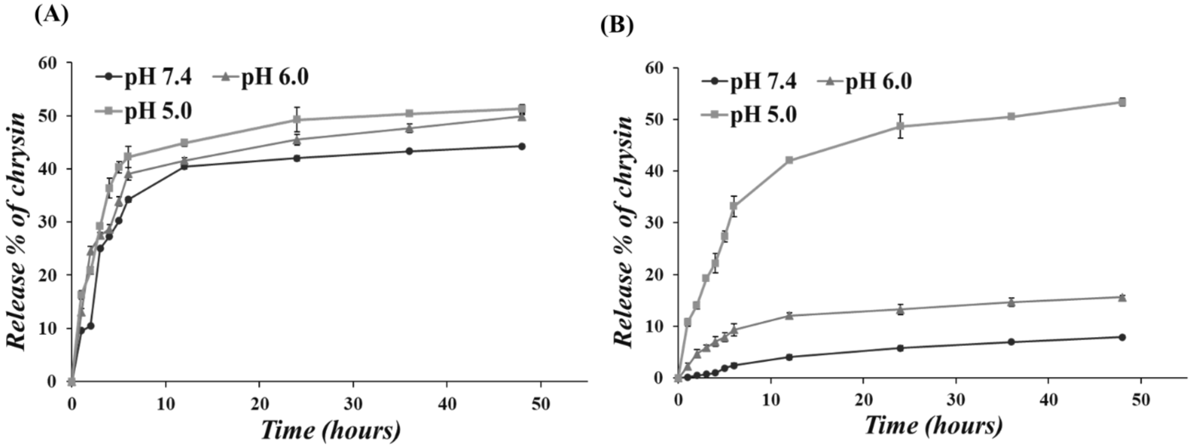

Figure 7: ***pH-dependent release of chrysin:*** *The release profiles of Chr from (A) Chr-mSiO$_2$ (B) Chr-mSiO$_2$@PAA nanocomposites under different pH conditions (pH 7.4, 6.0 and 5.0) for a time span of 0-48 hours.*

Within first 6 hours, a burst effect was evident that seemed to be related to release of surface-adsorbed nanocarrier (Jabbari et al., 2018). Release increased with time over a period of 48 hours at pH 7.4. However, at a lower pH (pH 5), chrysin release did not change significantly. Such pH-independent behavior of chrysin is probably due to lack of ionic interaction with $mSiO_2$ nanocarrier. Here also, chrysin release reached its peak at 48 hours (Figure 7B). However, in case of Chr-$mSiO_2$@PAA, only about 7.92 ± 0.33 % chrysin was released after 48 hours at pH 7.4. While, at pH 6.0 and pH 5.0, total release of chrysin were recorded to be 15.62 ± 0.32 % and 53.33 ± 0.76 % respectively. This may result from the partial detachment and hydrolyzation of PAA layer from the surface of Chr-$mSiO_2$@PAA under acidic condition. PAA has a pKa value of 4.5; thus, around pH 5 it undergoes a reversible coil-to-globule conformational transition due to ionization state of its carboxylic group (Swift et al., 2016). Additionally, over the time of 0 – 48 hours, very little chrysin release can be seen from Chr-$mSiO_2$@PAA at pH 7.4; thus, under normal physiological condition this nanocomposite can be regarded as stable. Also, chrysin release at each distinct pH was higher with time (highest after 48 hours), indicating a clear time-dependent nature of chrysin release.

5.4.4. FA attachment resulted in higher Chr-$mSiO_2$ uptake and subsequent cargo release

When checked flow cytometrically, it was found that FA tagging attributed superior uptake of FITC-tagged $mSiO_2$ nanocarrier in MCF-7 cells (Figure 8A). This outcome was further validated through fluorescence microscopy (Figure 8C) as well as by confocal microscopy (Figure 9). Inline, intracellular release of chrysin was verified again. Intracellular concentration of chrysin was 5.5-fold higher when delivered through $mSiO_2$ entrapped condition than in free form. Additionally, there was another 1.8-fold increase in intracellular chrysin concentration in Chr-$mSiO_2$@PAA/FA-treated MCF-7 cells in comparison to that of the Chr-$mSiO_2$@PAA nanoconjugate (Figure 8B). Therefore, it can be said that chrysin entrapping inside $mSiO_2$ has increased its bioavailability. So, it can be said that FA-labelling on Chr-$mSiO_2$ nanohybrids has increased efficient $mSiO_2$ uptake due to ligand-receptor recognition and subsequent receptor-mediated endocytosis in MCF-7 cells (Xu et al., 2013).

However, compared to MCF-7 cells, much lesser amount of chrysin uptake was evident in Chr-$mSiO_2$@PAA/FA-treated non-cancerous NKE cells (Figure 8B). The finding implies folate receptor-oriented tumor cell selectivity of smart Chr-$mSiO_2$@PAA/FA which allows it to differentiate absence of folate receptor overexpression in NKE cells. Thus, all of these observations emphasize the superiority of this nano-formulation with chrysin and its subsequent flagging with FA moieties.

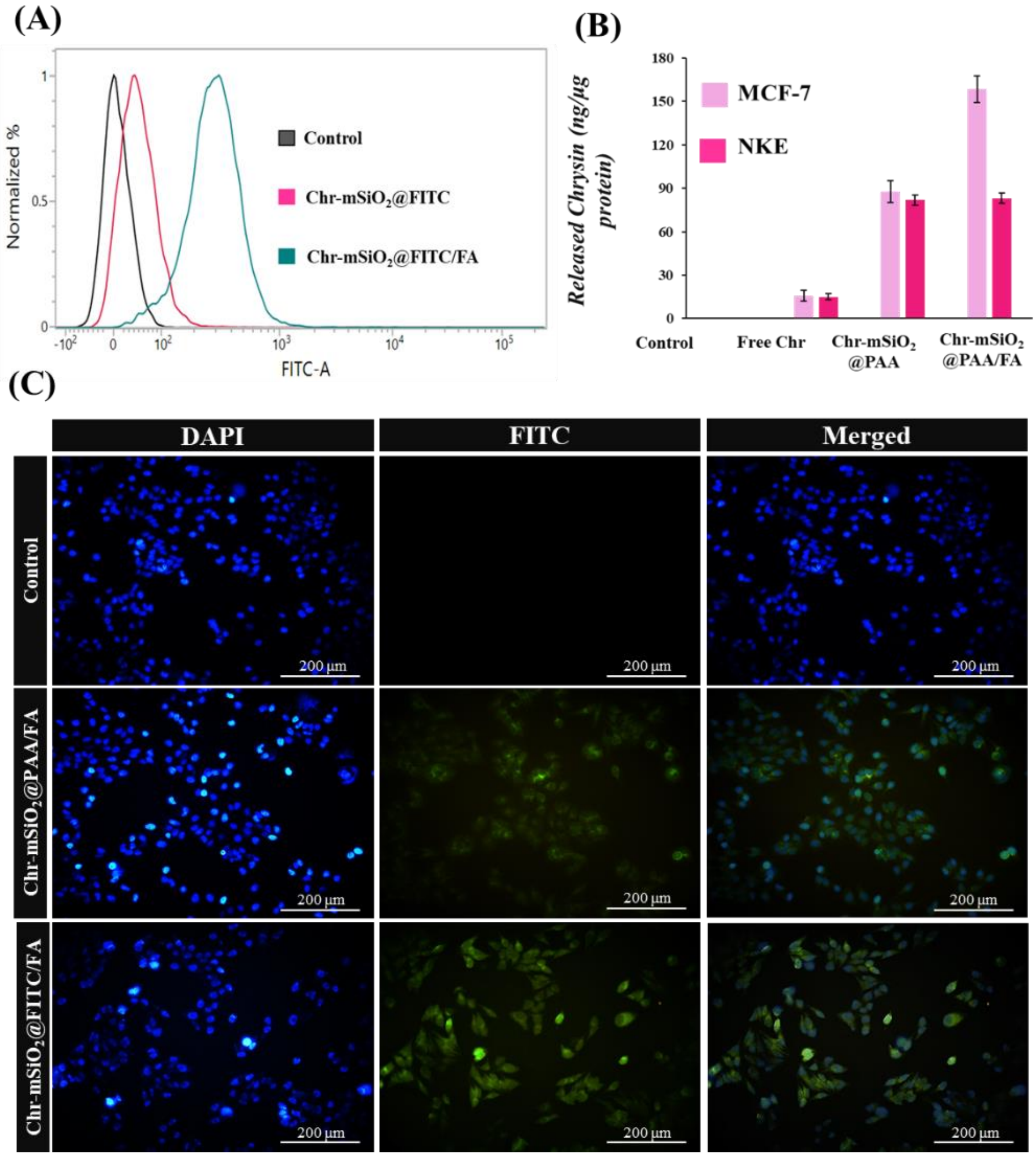

Figure 8: Study of mSiO$_2$ nanocarrier uptake and subsequent chrysin release: *(A) Study of intracellular uptake of FA conjugated mSiO$_2$ nanoparticles in contrast to untagged mSiO$_2$ by FACS. (B) Study of intracellular release of chrysin from Chr-mSiO$_2$@PAA and Chr-mSiO$_2$@PAA/FA in contrast to intracellular availability of free chrysin in MCF-7 and NKE cells. (C) Microscopic images of MCF-7 cells after 3 h incubation with free Chr (control), Chr-mSiO$_2$@FITC, Chr-mSiO$_2$@FITC/FA respectively.*

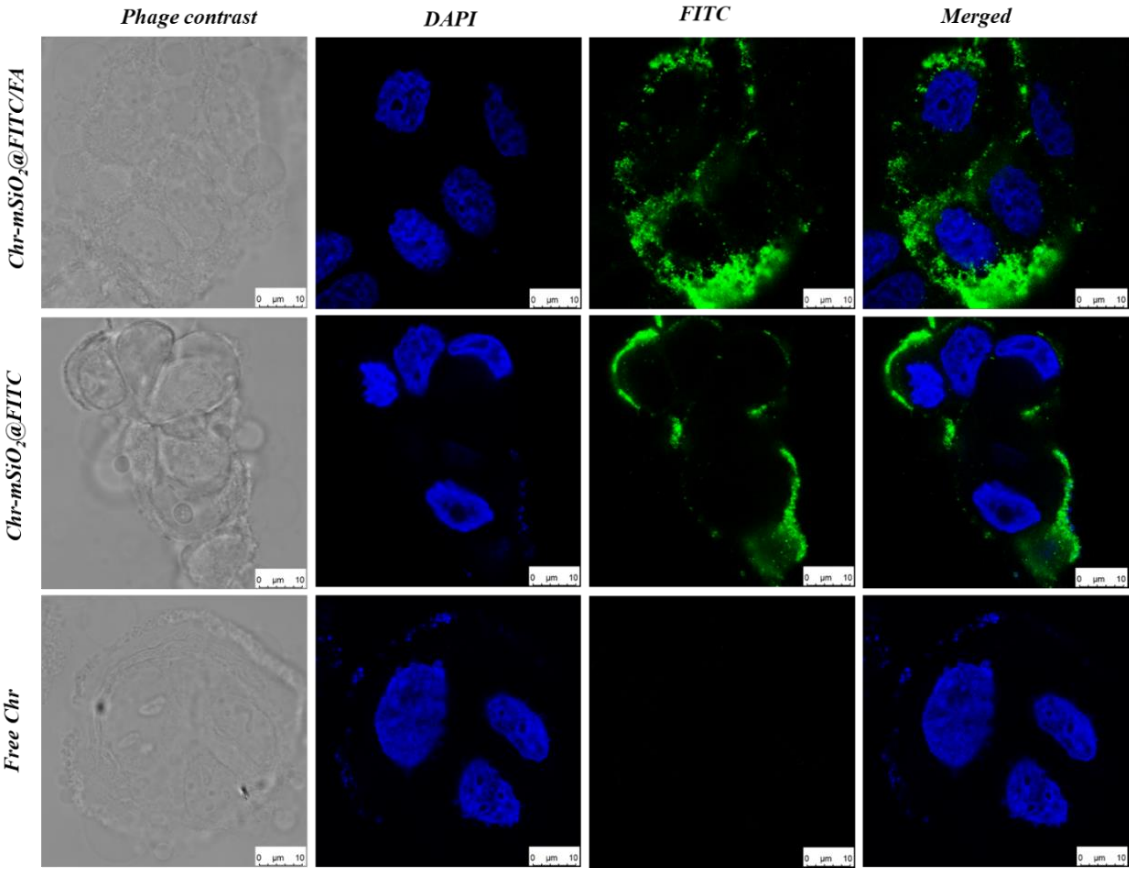

Figure 9: *Confocal laser scanning microscopic images of MCF-7 cells descripting in vitro cellular uptake of nanoconjugates after 3 h incubation with free Chr, Chr-mSiO$_2$@FITC and Chr-SiO$_2$@FITC/FA. Scale bar: 10 µm.*

5.4.5. Chr-mSiO$_2$@PAA/FA-mediated *in vitro* cytotoxicity

Cell killing ability of Chr-mSiO$_2$@PAA/FA was evaluated in both MCF-7 and NKE cells. Free chrysin showed a dose-dependent cytotoxicity in a range of 5-40 µg/ml in MCF-7 cells with a LC$_{50}$ value of 31.426 µg/ml (Figure 10A). Similar patterns of dose-dependance were exhibited by Chr-mSiO$_2$@PAA and Chr-mSiO$_2$@PAA/FA in MF-7 cells. At a particular concentration of chrysin, Chr-mSiO$_2$@PAA/FA (LC$_{50}$ 17.526 µg/ml) was found to be most cytotoxic may be attributed to the folate receptor-mediated enhanced endocytosis of Chr-mSiO$_2$@PAA/FA in comparison to Chr-mSiO$_2$@PAA (LC$_{50}$ 24.283 µg/ml) and free chrysin within MCF-7 cells.

Microscopic evaluation of treated MCF-7 cells exhibited presence of cellular shrinkage, membrane blebbing as well as apoptotic bodies that provided an idea about the probable apoptotic death of treated cells (Figure 10B). Later on, to ensure the nature of cell death, Annexin V-FITC-stained and nanohybrid-treated MCF-7 cells were scrutinized through fluorescence-assisted cell sorting (Figure 10C). At a specific concentration (10 µg/ml), Chr-mSiO$_2$@PAA/FA treatment imposed highest degree of apoptosis in MCF-7 cells (37.04 %) compared to free chrysin (13.06 %) and Chr-mSiO$_2$@PAA (21.81 %) treatments. FACS data was further validated by confocal laser scanning microscopy which also suggests increased apoptotic signal due to Chr-mSiO$_2$@PAA/FA-treatment in contrast to to free Chr and Chr-mSiO$_2$@PAA respectively (Figure 11). However, in case of NKE cells no remarkable cell killing was detected (Figure 10D

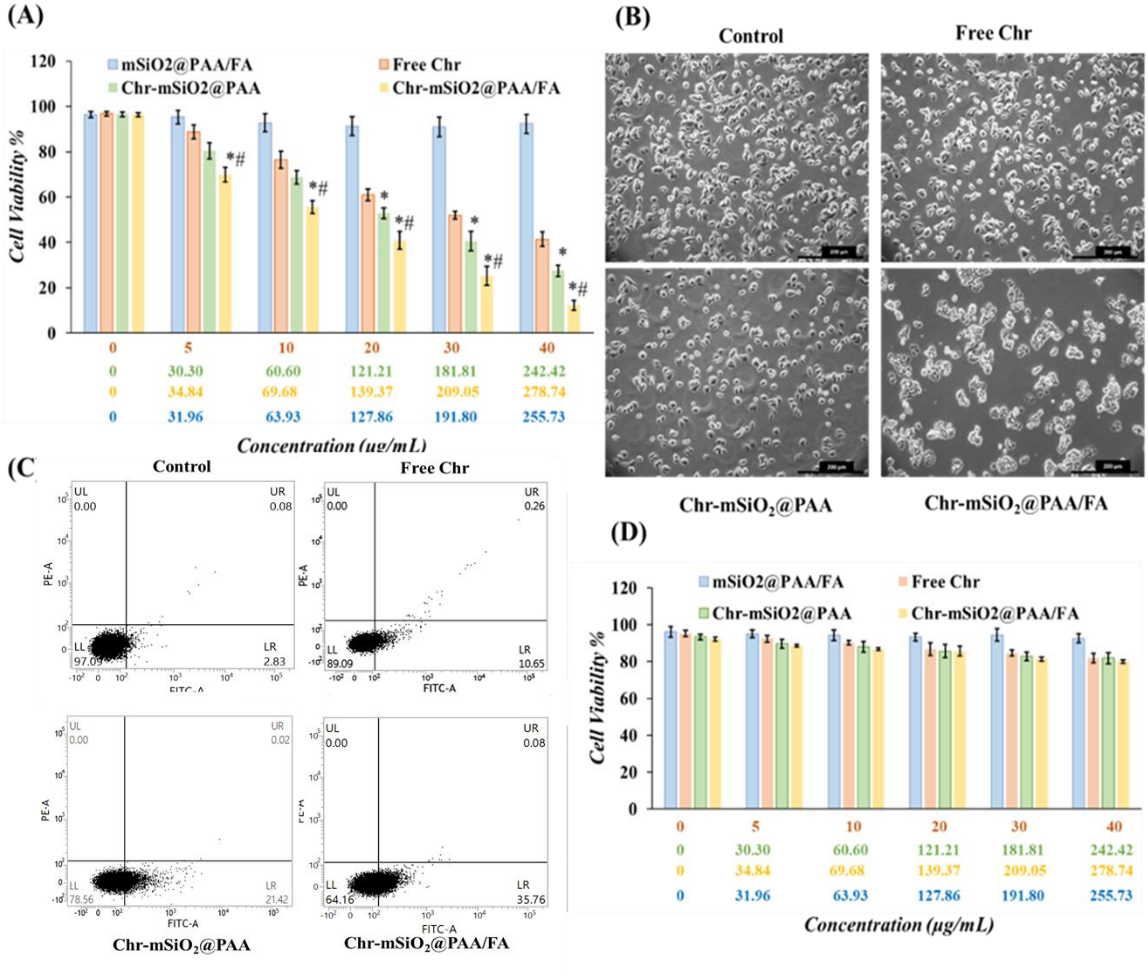

Figure 10: Cytotoxic nature of chrysin nanohybrid in the MCF-7 and NKE cells line: *Comparative study of cytotoxic ability of free Chr, Chr-mSiO$_2$@PAA and Chr-mSiO$_2$@PAA/FA by checking viabilities of (A) MCF-7 cells and (D) NKE cells after incubation with different concentrations of free Chr, Chr-mSiO$_2$@PAA and Chr-mSiO$_2$@PAA/FA for 24 h. Data are represented as mean ± SD (n = 5) where "*" and "#" represent significant differences with respect to chrysin and Chr-mSiO$_2$-PAA-treated groups, respectively, ($P^* < 0.05$, $P\# < 0.05$). (B) Optical microscopic images of MCF-7 cells*

incubated with free Chr, Chr-mSiO$_2$@PAA and Chr-mSiO$_2$@PAA/FA for 24 h (scale bar: 200 μm). (C) Detection of free Chr, Chr-mSiO$_2$@PAA and Chr-mSiO$_2$@PAA/FA induced apoptosis on MCF-7 cells via Annexin V-FITC staining. Dual parameter dot plot of FITC-labelled Annexin V fluorescence (x-axis) has been shown in logarithmic fluorescence intensity.

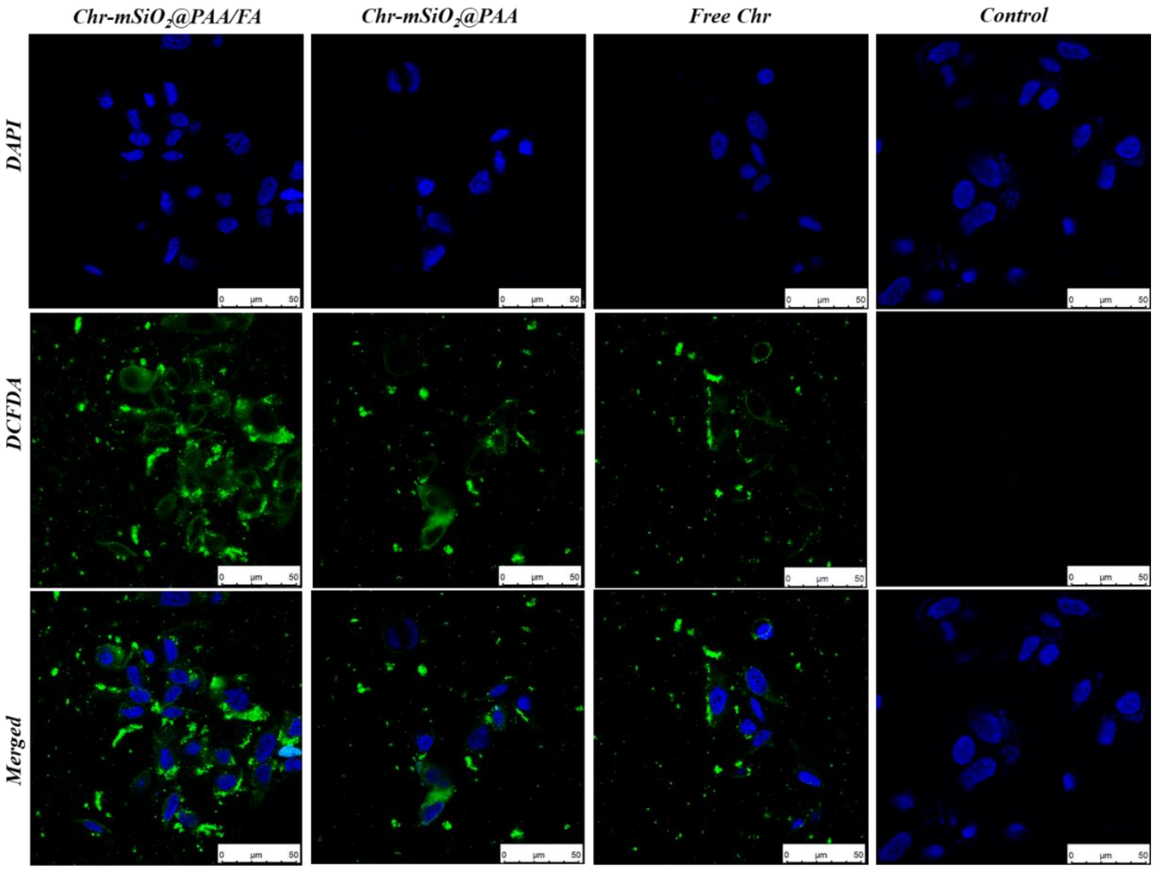

Figure 11: *Confocal laser scanning microscopic images defining free Chr, Chr-mSiO$_2$@PAA and Chr-mSiO$_2$@PAA/FA-treated induced apoptosis in MCF-7 cells via Annexin V-FITC staining. Scale bar: 50 μm.*

5.4.6. Chrysin nano-conjugates imposed changes in oxidative status of MCF-7 cells

In search of probable molecular mechanism behind selective cytotoxicity of chrysin-mSiO$_2$ nanodevice against MCF-7, we studied oxidative status of treated MCF-7 cells. Acknowledging the fact that increased cellular ROS unequivocally promotes intracellular oxidative stress, disturbing fine balance of cellular redox system, we performed DCFDA-assisted investigation of generated ROS in treated MCF-7 cells. Flow-cytometry (Figure 12A) as well as confocal laser scanning microscopy (Figure 12C) were performed to examine DCFDA-fluorescence.

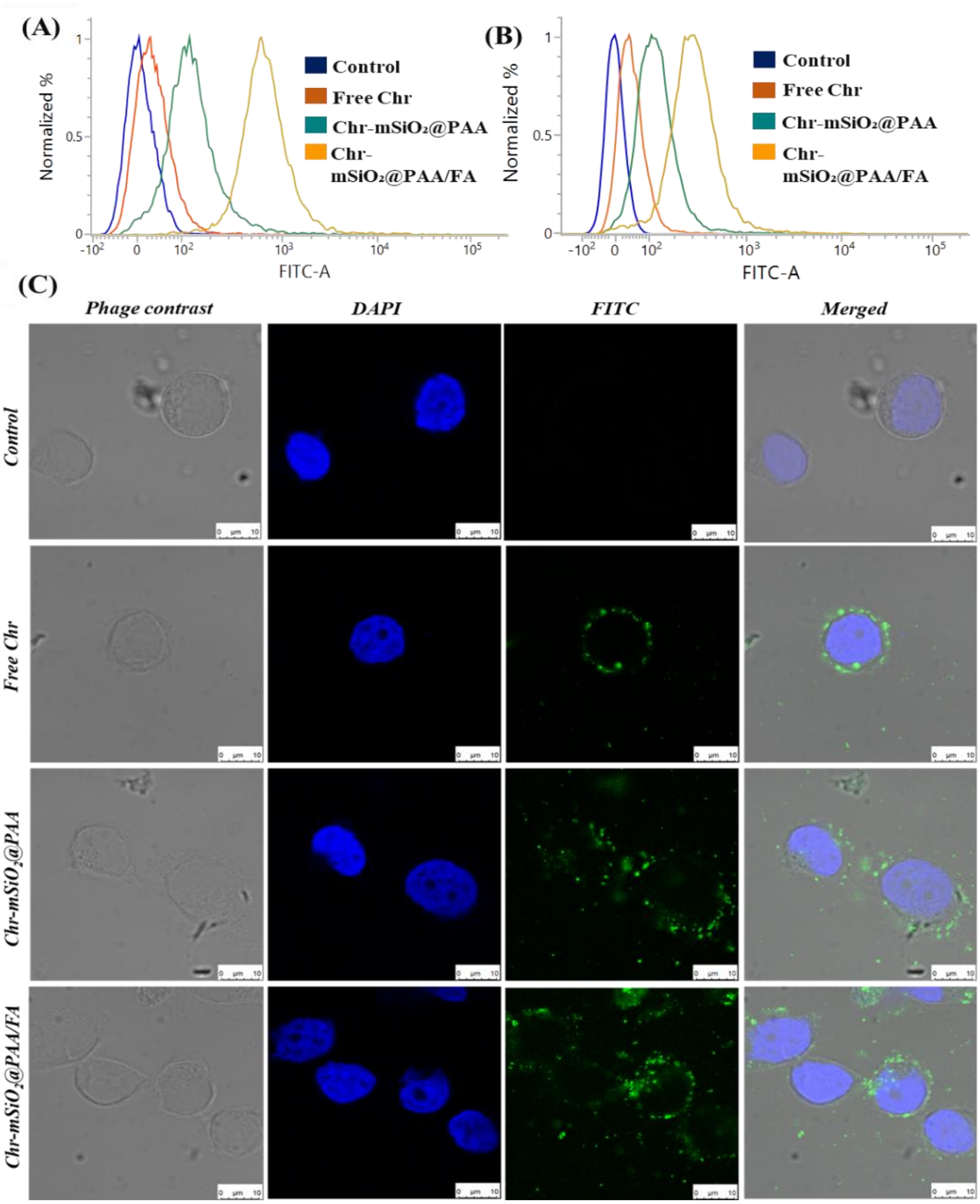

Figure 12: Chrysin nanohybrid treatment-mediated changes in intracellular ROS and mitochondrial matrix potential: *Flow cytometric analyses of changes in (A) ROS content and (B) mitochondrial potential in MCF-7 cells upon treatment with free chrysin, Chr-mSiO$_2$@PAA and Chr-mSiO$_2$@PAA/FA. (C) Validation of excess ROS generation by confocal laser scanning microscopy. Scale bar: 10 μm.*

Inline, it is well known that excessive cellular ROS can increase mitochondrial membrane porosity reducing mitochondrial membrane potential (MMP). Hence, a study of relative change in MMPs of treated MCF-7 cells was performed by JC-1 staining and further sorting of cells on the basis of fluorescence intensity. From the aforementioned experiments, it was found that Chr-mSiO$_2$@PAA/FA was most potent to induce excessive ROS enhancement (Figure 12A) and MMP disruption (Figure 12B) in MCF-7 cells in contrast to Chr-mSiO$_2$@PAA and free chrysin respectively.

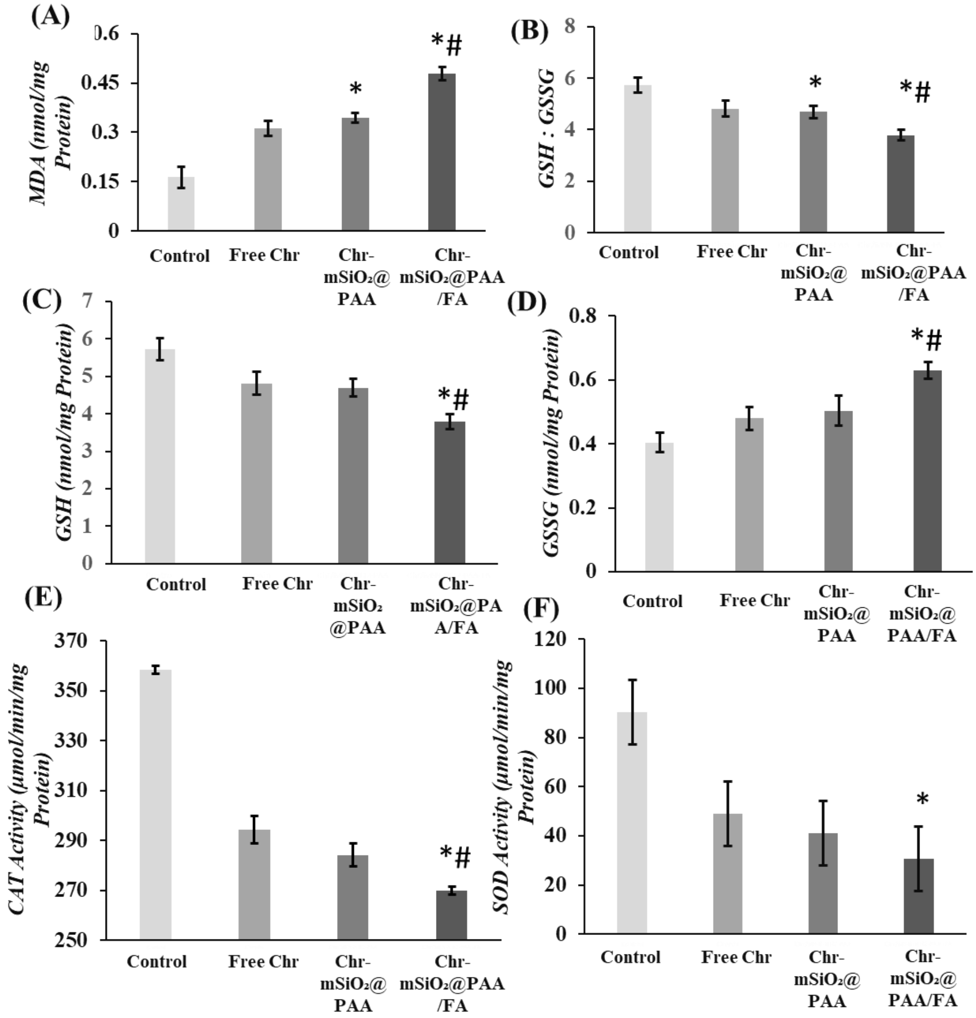

Figure 13: ***Oxidative status free Chr, Chr-mSiO$_2$@PAA and Chr-mSiO$_2$@PAA/FA-treated MCF-7 cells:*** *Spectrophotometric detection of (A) intracellular MDA content, (B) GSH to GSSG ratio, (C) GSH content, (D) GSSG content, (E) CAT activity and (F) SOD activity in treated MCF-7 cells.*

Apart from cellular ROS content, control and treated MCF-7 cells were also checked for their relative extent of protein carbonylation, GSH to GSSH ratio and catalytic activities of CAT as well as SOD. Cells exposed to Chr-mSiO$_2$@PAA/FA, showed lowest GSH:GSSG ratio along with significantly uplifted level of MDA content. Additionally, both CAT and SOD enzyme activities were highly compromised in Chr-

$mSiO_2$@PAA/FA-treated MCF-7 cells ensuring a cellular status of compromised redox system (Figure 13).

5.4.7. Chr-$mSiO_2$@PAA/FA can manipulate cell cycle progression in MCF-7

Motivated by the observations, we were curious to know whether Chr-$mSiO_2$@PAA/FA could modulate cell cycle distribution in MCF-7. Besides, chrysin has already been assigned to work as a cell cycle arresting agent according to the experiments performed elsewhere (Weng, Ho, and Lin 2005). When treated with Chr-$mSiO_2$@PAA/FA, distribution of MCF-7 cells exhibited stalled progression at G_0/G_1 stage in comparison with control group having lowered population of MCF-7 cells at G_0/G_1 phase (Figure 14A-14B).

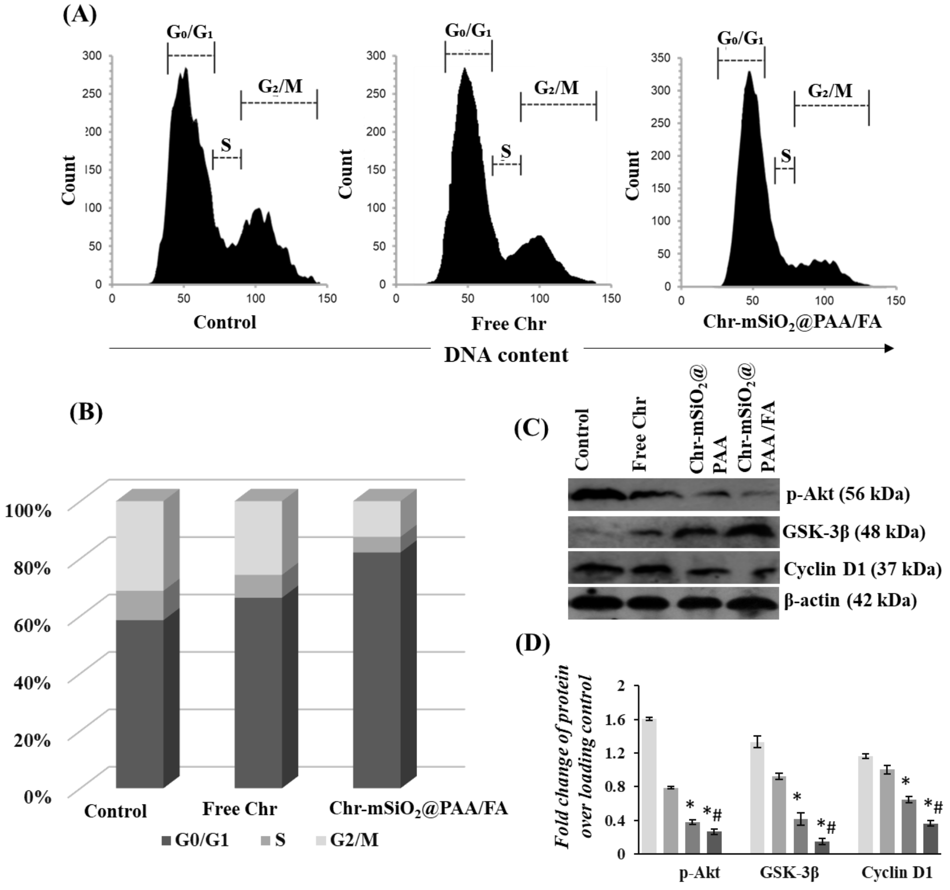

Figure 14: ***Cell cycle modulation by chrysin nanohybrid:*** *(A-B) Effect of free chrysin and Chr-$mSiO_2$-PAA/FA upon cell cycle progression of MCF-7 cells. (C) Immunoblot analysis of phospho-Akt, GSK-3β and cyclin-D1. β-actin was used as an internal control. (E) Densitometric analysis of the respective immunoblots. Data are representative of three individual experiments (n=3). "*" and "#"*

represent significant differences with respect to chrysin and Chr-mSiO$_2$-PAA-treated groups, respectively, ($P < 0.05$, $P\# < 0.05$).*

Thus, like free chrysin, mSiO$_2$-nanoconjugate of chrysin were found to impose G_0/G_1 arrest. However, it also must be noted that mSiO$_2$ incorporation and subsequent FA-tagging has remarkably increased the efficiency of free chrysin to impose cell cycle arrest *in vitro*.

5.4.8. Chrysin-nanoconjugates induced apoptosis in MCF-7 cells by checking cell cycle progression & cellular survival

One of the prime proteins that regulates cell survival and cellular growth by modulating cell cycle is Akt. Hence, often in several cancer types Akt is found to be elevated translationally (Shimura et al., 2012). Upon phosphorylation Akt gets activated which promotes cell cycle progression by phosphorylation-mediated cyclin D1 upregulation and subsequent inactivation of GSK-3β. In response to growth factors, cyclin D1 is considered as a chief regulator of cell cycle transition from G_1 to S phase in somatic cells (Neganova and Lako, 2008). Thus, inspired by the observation that chrysin-nanoconjugates can cause G_0/G_1 arrest *in vitro,* we checked translational expression of p-Akt and its downstream GSK-3β and cyclin D1 (Figure 14C-14D). Expression of both p-Akt and cyclin D1 were higher enough in control MCF-7 cells which were reduced significantly upon chrysin treatment, and even more after Chr-mSiO$_2$@PAA/FA treatment. Later on, we checked the translational expression of GSK-3β. Expression of GSK-3β was lowest in control MCF-7 cells and its expression was uplifted in treated groups being highest among Chr-mSiO$_2$@PAA/FA treated cells.

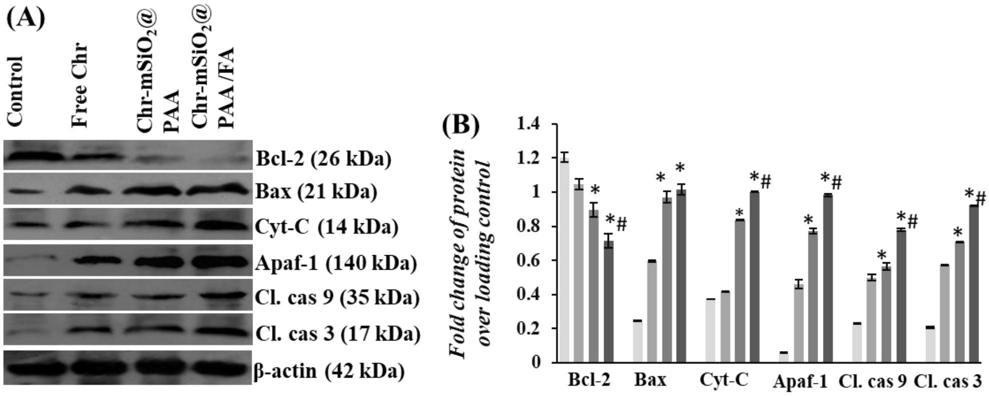

***Figure 15:** **Translational expressions of molecules related to intrinsic apoptosis pathway.** (A) Representative immunoblots of Bcl-2, Bax, cytochrome C, Apaf-1, cleaved caspase 9 and cleaved caspase 3. β-actin was used as an internal control. (B) Densitometric analysis of the respective immunoblots. Data*

are representative of three individual experiments (n=3). "" and "#" represent significant differences with respect to chrysin and Chr-mSiO$_2$-PAA-treated groups, respectively, ($P* < 0.05$, $P\# < 0.05$).*

p-Akt as well as increased ROS, both are capable of shifting balance between the antiapoptotic and pro-apoptotic cell machineries. Hence, we have also checked the expression of proapoptotic protein Bax and that of antiapoptotic protein Bcl-2 (Figure 15A-15B). It was found that chrysin enhances the ratio of Bax to Bcl-2 protein levels in MCF-7 cells. Following this observation, we have also studied the changes in translational expression of the components of intrinsic apoptosis, i.e., cytochrome-C, Apaf-1, cleaved caspase 9 and caspase 3 upon chrysin-nano-formulation treatment. All these proteins showed increased expression after chrysin treatment compared to untreated MCF-7 cells, suggesting possible action of chrysin through intrinsic apoptosis. The result indicated that effectivity of free chrysin was magnified further after its nano-encapsulation and further by FA functionalization.

5.4.9. NAC diminished Chr-mSiO$_2$@PAA/FA-imposed cell death in MCF-7 cells

NAC pretreatment inhibited excess intracellular ROS generation in Chr-mSiO$_2$@PAA/FA treated MCF-7 cells (Figure 16A).

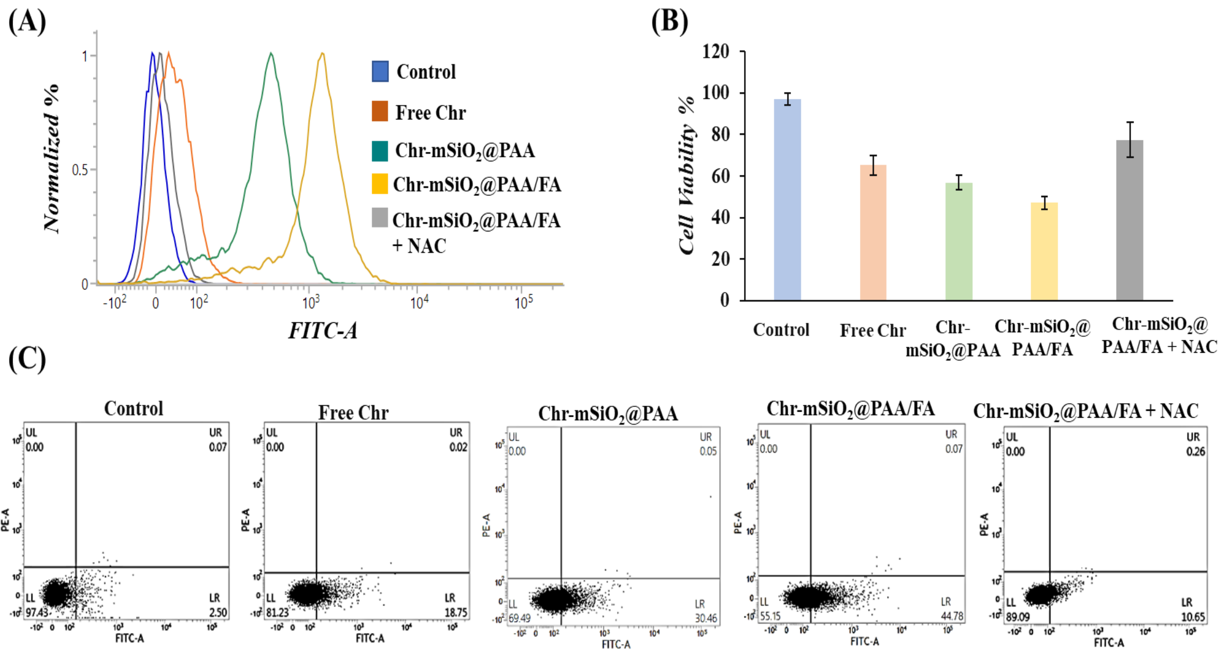

Figure 16: ***Effect of NAC pre-treatment:*** *(A) Changes in intracellular ROS content upon NAC pretreatment. (B) Effect of NAC pretreatment upon cell viability of MCF-7 cells. (C) (E) Effect of cellular apoptosis upon MCF-7 cells upon NAC treatment with or without LC$_{50}$ dose of Chr-mSiO$_2$-PAA/FA.*

Also, existing reports suggest that ROS can uplift of GSK-3β expression which further capable of decreasing cyclin D1 (Takahashi-Yanaga and Sasaguri, 2008). If so, our motto was to find out whether the chrysin-mediated enhanced ROS generation is the key ruler imparting the antineoplastic capacity to Chr-mSiO$_2$@PAA/FA. It was observed that NAC pretreated cells dramatically showed higher viability percentage even after treating with most potent Chr-mSiO$_2$@PAA/FA (Figure 16B). So, we hypothesized the obvious outcome would be reduced apoptosis in NAC pretreated MCF-7. Thus, to evaluate our perception, we studied percentage of apoptotic cells through Annexin V-FITC staining. It was found that NAC pretreatment was potent enough to reduce the overall apoptotic MCF-7 cell population significantly even in presence of highly potent Chr-mSiO$_2$@PAA/FA (Figure 16C). Alongside, we have also checked the translational expression of key apoptotic proteins of intrinsic pathway (Figure 17A-17B). It was found that the expression of antiapoptotic Bcl-2 was significantly higher in NAC pretreated cells accompanied by a decreased expression of Bax and cleaved caspase-3. Altogether, these results suggest that change in redox balance in MCF-7 cells by higher ROS generation is the chief operational hub controlling the antitumor activity of chrysin.

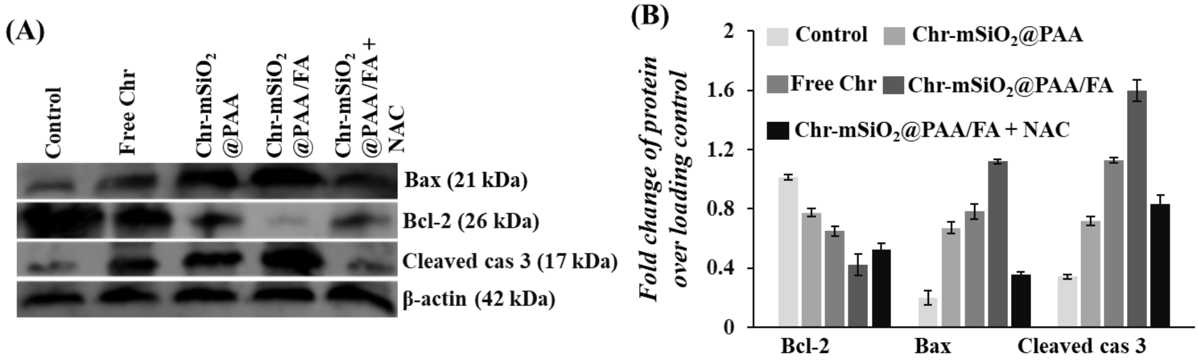

Figure 17: ***Effect of NAC pretreatment on translational expressions of molecules related to intrinsic apoptosis pathway in chrysin nanohybrid-treated MCF-7 cells:*** *(A) Representative immunoblots of Bax, Bcl-2 and cleaved caspase 3 upon NAC pretreatment. (D) Densitometric analysis of immunoblots of aforementioned molecules. Here, the data are representatives of three individual experiments (n=3) where "*" and "#" represent significant differences with respect to chrysin and Chr-mSiO$_2$-PAA-treated groups, respectively, (P* < 0.05, P# < 0.05).*

5.4.10. PAA-capping and FA-fabrication ensure increased chrysin uptake in tumor tissue

During HPLC, linearity of calibration curve for chrysin has been confirmed by $R^2 = 0.9998$. LOD (limit of detection) and LOQ (limit of quantification) were respectively found to be 1.16 % and 3.52 %. The retention time for chrysin was 3.4 min; whereas, the recovery percentage for chrysin solution of 3, 5, 15, 30 and 50 µg/ml concentrations were calculated respectively as 95.13 %, 102.77 %, 101.89 %, 98.45 % and 100.37 %. Accumulation of chrysin within tumor tissue has been shown to be improved in Chr-mSiO$_2$@PAA (from 9.96 µg/gm) compared to free chrysin (3.08 µg/gm tissue homogenized). Moreover, functionalization of Chr-mSiO$_2$@PAA with folic acid has further increased tissue accumulation of chrysin to 18.27 µg/gm tissue homogenized suggesting FA-guided selective enhanced drug accumulation and release at tumor site (Fig. 18A).

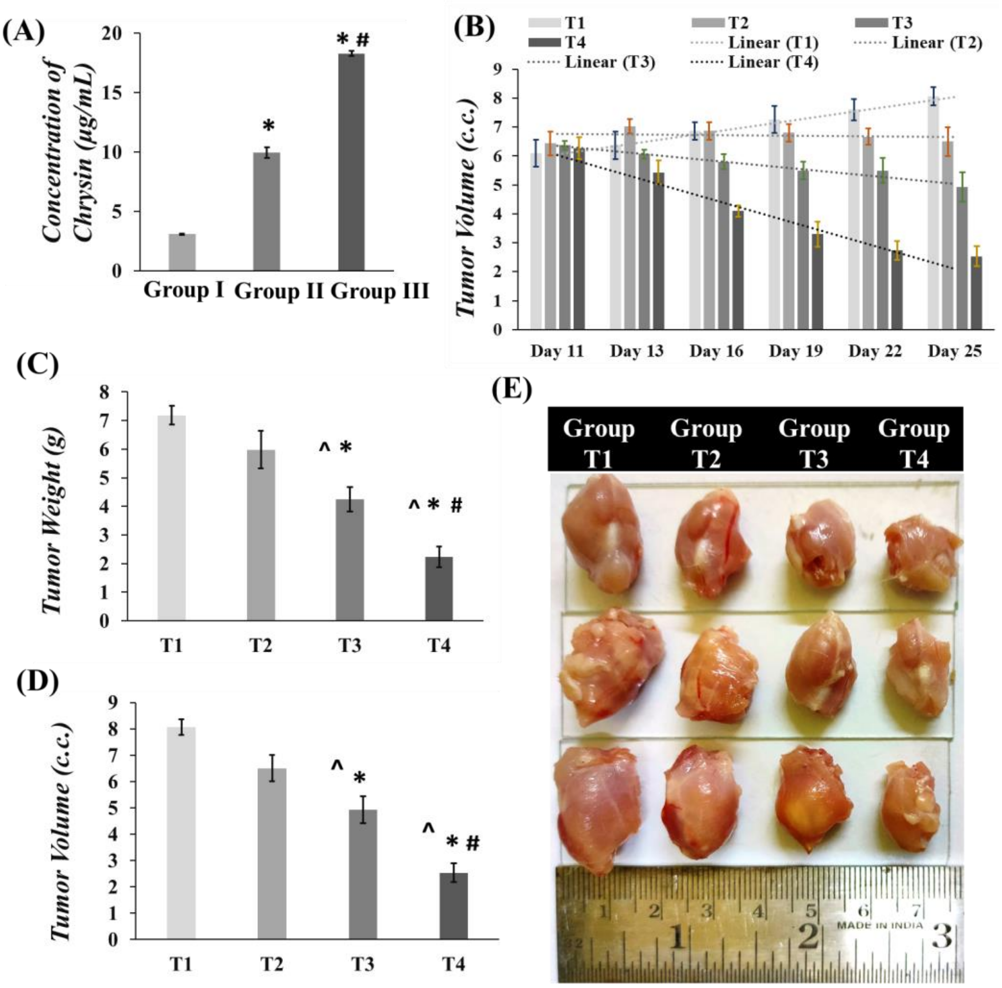

Figure 18: ***In vivo anti-tumor activities of chrysin nanohybrids: (A)*** *Detection of tissue absorption of chrysin in tumor-bearing mice treated with Chr, Chr-mSiO$_2$@PAA and Chr-mSiO$_2$@PAA/FA. "*" and "#" represent significant differences with respect to free Chr treated, Chr-mSiO$_2$-PAA treated and untreated groups respectively ($P* < 0.05$, $P\# < 0.05$ and $P\^{} * < 0.05$). (B) Reduction in tumor volume over the period of treatment. In vivo anti-tumorigenic activity of free Chr, Chr-mSiO$_2$@PAA and Chr-*

$mSiO_2$@PAA/FA explained through overall reduction in (C) tumor weight and (D) tumor volume. (E) Representative photographs of dissected tumor tissues showing overall reduction in tumor size.

5.4.11. $mSiO_2$@PAA/FA encapsulation uplifts *in-vivo* antitumor efficacy of free chrysin

Antitumor efficacy of chrysin has been shown to improve with $mSiO_2$-encapsulation when compared to its non-encapsulated free form. Tumor volume was found to increase gradually with time in T1 group where the animals were left untreated. Rest of the animals receiving intravenous treatment showed gradual decrease in tumor volume over the treatment period of two weeks where treatment with Chr-$mSiO_2$@PAA/FA was found to be most effective (Figure 18B). Additionally, at the day of dissection, the volume and mass of tumors were highest among the untreated animals. Rest of animals receiving chrysin injection either in free form or in $mSiO_2$-encapsulated form showed significant reduction in both tumor mass and volume (Figure 18C-18D). Reduction was highest among the animals of T4 group (Figure 18E).

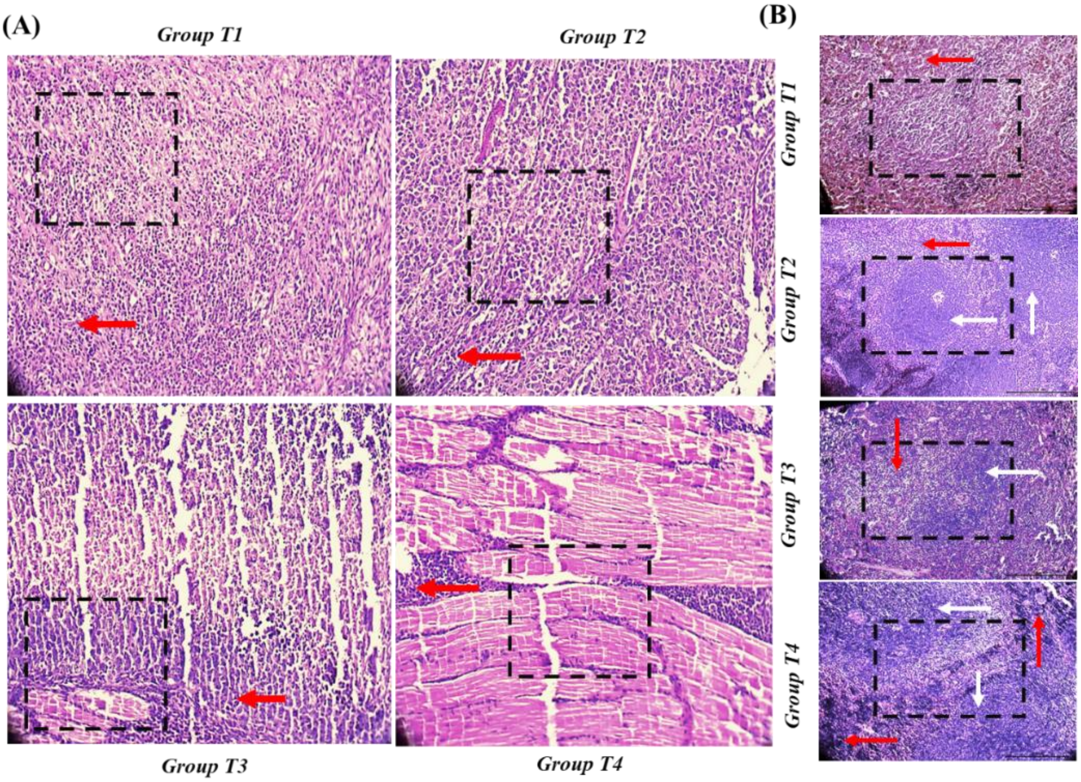

Figure 19:* *Histological analysis of resected tissues from tumor-bearing mice: *Microscopic assessment of H & E-stained micro tissue sections of (A) tumor tissues tissues (here, red arrows demarcate multinucleated cells and black-dotted selected areas signify tumor tissue architecture gradually resembling normal muscle architecture with subsequent higher grade of nanohybridization of*

chrysin) and (B) splenic tissues (here, red and white arrows demarcate red pulp and white pulp of spleen with black-dotted selected areas signifying extent tumor-induced immunological response through enlargement of splenic white pulp) under 20X magnification

Moreover, the findings from the H & E-stained sections of tumor tissues from all four experimental groups (T1-T4) were also in line (Figure 19A). Normal skeletal muscle tissue architecture was completely lost in the tumors of group T1 with several multinucleated cells. This condition was slightly improved in the tumor tissues resected from group T2, where tissue architecture was restored a bit but still there were enormous number of nuclei. Visible reduction in nuclei as well as restoration of muscle tissue architecture can be marked at first in tumors isolated from group T3. However, best recovery condition was found in tumors collected from Chr-mSiO_2@PAA/FA-treated mice (T4 group) where tissue architecture was good enough to recognize its muscle tissue origin with significantly lesser number of nuclei. These observations not only illustrate *in vivo* antitumor activity of chrysin but also suggest uplifted antitumor efficacy of chrysin due to mSiO_2-encasing and FA-guided tumor specific routing.

Furthermore, splenic profile of treated animals was examined (Figure 20A-20B). EAC is known to induce splenomegaly and splenic WBC infiltration in tumor-bearing mice that serve as markers for existing tumor load *in vivo* (Ghosh et al., 2022a). In free chrysin treated mice, EAC-induced splenomegaly was found to be reduced to great extent probably due to the anti-inflammatory effects of chrysin (Xiao et al., 2016) as well as reduction in tumor load; whereas reduction in splenomegaly and associated distortion in splenic tissue architecture (Figure 19B) in Chr-mSiO_2@PAA and Chr-mSiO_2@PAA/FA-treated mice are thought be a result of tumor load reduction.

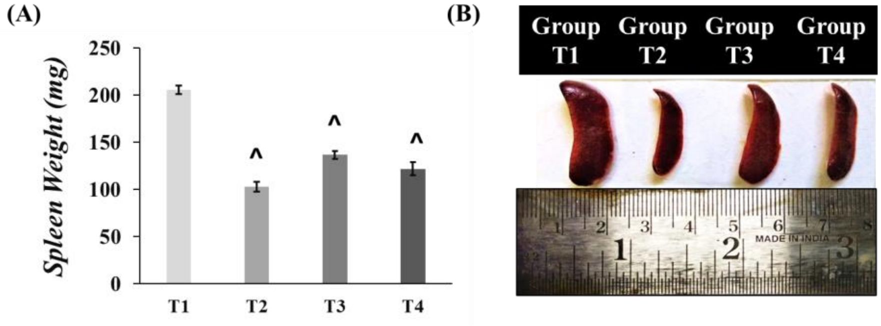

Figure 20: ***Changes in splenic profile explained:*** *by (A) change in splenic mass and (B) representative photographs of spleens removed from different experimental mice. "^" represents significant difference with respect to untreated group (P^ < 0.05).*

5.4.12. Chrysin nanoconjugates capable of inducing intrinsic apoptosis *in vivo*

To check whether decrease in tumor size and volume is due to activation of intrinsic apoptosis pathway within tumor tissues, we compared immunohistochemical expression of two key caspases typical to intrinsic apoptosis pathway, i.e., caspase 9 and caspase 3 (Figure 21). Expressions of both caspase 9 and caspase 3 were found to be elevated in treated tumor tissues in comparison to untreated ones. Expressions of both of these proteins were highest among the tumor tissues collected from group T4. This emphasizes increased efficiency of chrysin nanoconjugates upon FA functionalization for equivalent amount of chrysin. Also, the data suggest that the reduction in tumor size and mass is due to intrinsic apoptosis which lies in line with the findings from the *in vitro* observations.

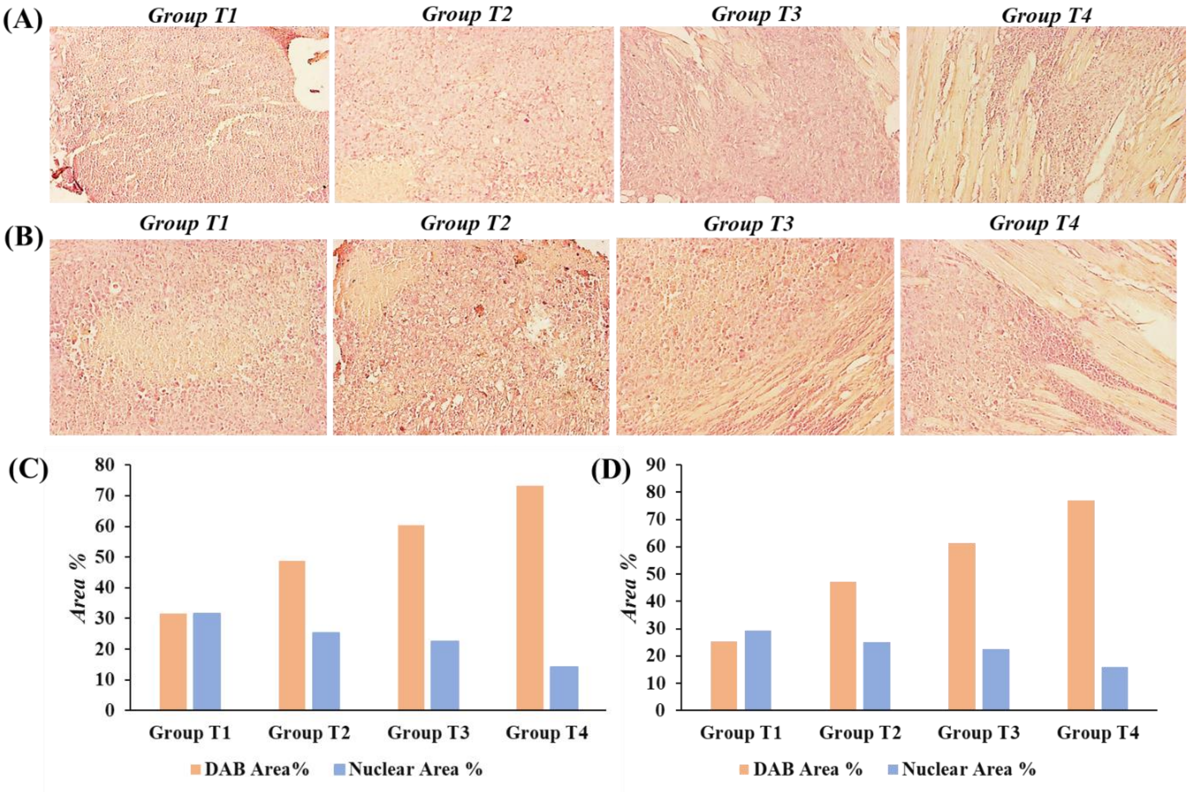

Figure 21: *Immunohistochemical detection of (C) caspase 9 and (D) caspase 3 in resected tumor tissue section viewed under 20X magnification of optical light microscope.*

5.4.13. Chrysin nanoconjugates are non-toxic to vital organs

The aim cancer nano-therapeutics is to gain cancer cell-specificity *in vivo* to minimalize unnecessary damage to healthy tissues. Hence, a nanohybrid should be smart enough to distinguish between cancer cells and healthy non-cancerous cell. Thus, we checked nanohybrid induced damage to heathy vital organs by a series of biochemical assays and histological evaluation. Hepatic serum markers such as ALP and ALT of animals belonging to group S2-S4 were within normal range. Similar remark was made by examining serum renal markers such as level of creatinine and BUN (Figure 22A-22D).

Additional histological examinations of H & E-stained pulmonary, hepatic, renal and cardiac tissue sections exhibited no significant sign of abnormality (Figure 22E). Thus, Chr-mSiO$_2$@PAA/FA can be regarded as safe for the purpose of *in vivo* treatment.

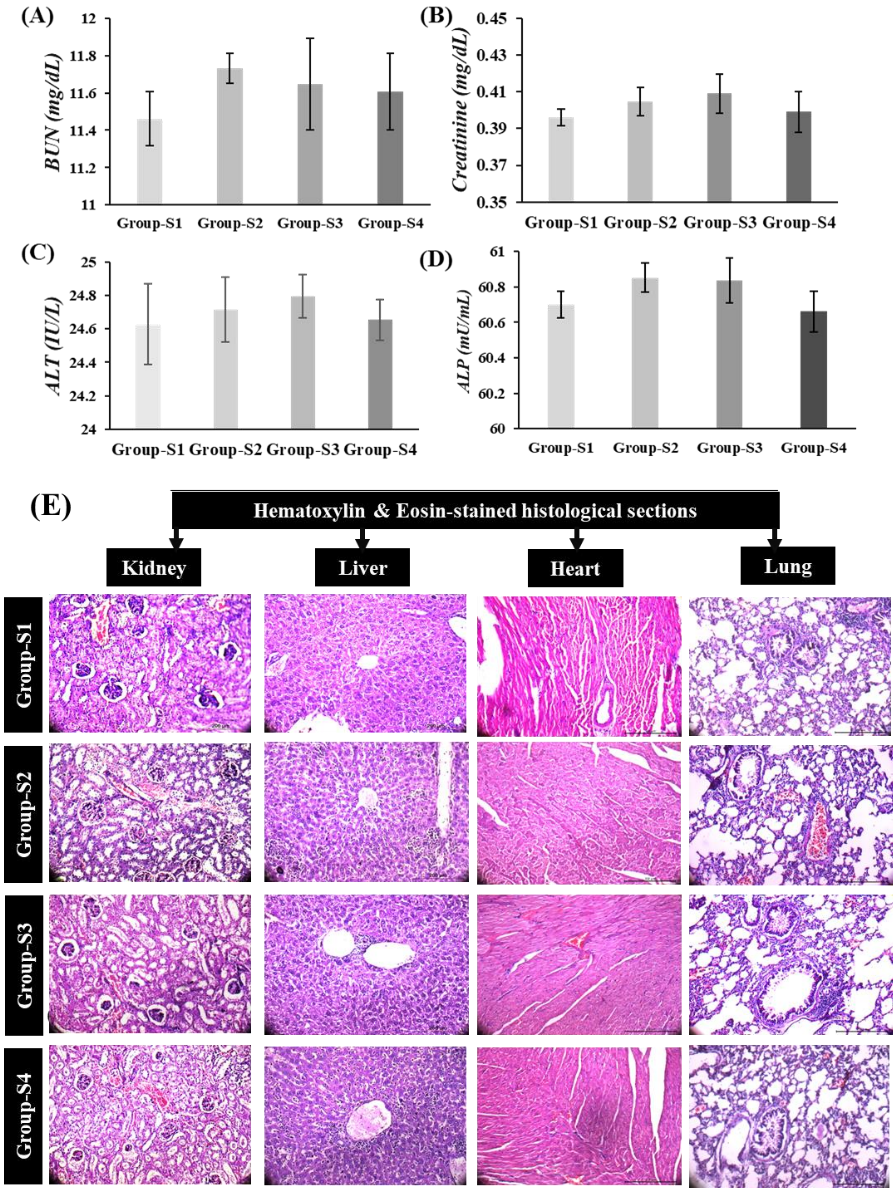

Figure 22: ***Analysis of systemic toxicity by assessing serum renal and hepatic parameters:*** *Estimation of serum (A) BUN, (B) Creatinine, (C) ALT and (D) ALP in different experimental groups of*

mice. Data are represented mean ± SD (n = 3). (E) Histological assessment of H & E-stained microsections of murine kidney, liver, heart and lung from different experimental groups with bright field microscopy under 20X magnification.

5.5. Conclusion

In summary, we have demonstrated the prospect of attaching nontoxic PAA as pore blocking agent on $mSiO_2$ to effectively control the release of uploaded cargo according to pH-gradient (Figure 23).

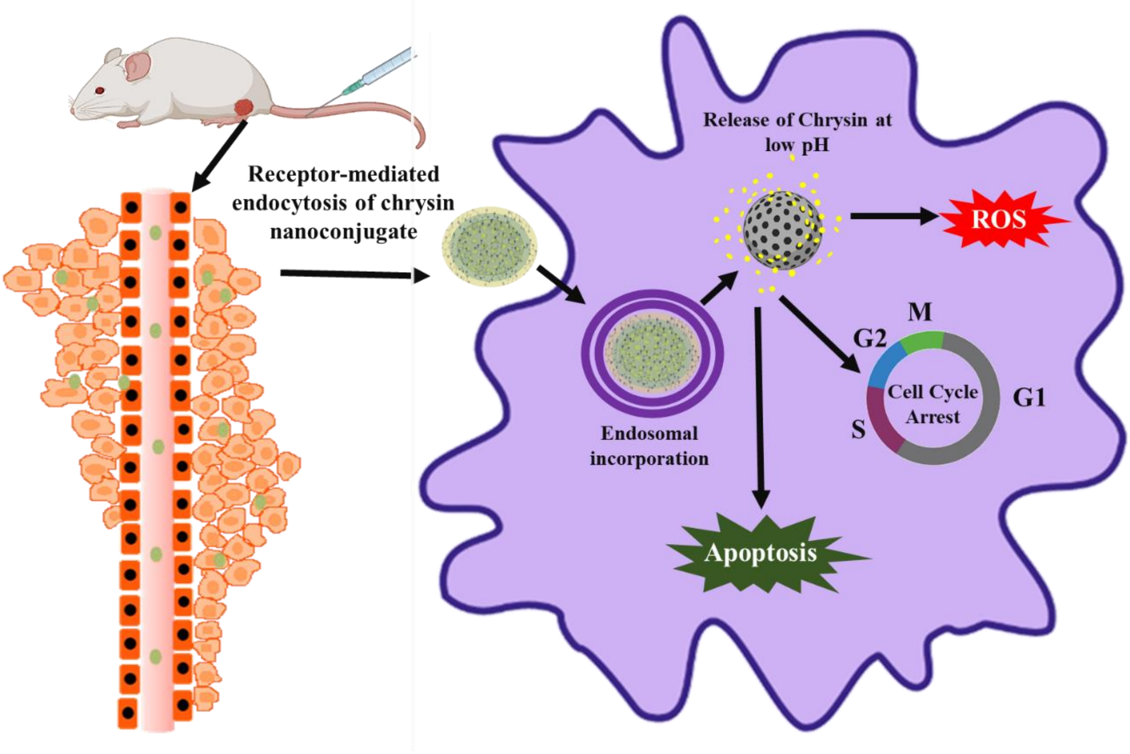

Figure 23: *Generalized scheme of anticancer activity exhibited by Chr-$mSiO_2$-PAA/FA.*

PAA capping tightly sealed the pores of $mSiO_2$ so that at neutral pH (7.4) negligible premature cargo release can be achieved fulfilling one of the important targets in nanomedicine to prevent uncontrolled drug release and associated side effects. PAA was selected to facilitate the covalent functionalization to the mesoporous silica scaffold through acid-liable amide bond formation. Moreover, the pH-triggered behavior of this hybrid system may bring interesting future applications. Furthermore, this nanostructure with mesoporous silica scaffold core was chemically vectorized with FA offered selective and higher cargo release capacity for chrysin. According to flow cytometry analysis, significant improvement was noticed in cellular uptake of FA-functionalized $mSiO_2$ nanodevice due to receptor-mediated endocytosis in MCF-7 cell lines. *In vivo* experiments in Swiss Albino mice demonstrated higher chrysin accumulation in the tumor tissue following PAA capping and FA functionalization; whereas, healthy cells of vital organs were found unaffected. Hence, FA vectorization allowed increased selectivity and specificity toward cancer cells. Lastly, the issue with chrysin being used as a potent anticancer agent due to its higher hydrophobicity has been smartly overcome by entrapping it inside the pores of $mSiO_2$. Thus, in general the bioavailability and anticancer functionality of chrysin was boosted many folds after its nanoformatting. Therefore, in view of non-toxic nature, an excellent drug release capacity, an enhanced and selective cellular uptake within the tumor tissue of living organisms, effective anticancer activities of such chrysin nanoformulation (Chr-$mSiO_2$@PAA/FA) opens up a highly promising pathway for effective breast cancer treatment.

5.6. References

Cheng, Wei, Junpeng Nie, Lv Xu, Chaoyu Liang, Yunmei Peng, Gan Liu, Teng Wang, Lin Mei, Laiqiang Huang, and Xiaowei Zeng. 2017. "pH-sensitive delivery vehicle based on folic acid-conjugated polydopamine-modified mesoporous silica nanoparticles for targeted cancer therapy." *ACS applied materials & interfaces* 9 (22):18462-18473.

Deshayes, Stephanie, Horacio Cabral, Takehiko Ishii, Yutaka Miura, Shutaro Kobayashi, Takashi Yamashita, Akira Matsumoto, Yuji Miyahara, Nobuhiro Nishiyama, and Kazunori Kataoka. 2013. "Phenylboronic acid-installed polymeric micelles for targeting sialylated epitopes in solid tumors." *Journal of the American Chemical Society* 135 (41):15501-15507.

Garcia-Bennett, Alfonso, Matthias Nees, and Bengt Fadeel. 2011. "In search of the Holy Grail: folate-targeted nanoparticles for cancer therapy." *Biochemical pharmacology* 81 (8):976-984.

Ghosh, Noyel, Sharmistha Chatterjee, Debanjana Biswal, Nikhil Ranjan Pramanik, Syamal Chakrabarti, and Parames C Sil. 2022. "Oxidative stress imposed in vivo anticancer therapeutic efficacy of novel imidazole-based oxidovanadium (IV) complex in solid tumor." *Life Sciences* 301:120606.

Giret, Simon, Michel Wong Chi Man, and Carole Carcel. 2015. "Mesoporous-Silica-Functionalized Nanoparticles for Drug Delivery." *Chemistry–A European Journal* 21 (40):13850-13865.

Jabbari, Sepideh, Aliyeh Ghamkhari, Yousef Javadzadeh, Roya Salehi, and Soodabeh Davaran. 2018. "Doxorubicin and chrysin combination chemotherapy with novel pH-responsive poly [(lactide-co-glycolic acid)-block-methacrylic acid] nanoparticle." *Journal of Drug Delivery Science and Technology* 46:129-137.

Khosravian, Pegah, Mehdi Shafiee Ardestani, Mehdi Khoobi, Seyed Naser Ostad, Farid Abedin Dorkoosh, Hamid Akbari Javar, and Massoud Amanlou. 2016. "Mesoporous silica nanoparticles functionalized with folic acid/methionine for active targeted delivery of docetaxel." *OncoTargets and therapy* 9:7315.

Kundu, Mousumi, Sharmistha Chatterjee, Noyel Ghosh, Prasenjit Manna, Joydeep Das, and Parames C Sil. 2020. "Tumor targeted delivery of umbelliferone via a smart mesoporous silica nanoparticles controlled-release drug delivery system for increased anticancer efficiency." *Materials Science and*

Engineering: C 116:111239.

Kundu, Mousumi, Pritam Sadhukhan, Noyel Ghosh, Sharmistha Chatterjee, Prasenjit Manna, Joydeep Das, and Parames C Sil. 2019. "pH-responsive and targeted delivery of curcumin via phenylboronic acid-functionalized ZnO nanoparticles for breast cancer therapy." *Journal of advanced research* 18:161-172.

Lu, Jie, Monty Liong, Zongxi Li, Jeffrey I Zink, and Fuyuhiko Tamanoi. 2010. "Biocompatibility, biodistribution, and drug-delivery efficiency of mesoporous silica nanoparticles for cancer therapy in animals." *Small* 6 (16):1794-1805.

Mishra, Snehasis, Krishnendu Manna, Utpal Kayal, Moumita Saha, Sauvik Chatterjee, Debraj Chandra, Michikazu Hara, Sriparna Datta, Asim Bhaumik, and Krishna Das Saha. 2020. "Folic acid-conjugated magnetic mesoporous silica nanoparticles loaded with quercetin: A theranostic approach for cancer management." *RSC advances* 10 (39):23148-23164.

Neganova, Irina, and Majlinda Lako. 2008. "G1 to S phase cell cycle transition in somatic and embryonic stem cells." *Journal of anatomy* 213 (1):30-44.

Sadhukhan, Pritam, Sukanya Saha, Krishnendu Sinha, Goutam Brahmachari, and Parames C Sil. 2016. "Selective pro-apoptotic activity of novel 3, 3′-(aryl/alkyl-methylene) bis (2-hydroxynaphthalene-1, 4-dione) derivatives on human cancer cells via the induction reactive oxygen species." *PloS one* 11 (7):e0158694.

Salinas, Yolanda, Carolin Hoerhager, Alba Garcia-Fernandez, Marina Resmini, Felix Sancenon, Ramon Matinez-Manez, and Oliver Brueggemann. 2018. "Biocompatible phenylboronic-acid-capped ZnS nanocrystals designed as caps in mesoporous silica hybrid materials for on-demand pH-triggered release in cancer cells." *ACS applied materials & interfaces* 10 (40):34029-34038.

Sargazi, Saman, Ushna Laraib, Mahmood Barani, Abbas Rahdar, Iqra Fatima, Muhammad Bilal, Sadanad Pandey, Rakesh K Sharma, and George Z Kyzas. 2022. "Recent trends in the mesoporous silica nanoparticles with rode-like morphology for cancer theranostics: a review." *Journal of Molecular Structure*:132922.

Sengupta, Somoshree, and Vamsi K Balla. 2018. "A review on the use of magnetic fields and ultrasound for non-invasive cancer treatment." *Journal of advanced research* 14:97-111.

Shimura, T, N Noma, T Oikawa, Y Ochiai, S Kakuda, Y Kuwahara, Y Takai, A Takahashi, and M Fukumoto. 2012. "Activation of the AKT/cyclin D1/Cdk4 survival signaling pathway in radioresistant cancer stem cells." *Oncogenesis* 1 (6):e12-e12.

Sun, Qinyan, Fengyu Liu, Zhenfu Wen, Jing Xia, Hongjuan Li, Yongqian Xu, and Shiguo Sun. 2022. "Combined effect of heat shock protein inhibitor geldanamycin and free radicals on photodynamic therapy of prostate cancer." *Journal of Materials Chemistry B* 10 (9):1369-1377.

Swift, Thomas, Linda Swanson, Mark Geoghegan, and Stephen Rimmer. 2016. "The pH-responsive behaviour of poly (acrylic acid) in aqueous solution is dependent on molar mass." *Soft matter* 12 (9):2542-2549.

Takahashi-Yanaga, Fumi, and Toshiyuki Sasaguri. 2008. "GSK-3β regulates cyclin D1 expression: a new target for chemotherapy." *Cellular signalling* 20 (4):581-589.

Walle, T, Y Otake, JA Brubaker, UK Walle, and PV Halushka. 2001. "Disposition and metabolism of the flavonoid chrysin in normal volunteers." *British journal of clinical pharmacology* 51 (2):143-146.

Wang, Kaili, Junya Lu, Jiali Li, Yinlu Gao, Yuling Mao, Qinfu Zhao, and Siling Wang. 2021. "Current trends in smart mesoporous silica-based nanovehicles for photoactivated cancer therapy." *Journal of Controlled Release* 339:445-472.

Wang, Lan, Yuhuan Zhang, Ying Han, Qi Zhang, Zhenfu Wen, Hongjuan Li, Shiguo Sun, Xin Chen, and Yongqian Xu. 2021. "Nanoscale photosensitizer with tumor-selective turn-on fluorescence and activatable photodynamic therapy treatment for COX-2 overexpressed cancer cells." *Journal of Materials Chemistry B* 9 (8):2001-2009.

Weng, Meng-Shih, Yuan-Soon Ho, and Jen-Kun Lin. 2005. "Chrysin induces G1 phase cell cycle arrest in C6 glioma cells through inducing p21Waf1/Cip1 expression: involvement of p38 mitogen-activated protein kinase." *Biochemical pharmacology* 69 (12):1815-1827.

Xiao, Xuecheng, Yangyang Liu, Manman Guo, Weidong Fei, Hongyue Zheng, Rongrong Zhang, Yan Zhang, Yinghui Wei, Guohua Zheng, and Fanzhu Li. 2016. "pH-triggered sustained release of arsenic trioxide by polyacrylic acid capped mesoporous silica nanoparticles for solid tumor treatment in vitro and in vivo." *Journal of biomaterials applications* 31 (1):23-35.

Xu, Shi, Bogdan Z Olenyuk, Curtis T Okamoto, and Sarah F Hamm-Alvarez. 2013. "Targeting receptor-mediated endocytotic pathways with nanoparticles: rationale and advances." *Advanced drug delivery reviews* 65 (1):121-138.

Xu, Xiaoyan, Chao Wu, Andi Bai, Xuan Liu, Huiling Lv, and Ying Liu. 2017. "Folate-functionalized mesoporous silica nanoparticles as a liver tumor-targeted drug delivery system to improve the antitumor effect of paclitaxel." *Journal of Nanomaterials* 2017.

Zeng, Yi-Bo, Nan Yang, Wei-Sheng Liu, and Ning Tang. 2003. "Synthesis, characterization and DNA-binding properties of La (III) complex of chrysin." *Journal of Inorganic Biochemistry* 97 (3):258-264.

Summary

Summary

The current female population continues to experience mortality and morbidity due to breast cancer. Many ground-breaking studies in the field of cancer therapeutics have resulted in significant improvements in current therapeutic approaches, which taken together have improved disease prognosis day by day. From a clinical perspective, however, the only effective treatments for breast cancer are combinations of any two or three of the following: chemotherapy, radiotherapy, hormone replacement therapy, surgery, or any two or three of these. Even though such methods continue to be effective in eliminating cancer cells, they frequently cause unintended systemic harm to healthy body cells or become completely ineffective as a result of the development of resistance. We have concentrated on researching the anticancer effectivities of specific synthetic metallic compounds that are safe to use *in vivo* when used within the recommended dosage in order to prevent such treatment-related anomalies.

In contrast to platinum-containing metallodrug cisplatin, we have chosen vanadium-containing ones. In our first study, the anticancer effectivity of 1-allyl imidazole substituted oxidovanadium complex (IV) (VOL) against PR$^+$ breast carcinoma was observed. This compound was found to mitigate MCF-7 breast cancer cell proliferation by increasing intracellular ROS burden and decreasing cellular antioxidant system efficacy. Increased oxidative stress was found to sensitize cells for apoptosis both through mitochondrial dysfunction and extracellular modality. When checked in the murine system (Swiss Albino mice), VOL was implicated to exhibit anti-tumor efficacy replicating the same mechanistic approach as *in vitro*.

Another similar oxidovanadium complex (IV) with 1-methyl imidazole substitution (OVMI) was checked for its probable antineoplastic efficacy against more aggressive TNBC. It was observed to pose excessive intracellular oxidative load in addition to UPR-mediated ER stress *in vitro*. Besides, increased ROS-mediated mitochondrial dysfunction and Ca^{2+}-mediated mitochondrial swelling both offered OVMI-triggered apoptosis of human TNBC cell MDA-MB-231. Apart from that, OVMI was investigated to diminish the migratory properties of MDA-MB-231 cells along with the decrease in translational expressions of certain key metastatic markers. When observed *in vivo* a similar mechanistic approach was taken by OVMI.

When considering natural compounds, there are several phytochemicals with anticancer efficacies that can be used in this regard to mitigate off-target side effects along with effective anticancer shields. However, poor water solubility, lower gut absorption, and quick systemic clearance led to lower bioavailability of such phytochemicals. In our last chapter, we have described how a smart targeted nanocarrier can be designed that be effective in unloading drugs specifically at the target area only through pH responsiveness. This not only reduces off-target drug unloading but also increases the effectiveness of the concerned anti-cancer agent at the tumor site. Chrysin which has already been highlighted as an anticancer agent in many other scientific literatures, has been chosen as a model compound owing to very poor water solubility and bioavailability. Here, we have studied folic acid-guided targeted delivery of chrysin and its pH-dependent release from mesoporous silica nanocarrier specifically to breast cancer cells (having overexpressed folic acid receptor) limiting chances of off-target toxicity caused by conventional chemotherapy along with enhanced antineoplastic efficacy and effective tumor-regression capability.

Abbreviations

Abbreviations

AIF: Apoptosis inducing factor; ALP: Alkaline phosphatase; ALP: Alanine transferase; AMPK: AMP-activated protein kinase; ANOVA: Analysis of variance; ANT: Adenine nucleotide translocator; Apaf-1: Apoptotic protease activating factor 1; APTES: 3-aminopropyl triethoxysilane; ATF4/6: Activating transcription factor 4/6; ATG: Autophagy related protein; ATM: Ataxia-Telangiectasia mutated; Bax: Bcl-2 associated X protein; BC: Breast cancer; Bcl-2: B-cell lymphoma 2; BRCA1/2: Breast CAncer gene 1/2; BSA: Bovine serum albumin; BUN: Blood urea nitrogen; CAT: Catalase; CDK: Cyclin dependent kinase; CHOP: C/EBP homologous protein; CTAB: Cetyltrimethylammonium bromide; DAPI: 4’,6-diamidino-2-phenylindole; DCFDA: 2’.7’-dichlorofluorescein diacetate; DCIS: Ductal carcinoma in situ; DDS: Drug delivery system; DEE: Drug entrapment efficiency; DISC: Death inducing signaling complex; DLC: Drug loading capacity; DLS: Dynamic light scattering; DMEM: Dulbecco’s modified eagle media; DNA: Deoxyribonucleic acid; DR: Death receptor; EAC: Ehrlich ascites carcinoma; EDC.HCl: 1-(3-dimethylaminopropyl)-3-ethyl carbodiimide hydrochloride; EDTA: Ethylenediaminetetraacetic acid; eIF-2α: Eukaryotic initiation factor 2α; EPR: Enhanced permeability and retention; ER: Estrogen receptor; ER: Endoplasmic reticulum; ERO1α: ER oxidoreductase 1α; ERS: ER stress; FA: Folic acid; FBS: Fetal bovine serum; FITC: Fluorescein isothiocyanate; FTIR: Fourier-transform infrared; GRP78: Glucose -regulated protein 78; GSH: Reduced glutathione; GSSG: Oxidized glutathione; H & E: Hematoxylin and eosin; HRP: Horseradish peroxidase; HER2: Human epidermal growth factor receptor 2; HIF1α: Hypoxia inducing factor 1α; HPLC: High pressure liquid chromatography; HR: Hormone receptor; HSP: Heat shock protein; ICAM1: Intracellular adhesion molecule 1; IL: Interleukin; IRE1α: Inositol requiring enzyme 1α; JC1: 5.5.6.6’-tetrachloro-1.1’3.3’ tetraethylbenzimidzoylcarbocyanine iodide; LDH: Lactate dehydrogenase; PERK: Protein kinase R-like ER kinase; PR: Progesterone receptor; MCP: Monocyte chemoattractant protein; MDA: Malonaldehyde; MMP: Mitochondrial membrane potential; mSiO$_2$: Mesoporous silica nanoparticle; mTOR: Mammalian target of rapamycin; MTT: 3-(4, 5-dimethylthiazol-2-yl)-2,5-diphenyl tetrazolium bromide; NADPH: Reduced nicotinamide adenine dinucleotide phosphate; NF-κB: Nuclear factor κB; NHS: N-hydroxy succinimide; NOX: NADPH oxidase; NRF2: Nuclear factor erythroid 2-related factor 2; OVMI : mononuclear dipicolinic acid-1-mrthyl imidazole-based oxidovanadium (IV) complex; PAA: Polyacrylic acid; PARP: Poly-(ADP-ribose)polymerase; PBS: Phosphate buffered saline; PGC-1α: Peroxisome proliferator-activated receptor gamma coactivator 1α; PI: Propidium iodide; PI3K: Phosphoinositide 3-kinase; Rb: Retinoblastoma; RIPA: Radio immunoprecipitation assay buffer; ROS: Reactive oxygen species; RPMI: Roswell park memorial institute medium; SDS: Sodium dodecyl sulphate; SEM: Scanning electron microscope; SOD: Superoxide dismutase; TBS: Tris buffered saline; TEM: Transmission electron microscope; TEOS: Tetra ethoxy silane; TNBC: Triple negative breast carcinoma; TNF-α: Tumor necrosis factor α, TNFR: TNFα receptor; TRADD: TNFR associated death domain; TRAILR: TNF-related apoptosis inducing ligand receptor; TUNEL: terminal deoxynucleotidyl transferase dUTP nick end labeling; UPR: Unfolded protein response; VCAM1: Vascular cell adhesion molecule 1; VDAC: Voltage-dependent anion channel; VEGF: Vascular endothelial growth factor; VOL: mononuclear dipicolinic acid-1-allyl imidazole-based oxidovanadium (IV) complex; XBP1: X-box binding protein 1.

List of Publications

Original articles

1. **Ghosh, Noyel**, Sharmistha Chatterjee, Debanjana Biswal, Nikhil Ranjan Pramanik, Syamal Chakrabarti, and Parames C Sil. 2022. "Oxidative stress imposed in vivo anticancer therapeutic efficacy of novel imidazole-based oxidovanadium (IV) complex in solid tumor." *Life Sciences* 301:120606. doi: https://doi.org/ https://doi.org/10.1016/j.lfs.2022.120606

2. **Ghosh, Noyel**, Mousumi Kundu, Sumit Ghosh, Abhishek Kumar Das, Samhita De, Joydeep Das, and Parames C Sil. 2023. "pH-responsive and targeted delivery of chrysin via folic acid-functionalized mesoporous silica nanocarrier for breast cancer therapy." International Journal of Pharmaceutics 631:122555. doi: https://doi.org/10.1016/j.ijpharm.2022.122555

3. **Sadhukhan, Pritam**, Mousumi Kundu, Sharmistha Chatterjee, Noyel Ghosh, Prasenjit Manna, Joydeep Das, and Parames C Sil. 2019. "Targeted delivery of quercetin via pH-responsive zinc oxide nanoparticles for breast cancer therapy." *Materials science and engineering: C* 100:129-140. doi: https://doi.org/10.1016/j.msec.2019.02.096

4. Kundu, Mousumi, Pritam Sadhukhan, **Noyel Ghosh**, Sharmistha Chatterjee, Prasenjit Manna, Joydeep Das, and Parames C Sil. 2019. "pH-responsive and targeted delivery of curcumin via phenylboronic acid-functionalized ZnO nanoparticles for breast cancer therapy." *Journal of advanced research* 18:161-172. doi: https://doi.org/10.1016/j.jare.2019.02.036

2. Kundu, Mousumi, Sharmistha Chatterjee, **Noyel Ghosh**, Prasenjit Manna, Joydeep Das, and Parames C Sil. 2020. "Tumor targeted delivery of umbelliferone via a smart mesoporous silica nanoparticles controlled-release drug delivery system for increased anticancer efficiency." *Materials Science and Engineering: C* 116:111239. doi: https://doi.org/10.1016/j.msec.2020.111239

3. Kundu, Mousumi, Pritam Sadhukhan, **Noyel Ghosh**, Sumit Ghosh, Sharmistha Chatterjee, Joydeep Das, Goutam Brahmachari, and Parames C Sil. 2021. "In vivo therapeutic evaluation of a novel bis-lawsone derivative against tumor following delivery using mesoporous silica nanoparticle based redox-responsive drug delivery system." *Materials Science and Engineering: C* 126:112142. doi: https://doi.org/10.1016/j.msec.2021.112142

4. Ghosh, Sumit, Mousumi Kundu, Sayanta Dutta, Sushweta Mahalanobish, **Noyel Ghosh**, Joydeep Das, and Parames C. Sil. 2022. "Enhancement of anti-neoplastic effects of cuminaldehyde against breast cancer via mesoporous silica nanoparticle based targeted drug delivery system." Life Sciences 298:120525. doi: https://doi.org/10.1016/j.lfs.2022.120525.

5. Tejwan, Neeraj, Mousumi Kundu, **Noyel Ghosh**, Sharmistha Chatterjee, Anirudh Sharma, Th Abhishek Singh, Joydeep Das, and Parames C. Sil. 2022. "Synthesis of green carbon dots as bioimaging agent and drug delivery system for enhanced antioxidant and antibacterial efficacy." Inorganic Chemistry Communications 139:109317. doi: https://doi.org/10.1016/j.inoche.2022.109317.
6. Dutta, Sayanta, Pratik Chakraborty, Susmita Basak, Sumit Ghosh, **Noyel Ghosh**, Sharmistha Chatterjee, Saikat Dewanjee, and Parames C. Sil. 2022. "Synthesis, characterization, and evaluation of in vitro cytotoxicity and in vivo antitumor activity of asiatic acid-loaded poly lactic-co-glycolic acid nanoparticles: A strategy of treating breast cancer." Life Sciences 307:120876. doi: https://doi.org/10.1016/j.lfs.2022.120876.
7. Abhishek Singh, Th, Pritam Sadhukhan, **Noyel Ghosh**, Neelam Thakur, Anirudh Sharma, Neeraj Tejwan, Ashok Pabbathi, Joydeep Das, and Parames C. Sil. 2023. "Targeted delivery of rutin into breast cancer cells via using phenylboronic acid functionalized MgO nanoparticles." Materials Science and Engineering: B 296:116623. doi: https://doi.org/10.1016/j.mseb.2023.116623.

Review articles

1. **Ghosh, Noyel**, Uday Hossain, Ankita Mandal, and Parames C Sil. 2019. "The Wnt signaling pathway: a potential therapeutic target against cancer." Annals of the New York Academy of Sciences 1443 (1):54-74. doi: https://doi.org/10.1111/nyas.14027
2. Kumar Das, Abhishek, **Noyel Ghosh** [contributed equally], Ankita Mandal, and Parames C. Sil. 2023. "Glycobiology of cellular expiry: Decrypting the role of glycan-lectin regulatory complex and therapeutic strategies focusing on cancer." Biochemical Pharmacology 207:115367. doi: https://doi.org/10.1016/j.bcp.2022.115367.
3. Banerjee, Sharmistha, Sumit Ghosh, Ankita Mandal, **Noyel Ghosh**, and Parames C Sil. 2020. "ROS-associated immune response and metabolism: a mechanistic approach with implication of various diseases." Archives of toxicology 94:2293-2317. doi: https://doi.org/10.1007/s00204-020-02801-7
4. Singh, Th Abhishek, Anirudh Sharma, Neeraj Tejwan, **Noyel Ghosh**, Joydeep Das, and Parames C Sil. 2021. "A state of the art review on the synthesis, antibacterial, antioxidant, antidiabetic and tissue regeneration activities of zinc oxide nanoparticles." Advances in Colloid and Interface Science 295:102495. doi: https://doi.org/10.1016/j.cis.2021.102495

Book chapter

1. **Ghosh, Noyel**, and Parames C. Sil. 2021. "Chapter 5 - Mitochondria and apoptosis." In Mitochondrial Physiology and Vegetal Molecules, edited by Marcos Roberto de Oliveira, 127-149. Academic Press.
2. **Ghosh, Noyel**, Sharmistha Chatterjee, Mousumi Kundu, and Parames C Sil. 2022. "Oxidative Stress-Dependent Anticancer Potentiality of Nanotherapeutic Zinc Oxide." In Handbook of Oxidative Stress in Cancer: Therapeutic Aspects, 1-22. Springer.
3. **Ghosh, Noyel**, Sharmistha Chatterjee, and Parames C Sil. 2022. "Evolution of antioxidants over times (including current global market and trend)." In Antioxidants Effects in Health, 3-32. Elsevier.
4. Sarkar, Sayanta, **Noyel Ghosh**, Mousumi Kundu, and Parames C Sil. 2020. "Nrf2 and Inflammation-Triggered Carcinogenesis." Nrf2 and its Modulation in Inflammation:129-152.
5. Karmakar, Arnab, Abhishek K Das, **Noyel Ghosh**, and Parames C Sil. 2022. "Superoxide dismutase." In Antioxidants Effects in Health, 139-166. Elsevier.
6. Mahalanobish, Sushweta, **Noyel Ghosh**, and Parames C Sil. 2022. "Panax quinquefolium (American Ginseng) and Physostigma venenosum (Calabar Bean)." In Herbs, Shrubs, and Trees of Potential Medicinal Benefits, 179-202. CRC Press.

Original Reprints

Life Sciences 301 (2022) 120606

Contents lists available at ScienceDirect

Life Sciences

journal homepage: www.elsevier.com/locate/lifescie

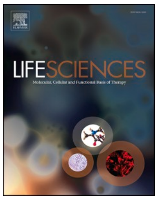

Oxidative stress imposed *in vivo* anticancer therapeutic efficacy of novel imidazole-based oxidovanadium (IV) complex in solid tumor

Noyel Ghosh [a], Sharmistha Chatterjee [a], Debanjana Biswal [b], Nikhil Ranjan Pramanik [c], Syamal Chakrabarti [b], Parames C. Sil [a,*]

[a] *Division of Molecular Medicine, Bose Institute, P-1/12, CIT Scheme VII M, Kolkata 700054, India*
[b] *Department of Chemistry, University College of Science, 92, Acharya Prafulla Chandra Road, Kolkata 700009, West Bengal, India*
[c] *Department of Chemistry, Bidhannagar College, EB-2, Salt Lake, Kolkata 700064, India*

ARTICLE INFO

Keywords:
Vanadium
Anticancer
ROS
Apoptosis
Cisplatin

ABSTRACT

Vanadium is a transitional metal having several therapeutic aspects that can be exploited for its anticancer activity. Herein, we have verified anticancer effectivity of synthesized novel water soluble mononuclear dipicolinic acid-1-allyl imidazole-based oxidovanadium (IV) complex [VOL(1-allylimz)$_2$] with respect to anticancer effectivity of known standard platinum-based anticancer agent cisplatin. In current work, we have verified VOL (1-allylimz)$_2$ as highly potential anticancer agent selectively against human breast cancer cells. VOL(1-allylimz)$_2$ has been noticed to elicit dose dependent cytotoxicity in MCF-7 cell line through induction of intracellular oxidative stress and mitochondrial membrane potential. Apart from *in vitro* validation, *in vivo* studies in male Swiss Albino mice also have seen to portray dose-dependent anticancer effect of [VOL(1-allylimz)$_2$], where indications of oxidative stress induction became prominent too. Besides, both mitochondrial as well as extra-mitochondrial apoptosis in tumor cells have been shown to be induced by [VOL(1-allylimz)$_2$] treatment, together enforcing its anticancer potency. In contrast to cisplatin, which shows high chances of nephrotoxicity in cancer patients, [VOL(1-allylimz)$_2$] has been found to be comparatively safe for *in vivo* studies.

1. Introduction

Depending on the fact that metal ions can selectively regulate a wide range of cellular processes, designing and synthesis of metallodrugs was initiated in the field of medicinal chemistry aiming to find cure for ‘difficult to treat’ diseases such as cancer. Till date cancer has been considered as one of the most fatal diseases causing severe mortality over the world. Among several cancer types, incidence of breast cancer is most common among worldwide female population [1]. According to current statistical count, nearly 1.3 million females suffer from mammary carcinoma [2,3]. In this context, metallodrugs were considered as highly potential anticancer agents from decades. Example of metallodrugs include popular platinum complexes such as cis-[Pt(NH3)2Cl2] [4] and its derivatives oxoplatin and carboplatin [5] which are used as popular chemotherapeutic agents in combination with radiation and other medication in cancer treatment. Interaction between genomic DNA and platinum is essential for exerted cell killing by platinum-based drugs [6,7]. After initial phase of intensive interest in platinum-based metallodrugs, other potential anticancer metal complexes including gold, palladium, copper, iron-based metallodrugs were also assayed which could follow distinct cell-death mechanisms beyond DNA binding [8,9]. Despite of being an efficient anticancer mediator, most of the metallodrugs especially, platinum-based drugs, mostly cisplatin exhibit a huge number of adverse effects due to low target selectivity and high off-target toxicity. Thus, introduction of metallodrugs with potent anticancer efficacy and minimal collateral systemic toxicity are of utmost importance in field of cancer therapy. In this regard, though the pharmacological potentials of vanadium as a metallodrug was first exploited in diabetes management, nearly 50 years back vanadium was first implicated in field of cancer research [10]. Till then, multiple arrays of vanadium compounds have arisen as prospective therapeutic agents for cancer treatment and management. Vanadium is a well-known first row transitional metal having an electronic configuration of [Ar]3d^{3}4s^2 with two naturally occurring isotopes, ^{50}V and ^{51}V. Presence of vanadium in abiotic [4] and biotic systems [11] of both marine and terrestrial origins are well established. Among the several elements found on earth, vanadium is the 22nd most abundant one (0.013% *w*/w). Human blood plasma contains nearly 200 nM of vanadium and while in tissues, such as kidney, liver and bone, its concentration is approximately 0.3 mg kg^{-1}

---

* Corresponding author at: Division of Molecular Medicine, Bose Institute, P-1/12, CIT Scheme VII M, Kolkata 700054, West Bengal, India.
E-mail address: parames@jcbose.ac.in (P.C. Sil).

https://doi.org/10.1016/j.lfs.2022.120606
Received 6 April 2022; Received in revised form 26 April 2022; Accepted 28 April 2022

Abbreviations

ALP	Alkaline phosphatase
ALT	Alanine aminotransferase
Bax	Bcl-2-associated X
BCA	Bicinchoninic acid
Bcl-2	B-cell lymphoma 2
BUN	Blood urea nitrogen
CAT	Catalase
CIS	Cistplatin
FITC	DCFDA dichlorodihydrofluorescein diacetate Fluorescein isothiocyanate
GSSG	Oxidized glutathione
GSH	Reduced glutathione
HRP	Horseradish peroxidase
IHC	Immunohistochemistry
JC1	tetraethylbenzimidazolylcarbocyanine iodide
LDH	Lactate dehydrogenase
MDA	Malonaldehyde
MMP	Mitochondrial membrane potential
MTT	3-(4 5-dimethylthiazol-2-yl)-2 5-diphenyltetrazolium bromide
NAC	*N*-acetylcysteine
PBS	Phosphate buffered saline
RIPA	Radioimmune precipitation assay
ROS	Reactive oxygen species
SOD	Superoxide dismutase
SDS	Sodium dodecyl sulfate
TBARS	thiobarbituric acid reactive substance
VOL	mononuclear dipicolinic acid-1-allyl imidazole-based oxidovanadium (IV) complex [VOL(1-allylimz)$_2$]

[12,13]. From biological aspects, only two of higher oxidation states of vanadium, *i.e.*, V(IV) and V(V) are of our interest [14] as these two oxidation states of vanadium are capable of forming cationic and anionic complexes within physiological pH (2–8) range. Intracellularly, vanadium exists mostly in tetravalent form, producing vanadyl ion (VO^{2+}) in association with protein [15]. However, only 1% vanadyl ions remain in free unbound state [16]. Besides, pentavalent form of vanadium mostly occurs extracellularly as vanadate ion or (VO_3^-). Based on structural similarities, anticancer vanadium complexes can be grouped as organometallic vanadocene, polyoxovanadate complexes, binary& tertiary peroxivanadates, vanadium peroxide-betaine complexes and most importantly oxidovanadium complexes [4].

Universally, vanadium has been recorded that vanadium inhibits tumor growth by inhibiting uncontrollable tumor cell proliferation and inducing apoptosis. The potentials of vanadium complexes in ROS-RNS-driven apoptosis [17], involvement in autophagy [10,18], cell differentiation and even in anoikis mechanistic procedures [19] or in oncogene modulation [20] either individually or collectively contribute to the possibility of designating vanado-drugs as potent anticancer agents.

In current manuscript, we have extensively studied anticancer role of novel water soluble mononuclear dipicolinic acid-1-allyl imidazole-based oxidovanadium (IV) complex [VOL(1-allylimz)$_2$]. For easy interpretation, the compound has been denoted as VOL in rest of the manuscript. Anticancer role of was VOL demonstrated earlier in human hepatocellular carcinoma cell line Hep3B in a previous study made by our collaborator [21]. Keeping the outcome in mind, here we have explored anticancer efficacy of VOL in human breast cancer cell line MCF-7. Also, we have compared its effectivity with a widely-used platinum-based metallodrug cisplatin (CIS) *in vitro*. Once found to be highly effective like CIS, VOL was also scrutinized for the mechanism of its *in vivo* antitumor activities and probable systemic toxicities (if any) within EAC-induced solid tumor-bearing male Swiss albino mice.

2. Experimental section

2.1. Chemicals and reagents

Cell culture media (RPMI-1640) along with other necessary ingredients for preparation of culture media, like amino acids and antibiotics, *etc.*, were procured from HIMEDIA (Mumbai, India). Cytiva HyClone™. Foetal bovine serum (FBS), RevertAid First Strand cDNA Synthesis Kit, DreamTaq Green PCR Master Mix (2×) were bought from Fisher Scientific (ThermoFisher Scientific, Logan, Utah, USA). Methylthiazolyldiphenyl-tetrazolium bromide (MTT) for cell viability study was purchased from Sisco Research Laboratory, Mumbai, India. Ribonuclease, FITC-Annexin V (Fluorescein isothiocyanate conjugated Annexin V), *N*-acetylcysteine, BCA (bicinchonic acid) assay kit were obtained from Thermo Fisher Scientific (USA). Cisplatin was provided by Sigma (St. Louis, MO). Mononuclear dipicolinic acid-1-allyl imidazole-based oxidovanadium (IV) complex [VOL(1-allylimz)$_2$] was synthesized from Biswal et al. [21], Department of Chemistry, University of Calcutta. Protease and phosphatase inhibitors, coumaric acid and luminol were procured from Sigma (Missouri, USA). Required antibodies and Immunohistochemistry kit were bought from Cell Signaling Technology (Danvers, MA, USA) and Abcam (Cambridge, UK). Other essential chemicals and reagents were purchased from local sellers of Kolkata, India, and were of analytical grades with high purity.

2.2. Methods

2.2.1. Cell culture

In the present study, human breast cancer cell line MCF-7 and one normal cell line, human normal kidney epithelial cell line NKE were used. Former cell line was purchased from NCCS, Pune and NKE was given as a gift by Dr. Kaushik Biswas, Bose Institute. At 37 °C temperature, both of these cells were cultured in RPMI-1640 media supplemented with 10% FBS and required antibiotics and antifungal agents (penicillin [100 U mL^{-1}], streptomycin [100 μg/mL], gentamycin [50 μg/mL] and amphotericin B [2.5 μg/mL]) within a humidified incubator with a 5% CO_2 concentration.

2.2.2. Determination of VOL imposed in vitro cytotoxicity

Cells were initially seeded in separate 96-well flat-bottomed plates and were cultured at an approximate density of 0.5×10^5 cells per well in 100 μL media. The cells were then exposed to varying doses of VOL in a range from 10 to 40 μg/mL, for 48 h. In this context, time-dependent assay was conducted previously to find the optimum time of exposure and pertinent assay conditions (data not shown). Following 48 h of incubation at 37 °C temperature, cells were subjected to 1× PBS solution of MTT solution (0.5 mg mL^{-1}) to determine the percentage of cell death according to the method described elsewhere [22,23]. After 4 h of incubation in MTT solution, purple MTT formazan was dissolved in DMSO followed by absorbance calculation at 570 nm.

2.2.3. Dosage for in vitro treatment

In order to compare the cytotoxicity of VOL in respect to a known anticancer agent CIS, MTT assay for CIS was also performed in both cancerous MCF-7 cells and in non-cancerous NKE (in a range concentration from 10 to 40 μg/mL). Additionally, a series of other *in vitro* experiments were also made in both MCF-7 and NKE cell lines with their respective LC_{50} doses.

2.2.4. Determination of in vitro LDH activity

In vitro release of lactate dehydrogenase (LDH) was measured after treating the cells with LC_{50} concentration of VOL using the LDH assay kit [24]. Experiment was done following the protocol provided by the manufacturer (Sigma-Aldrich) to confirm cellular damage.

2.2.5. Detection of VOL treatment-induced in vitro apoptosis

Induction of apoptosis was analysed using FITC-tagged Annexin-V buffer solution. MCF-7 cells, at an approximate 80% confluency, were incubated with LC_{50} dose of VOL and CIS. Followed by a treatment period of 48 h, treated MCF-7 cells were scraped and then centrifuged at 300 ×*g* for 5 min at room temperature. Obtained cell pellets were then washed in 1× PBS followed by further suspension in the Annexin V-binding buffer containing 1 μL of Annexin V/FITC for 5 min at room temperature under dark condition. Finally, the incubated cell pellets were analysed *via* flow cytometry (FACS Verse) at the excitation wavelength of 488 nm and emission wavelength of 520 nm [25]. A similar study was made in NKE cells using the same concentration of VOL & CIS used to treat MCF-7 cells for this experiment.

2.2.6. Detection and measurement of intracellular ROS

Intracellular ROS was detected using fluorescent H_2DCFDA dye following the protocol defined by Cossarizza [26]. In short, both MCF-7 and NKE cells were incubated with optimum toxic doses of VOL and CIS for 48 h. Cells were then scrapped and centrifuged at 300 ×*g* for 5 min at room temperature followed by cell pellet collection, resuspension of cell pellet in 1× PBS and incubation with 2 μM of H_2DCFDA (in the dark at 37 °C for 20 min). The resulted green fluorescence emitting samples were then flow cytometrically analysed by FACS Verse at 488 nm excitation and 520 nm emission wavelengths respectively [27].

2.2.7. Determination of in vitro mitochondrial membrane potential

MMP of VOL and CIS-treated MCF-7 cells was determined following the previously established method of Saha et al. [28], and compared with respect to the MMP of untreated control cells. MMP detection was made in both MCF-7 and non-cancerous NKE cells. VOL and CIS-treated cells (at respective optimum concentrations) were incubated with 5 mM JC-1 dye for 30 min at 37 °C in dark. Following incubation, cell pellet collection by centrifugation at 300 ×*g* for 5 min and 1× PBS resuspension, fluorescently labelled cells were analysed flow-cytometrically at excitation and emission wavelengths of 530 nm and 590 nm respectively in a BD FACS Calibur Flow Cytometry System (BD Biosciences) [29].

2.2.8. Estimating intracellular GSH/GSSG ratio

The reduced glutathione (GSH) level of the treated cells was determined by using Ellman's reagent (*i.e.*, DTNB solution) following a previously described protocol [30,31]. Initially, the cells were treated with VOL and CIS at its LC_{50} doses. Cells were sonicated and centrifuged for 15 min at 1200 ×*g* for total protein isolation to which Ellman's reagent was added, and the absorbance was measured at 412 nm. Again, glutathione (GSSG) level was measured following the method described by Hissin and Hilf [32]. Initially, 0.04 M NEM was added to the samples to prevent GSH oxidisation to GSSG followed by 30 min incubation and addition of Ellman's reagent and 300 mM Na_2HPO_4. Finally, absorbance was recorded at 420 nm. Similarly intracellular GSH/GSSG ratio was checked in NKE cell line as well.

2.2.9. Estimation of in vitro lipid peroxidation

To justify the condition of cellular oxidative stress in the MCF-7 cells, the extent of lipid peroxidation was studied by calculating the level of intracellular malondialdehyde (MDA). In short, the control and treated NKE and MCF-7 cells were sonicated, added to 0.67% thiobarbituric acid and 20% trichloro acetic acid mixture. The sample mixtures were then heated for 60 min at 100 °C for 1 h followed by a rapid ice cooling. Next, followed by centrifugation the supernatants were checked for spectrophotometric absorbance of thiobarbituric acid reactive substance (TBARS) at 535 nm wavelength [33]. As 99% of TBARS exist as MDA, concentration of TBAR was later calculated using the molar extinction coefficient of MDA ($1.56 \times 105\ M^{-1}\ cm^{-1}$).

2.2.10. Assessment of antioxidant enzyme activities

Activities of intracellular antioxidant enzyme catalase (CAT) and superoxide dismutase (SOD) were checked in both cell line after treatment with respective LC_{50} doses of VOL and CIS. The activity of CAT and SOD were estimated spectrophotometrically following protocols demonstrated elsewhere [34–36].

2.2.11. In vitro inhibitor studies

Both cell types were treated at a confluency of 80% with 20.83 μg/mL VOL and 5 mM NAC in conjugation and with VOL alone [22]. MTT assay was carried out after treating MCF-7 cells with VOL and NAC in separate sets of experiments under similar conditions, and calculating the cell viabilities in both cases. Moreover, cells were also checked for intracellular ROS content following the method described earlier along with for their intracellular GSH/GSSG ratio, activities of SOD and CAT and the results were analysed and compared to draw a conclusive idea about the oxidative-stress inducing properties of VOL in cancer cells.

2.2.12. Experimental set-up to assess in vivo antitumor activity of VOL

At first, a total of 36 male Swiss albino mice (4–6 weeks old) with average body weight of 25 g were collected from central animal house of the Bose Institute, Kolkata, India. Mice were further acclimatized to laboratory environment for 2 weeks keeping them in alternative 12 h light & dark cycle and provided with sterile food and water *ad libitum*. Any further experimental planning and procedure were done by following rules and regulations of Institutional Animal Ethics Committee (IAEC), Bose Institute, Kolkata [IAEC/BI/142/2019], CPCSEA (Committee for the Purpose of Control and Supervision on Experiments on Animals), Ministry of Environment and Forests, New Delhi, India (1796/PO/Ere/S/14/CPCSEA). In order to grow solid tumors, randomly selected eighteen mice out of 24 mice received EAC (Ehrlich ascites carcinoma) cells (at a density of 10^7 cells/50 μL in each mouse) containing intramuscular injections at their left flanks. Rest of the 18 mice were kept uninoculated for toxicological studies. 10 days after injection eighteen tumor-bearing mice were further grouped as follows:

Group I – tumor bearing mice receiving intravenous injection of 0.9% saline water.

Group II – tumor bearing mice receiving intravenous injection of VOL at a concentration of 10 mg kg^{-1} body weight.

Group III – tumor bearing mice receiving intravenous injection of VOL at a concentration of 20 mg kg^{-1} body weight.

All of the tumor bearing mice received intravenous injection *via* tail vein with respective doses on alternate days, for a total of 14 days. Animal were kept under day-to-day observation for the any changes in their body weight, tumor volume and overall vigour. After completion of the 14-day treatment period, the experimental animals were sacrificed. The tumors from animals belonging to Groups I, II and III were carefully removed from the bodies, physically examined for weight and volume. Tumor volume was measured employing ellipsoid volume equation, *i.e.*, volume = (length × breadth × height × 0.5). Lastly, tissues were stored separately for further histological, molecular and immunohistochemical studies. Besides, a ruler was used to determine the lengths of the collected spleens from animals of all the groups to observe signs of splenomegaly, if any.

2.2.13. Histological analysis of collected tissues

The tissues collected from experimental animals of relevant experimental groups were cleaned and fixed in 10% formalin. Fixed tissue sections were processed for embedding in paraffin blocks and further sectioning. Microtome sections of the tissues of an approximate thickness of 5 μm were then obtained on slides, which underwent the process of serial dehydration and rehydration. Tissue sections were then double-stained with hematoxylin and eosin followed by further dehydration and subsequent mounting in DPX (distyrene, plasticizer, and xylene) [37]. Finally, the stained tissue sections were viewed under a light microscope at 20× magnification to determine the histological changes that have occurred in the body tissues upon VOL treatment.

2.2.14. *Assessment of SOD and CAT activity in dissected tumor tissue*

Activity of antioxidant enzymes such as SOD and CAT were checked in dissected tumor tissues. At the beginning, tumor tissues collected from Group-I–III were homogenized using RIPA lysis buffer and were checked spectrophotometrically for protein concentration using BCA protein concentration measuring kit. Once measured, the activity of CAT and SOD were estimated spectrophotometrically following protocols mentioned earlier [34,35], in order to verify the oxidative changes occurring in tumor tissues of the experimental animals upon treatment with VOL.

2.2.15. *Estimating lipid peroxidation in tumor tissues*

The condition of oxidative stress at the tumor tissue level in the *in vivo* system was assessed spectrophotometrically following the protocol described earlier in the manuscript [38].

2.2.16. *RNA extraction and reverse transcriptase PCR*

To determine the transcriptional expression of our interest in VOL treated tumor tissues, RNA was extracted from the collected tumor tissues of the animals of the three experimental groups (I, II, and III) using TRIZOL, following the manufacturer's protocol (Invitrogen, Carlsbad, CA). The concentration of total RNA was spectrophotometrically measured in a nanodrop (Hellma Tray Cell Type 105.810) after its isolation. cDNA was prepared from 2 μg RNA using Thermo Scientific Verso cDNA synthesis kit, following the manufacturer's protocol (Thermo Scientific, USA) followed by a PCR reaction was conducted in a thermal cycler according to the protocol as established by Banerjee et al. [39]. Amplified PCR-products were stored at 4 °C and sequenced verified. The, then PCR products were electrophoresed in 1.5% agarose gel according to the cognate annealing temperatures of the respective primers (Table 1). A control sample containing all reverse transcriptase reagents excluding reverse transcriptase enzyme was also electrophoresed to ensure the amplified PCR products were not contaminated with genomic DNA. As, no product was generated from such control sample, it ensured lack of genomic DNA contamination.

Table 1
Sequence, amplicon size and annealing temperature of primers used for RT-PCR analysis of respective genes.

Gene name	Primer sequence (5′-3′)	Annealing temperature (°C)	Amplicon size (bp)
CAT	FP: *CACACTCACACACACTCATACA* RP: *CACACTCACACACACTCATACA*	50	178
TNF-α	FP: *TCTCAGAATGAGGCTGGATAAG* RP: *CCCGGCCTTCCAAATAAATAC*	55	188
IL-1β	FP: *GAGTGTGGATCCCAAGCAATA* RP: *TCCTGACCACTGTTGTTTCC*	45	174
IL-6	FP: *GATAAGCTGGAGTCACAGAAGG* RP: *TTCTGACCACAGTGAGGAATG*	58.7	163
MCP-1	FP: *GAAGGAATGGGTCCAGACATAC* RP: *CACTCCTACAGAAGTGCTTGAG*	55	190
GAPDH	FP: *GGAGAAACCTGCCAAGTATGA* RP: *CCAGGAAATGAGCTTGACAAAG*	50	193

2.2.17. *Immunoblotting*

The collected sample tumor tissues (stored at −80 °C) were lysed using the lysing RIPA buffer as following the method established elsewhere [33]. To segregate and purify the protein, the tissue homogenate was centrifuged at 1200 ×*g* for 10 min at 4 °C. The supernatant (protein-rich fraction) was then collected, and the total protein content in each sample was determined by following the protocol of BCA assay kit. The protein samples were then stored at −80 °C for future use.

Immunoblotting was performed by resolving equal amounts of protein in an SDS-polyacrylamide gel by electrophoresis followed by transfer on PVDF membranes. Non-specific interactions on PVDF membranes were blocked with 5% BSA (in TBST buffer) for 1 h at room temperature. Then the membranes were incubated overnight at 4 °C with primary antibodies of interest (at 1:1000 dilution). Following three times TBST washes membranes were incubated with HRP-conjugated secondary antibody (at 1:20000 dilution) at room temperature for 2 h. Finally, the membranes were developed onto X-ray plates using ECL solution (HRP substrate).

2.2.18. *Immunohistochemistry*

Tissue microsections were obtained on poly-L-lysine-coated slides. Tissue section-containing glass slides were then subjected to the protocol of immunohistochemical analysis as established by Kundu et al. [23]. Sections were deparaffinized, rehydrated, incubated overnight at 4 °C with the specific primary antibodies in a damp followed by next day-wash and HRP-tagged secondary antibody exposure at room temperature for 30 min. DAB (3,3′-diaminobenzidine tetrahydrochloride) was finally added to the sections as an HRP substrate. The tissue sections were then counterstained with hematoxylin, dehydrated and were mounted with DPX. These H & E-stained tissue sections were then observed under a bright field microscope at a magnification of 20×.

2.2.19. *Experimental set-up for toxicological evaluation*

To ascertain VOL treatment based systemic toxicity eighteen wild type male Swiss albino mice were divided in three groups and they received intravenous injection as follows:

Group IV – wildtype mice receiving intravenous injection of 0.9% saline water.

Group V – wildtype mice receiving intravenous injection of aqueous solution of VOL (10 mg kg^{-1} body weight).

Group VI – wildtype mice receiving intravenous injection of aqueous solution of VOL (20 mg kg^{-1} body weight).

All of these animals were examined for any change in their coat colour, body weight etc. Experimental animals received injections on alternate days for a total of 14 days after which animals were sacrificed and blood from each experimental animals was collected by puncturing left ventricle of heart with a fine needle. Also, vital organs such as livers and kidneys were collected.

2.2.20. *Assessment of toxicological serum parameters*

Serum was isolated from collected blood samples by centrifugation [40]. Level of alkaline phosphatase (ALP), alanine transferase (ALT), two well-known hepatic toxicity markers were assessed following the protocol of assay kit (Span Diagnostic Ltd., India) [41]. Besides, renal toxicity markers such as blood urea nitrogen (BUN) and creatinine level in serum were also checked.

2.2.21. *Physical assessment of splenic profile*

The spleens collected from experimental animals of group I–IV and were scrutinized to check if VOL could reduce the cancer-induced splenomegaly in tumor-bearing animals, thus indicating a strong healthy parameter of reduced inflammation in splenic tissue.

2.2.22. *Statistical analysis*

All the results of the experiments conducted throughout this study, are represented as their mean ± standard deviation (SD), after performing at least three independent sets of experiments. The statistical analyses overall were performed using ANOVA (one-way analysis of variance), and to compare the mean values within the groups themselves, Tukey's test was also performed. A *P*-value that came out to be less than 0.05 was considered statistically significant in this study.

3. Results and discussions

3.1. *VOL is differentially cytotoxic to breast cancer cells at a dose comparable to that of cisplatin*

The cytotoxicity of VOL on MCF-7 breast cancer cells was assessed through performing MTT assay. Cellular toxicity and percentage of cell death increased along with increasing the doses of VOL. In MCF-7 cell line, LC_{50} dose of VOL came out to be 20.825 μg/mL. However, LC_{50} value of VOL in NKE was much higher (104.723 μg/mL) showing its selective cytotoxicity towards cancer cells (Fig. 1A).

Besides, cytotoxicity of VOL was compared to that of the known anticancer agent CIS. LC_{50} doses for CIS in MCF-7 and non-cancerous NKE cells were recorded to be 21.136 and 24.616 μg/mL respectively (Fig. 1B).

Furthermore, the extent cytotoxic effects of VOL and CIS obtained from MTT assay were validated by assessing the amount of LDH leakage from the cells (Fig. 1C). In MCF-7 cells, exposures of VOL and CIS both resulted in significant amount of LDH leakage (82.909 U L^{-1} and 81.099 U L^{-1} respectively). However, in non-cancerous NKE cell line, VOL triggered only a bit of LDH leakage in contrast to significantly higher LDH leakage upon CIS treatment (76.211 U L^{-1}). Thus, unlike CIS, VOL was found to be distinctively toxic to cancer cells showing no remarkable toxicity for normal cells such as NKE.

3.2. *VOL induces apoptosis in breast cancer cells in dose dependent manner*

Annexin-V-mediated flowcytometric assay was carried out for understanding the mode of cell death inflicted by VOL. As depicted in the Fig. 2, presence of cells in the 4th quadrants of dot plots indicates apoptotic mode of cell death by VOL. Like CIS, VOL at its LC_{50} dosage was also found to be highly potent to cause apoptotic death of human breast cancer cells MCF-7. However, CIS caused apoptosis in NKE cell population to significant percentage in contrast to VOL which was found to be merely toxic to normal NKE cells.

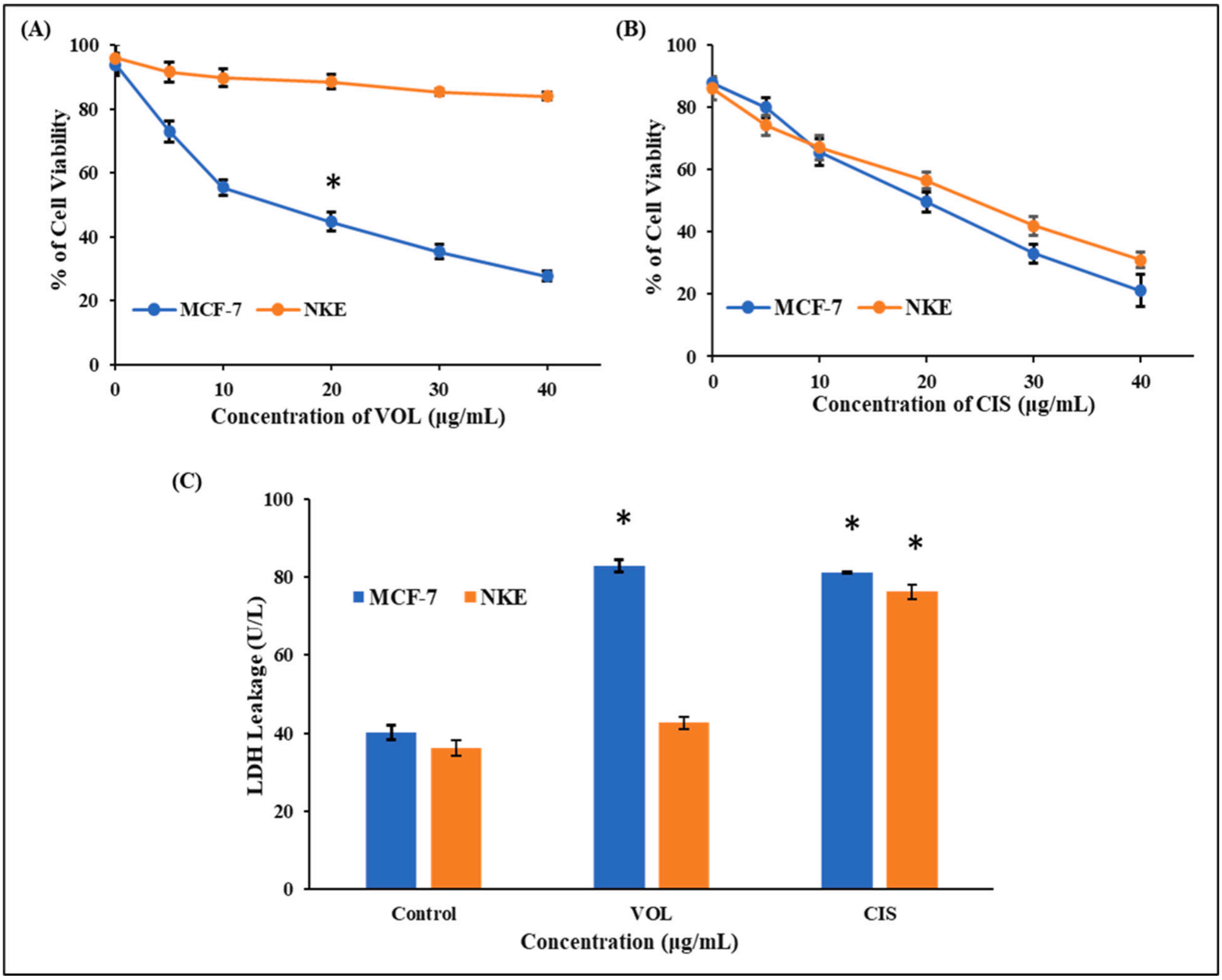

Fig. 1. Cytotoxic effect of VOL in MCF-7 cells in comparison with known anticancer agent cisplatin: Dose dependant cytotoxicity of (A) VOL and (B) in MCF-7 and NKE cell lines in a range of 0–40 μg/mL concentration detected through MTT assay. (C) Comparison of VOL (20.83 μg/mL) and CIS (21.13 μg/mL)-mediated cytotoxicity in MCF-7 and NKE cells detected *via* LDH leakage assay. All the data are representative of three independent experiments. "*" represents significant difference with the control group ($P^* < 0.05$).

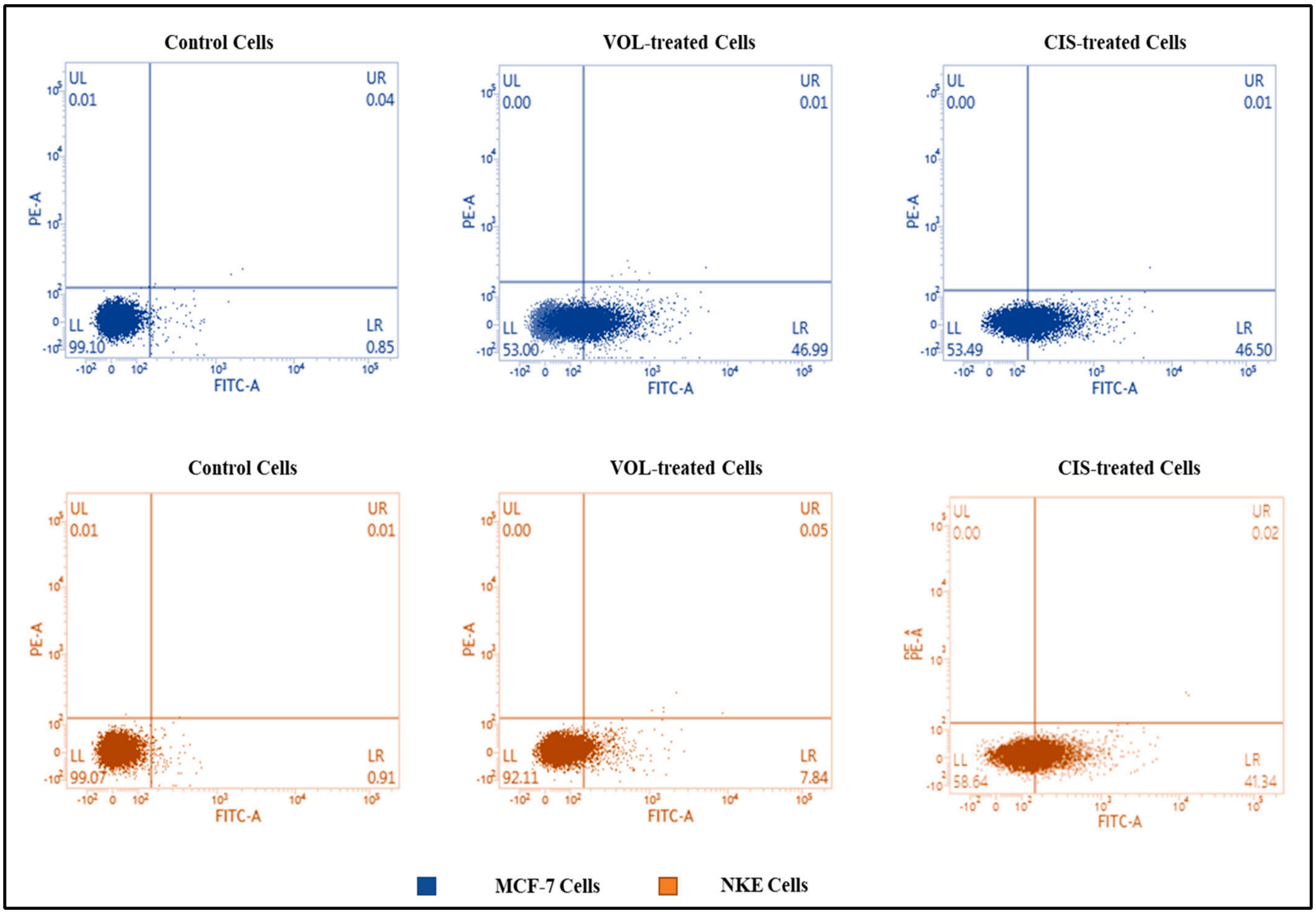

Fig. 2. Detection of VOL and CIS-induced apoptosis in both MCF-7 and NKE cell lines: MCF-7 and NKE cells pretreated with desired compounds (20.83 μg/mL of VOL and 21.12 μg/mL of CIS) were subjected to Annexin-V-FITC staining and subsequent flowcytometric study. Here, a dual parameter dot plot has been prepared with an x-axis representing the logarithmic fluorescence of FITC-labelled Annexin V.

3.3. VOL treatment differentially imposed oxidative stress in the breast cancer cells

ROS play a crucial role in apoptosis induction both in physiologic and pathologic condition. Hence, intracellular ROS generation was checked flow cytometrically using fluorescent DCFDA dye. An increase in green fluorescence was observed in VOL treated MCF-7 cells in comparison to untreated cells and VOL treated normal kidney cells. Otherwise, ROS induction was significantly higher in both CIS-treated breast cancer and normal kidney cell lines (Fig. 3A & B). This observation indicates significant differential enhancement in intracellular ROS in human breast cancer cells. Uplifted intracellular ROS is a hallmark of overall cellular oxidative stress. In order to confirm the condition of cellular oxidative stress several cellular antioxidant markers such as activities of antioxidant enzymes SOD, CAT, extent of lipid peroxidation (MDA) and the ratio of GSH-GSSG *etc.* were tested as well (Fig. 3C–F). CIS and VOL exposure significantly hampered the antioxidant activities of CAT and SOD in MCF-7 cells. Exposure to both of these compounds resulted a significant lowering in reduced glutathione level (GSH) along with an enhanced oxidized glutathione (GSSG) level in MCF-7 cells. NKE cells after being exposed to CIS, showed much reduced GSH-GSSG ratio, in contrast to NKE cells where a normal range of GSH-GSSG ratio was maintained. Besides, VOL treatment significantly uplifted malondialdehyde (MDA) amount in the breast cancer cells barring the non-cancerous cells which clearly denotes that VOL-driven oxidative stress induction is breast cancer cell specific. SOD and CAT form a part of first line defence system that act to suppress or prevent the formation of free radicals or reactive species in cells. Decreased activities of such enzymes indicate faulty cellular oxidative stress management system resulting in excessive load of ROS. In line, glutathione, a substance made from three amino acid cysteine, glutamic acid and glycine aids in the resistance of oxidative stress. It exists in a ratio of GSH to GSSG. Normal cells account 90% glutathione in GSH form. However, an increased ratio of GSSG to GSH indicates a status of oxidative stress. Consequently, that results in increased level of oxidation to cellular macromolecules such as proteins. Thus, reduced SOD, CAT activities in association with increased GSSG-GSH ratio and cellular MDA content cumulatively indicate a condition of cellular oxidative stress which emphasise ROS generating ability of VOL to be involved in its differential anticancer activity.

3.4. VOL treatment selectively hampered MMP in breast cancer cells

Induction of apoptosis and uplifted cellular ROS both are often related to increased mitochondrial permeability and dysfunction. Hence, we checked for the relative change in mitochondrial membrane potential of untreated cells with that of the CIS and VOL-treated cells (Fig. 4A & B). Increase in green fluorescence with concomitant loss of red fluorescence was considered as the notion of reducing MMP. CIS was capable of reducing mitochondrial membrane potential both in cancerous and non-cancerous cell lines. Whereas, VOL was able to induce reduction in MMP selectively in MCF-7 cells, change in MMP was negligible among VOL treated NKE cells. Such observation also indicated that mitochondrial malfunction could be the key for apoptotic death of breast cancer cells.

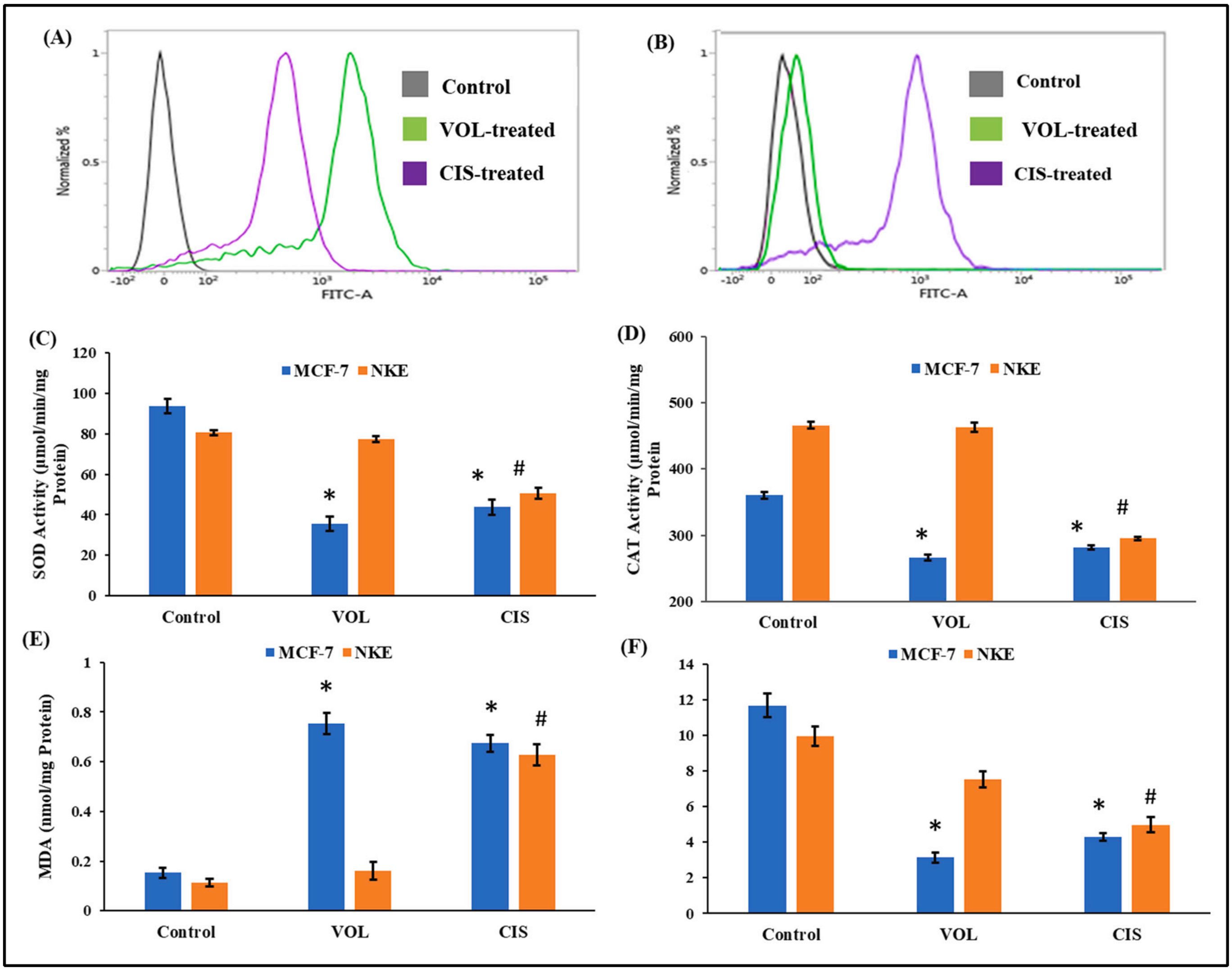

Fig. 3. Determination of oxidative status of MCF-7 and NKE cells upon VOL and CIS treatment: VOL differentially induces increased oxidative load in MCF-7 cells, whereas, CIS-mediated enhanced oxidative stress is prominent in both cancer and normal cells.

DCFH-DA staining to show uplifted ROS production due to 20.83 μg/mL VOL and 21.13 μg/mL CIS treatment. ROS production in (A) MCF-7 breast cancer cells and (B) in normal NKE cells.

This result was observed by determining (C) SOD and (D) CAT activities in VOL and CIS treated MCF-7 and NKE cells. Additionally, (E) & (F) represent MDA and GSH: GSSG content in cancer and non-cancerous NKE cells treated with 20.83 μg/mL VOL and 21.13 μg/mL CIS. Each column is represented as mean ± SD, $n = 6$. "*" represents the significant difference with respect to control MCF-7; whereas, "#" represents significant difference with respect to the Control NKE cells. ($P^* < 0.05$). Each data is representative of three independent experiments.

3.5. Involvement of ROS is at the central to the VOL-mediated cell death

From above results, we were curious to know the impact of ROS in overall effectivity of VOL mediated cell death. NAC which is a well-known ROS blocker was used to satisfy our curiosity. When treated with NAC in addition to LC_{50} dose of VOL, it usually lowered overall intracellular ROS in MCF-7 cells compared to those treated with LC_{50} dose of VOL alone (Fig. 5A). Also, similar observations were made in case of enzymatic activities of intracellular CAT and SOD (Fig. 5C & D). Apart from that, NAC addition was found to significantly reverse VOL assisted cell death in MCF-7 cells (Fig. 5B). Reduction in VOL driven apoptotic cell death due to NAC pre-treatment was confirmed by flow-cytometric sorting of annexin-V-stained control and treated MCF-7 cells (Fig. 5E), suggesting ROS to be the key role player for VOL induced breast cancer cell death.

3.6. VOL causes reduction in tumor weight and volume

EAC-originated solid tumors from sacrificed experimental mice were checked for their weights and volumes. The mean weight and volume of each experimental group (Groups I, II, and III) were plotted to easily understand the change graphically. It was found that VOL significantly decreased the tumor size, both in terms of weight and volume in the treated groups (Fig. 6A & B), as compared to the untreated group (Group I), in which the tumors had grown to significantly large sizes over the treatment period (Fig. 6D). The results were more pronounced for the higher dose-treated group (Group III, 20 mg kg^{-1}).

3.7. VOL treatment repairs disrupted tumor tissue architecture

The tumor tissues were studied for their histological details by interpreting the H & E-stained tumor sections (Fig. 6E). Increase in micronuclei and disruption of tissue architecture are hallmarks of solid tumor. Both of these signs were most pronounced in untreated tumor

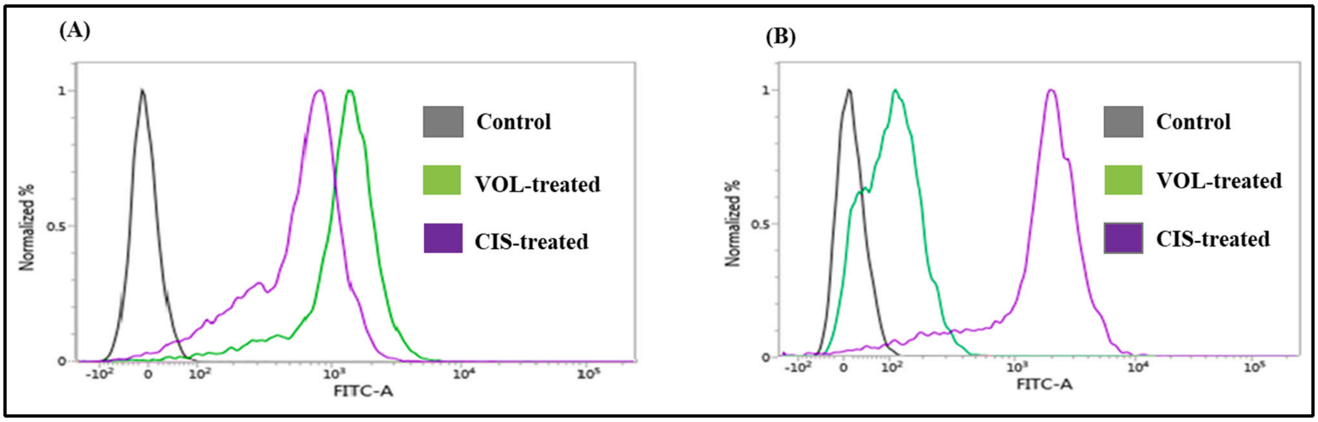

Fig. 4. Detection of VOL and CIS-imposed MMP induction: Effect of 20.83 μg/mL VOL and 21.13 μg/mL CIS treatment upon mitochondrial membrane potential in (A) MCF-7 cells and (B) NKE cells respectively represented by the monomeric green fluorescence of the JC-1 dye. All data are representative of three independent experiments.

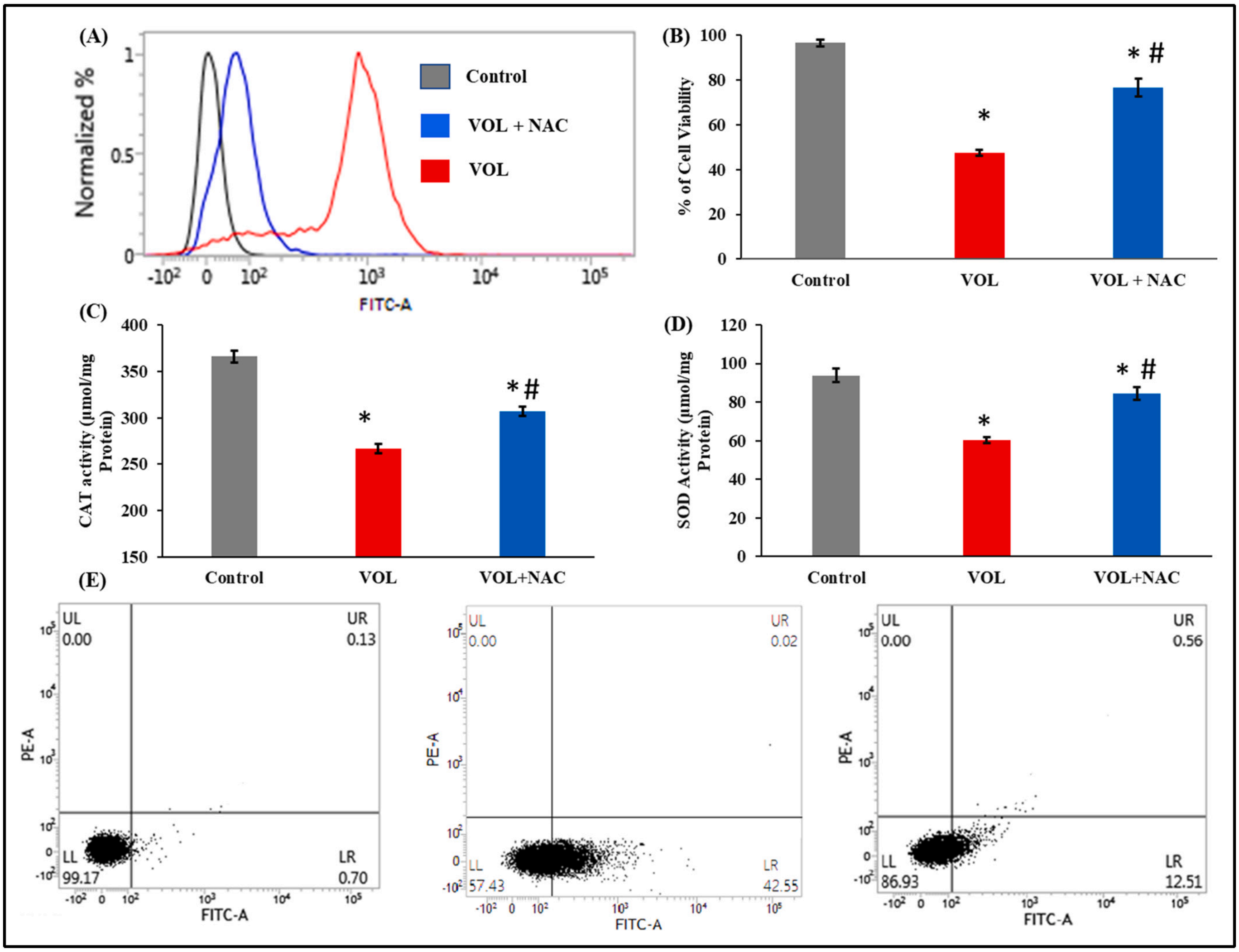

Fig. 5. NAC inhibits VOL induced ROS and subsequent cell killing in MCF-7 cells: (A) Histogram showing comparative intracellular ROS content in MCF-7 cells treated with LC_{50} dose of VOL alone and with 5 mM NAC due to green fluorescence of DCFH-DA. (B), (C) & (D) Effect on cell viability, CAT and SOD activities of MCF-7 cells upon exposure to 20.83 μg/mL VOL alone and in combination with 5 mM NAC. Each column is represented as mean ± SD, $n = 6$. "*" represents the significant difference between the normal control and VOL treated cells; whereas, "#" represents significant difference between VOL-treated and VOL + NAC treated cells. ($P^* < 0.05$). Data are representatives of three independent studies.

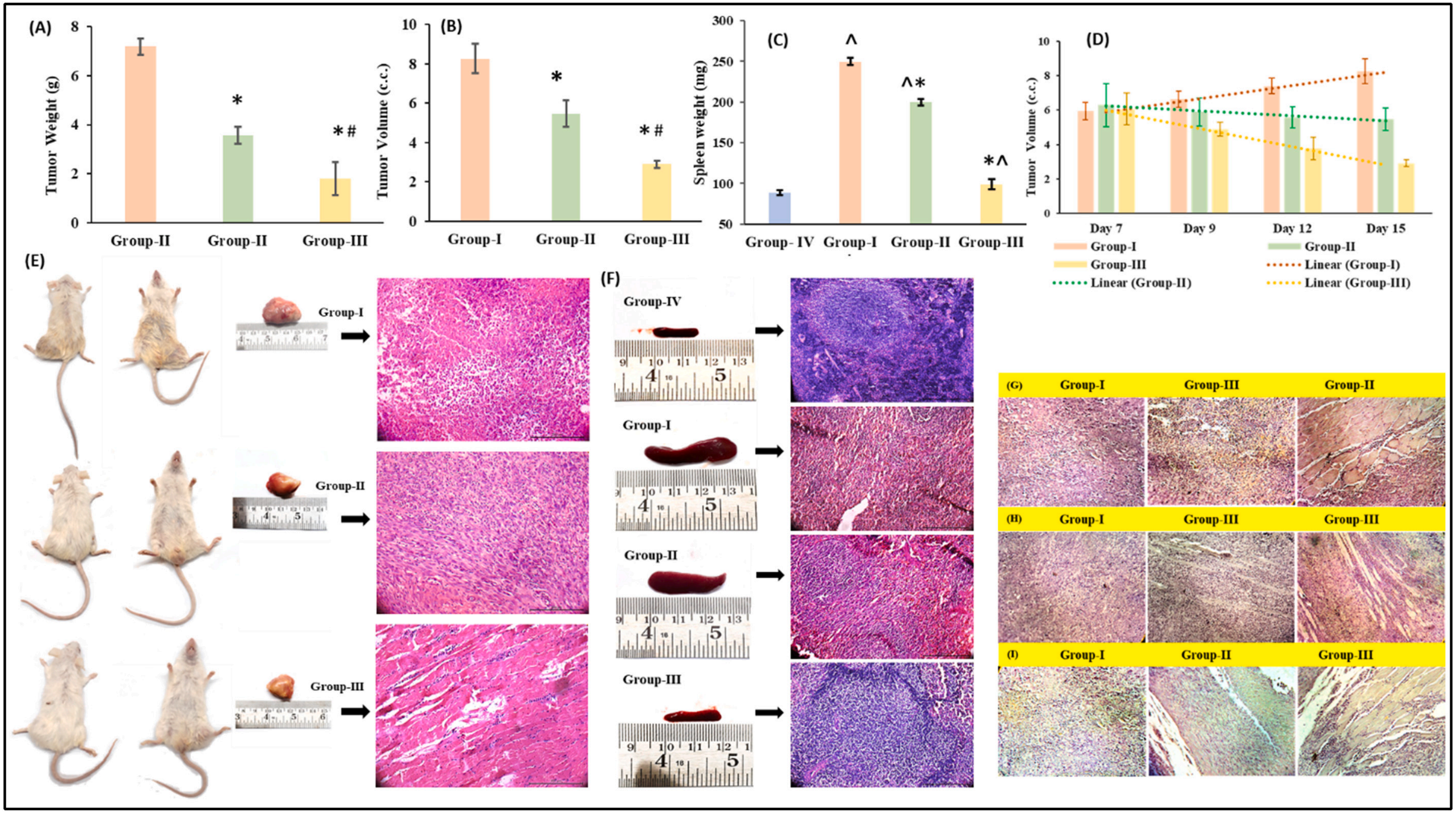

Fig. 6. VOL regresses *in vivo* tumor load in male Swiss Albino mice: (A) Dose-dependent reduction in tumor mass (expressed in gram) upon VOL treatment. (B) Dose-dependent reduction in tumor volumes (expressed in cubic centimeter) upon VOL administration. (C) Comparative study of weight of dissected spleens from experimental mice of Group I–IV. (D) Relative changes in tumor volume (expressed in cubic centimeter) over the course of 15 experimental days. (E) Representative photographs of dorsal and ventral views of tumor bearing mice, respective dissected tumor tissues and their histological appearance with H & E staining. All data are representative of experiments repeated for three times. (F) Representative photographs of dissected spleens from experimental mice of Group I–IV and their respective H & E-stained histological sections (at 20× magnification). Representative photographs showing the immunohistochemical expression of (G) cleaved caspase-8, (H) cleaved caspase-9 and (I) cleaved caspase-3 in tumor tissues (20× magnification). Each column is represented as mean ± SD, *n* = 6. “^” represents the significant difference with respect to the Group-IV, “*” represents the significant difference with respect to the Group-I; whereas, “#” represents significant difference with respect to Group-II. ($P^* < 0.05$).

tissue sections; whereas, tumor sections of VOL-treated mice showed signs of betterment. Both of these characteristics were found to have significant improvement with increase in dose of VOL. In the higher dose group (Group III), tumor micronuclei are barely visible in significant number and the tissue architecture was found to have nearly returned to normal muscle tissue architecture.

3.8. *VOL treatment reduces splenomegaly in tumor-bearing mice*

The splenic size and weight were considered as inflammatory markers *in vivo* which was imposed by EAC-incorporation. It was observed that VOL reduced splenomegaly in the treated animals of Group-II and III, as compared to that of the untreated control group (Group-I) (Fig. 6C). The results indicated that VOL treatment did not induce major toxicity in the animal bodies as a whole; rather, it was successful in reducing the extent of splenomegaly in the treated animals of Group-II and III, indicating an overall reduction of cancer load in treated tumor-bearing animals. To validate further we studied H & E-stained splenic tissue sections from experimental animals of group I–IV (Fig. 6E). There were no signs of disparity in splenic tissue architecture even in wild type tumor non-bearing mice. These observations not only ensure tumor healing property of VOL but also mark it to be safe for *in vivo* usage.

3.9. *VOL altered in vivo redox balance in tumor tissue*

The activities of antioxidant enzymes SOD and CAT in tumor tissues were studied (Fig. 7A & B) from tumor tissue homogenates of respective experimental animals to find whether the *in vivo* results were in line with the results of the *in vitro* assays. CAT is a highly significant phase II detoxification enzyme which is essential to prevent ROS-driven cancer cell damage. In this regard, SOD2 or MnSOD functions similarly. Thus, apart from measuring activities of these two enzymes in tumor tissue, we also analysed transcriptional and translational level of CAT and SOD2 respectively *in vivo* (Fig. 7D & E). It was found that results from *in vivo* study indeed corroborated the *in vitro* results, albeit with certain degrees of variation owing to *in vivo* physiology. Antioxidant activities of CAT and SOD2 were lowered parallelly with their expression level in VOL treated group in contrast to tumor control group. Additionally, with increasing dose, VOL was able uplift lipid peroxidation in tumor tissues as well (Fig. 7C). Thus, it can be inferred that, VOL can potentially hamper red-ox balance in tumor tissue.

3.10. *VOL altered Bcl-2-family proteins inducing intrinsic apoptotic effect*

To check the expressions of various pro-apoptotic and anti-apoptotic proteins in the tumor tissues at translational level, data from Western blotting were considered. Result from previous MMP determination hinted us about mitochondrial dysfunctionality. Hence, we wanted to check the transcriptional as well as translational expression of key molecules associated with mitochondria-based apoptotic pathway. In this course, we found VOL treatment dose-dependently reduced Bcl2/Bax ratio. Reduction in Bcl-2/Bax ratio is a hallmark, leading the cell towards intrinsic apoptotic death. Moreover, loss of MMP is associated with increased mitochondrial permeability causing the release of mitochondrial protein cytochrome C. Thus, translational expression of cytochrome C was noticed. Thereafter, we have checked increased expression Apaf-1 confirmed apoptosome formation. Further, to confirm specific caspase activation we checked expression level of cleaved caspase 9 and cleaved caspase 3, both of which were expressed higher in tumor tissue treated with 20 mg of VOL (Fig. 8A).

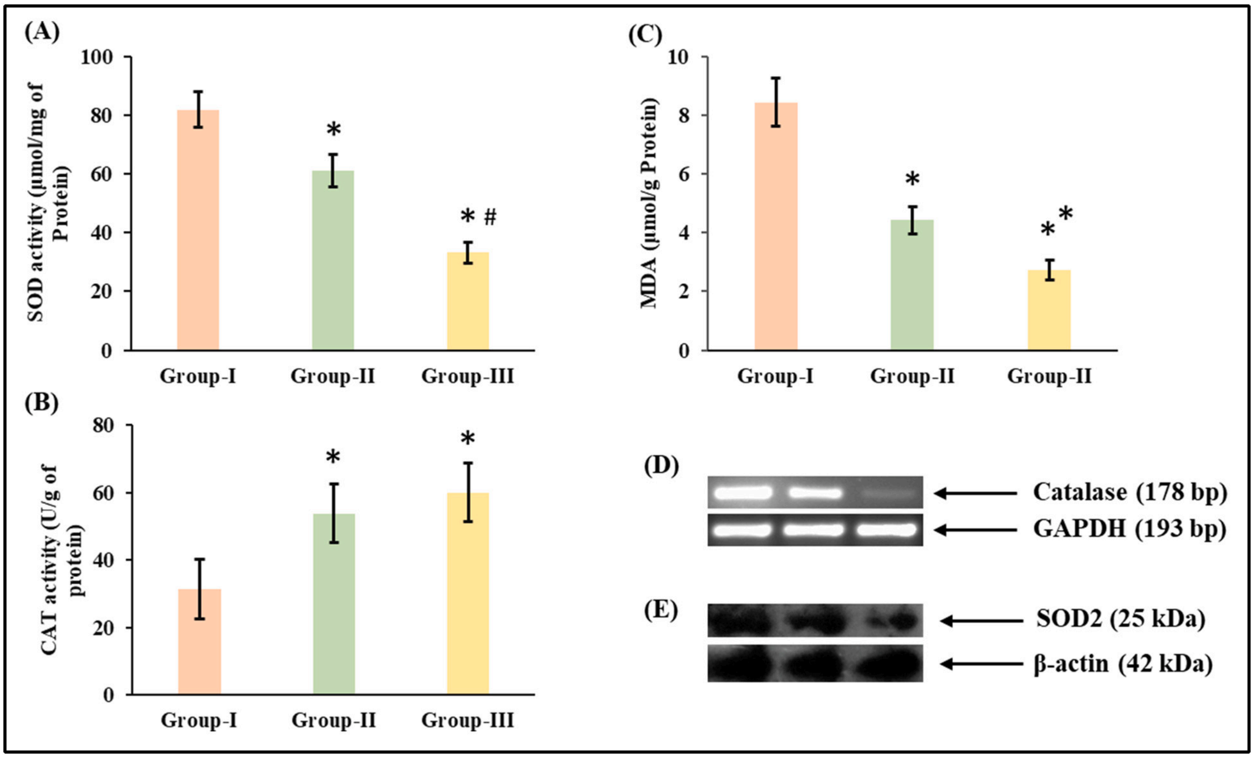

Fig. 7. Changes of *in vivo* tumor tissue antioxidant parameters after VOL application: (A) SOD and (B) CAT activities in tumor tissues of respective experimental groups. (C) represents the MDA levels in tumor tissue after being treated with 10 mg kg^{-1} and 20 mg kg^{-1} doses of VOL (expressed in terms of μmol/g of protein). (D) & (E) respectively represent expression of CAT and SOD2 in tumor tissue. Expression of CAT was assessed through RT-PCR; whereas, SOD2 expression was studied by Western blot analysis. Data shown here are representatives of three individual experiments. Each column has been plotted as mean ± SD, $n = 6$. "*" represents the significant difference with respect to the Group-I; whereas, "#" represents significant difference with respect to Group-II. ($P^* < 0.05$).

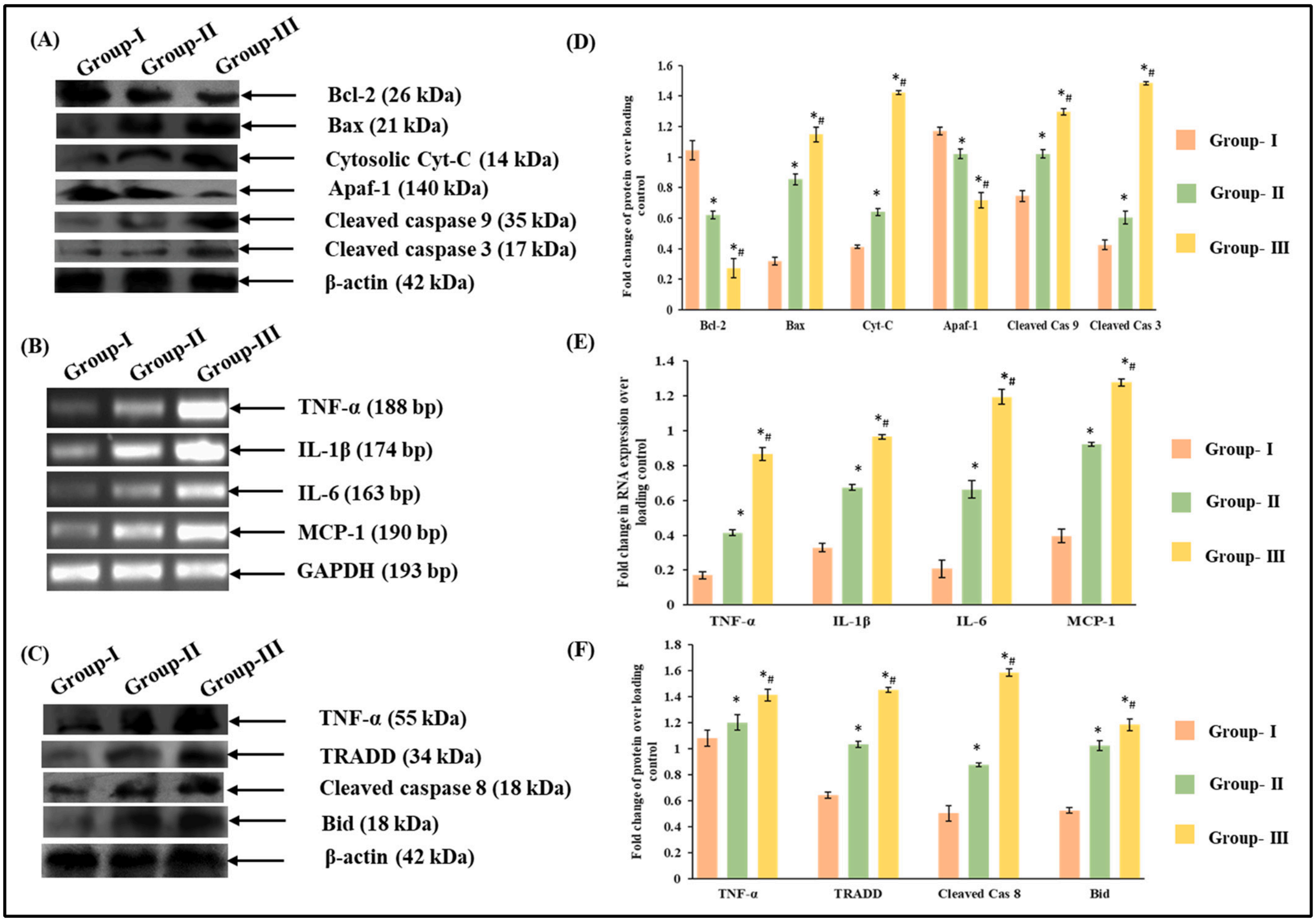

Fig. 8. VOL-induced *in vivo* tumor reduction is related to upregulation of apoptotic and inflammatory markers: (A) Immunoblot analysis of Bcl-2, Bax, cytosolic Cyt C, apaf-1, cleaved caspase 9 and 3 from whole lysate of tumor tissues obtained from respective experimental groups suggesting VOL is capable of inducing mitochondria-dependent intrinsic apoptotic pathway. β-actin has been sued as the loading control here. (B) RT-PCR analysis of transcriptional expression of inflammatory markers such as TNF-α, IL-1β, IL-6, MCP-1 in tumor tissues from all three experimental groups. GAPDH expression has been used as loading control. (C) Quantification of protein expression of TNF-α, TRADD, cleaved caspase-8 and Bid (with respect to loading control β-actin) from whole lysate of tumor tissues of all the three groups by Western blot analysis. (D–F) Densitometric analysis data are represented as the mean ± SD of three different experimental sets. “*” represents the significant difference with respect to the Group-I; whereas, “#” represents significant difference with respect to Group-II. ($P^* < 0.05$).

3.11. *VOL concomitantly induced extra-mitochondrial apoptosis in tumor tissues*

As we noticed significant tumor-related inflammatory splenomegaly in experimental tumor bearing mice, we were keen to know whether inflammatory signals were boosted in VOL treated tumor tissue as well. Hence, expression of pro-inflammatory cytokines such as tumor necrosis factor-α (TNF-α), interleukins (IL-6, IL-1β) were examined at transcriptional level (Fig. 8B). Inflammatory cytokines are known to upregulate chemokine production resulting in leucocyte infiltration. In present study, we checked for any alternation in transcriptional expression of monocyte chemo-attractant protein-1 (MCP-1) due to VOL treatment. Also, by Western blotting we checked the expression of tumor necrosis factor-α (TNF-α) in tumor tissues collected from experimental mice from Group-I–III. In our study, we found the expression of TNF-α to be upregulated both at transcriptional and translational levels due to VOL treatment. Additionally, as interpreted from RT-PCR data, VOL treatment was also noticed to uplift IL-1β, IL-6 and MCP-1 mRNA expression. Apart from inflammatory response TNF-α is capable of inducing apoptosis too. Thus, we also investigated translational expression of genes involved in TNF-α-mediated extrinsic apoptotic pathway (Fig. 8C). So, downstream to TNF-α, expression of TNFR1-associated death domain protein (TRADD) as well as that of the cleaved caspase-8 were found elevated. Further, downstream, increased Bid expression was enough to link TNF-α-mediated extrinsic apoptotic pathway with intrinsic one.

3.12. *VOL induces higher expression of cleaved caspases 9, 8 and 3 in tumor tissue in vivo with dose-dependency*

To visualise the changes induced by VOL treatment *in vivo*, we performed immunohistochemical experiment to study the expressions and localisations of Caspase-8, 9 and 3 in the tumor tissues of experimental animals (Fig. 6G–I). The extent and intensity of DAB expression was considered as the marker of expression of the proteins of interest. It was observed that the IHC results were in line with the results obtained from Western blotting. Caspase-9, caspase-8 and caspase-3 as well showed higher expression and localisation in the tumor tissues obtained from animals of Group-III, that were treated with the higher dose as compared to that of Group-II. The untreated group, as expected, showed negligible expressions of these three pro-apoptotic proteins.

3.13. *VOL is overall non-toxic to healthy body tissues*

The VOL treated mice were regularly checked for any changes in their coat colour, or reduction in weight, throughout the treatment period, to get a hint of any toxicity that was occurring in the animals' bodies due to the treatment. Furthermore, there was no change in coat colour of treated animals (Fig. 6D), the tumors visibly reduced in size in animals of Group-III, and the mice belonging to Groups II, III, IV, V and VI continued to grow normally in terms of body weight (as compared to sporadic rise in body weights of mice from Group-I), that is, there was no reduction or halt in their growth (Fig. 9A).

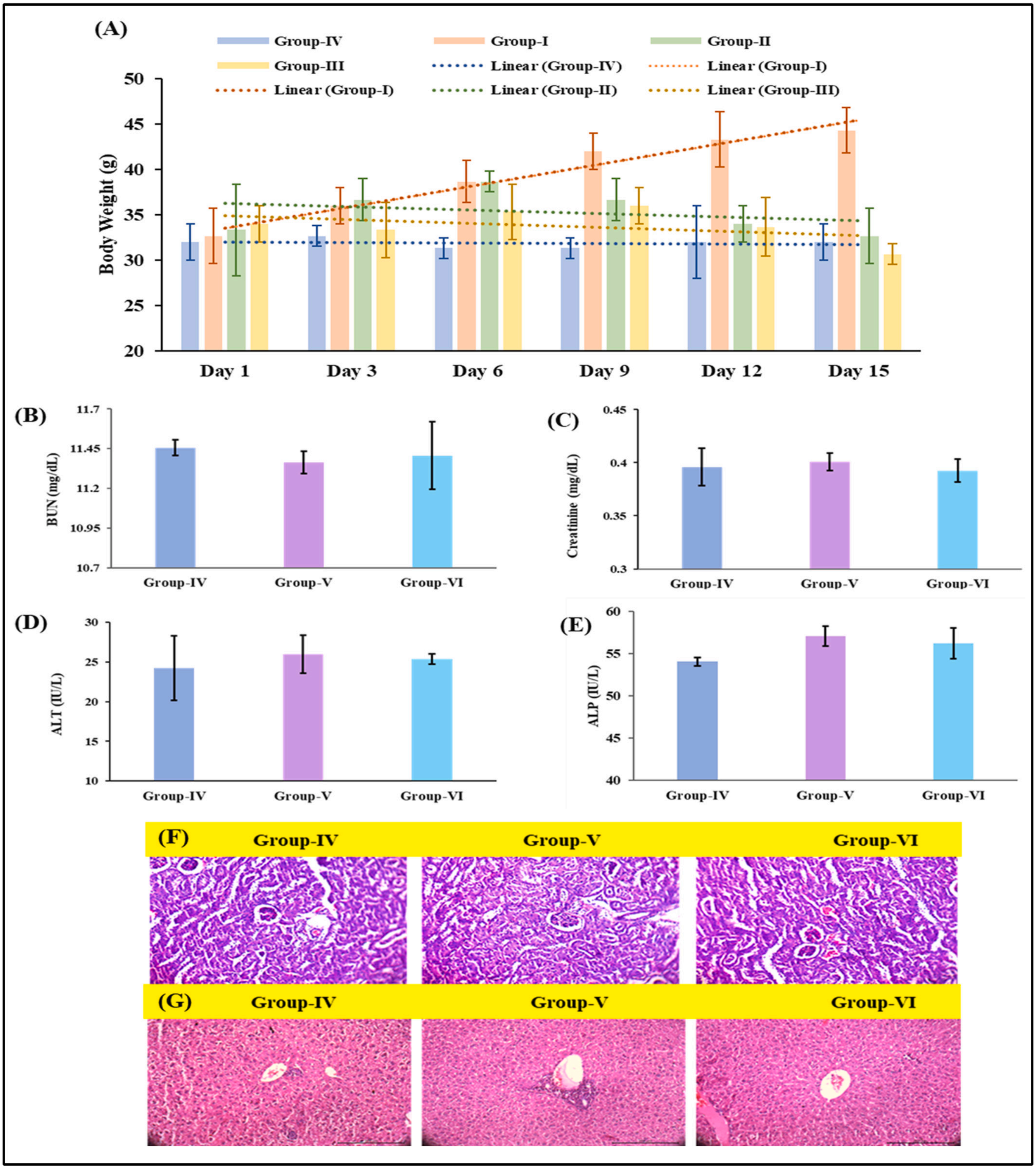

Fig. 9. *In vivo* systemic toxicity profile of VOL: (A) Body weight (in gram) of experimental mice from Group-I–IV; (B) Serum creatinine level; (C) Serum BUN level; (D) Serum ALT level; (E) Serum ALP level of experimental mice of Group-IV–VI. Each column is represented as mean ± SD, $n = 6$. (F) Representative H & E-stained histological sections of renal and hepatic tissues under 20× magnification.

3.14. VOL does not alter basic liver and kidney parameters significantly

The serum obtained from treated and untreated experimental animals from all six groups were checked for the levels of major liver and kidney health parameters, that is, ALT, ALP, BUN and creatinine (Fig. 9B–D). The experiments gave promising results as it was observed that VOL treatment in any of the two doses did not render any major toxicity to the animals belonging to group-V and VI. This result was further strengthened by observing H & E-stained kidney and liver tissue sections from respective experimental groups establishing no significant systemic cytotoxicity of our candidate compound VOL (Fig. 9F & G). The levels of all the four toxicity parameters remained nearly similar to that of control healthy animals of group-IV.

4. Conclusion

The present work demonstrates potent anticancer activities of synthesized novel oxidovanadium complex VOL, which has been summarised in Fig. 10. VOL was found to exert dose-dependent cytotoxicity in human breast cancer cells with an almost equal anticancer potency of cisplatin. Due to off-target toxicity, cisplatin is known to cause some serious side effects related to healthy tissues in cancer patient [6,42]. However, in contrast to such popular platinum-based metallodrug cisplatin, VOL exhibited minimal toxicity to normal cell *in vitro* which was validated both by MTT and LDH leakage assays. Additionally, VOL was recorded with no serious toxicity vital organs such as liver and kidney when checked *in vivo* as well. Getting normal serum hepatic and

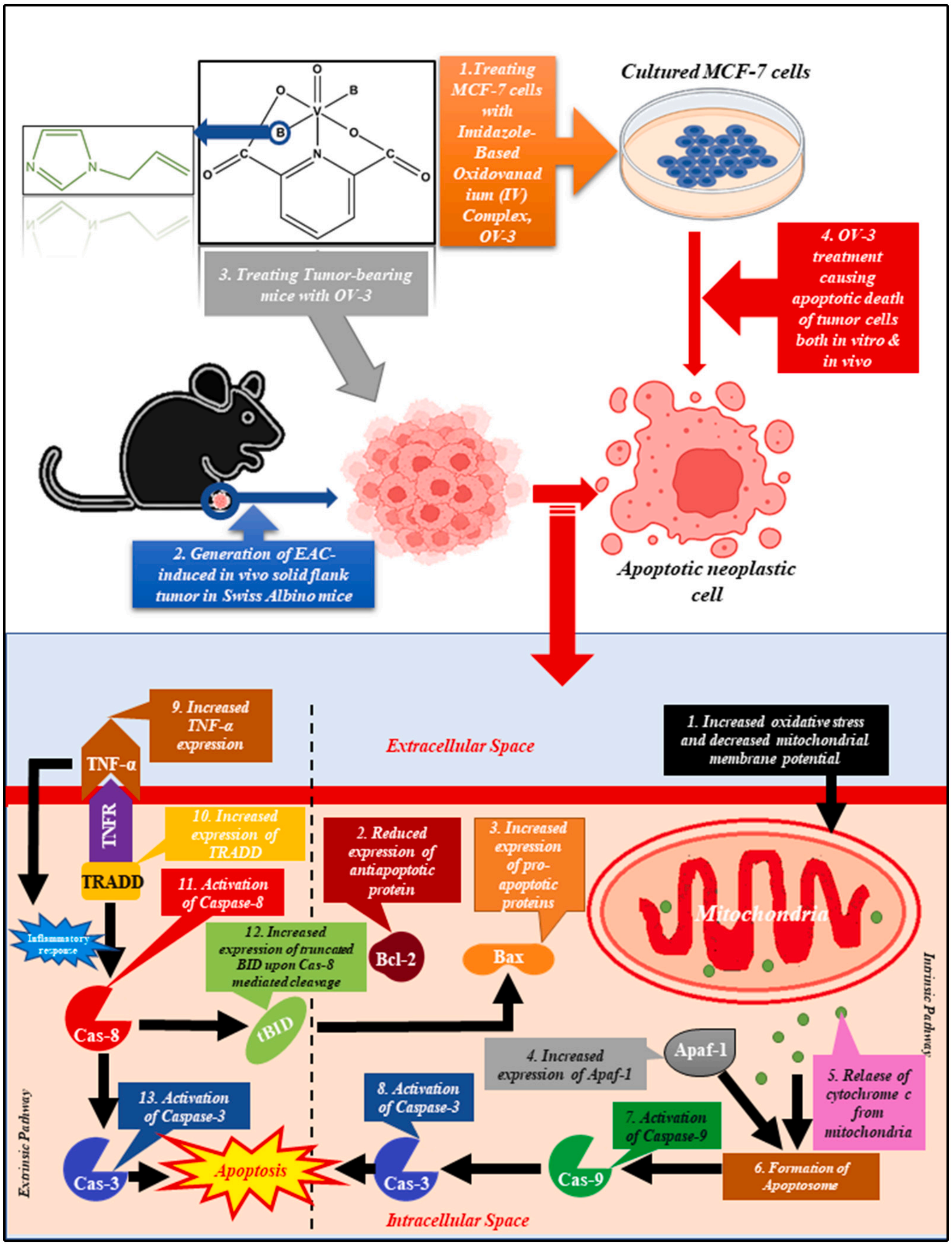

Fig. 10. Schematic diagram representing the anti-cancer activity of VOL: *In vitro* (in MCF-7 cells) and *in vivo* (in Swiss Albino mice) anti-tumor efficacy of novel water soluble mononuclear dipicolinic acid-imidazole based oxidovanadium (IV) complex VOL.

renal toxicity markers along with normal histological interpretation of liver and kidney sections are enough to satisfy its minimal off-target toxicity though VOL was potent enough to reduce tumor volume and mass over just a 14-day-long treatment period. Moreover, splenomegaly imposed in tumor bearing mice was found to show betterment with increasing dose of VOL in Swiss Albino mice. When, investigated deep into its working mechanism, VOL was found to activate both intrinsic and extrinsic pathway of programmed cell death. VOL was recorded to trigger mitochondrial apoptosis by alternating fine balance between cellular pro-apoptotic and anti-apoptotic factors. Increased intracellular ROS load and subsequent decreased mitochondrial potential came out as the chief controller here. Study with NAC, clearly indicated towards ROS-dependent apoptosis induction by VOL. In order to bypass oxidative stress tumor cells are known have higher than normal level and/or activity of antioxidant enzymes [43]. VOL was recorded to reduce antioxidant enzyme activity and level both *in vitro* and *in vivo* increasing the overall possibility of intrinsic apoptosis induction. Besides, VOL was found to trigger higher inflammatory response in tumor tissues which was further observed to elicit extra-mitochondrial apoptosis. Moreover, *in vivo* immunoblot analysis was found the merger of extrinsic apoptotic pathway with the intrinsic one, together attributing a stronger cell killing ability of VOL From the observations made here, it can be postulated that like most of oxidovanadium complex, oxidative damage seems to be the main mechanism by which VOL initiates apoptosis. Unlike platinum-containing drugs such as CIS that form potentially mutagenic covalent DNA adducts, anticancer activity of oxidovanadium complexes such as VOL is mostly due to their non-covalent DNA interaction and ability for ROS production [44]. In contrast to CIS, metallodrugs such as VOL function by inhibiting DNA synthesis and exerting antimitotic activity. Epigenetic changes at cellular and molecular levels due to DNA adduct formation (by interaction at N7 reaction centre of purines of deoxynucleotides) is the main key behind CIS-driven chemoresistance which can be bypassed through the use of metallodrugs such as VOL which follow a separate cell killing mechanism in cancer cells. Additionally, reduced accumulation of platinide drugs, increased level of DNA damage repair, increased detoxification by GSH are thought to be also responsible for CIS-mediated chemoresistance [45]. In this context, anticancer oxidovanadate compounds such as VOL must be scrutinized further. However, briefly, VOL and CIS, despite of their similar anticancer and tumor-inducing properties, differ fundamentally in their mode of action. Based on several existing reports, it is well known that vanadium (IV)-containing inorganic compounds are capable of 2′-deoxyguanosine hydroxylation and subsequent ROS-mediated DNA breakage [46,47]. Additionally, VOL has been observed to induce anticancer effect *via* inducing ROS prior to change in oxidative status of cell and related increase in mitochondrial permeability. Thus, so far as discussed, VOL can represent a potent anticancer metallodrug as platinide alternatives in breast cancer treatment.

CRediT authorship contribution statement

Noyel Ghosh: Conceptualization, Methodology, Software, Validation, Data curation, Formal analysis, Investigation, Writing – original draft, Visualization, Writing – review & editing. **Sharmistha Chatterjee:** Methodology, Validation, Data curation, Formal analysis, Investigation, Visualization. **Debanjana Biswal:** Methodology, Investigation. **Nikhil Ranjan Pramanik:** Methodology, Investigation, Visualization. **Syamal Chakrabarti:** Methodology, Investigation, Visualization. **Parames C. Sil:** Conceptualization, Validation, Data curation, Formal analysis, Visualization, Writing – review & editing.

Declaration of competing interest

The authors declare that they have no known competing financial interests or personal relationships that could have appeared to influence the work reported in this paper.

Acknowledgements

The authors acknowledge DST and UGC for proving financial assistance. Authors are thankful to our lab members Dr. Pritam Sadhukhan for helping with the planning of experiments and Abhishek Kumar Das for helping in execution of the experiments. We extend our sincere gratitude to all of them.

References

[1] N. Li, Z. Wang, Y. Zhang, K. Zhang, J. Xie, Y. Liu, W. Li, N. Feng, Curcumin-loaded redox-responsive mesoporous silica nanoparticles for targeted breast cancer therapy, Artif. Cells Nanomed. Biotechnol. 46 (sup2) (2018) 921–935.

[2] A. Gupta, K. Shridhar, P. Dhillon, A review of breast cancer awareness among women in India: cancer literate or awareness deficit? Eur. J. Cancer 51 (14) (2015) 2058–2066.

[3] N. Sawada, Risk and preventive factors for prostate cancer in Japan: the Japan public health center-based prospective (JPHC) study, J. Epidemiol. 27 (1) (2017) 2–7.

[4] H. Baharum, W.-C. Chu, S.-S. Teo, K.-Y. Ng, R.A. Rahim, C.-L. Ho, Molecular cloning, homology modeling and site-directed mutagenesis of vanadium-dependent bromoperoxidase (GcVBPO1) from Gracilaria changii (Rhodophyta), Phytochemistry 92 (2013) 49–59.

[5] S. Ahmad, A.A. Isab, S. Ali, A.R. Al-Arfaj, Perspectives in bioinorganic chemistry of some metal based therapeutic agents, Polyhedron 25 (7) (2006) 1633–1645.

[6] D. Wang, S.J. Lippard, Cellular processing of platinum anticancer drugs, Nat. Rev. Drug Discov. 4 (4) (2005) 307–320.

[7] S.E. Sherman, S.J. Lippard, Structural aspects of platinum anticancer drug interactions with DNA, Chem. Rev. 87 (5) (1987) 1153–1181.

[8] E.J. Anthony, E.M. Bolitho, H.E. Bridgewater, O.W. Carter, J.M. Donnelly, C. Imberti, E.C. Lant, F. Lermyte, R.J. Needham, M. Palau, Metallodrugs are unique: opportunities and challenges of discovery and development, Chem. Sci. 11 (48) (2020) 12888–12917.

[9] E. Boros, P.J. Dyson, G. Gasser, Classification of metal-based drugs according to their mechanisms of action, Chem 6 (1) (2020) 41–60.

[10] E. Kioseoglou, S. Petanidis, C. Gabriel, A. Salifoglou, The chemistry and biology of vanadium compounds in cancer therapeutics, Coord. Chem. Rev. 301 (2015) 87–105.

[11] D.C. Crans, K.A. Woll, K. Prusinskas, M.D. Johnson, E. Norkus, Metal speciation in health and medicine represented by iron and vanadium, Inorg. Chem. 52 (21) (2013) 12262–12275.

[12] D. Rehder, Bioinorganic Vanadium Chemistry 30, John Wiley & Sons, 2008.

[13] D. Rehder, The role of vanadium in biology, Metallomics 7 (5) (2015) 730–742.

[14] A.S. Tracey, G.R. Willsky, E.S. Takeuchi, Vanadium: chemistry, biochemistry, pharmacology and practical applications, CRC Press, 2007.

[15] H. Zaporowska, A. Scibior, Hematological effects of vanadium on living organisms, in: Advances in Environmental Science and Technology-New York 31, 1998, pp. 135–158.

[16] A.M. Evangelou, Vanadium in cancer treatment, Crit. Rev. Oncol. Hematol. 42 (3) (2002) 249–265.

[17] I.E. Leon, V. Porro, A.L. Di Virgilio, L.G. Naso, P.A.M. Williams, M. Bollati-Fogolín, S.B. Etcheverry, Antiproliferative and apoptosis-inducing activity of an oxidovanadium (IV) complex with the flavonoid silibinin against osteosarcoma cells, J. Biol. Inorg. Chem 19 (1) (2014) 59–74.

[18] Y. Wu, Y. Ma, Z. Xu, D. Wang, B. Zhao, H. Pan, J. Wang, D. Xu, X. Zhao, S. Pan, Sodium orthovanadate inhibits growth of human hepatocellular carcinoma cells in vitro and in an orthotopic model in vivo, Cancer Lett. 351 (1) (2014) 108–116.

[19] A.P. Gonçalves, A. Videira, P. Soares, V. Máximo, Orthovanadate-induced cell death in RET/PTC1-harboring cancer cells involves the activation of caspases and altered signaling through PI3K/Akt/mTOR, Life Sci. 89 (11–12) (2011) 371–377.

[20] S. Petanidis, E. Kioseoglou, M. Hadzopoulou-Cladaras, A. Salifoglou, Novel ternary vanadium-betaine-peroxido species suppresses H-ras and matrix metalloproteinase-2 expression by increasing reactive oxygen species-mediated apoptosis in cancer cells, Cancer Lett. 335 (2) (2013) 387–396.

[21] D. Biswal, N.R. Pramanik, S. Chakrabarti, N. Chakraborty, K. Acharya, S.S. Mandal, S. Ghosh, M.G. Drew, T.K. Mondal, S. Biswas, Lewis base controlled supramolecular architectures via non-covalent interactions of dioxomolybdenum (vi) complexes with an ONS donor ligand: DFT calculations and biological study, New J. Chem. 39 (4) (2015) 2778–2794.

[22] J. Das, A. Sarkar, P.C. Sil, Hexavalent chromium induces apoptosis in human liver (HepG2) cells via redox imbalance, Toxicol. Rep. 2 (2015) 600–608.

[23] M. Kundu, P. Sadhukhan, N. Ghosh, S. Ghosh, S. Chatterjee, J. Das, G. Brahmachari, P.C. Sil, In vivo therapeutic evaluation of a novel bis-lawsone derivative against tumor following delivery using mesoporous silica nanoparticle based redox-responsive drug delivery system, Mater. Sci. Eng. C 126 (2021), 112142.

[24] G. Fotakis, J.A. Timbrell, In vitro cytotoxicity assays: comparison of LDH, neutral red, MTT and protein assay in hepatoma cell lines following exposure to cadmium chloride, Toxicol. Lett. 160 (2) (2006) 171–177.

[25] J. Ghosh, J. Das, P. Manna, P.C. Sil, Cytoprotective effect of arjunolic acid in response to sodium fluoride mediated oxidative stress and cell death via necrotic pathway, Toxicol. in Vitro 22 (8) (2008) 1918–1926.

[26] A. Cossarizza, R. Ferraresi, L. Troiano, E. Roat, L. Gibellini, L. Bertoncelli, M. Nasi, M. Pinti, Simultaneous analysis of reactive oxygen species and reduced glutathione content in living cells by polychromatic flow cytometry, Nat. Protoc. 4 (12) (2009) 1790–1797.

[27] P. Sadhukhan, S. Saha, P.C. Sil, Anti-oxidative effect of genistein and mangiferin on sodium fluoride induced oxidative insult of renal cells: a comparative study, Biomark. J. 2 (1) (2016).

[28] S. Saha, P. Sadhukhan, K. Sinha, N. Agarwal, P.C. Sil, Mangiferin attenuates oxidative stress induced renal cell damage through activation of PI3K induced akt and Nrf-2 mediated signaling pathways, Biochem. Biophys. Rep. 5 (2016) 313–327.

[29] M. Kundu, P. Sadhukhan, N. Ghosh, S. Chatterjee, P. Manna, J. Das, P.C. Sil, pH-responsive and targeted delivery of curcumin via phenylboronic acid-functionalized ZnO nanoparticles for breast cancer therapy, J. Adv. Res. 18 (2019) 161–172.

[30] A. Sarkar, J. Das, P. Manna, P.C. Sil, Nano-copper induces oxidative stress and apoptosis in kidney via both extrinsic and intrinsic pathways, Toxicology 290 (2–3) (2011) 208–217.

[31] S. Pal, P.B. Pal, J. Das, P.C. Sil, Involvement of both intrinsic and extrinsic pathways in hepatoprotection of arjunolic acid against cadmium induced acute damage in vitro, Toxicology 283 (2–3) (2011) 129–139.

[32] P.J. Hissin, R. Hilf, A fluorometric method for determination of oxidized and reduced glutathione in tissues, Anal. Biochem. 74 (1) (1976) 214–226.

[33] P. Sadhukhan, S. Saha, K. Sinha, G. Brahmachari, P.C. Sil, Selective pro-apoptotic activity of novel 3, 3′-(aryl/alkyl-methylene) bis (2-hydroxynaphthalene-1, 4-dione) derivatives on human cancer cells via the induction reactive oxygen species, PLoS One 11 (7) (2016), e0158694.

[34] M. Sinha, P. Manna, P.C. Sil, Taurine, a conditionally essential amino acid, ameliorates arsenic-induced cytotoxicity in murine hepatocytes, Toxicol. in Vitro 21 (8) (2007) 1419–1428.

[35] P. Kakkar, B. Das, P. Viswanathan, A Modified Spectrophotometric Assay of Superoxide Dismutase, 1984.

[36] J. Bonaventura, W. Schroeder, S. Fang, Human erythrocyte catalase: an improved method of isolation and a reevaluation of reported properties, Arch. Biochem. Biophys. 150 (2) (1972) 606–617.

[37] A.H. Fischer, K.A. Jacobson, J. Rose, R. Zeller, Hematoxylin and eosin staining of tissue and cell sections, Cold Spring Harb. Protoc. 2008 (5) (2008), pdb.prot4986.

[38] H. Ohkawa, W. Ohishi, K. Yagi, Colorimetric method for determination of MDA activity, Biochemistry 95 (1979) 351.

[39] S. Banerjee, S. Ghosh, K. Sinha, S. Chowdhury, P.C. Sil, Sulphur dioxide ameliorates colitis related pathophysiology and inflammation, Toxicology 412 (2019) 63–78.

[40] S. Parasuraman, R. Raveendran, R. Kesavan, Blood sample collection in small laboratory animals, J. Pharmacol. Pharmacother. 1 (2) (2010) 87.

[41] M. Ahir, S. Bhattacharya, S. Karmakar, A. Mukhopadhyay, S. Mukherjee, S. Ghosh, S. Chattopadhyay, P. Patra, A. Adhikary, Tailored-CuO-nanowire decorated with folic acid mediated coupling of the mitochondrial-ROS generation and miR425-PTEN axis in furnishing potent anti-cancer activity in human triple negative breast carcinoma cells, Biomaterials 76 (2016) 115–132.

[42] R.A. Alderden, M.D. Hall, T.W. Hambley, The discovery and development of cisplatin, J. Chem. Educ. 83 (5) (2006) 728.

[43] S. George, H. Abrahamse, Redox potential of antioxidants in cancer progression and prevention, Antioxidants 9 (11) (2020) 1156.

[44] L. Kuo, A. Li, T. Marks, Metal Ions in Biological Systems: Metallocene Interactions With DNA and DNA-processing Enzymes 33, Marcel Dekker, 1996.

[45] S.-H. Chen, J.-Y. Chang, New insights into mechanisms of cisplatin resistance: from tumor cell to microenvironment, Int. J. Mol. Sci. 20 (17) (2019) 4136.

[46] X. Shi, H. Jiang, Y. Mao, J. Ye, U. Saffiotti, Vanadium (IV)-mediated free radical generation and related 2′-deoxyguanosine hydroxylation and DNA damage, Toxicology 106 (1–3) (1996) 27–38.

[47] X. Shi, P. Wang, H. Jiang, Y. Mao, N. Ahmed, N. Dalal, Vanadium (IV) causes 2'-deoxyguanosine hydroxylation and deoxyribonucleic acid damage via free radical reactions, Annals of Clinical & Laboratory Science 26 (1) (1996) 39–49.

International Journal of Pharmaceutics 631 (2023) 122555

Contents lists available at ScienceDirect

International Journal of Pharmaceutics

journal homepage: www.elsevier.com/locate/ijpharm

pH-responsive and targeted delivery of chrysin via folic acid-functionalized mesoporous silica nanocarrier for breast cancer therapy

Noyel Ghosh [a], Mousumi Kundu [a], Sumit Ghosh [a], Abhishek Kumar Das [a], Samhita De [a], Joydeep Das [b,*], Parames C. Sil [a,*]

[a] *Division of Molecular Medicine, Bose Institute, P-1/12, CIT Scheme VII M, Kolkata 700054, India*
[b] *Department of Chemistry, Physical Sciences, Mizoram University, Aizawl 796004, Mizoram, India*

A R T I C L E I N F O

Keywords:
Cancer
Chrysin
Mesoporous silica nanoparticle
pH-dependent drug release
Receptor-mediated targeted drug delivery

A B S T R A C T

Cancer is a disease of global importance. In order to mitigate conventional chemotherapy-related side effects, phytochemicals with inherent anticancer efficacy have been opted. However, the use of nanotechnology is essential to enhance the bioavailability and therapeutic efficacy of these phytochemicals. Herein, we have formulated folic acid conjugated polyacrylic acid capped mesoporous silica nanoparticles (~47.6 nm in diameter) for pH-dependent targeted delivery of chrysin to breast cancer (MCF-7) cells. Chrysin loaded mesoporous silica nanoparticles (Chr- $mSiO_2$@PAA/FA) have been noted to induce apoptosis in MCF-7 cells through oxidative insult and mitochondrial dysfunction with subsequent G_1 arrest. Further, in tumor bearing mice, intravenous incorporation of Chr-$mSiO_2$@PAA/FA has been noticed to enhance the anti-neoplastic effects of chrysin via tumor site-specific accumulation. Enhanced cytotoxicity of chrysin contributed towards *in vivo* tumor regression, restoration of normalized tissue architecture and maintenance of healthy body weight. Besides, no serious systemic toxicity was manifested in response to Chr-$mSiO_2$@PAA/FA administration *in vivo*. Thus, the study evokes about the anticancer potentiality of chrysin and its increased therapeutic activity via incorporation into folic acid conjugated mesoporous silica nanoparticles, which may hold greater impact in field of future biomedical research.

1. Introduction

Despite of the remarkable advances in fundamental cancer biology in the last quarter century, cancer stands as the second leading cause for common death involving approximately 10 million deaths worldwide as recorded in 2020 (Ghosh et al., 2019; Sung et al., 2021). Conventional cancer therapeutic strategies such as tumor removal surgery, hormone therapy, chemotherapy, radiation or even immunotherapy offer only limited benefit in cancer treatment leading to collateral damage to vital organs and reduction in patients' average survival rates (Sengupta and Balla, 2018). Such disparity calls for the significance of advanced and thoughtful strategies facilitating cancer therapeutics (Das et al., 2022a).

Abbreviations: ALP, Alkaline phosphatase; ALT, Alanine aminotransferase; APTES, (3-Aminopropyl) triethoxysilane; Bax, Bcl-2-associated X; BCA, Bicinchoninic acid; Bcl-2, B-cell lymphoma 2; BSA, Bovine serum albumin; BUN, Blood urea nitrogen; CAT, Catalase; CTAB, *N*-cetyltrimethylammonium bromide; DAPI, 4′,6-diamidino-2-phenylindole; DCFDA, Dichlorodihydrofluorescein diacetate; DEE, Drug entrapment efficiency; DDS, Drug delivery system; DLC, Drug loading content; DLS, Dynamic light scattering; DMEM, Dulbecco's Modified Eagle's Medium; DMSO, Dimethyl sulfoxide; EAC, Ehrlich ascites carcinoma; EDC, 1-(3-dimethylaminopropyl)-3-ethyl carbodiimide hydrochloride; EPR, Enhanced permeability and retention effect; FA, Folic acid; FACS, Fluorescence-activated single cell sorting; FBS, Fetal bovine serum; FITC, Fluorescein isothiocyanate; FTIR, Fourier transform infrared spectroscopy; GSSG, Oxidized glutathione; GSH, Reduced glutathione; HPLC, High performance liquid chromatography; H_2O_2, Hydrogen peroxide; HRP, Horseradish peroxidase; IHC, Immunohistochemistry; JC1, Tetraethylbenzimidazolylcarbocyanine iodide; K_2-EDTA, Dipotassium ethylene diamine tetraacetic acid; LDH, Lactate dehydrogenase; MDA, Malonaldehyde; MMP, Mitochondrial membrane potential; mSiO2, Mesoporous silica nanoparticle; MTT, 3-(4,5-dimethylthiazol-2-yl)-2,5-diphenyltetrazolium bromide; NAC, *N*-acetylcysteine; NaCl, Sodium chloride; NaOH, Sodium hydroxide; NHS, *N*-hydroxy succinimide; PAA, Polyacrylic acid; PBS, Phosphate buffered saline; PI, Propidium iodide; RIPA, Radioimmune precipitation assay; ROS, Reactive oxygen species; RPMI, Roswell Park Memorial Institute; SOD, Superoxide dismutase; SDS, Sodium dodecyl sulfate; TBARS, Thiobarbituric acid reactive substance; TEOS, Tetraethylorthosilicate.

* Corresponding authors at: Division of Molecular Medicine, Bose Institute, P-1/12, CIT Scheme VII M, Kolkata 700054, West Bengal, India.
E-mail addresses: jdchem83@gmail.com, joydeep@mzu.edu.in (J. Das), parames@jcbose.ac.in, parames_95@yahoo.co.in (P.C. Sil).

https://doi.org/10.1016/j.ijpharm.2022.122555
Received 10 August 2022; Received in revised form 21 December 2022; Accepted 24 December 2022

In this context, the dreadful effects of traditional cancer therapeutics can be easily bypassed by replacing them with naturally occurring plant derived polyphenolic anticancer compounds. Among various polyphenolic compounds, chrysin (5,7-dihydroxyflavone) extracted from honey, propolis, passion flowers, etc. was initially known for its anti-inflammatory and antioxidant roles (Pushpavalli et al., 2010; Samarghandian et al., 2016). Later on, researches elucidated its proapoptotic effects on several human cancers including gastric (Chen et al., 2021), colorectal (Salama and Allam, 2021), pancreatic (Zhou et al., 2021), breast (Azar et al., 2021) and prostate (Ganai et al., 2021) carcinomas. It was found to mitigate chemo resistance of adriamycin and cisplatin in non-small cell lung carcinoma as well (Xu et al., 2018). However, poor solubility and lower bioavailability due to insufficient absorption and rapid metabolism are the most common challenges for administering chrysin in cancer therapeutics (Walle et al., 2001). In line, bioavailability and potency of chrysin can be upgraded by the assistance of specific targeting ligand-labeled smart nano-drug delivery system (nano-DDS) which will be capable to induce specific interaction with tumor cells and intelligent stimulus-boosted drug unloading performance at tumor microenvironment (Sun et al., 2022; Wang et al., 2021b).

When injected intravenously, in addition to enhanced permeability and retention (EPR) effect (Matsumura and Maeda, 1986), circulating nanoparticles can specifically gathered at the tumor site through surface functionalization with cognate ligand molecules which are proficient of recognizing tumor-specific receptor molecules (Deshayes et al., 2013). Therefore, in a targetable *n*-DDS the surface of the core nanocarriers are often properly harmonized with cognate targeting moieties such as hormones, aptamers (Farokhzad and Langer, 2006), vitamins, peptides, antibodies etc (Cheng et al., 2017; Salmaso et al., 2004). Additionally, an ideal 'smart' DDS must avoid premature unloading at nonspecific sites and should be capable of tailoring therapeutic agents by distinguishing healthy cells from the neoplastic ones (Garcia-Bennett et al., 2011; Salinas et al., 2018; Wang et al., 2021a; Zhu and Chen, 2015). Among various stimuli-guided drug release mechanisms of nanocarriers, change in pH is the most studied one, due to unequivocal occurrence of pH gradient in tumor microenvironment (Kundu et al., 2019). Understanding all the requirements to synthesize successful nano-DDS for chrysin, in the current work, we have formulated, folic acid (FA) ligated, polyacrylic acid (PAA) coated mesoporous silica nanoparticles ($mSiO_2$) with chrysin infiltration which in assemblage act as a superior 'molecular gates' delivering its cargo following the change in pH specific to tumor cells.

$mSiO_2$ has been selected due to its phenomenal features of silica scaffold which is suitable for pH-guided drug unloading at tumor site (Lu et al., 2010; Salinas et al., 2018). The ordered porous network of $mSiO_2$ allows controlled loading of therapeutic agents and their steady release kinetics (Giret et al., 2015; Lei et al., 2019). Overall non-toxicity and chemical inertness of $mSiO_2$ make them suitable as biocompatible *in vivo* therapeutic nanocarrier. Additionally, bigger surface area and the ease of its surface modification using the popular alkoxysilane chemistry uphold $mSiO_2$ as ideal candidate for smart nano-DDS (Renner et al., 2020; Xu et al., 2022). PAA was chosen as it behaves distinctly in different pH. At neutral or basic environment, PAA remains deprotonated and hydrophilic; whereas, at much lower pH it entangles to precipitate and behaves hydrophobically (Peng et al., 2013). Additionally, PAA can be conjugated easily upon $mSiO_2$s' surface either electrostatically or by covalent bonding (Yuan et al., 2011). Besides, PAA installation upon aminated $mSiO_2$ enables controlled release of chrysin as well (Kundu et al., 2020). Whereas, FA which basically belongs to water-soluble vitamin B-complex family, is stable and nonimmunogenic (Chowdhuri et al., 2016; Salmaso et al., 2004; Tao et al., 2015); thus, using it as a tagging agent prevents immunogenic recognition of $mSiO_2$ nanocarrier by reticuloendothelial system and prolongs the overall circulation time. Furthermore, FA exhibits higher affinity for folate receptors (a type of folate-binding glycosylphosphatidylinositol (GPI)-linked cell surface receptor) (Porta et al., 2013). Folate receptors are overexpressed on variety of cancer tissues including breast (Karamipour et al., 2015; Leamon and Reddy, 2004), ovarian, lung, kidney and cancers arrived from epithelial tissue (Garin-Chesa et al., 1993; Parker et al., 2005). However, sarcoma, lymphoma as well as carcinomas originating from bladder, liver, prostate and testicles lack expression of folate receptors. On the other hand, they are expressed on limited basis on the apical surfaces of polarized epithelia of normal tissues including lung, choroid plexus, kidney and placenta etc (Parker et al., 2005). Such precision enables folate-tagged nanocarrier for selectively target cancer cells. After attachment of folate to the folate receptor within caveolae, they are internalized via endocytic pathway. At the acidic pH (pH 5.0) of endosomes, folic acid dissociates from the receptor for the required drug release (Zwicke et al., 2012). Here, we have invented novel nano-DDS using FA-targeted $mSiO_2$ using PAA-assisted pH-dependent release of chrysin specific to tumor cells reducing collateral damages. In addition to mesoporous silica-based nano-DDS, we have also studied enhanced cellular uptake of chrysin nano-formulation and reactive oxygen species (ROS)-induced enhanced apoptotic as well as anticancer potency of chrysin in human breast carcinoma cells MCF-7. Also, molecular pathway responsible for chrysin-based nano-DDS induced apoptosis of MCF-7 cells has been studied translationally with the same, replicated *in vivo* using Ehrlich Ascites Carcinoma (EAC) cell induced solid tumors in Swiss Albino mice.

2. Experimental section

2.1. Chemicals

PAA, chrysin and 99 % extra pure APTES were bought from Sigma-Aldrich. FA, NaOH, NaCl, disodium hydrogen phosphate dihydrate, 99 % pure EDC. HCl, TEOS, CTAB, 97 % NHS, MTT reagent and BSA were purchased from SRL, India. VECTASHILD mounting medium was purchased from Vector Laboratories, Inc. Burlingame, CA 94010. Ethanol and DMSO were obtained from Merck. DMEM, RPMI-1640, antibiotics and amino acids were provided by Hi-Media, India. Fetal bovine serum (FBS) was obtained from Thermo Scientific Hy-Clone, USA. BCA kit was obtained from Thermo Fisher Scientific, USA. Antibodies were provided by Abcam (Cambridge, UK), Cell Signaling (USA), Novus Biologicals (USA) and BioBharti Life Sciences Private Limited, India.

2.2. Preparation of amine functionalized $mSiO_2$

Preparation of $mSiO_2$ was done by adapting the method described in previously reported literature (Kundu et al., 2021; Xiao et al., 2014). In a nutshell, 1 gm of CTAB and 280 mg of NaOH were dissolved in 480 mL ultrapure deionized water at 80 °C with vigorous stirring. Next, 6.7 mL of TEOS was added in drop-wise fashion at a point when previous solution became transparent. In order to get aminated $mSiO_2$, 1 mL of APTES was added and left for 5 h of stirring followed by centrifugation. At the end, the surfactant was washed off by refluxing the synthesized product with a mixture of 500 mL ethanol and 6 mL concentrated HCl for 24 h at 78 °C temperature. Finally, the end product was obtained by several times absolute ethanol-wash followed by the centrifugation at 6000 rpm for 10 min and subsequent oven-drying.

2.3. Synthesis of chrysin entrapped $mSiO_2$ (Chr-$mSiO_2$)

For chrysin entrapment, dispersed solution of amine-functionalized $mSiO_2$ was added to DMSO solution of chrysin at 1:2 feed ratio and was kept under stirring condition using magnetic stirrer at 400 rpm for 24 h at room temperature. At this point drug loading profile was checked by calculating drug loading content (DLC) and drug entrapment efficiency (DEE) of $mSiO_2$-Chr through UV–vis spectroscopy at 315 nm. A calibration curve was drawn using absorbance values at distinct known concentrations. DLC and DEE were calculated as follows (Kundu et al., 2019):

DLC (%) = (weight of chrysin lodged in nanoparticle)/(total weight of nanoparticle) × 100.

DEE (%) = (weight of chrysin lodged in nanoparticle)/(weight of chrysin used for drug loading) × 100.

2.4. PAA fabrication upon Chr-mSiO$_2$ (Chr-mSiO$_2$@PAA)

Dispersed solution of Chr-mSiO$_2$ was added to PAA solution in 1:1 wt ratio and was kept stirring at 400 rpm using a magnetic stirrer at 100 °C for 2 h to formulate Chr-mSiO$_2$@PAA (Peng et al., 2013; Xiao et al., 2014).

2.5. Formulation of FA-tagged Chr-mSiO$_2$@PAA (Chr-mSiO$_2$@PAA/FA)

The free carboxyl groups of PAA at Chr-mSiO$_2$@PAA surface were activated by addition of EDC and NHS in a 3 h-long stirring condition with the help of a magnetic stirrer at 400 rpm. Finally, FA (dissolved in DMSO) was added to the reaction mixture in 2:1 wt ratio to Chr-mSiO$_2$@PAA and kept for 24 h in stirring condition to get final nanocomposite, Chr-mSiO$_2$@PAA/FA.

2.6. Preparation of fluorescein isothiocyanate (FITC) tagged mSiO$_2$ nanodevice

In order to check FA receptor-based increased chrysin nanoconjugate uptake, Chr-mSiO$_2$ was tagged with FITC and were processed further to produce Chr-mSiO$_2$@FA/FITC according to method described elsewhere (Hakeem et al., 2016; Zhai et al., 2012). Briefly, Chr-mSiO$_2$ and Chr-mSiO$_2$@FA were mixed with ethanolic solution of FITC and were kept stirring using magnetic stirrer for 24 h at 400 rpm in dark to obtain Chr-mSiO$_2$@FITC and Chr-mSiO$_2$@FA/FITC respectively.

2.7. Characterization

Size of the nanoparticle was measured using transmission electron microscope or TEM (Tecnai G2 TF-20–200 KV). Morphology and the structure of the synthesized nanoconjugates were observed by scanning electron microscope or SEM (JSM7600F, JEOL, Japan). To clarify successful loading of chrysin and further addition of PAA and FA, a series of experiments were performed. The Fourier-transform infrared (FTIR) spectra of the samples were collected in a range of 4000 cm^{-1}–400 cm^{-1} with FTIR-analyzer (NEXUS-470, Nicolet, USA) using KBr pellets. UV–vis spectra of the nanocomposites were recorded using Shimadzu spectrophotometer. Furthermore, both hydrodynamic size and zeta potential of the synthesized nanoconjugates were measured from their aqueous suspension through dynamic light scattering (DLS) using Delsa™ Nano C particle size analyzer, Beckman Coulter, Brea, CA, USA.

2.8. Hemolytic assay

Hemolytic study of nanoconjugates was performed according to the protocol established elsewhere (Chen et al., 2019b; Evans et al., 2013). Initially, 2 mL human blood was collected in K$_2$-EDTA coated vials to prevent blood coagulation. Collected blood was centrifuged for 5 min at 500 × *g*; after which sedimented pellet and plasma supernatant volume was marked on hematocrit tube. Next, plasma was discarded and replaced by 150 mM NaCl solution and mixed well. Then, the solution was centrifuged again at 500 × *g* for 5 min. This time, supernatant was discarded again and replaced by equal volume of PBS (pH 7.4). RBC solution was 50 times diluted further using PBS. Then, 100 µL of mSiO$_2$ and mSiO$_2$@PAA/FA solutions of five different concentrations (0.5, 1.0, 2.0, 4.0, 8.0, 10.0 mg mL^{-1}) were added to diluted 1.9 mL of RBC solution to get final mSiO$_2$ and mSiO$_2$@PAA/FA solutions of 25, 50, 100, 200, 400 and 500 µg mL^{-1} concentrations. The solutions were shaken at 100 rpm for 1 h at 37 °C temperature followed by centrifugation at 500 × *g* for 5 min. Finally, supernatants were analyzed spectrophotometrically at 541 nm. 100 µL of each 20 % triton-X-100 and 1X PBS (pH 7.4) were used as positive and negative controls respectively. Hemolysis percentage was calculated as follows (Chen et al., 2019b):

Hemolysis % = (absorbance of samples − absorbance of negative control)/(absorbance of positive control − absorbance of negative control) × 100.

2.9. Protein adsorption assay

Protein adsorption onto the surface of synthesized nanoparticles was estimated by studying adsorption of BSA [34]. 60 mg of BSA was dissolved in 100 mL of distilled water. Then 5 mL of each 2 mg mL^{-1} PBS suspension of mSiO$_2$, mSiO$_2$@PAA and mSiO$_2$@PAA/FA were added to 5 mL of prepared BSA solution. Sample mixtures were kept in shaking condition at 135 rpm for 4 h at 37 °C temperature; after which upper clear solutions were collected and subsequent BSA concentrations were checked by BCA kit at 562 nm. Adsorbed amount of BSA for each sample was calculated using the following equation (Chen et al., 2019b).

BSA adsorption = [(initial concentration of BSA − concentration of BSA in samples) × volume of sample solution]/weight of nanoparticle added.

2.10. Study of chrysin release profile

In order to justify drug release content from nanoconjugates within acidic tumor microenvironment, a mimicking laboratory situation was created extracellularly using PBS (154 mM) of three distinct pH (pH 7.4, pH 6.0 and pH 5.0). To analyze the *in vitro* pH dependent release of chrysin from Chr-mSiO$_2$ and Chr-mSiO$_2$@PAA, PBS was supplemented with 0.1 % Tween 80 to maintain the sink condition for chrysin dissolution in release media (Lungare et al., 2016). 2 mg chrysin containing mSiO$_2$ were dispersed into 2 mL of release medium which were sonicated throughout the experimental time maintained at 100 rpm and 37 °C. Sample were transferred at set time interval and the volume was replaced with an equal volume of pre-warmed release medium (Lungare et al., 2016). Then amount of released chrysin in original buffer solution was determined spectrophotometrically at 315 nm on specific time spots within 0–48 h time span. Percentage of drug release was calculated as (Jabbari et al., 2018):

Drug release (%) = (amount of drug in release medium at time t/amount of drug entrapped in nanoparticle) × 100.

2.11. Cell culture

Human breast adenocarcinoma (MCF-7) cells were purchased from National Centre for Cell Science (NCCS), Pune and noncancerous normal human kidney epithelial (NKE) cells were acquired from Prof. Kaushik Biswas as a gift to satisfy experimental needs. At 37 °C and in a humified 5 % CO$_2$ incubator, both types of cells were routinely maintained in 75 cm^2 culture flasks using RPMI-1640 media with 10 % FBS, streptomycin (0.1 gm L^{-1}) and penicillin (1,00,000 IU/L) incorporation. Cells were allowed to attain monolayered confluency of 70 % (with 5 × 10^5 cell seeding concentration) for any further treatment.

2.12. Study of in vitro cellular uptake and release

MCF-7 cells were treated with equivalent dose of Chr-mSiO$_2$@FITC and Chr-mSiO$_2$@FITC/FA for 3 h, and then washed with 1X PBS. The cell suspension was further centrifuged at 6000 rpm for 5 min to get the cell pellet which was resuspended in 1X PBS and analyzed flowcytometrically at 520 nm to check $mSiO_2$-nanoparticle uptake (Kundu et al., 2021). Apart from that confocal laser scanning microscopy was further used in order to check cellular uptake. MCF-7 cells were precultured on coverslip directly overnight. Afterward, the cells were incubated with Chr-$mSiO_2$@FITC and Chr-$mSiO_2$@FITC/FA (equivalent Chr concentration of 1 μg mL^{-1}) at 37 °C. At predetermined time intervals, the cells were washed with PBS thrice and were mounted with VECTASHIELD mounting media. Finally, the cells were subjected to the CLSM observation (Chen et al., 2019a).

For studying intracellular release of chrysin from nanohybrids, MCF-7 cells were treated with the equivalent dose of free chrysin, Chr-$mSiO_2$@PAA and Chr-$mSiO_2$@PAA/FA for 24 h. After that, the cells were washed with 1X PBS and lysed in lysis buffer. Supernatants from these three treatment groups were then obtained via centrifugation at 6000 rpm for 5 min and checked the amount of released chrysin spectrophotometrically at 315 nm. Release pattern of chrysin was similarly studied on NKE cells as well.

2.13. *Cytotoxicity assay of synthesized chrysin nanoconjugates*

MTT assay was performed to evaluate cytotoxicity of chrysin and chrysin-loaded nanoconjugates. At 70 % confluence, cultivated MCF-7 cells at a density of 1×10^5 cells per well, were chemosensitized with free chrysin, Chr-$mSiO_2$@PAA and Chr-$mSiO_2$@PAA/FA and $mSiO_2$@-PAA/FA. Treatment included a range of five doses (5–40 μg mL^{-1}) for free chrysin and corresponding equivalent concentrations of chrysin-loaded nanoconjugates. Post-24 h of treatment, media was discarded and 100 μL of 0.5 mg mL^{-1} MTT solution was added to each well. After 4 h of incubation at 37 °C, each well received 100 μL DMSO to dissolve purple formazan crystal of MTT and corresponding absorbance was estimated at 570 nm on a microplate reader (Kundu et al., 2019) and the cell viability was calculated. Besides, a similar experiment was carried out for NKE cells.

2.14. *Determination of mode of cell death*

For studying the mode of cell death, 70 % confluent MCF-7 cells were cultured in 6 well plates and exposed to 10 μg mL^{-1} of free chrysin, Chr-$mSiO_2$@PAA and Chr-$mSiO_2$@PAA/FA. After 24 h of incubation cells were mildly scraped and centrifuged for 5 min at 300 × *g* and room temperature. Derived cell pellet was washed in 1X PBS and suspended in 1X Annexin V binding buffer. Next, Annexin V/FITC (1 μL) was incorporated in cell suspension and incubated in dark at room temperature for 5 min followed by quick excitation at 488 nm and analysis fluorescent emission at 520 nm employing FACSVerse cell sorter (Sadhukhan et al., 2016; Sarkar et al., 2016). FACSuite software was employed for data quantification where Annexin V/FITC positive cells were contemplated as apoptotic cells.

Apart from that, mode of cell death was studied through confocal microscopy as well. MCF-7 cells were grown on coverslips in a 12-well plate. Cells were incubated for 24 h with 10 μg mL^{-1} of free Chr, Chr-$mSiO_2$@PAA and Chr-$mSiO_2$@PAA/FA. After diluting Annexin-V/FITC within Annexin-V/FITC binding buffer in a 1:100 ratio, cells on the coverslips were incubated in Annexin V/FITC for 1 h. Next, the cells were washed twice in Annexin-V binding buffer, mounted using VECTASHIELD mounting media, and finally were checked through confocal laser scanning microscopy.

2.15. *Detection of cumulative intracellular ROS*

Intracellular ROS content in MCF-7 cells was made using DCFH-DA (2,7-dichlorodihydro-fluorescein di acetate) (Kundu et al., 2019). For this experiment, MCF-7 cells were seeded (2×10^5) and subsequently, cells were treated in four groups with doses equivalent to the LC_{50} doses of free chrysin, Chr-$mSiO_2$@PAA and Chr-$mSiO_2$@PAA/FA respectively. Later, cells were scraped and centrifuged (at room temperature and 300 × *g* for 5 min) to obtain cell pellet which was suspended in 1 mL PBS. Finally, $DCFH_2$-DA was added to the cell suspension to the final concentration of 2 μM followed by 20 min incubation at 37 °C in dark. Lastly, cells were washed, resuspended in 1X PBS and ROS measurement was carried out at 525 nm employing FACS Calibur flowcytometry. Besides, generated ROS was detected via confocal microscopy using the same DCFH-DA dye in contrast with nuclear staining with DAPI (Sadhukhan et al., 2016).

2.16. *Detection of in vitro mitochondrial membrane potential (MMP)*

Following the treatment with nano-chrysin-formulations, MMP was determined according to the protocol described previously (Sadhukhan et al., 2019) using JC-1 dye. In brief, free chrysin, Chr-$mSiO_2$@PAA and Chr-$mSiO_2$@PAA/FA-treated MCF-7 cells were incubated with 5 mM JC-1 dye and were kept at 37 °C for 30 min. Following centrifugation at 300 × *g* for 5 min, MCF-7 cells were suspended in PBS and were subjected to flow cytometric analysis using their fluorescence emission at 525 nm by BD FACS Caliber flow cytometer.

2.17. *Detection of in vitro GSSG and GSH content*

Intracellular GSH content was quantified using Ellman's reagent following the procedure described elsewhere (Sarkar et al., 2011). Briefly, post-treatment with chrysin, Chr-$mSiO_2$@PAA and Chr-$mSiO_2$@PAA/FA, whole cell lysates of MCF-7 cells from different experimental groups were obtained and centrifuged at 12000 rpm for 15 min. Next, Ellman's reagent (DTNB solution) was added to the cell lysates and the absorbance was recorded at 412 nm based on DTNB reduction. Cellular GSH content was calculated with reference to a GSH standard curve and values were expressed in μmol mg^{-1} of protein.

GSSG content was then detected following the method described by Hissin and Hilf in 1976 (Hissin and Hilf, 1976). Similar to GSH estimation procedure, cell lysate from each experimental group was first added up with 400 mM NEM to limit further oxidation of GSH to GSSG, followed by 30 min incubation at room temperature. Following the incubation, 300 mM Na_2HPO_4 and DNTB solution were added. Lastly, spectrophotometric absorbance was calculated again at 412 nm (Sinha et al., 2007).

2.18. *Assessment of in vitro lipid peroxidation*

Post-treatment with nano-formulations, the occurrence of increased oxidative stress was ensured by assessing extent of intracellular lipid peroxidation in both control and treated groups. Lipid peroxidation was measured in term of MDA content (Manna et al., 2009; Sadhukhan et al., 2016). In gist, cells from different experimental groups were lysed to obtain whole cell lysate. Cell lysates were treated with 0.67 % thiobarbituric acid and 20 % trichloro acetic acid. The mixtures were heated at 100 °C for 60 min, cooled down to room temperature and then were centrifuged to eliminate any precipitate. Finally, the clear supernatants were evaluated spectrophotometrically for absorbance at 535 nm.

2.19. *Assessment of ROS-scavenging enzymes*

Activity of ROS-scavenging antioxidant enzymes such as SOD and CAT were assayed from the cell lysate of control and treated experimental groups of MCF-7 cells. The procedure followed here, has been describe somewhere else (Sinha et al., 2007).

2.20. *Cell cycle analysis*

Cultured MCF-7 cells were analyzed for cell cycle progression after being treated with free chrysin and Chr-$mSiO_2$@PAA/FA. Cell cycle analysis was made flow-cytometrically using the protocol of Riccardi et al (Das et al., 2015; Riccardi and Nicoletti, 2006). Concisely, after synchronized culture, MCF-7 cells were exposed to desired doses of Chr-mSiO$_2$@PAA/FA and MSN-NH$_2$-PAA-FA. After 24 h of harvesting, cells were washed with cold PBS and were fixed with 70 % ethanol for 4 h at 4 °C temperature. Following fixation, cells were centrifuged at 1500 rpm for 4 min followed by 2 % FBS supplemented PBS wash twice and ribonuclease treatment. Thereafter, 50 μg mL^{-1} PI was used to incubate cells for 30 min at 37 °C followed by fluorescence measurement at 617 nm using FACS calibur system (BD biosciences) by the Cell Quest software. ModFit LT software (BD Biosciences) was employed to examine the percentages of MCF-7 cells in respective cell cycle phases. Here, PI fluorescence has been calculated along x-axis displaying DNA content versus cell counts along y-axis.

2.21. Protein extraction & immuno-blotting

For immunoblotting, MCF-7 cells were plated in 96-wells at 70 % confluency. Cells were treated with LC$_{50}$ dose of free chrysin and corresponding equivalent doses of Chr-mSiO$_2$@PAA and Chr-mSiO$_2$@PAA/FA respectively in contrast to a batch of cells left untreated (control group). After 24 h of treatment, cells were washed with 1X PBS, resuspended and were lysed by buffer solution containing 0.5 % sodium deoxycholate, 150 mM sodium chloride, Triton X-100, 50 mM Tris and 0.1 % SDS. During lysis, buffers were supplemented with phosphatase and protease inhibitors (pH 8). Following lysis, lysate was centrifuged at 12000 rpm for 10 min at 4 °C. Supernatants from the centrifuged samples were collected and utilized for protein concentration measurement at 562 nm using BCA assay kit (Das et al., 2022b; Ghosh et al., 2022a).

Next, equal amount of proteins from each experimental group were resolved on SDS-PAGE gel (10–12 %), transferred on PVDF membranes following the established standard protocol (Ghosh et al., 2018; Ghosh et al., 2022b; Sadhukhan et al., 2016). To avoid non-specific protein binding, membranes were blocked with 5 % BSA solution. Afterwards, membranes were probed with specific primary antibodies (1:1000 dilution) against β-actin (internal loading control), GSK-3β, cyclin D1, p-Akt, cytochrome *C*, Apaf-1, Bax, Bcl-2, cleaved caspase 9 and cleaved caspase 3 for 24 h at 4 °C temperature. On next day, 2 h of incubation with HRP-conjugated secondary antibody (1:20,000 dilution) was employed to cross-mount primary antibodies after through washing with wash buffer. Finally, ECL solution was used to visualize protein expression on X-ray films (Sarkar and Sil, 2014).

2.22. Inhibitor study

To check whether the cell-killing ability of Chr-mSiO$_2$ is ROS-influenced, a batch of MCF-7 cells pre-treated with 5 mM of NAC (a highly effective antioxidant) were retreated with Chr-mSiO$_2$@PAA/FA (Das et al., 2015; Ghosh et al., 2022a) and were compared with MCF-7 cells treated with Chr-mSiO$_2$@PAA/FA (15 μg mL^{-1}) alone for a series of studies. Cells were compared on the basis of their intracellular ROS content, percentage of cell viability through MTT assay, extent of apoptotic cell death via Annexin V staining and immunoblot analysis for Bcl-2, Bax and cleaved caspase-3.

2.23. EAC-induced tumor regression study in Swiss Albino mice

Thirty Swiss Albino mice (4–6 weeks old and weighing 23–25 gm) obtained from central animal house of Bose Institute, Kolkata, India, were acclimatized in a temperature-controlled laboratory room with proper twelve-hour light–dark cycle furnishing with proper food and water *ad libitum*. Any further experimental planning was done according to the guidelines provided by Institutional Animal Ethics Committee (IAEC) of Bose Institute, Kolkata [Approval no. IAEC/BI/142/2019]. *In vivo* experimental facilities were registered with Committee for the Purpose of Control and Supervision on Experiments on Animals (CPCSEA), Ministry of Environment and Forests, New Delhi, India (1796/PO/Ere/S/14/CPCSEA) (Kundu et al., 2021). Protocol of tumor inoculation has been summarized in Table 1. Briefly, once acclimatized, 1 × 10^7 EAC cells in 50 μL of PBS were injected intramuscularly in the left flanks of twenty-four mice (on 1st day) and tumors were allowed to grow. After 10 days of tumor inoculation (on 10th day), 24 tumor-bearing mice were divided randomly in four (n = 6/groups) groups (T1, T2, T3 and T4). Wild type mice receiving no EAC injection were designated to group T0. For next 14 days (11th-24th day), mice of all four groups (T1-T4) received intravenous treatment through tail veins as follows:

T0 – control mice.
T1 – treated with intravenous PBS of pH 7.4 (tumor control).
T2 – treated with intravenous chrysin solution (10 mg kg^{-1} body weight).
T3 – treated with intravenous Chr-mSiO$_2$@PAA solution (60.60 mg kg^{-1} body weight).
T4 – treated with intravenous Chr-mSiO$_2$@PAA/FA solution (74 mg kg^{-1} body weight).

During 14 days of treatment each mice received 7 doses of intravenous injection at every alternative day. Mice were also checked for tumor volume on every treatment day. Measurement of tumor volume was done using following equation (Bhattacharya et al., 2015), for the mice in group T1-T4 were taken with the help of caliper also on alternative days.

$$\text{Tumor Volume} = [(\text{tumor length}) \times (\text{tumor width})^2]/2.$$

After completion of 14-day treatment, all mice were sacrificed (on 25th day) by cervical dislocation and precautions were taken to reduce pain and suffering of the animals. Tumors from each group (T1-T4) were collected and checked for respective weight and volume. To evaluate tumor- responsive splenomegaly, spleens were collected.

2.24. Study of in vivo chrysin accumulation in tumor tissue

HPLC was performed to calculate post-treatment assembled amount of chrysin in the tumor tissue. Thus, tumor-bearing mice were grouped into three groups namely, group-I (receiving free chrysin solution at 10 mg kg^{-1} wt intravenously), group-II (treated with intravenous Chr-mSiO$_2$@PAA solution at a dose of 60.60 mg kg^{-1} body weight) and lastly, group-III (treated with 74 mg kg^{-1} Chr-mSiO$_2$@PAA/FA solution intravenously). After 24 h of treatment, mice were sacrificed to collect tumors. 100 mg of tumor tissue from each experimental mice was homogenized using a solvent mixture of 75 % ethanol and 0.05 % DMSO. Homogenates were allowed to centrifuge for pellet sedimentation separation at 10,000 rpm for 15 min. Liquid portion of the supernatant was dried in nitrogen evaporator followed by dissolution of rest in methanol. Methanolic tumor tissue extract (20 μL) from each group was injected into a C$_{18}$ column (250 × 4.5 mm in dimension) at an optimized flow rate of 1 mL min^{-1} using acetonitrile and methanol (65:35) mixture as solvent system (Bharathi, 2019). Lastly, HPLC detection was made on 315 nm spectrophotometrically. For calculating the amount of chrysin in tissue sample solutions, standard methanolic solution of chrysin was prepared and calibrated at five different concentrations (3, 5, 15, 30 and 50 μg mL^{-1}).

2.25. Immunohistochemical study of in vivo proapoptotic behavior of chrysin nanohybrid

Immunohistochemical study was performed for caspase-9 and caspase-3. Formalin-fixed tumor tissues from experimental groups T1-T4 were processed in paraffin blocks and micro-sectioned followed by attachment on sterile poly-L-lysine-coated glass slides (Kundu et al., 2020). Tissue sections were deparaffinized and rehydrated through serial down-gradation of absolute ethanol to water. Antigen retrieval was

Table 1
Protocol of tumor inoculation in Swiss Albino mice.

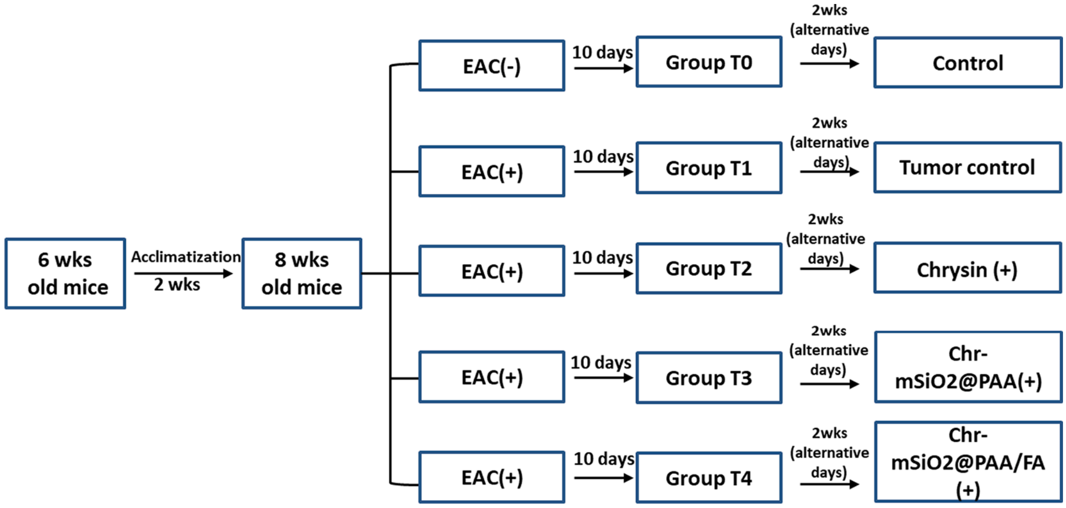

performed by using trypsin solution (0.05 %, pH 7.8). Rest of the assay was executed following protocol provided with IHC assay kit (Abcam, ab80437). In short, endogenous peroxidase blocking was accomplished by kit-based H_2O_2 blocking solution. To avoid non-specific binding, next a protein block was used to incubate the sections for 10 min prior to the overnight incubation with anti-caspase 3 and anti-caspase 9 antibodies at 4 °C temperature. On next day, incubation with Horseradish Peroxidase (HRP)-conjugated secondary antibody was carried out followed by a chromogenic HRP substrate 3, 3′-diaminobenzidine tetrahydrochloride (DAB) application. Hematoxylin was used to counter stain nuclei present in tissue sections and DPX was applied for mounting. Finally, stained tumor tissue sections were examined under 20X microscopic magnification (Ghosh et al., 2022a).

2.26. *In vivo systemic toxicity assessment*

To investigate nanoparticle induced systemic toxicity, healthy Swiss Albino mice were divided into four groups (S1-S4), each group containing three (n = 3) mice. Groups and related treatment (for 14 days) were as follows:

S1 – control group of mice receiving 1X PBS (pH 7.4) intravenously.
S2 – mice treated with free chrysin intravenously (10 mg kg^{-1} body weight).
S3 – mice receiving intravenous Chr-$mSiO_2$@PAAtreatment (60.60 mg kg^{-1} body weight).
S4 – mice receiving intravenous Chr-$mSiO_2$@PAA/FA treatment (74 mg kg^{-1} body weight).

After completion of 14-day long treatment, mice were sacrificed and blood was collected from each mice puncturing left ventricle of heart with a disposable syringe. Collected blood was subjected to centrifugation for serum collection. Isolated serum from each group were tested for ALP and ALT as hepatic heath biomarkers along with creatinine and BUN estimation to check renal heath following the method described in respective estimation kits (Span Diagnostic Ltd., India) (Chowdhury et al., 2016). Additionally, to assess systemic toxicity through histology, livers, hearts, lungs and kidneys were collected and fixed in 10 % formalin solution for further use.

2.27. *Histological assessment*

For further investigation about the therapeutic efficacy of $mSiO_2$-nanoconjugates, tumor tissues fixed in 10 % formalin were double stained with hematoxylin and eosin (H & E) (Kundu et al., 2019). Additionally, hepatic, cardiac, lung and renal tissue sections (from S1–S4 groups) were also stained with H & E to ensure histocompatibility of nanoconjugates. After staining all sections were examined pathologically under light microscope at 20X magnification.

2.28. *Statistical analysis*

Every experiment was performed at least thrice under same experimental conditions. Results were expressed as mean ± standard deviation. Statistical analyses were performed through one way analysis of variance (ANOVA) followed by the Tukey test. In current manuscript, p-value < 0.05 was considered to be statistically significant for all experimental data analysis.

3. Results & discussion

3.1. *Synthesis & characterization of Chr-$mSiO_2$ nano-formulations*

The fabrication process of Chr-$mSiO_2$@PAA/FA has been pictorially illustrated in Fig. 1A. Briefly, synthesized $mSiO_2$ was amine functionalized initially, followed by chrysin entrapping into the pores of aminated mesoporous nanoparticles. Amine functionalization conferred positive charge to the bare $mSiO_2$ which was expected to ease the loading of negatively charged flavonoid inside the pores of $mSiO_2$. To avoid unnecessary drug leakage a coating of PAA was mounted on chrysin entrapped $mSiO_2$ (Chr-$mSiO_2$@PAA). Finally, Chr-$mSiO_2$@PAA/FA was synthesized by tagging FA on the PAA-coated nanoconjugate to provide selective targeting toward tumor cells.

Both TEM and SEM were performed to evaluate the actual size and overall morphology of the nanoparticles. Fig. 2A reveals well defined porous and nearly spherical morphology of bare $mSiO_2$. The average particle size was found to be 34.167 nm in diameter (Fig. 2D). After chrysin loading, PAA coating and FA mounting, the obtained final Chr-$mSiO_2$@PAA/FA exhibited almost similar nearly spherical morphology as that of the bare $mSiO_2$. In addition to increased average particle size of 47.619 nm, the blurry pore structure observed in the TEM image of Chr-$mSiO_2$@PAA/FA (Fig. 2B & 2E) suggests the presence of PAA and FA layers around. Corresponding SEM image of Chr-$mSiO_2$@PAA/FA also justifies the same (Fig. 2C & 2F). The EDX analysis also showed the presence of Si, C, O, and N in Chr-$mSiO_2$@PAA/FA (Fig. 2G).

The X-ray diffraction pattern for both bare $mSiO_2$ and final Chr-$mSiO_2$@PAA/FA have been depicted in Fig. 2H. No distinctive crystalline peak was found for both $mSiO_2$ and Chr-$mSiO_2$@PAA/FA. Both of

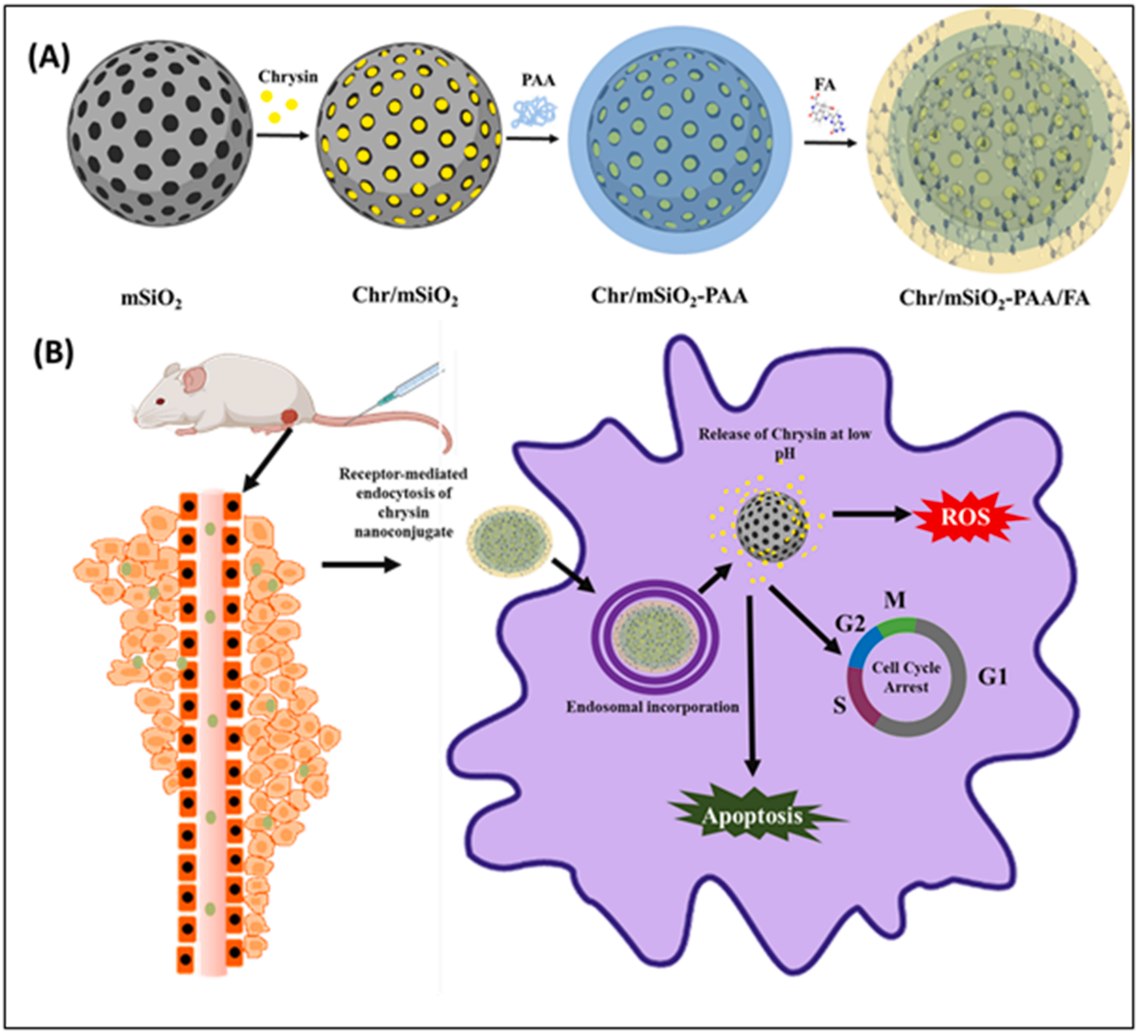

Fig. 1. (A) Schematic illustration of Chr-mSiO$_2$-PAA/FA synthesis. (B) Generalized scheme of anticancer activity exhibited by Chr-mSiO$_2$-PAA/FA.

them showed broad peaks at 2ϴ value between 20° to 30° which denoted amorphous nature of both mSiO$_2$ and Chr-mSiO$_2$@PAA/FA (Rameli et al., 2018).

To ensure successful loading of mSiO$_2$ with chrysin, as well as modification with PAA and FA, FTIR spectrum at each step was collected. As shown in Fig. 3A, spectral peak at 1075 cm^{-1} is due to Si—O stretching bond vibration for bare mSiO$_2$. Additional peaks at 1635 cm^{-1} and 3435 cm^{-1} are due to bending and stretching vibration of N—H bond which satisfy successful amine functionalization of mSiO$_2$ (Kundu et al., 2020). Additionally, a series of peaks can be found from 1653 cm^{-1} to 1245 cm^{-1} region in FTIR spectrum of chrysin, all of which are also noticeable in the FTIR spectrum of Chr-mSiO$_2$, suggesting effective chrysin loading inside the pores of mSiO$_2$. Two new peaks at 1634 cm^{-1} and 1564 cm^{-1} appeared in the FTIR spectrum of Chr-mSiO$_2$@PAA, revealing presence of C═O stretching vibration and N—H bending vibrations of amide linkage respectively. FTIR spectrum of Chr-mSiO$_2$@PAA/FA, similarly, shows peaks at 1682 cm^{-1}, 1635 cm^{-1} and 1570 cm^{-1} assigning stretching vibration of carboxylic acid group of lastly added FA along with C═O stretching vibration and N—H bending vibration of amide bond respectively (Dada, 2019; Kundu et al., 2020).

Synthesized nano-formulations were also evaluated by their UV–vis absorption spectra (Fig. 3B). For mSiO$_2$ and aminated mSiO$_2$, no absorption spectrum was obtained in a range wavelength from 250 nm to 400 nm (data not shown). However, for pure chrysin two absorption peaks were obtained; $\pi - \pi^*$ transition in benzoyl system created an intense band at 272 nm and another weak one at 315 nm was obtained due to absorbance of cinnamoyl system (Zeng et al., 2003). The second wavelength, i.e., 315 nm was considered as characteristic absorption wavelength of chrysin for further UV-based studies in this manuscript. Both of these peaks were also noticeable in absorption spectrum of Chr-mSiO$_2$, which again illustrates successful chrysin entrapment. Capping agent PAA, similarly as mSiO$_2$ didn't show any absorption spectrum in aforementioned UV–vis range (data not shown); thus, Chr-mSiO$_2$@PAA had no distinct absorption spectrum from that of the Chr-mSiO$_2$. However, distinctly reduced absorption intensity of Chr-mSiO$_2$@PAAwith respect to that of the Chr-mSiO$_2$, implied satisfactory PAA-layering around Chr-mSiO$_2$. Targeting molecule FA, showed a distinct absorption band at 289 nm. Similarly, Chr-mSiO$_2$@PAA/FA also exhibits characteristic absorption band 290 nm which is critical to $\pi - \pi^*$ transition of pterin ring of FA (Dada, 2019) revealing successful association of FA to Chr-mSiO$_2$. Also, second peak of free FA at 364 nm is also evident in UV–vis spectrum of Chr-mSiO$_2$@PAA/FA.

According to the standard curve of absorbance of chrysin, the drug loading content (DLC) and drug entrapment efficiency (DEE) of Chr-mSiO$_2$ were estimated spectrophotometrically at 315 nm and were valued respectively 22.77 % and 29.48 %. DLC for Chr-mSiO$_2$@PAA and Chr-mSiO$_2$@PAA/FA were found to be respectively 16.50 % and 14.35 %.

The hydrodynamic size of synthesized nanoconjugates was determined through dynamic light scattering. According to the data obtained and as presented in Fig. 3C, the average hydrodynamic size of bare mSiO$_2$ was 111.850 ± 5.303 nm; whereas, that of the Chr-mSiO$_2$, Chr-

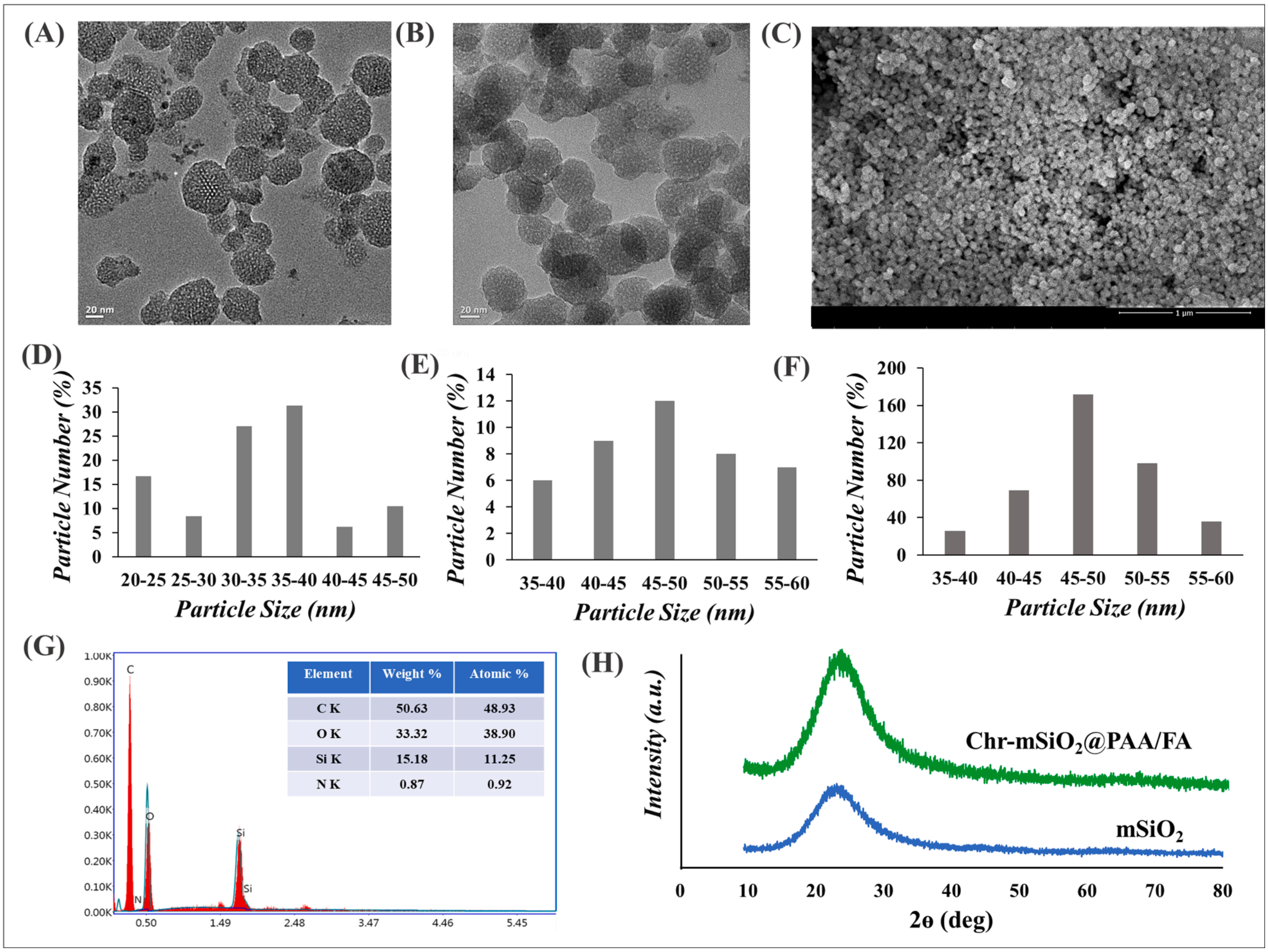

Element	Weight %	Atomic %
C K	50.63	48.93
O K	33.32	38.90
Si K	15.18	11.25
N K	0.87	0.92

Fig. 2. TEM photographs of (A) bare $mSiO_2$ and (B) Chr-$mSiO_2$@PAA/FA. (C) SEM photograph of Chr-$mSiO_2$@PAA/FA. Particle diameter distribution of (C) bare $mSiO_2$ (TEM), (D) Chr-$mSiO_2$-PAA/FA (TEM) and of (E) Chr-$mSiO_2$-PAA/FA (SEM). (F) EDX analysis of Chr-$mSiO_2$@PAA/FA. (G) XRD pattern of bare $mSiO_2$ and final chrysin nanoconjugate Chr-$mSiO_2$@PAA/FA.

$mSiO_2$@PAAand Chr-$mSiO_2$@PAA/FA were found to be 164.35 ± 15.485 nm, 264.9 ± 8.768 nm and 387.45 ± 4.030 nm respectively. Increased average hydrodynamic diameter in each step indicates the successful modification of initial $mSiO_2$ to Chr-$mSiO_2$@PAA/FA. Notably, sizes of synthesized nano-conjugates, obtained from DLS experiment are larger than the actual sizes calculated from TEM data. This is due to the formation of water layer surrounding the nanoparticles (Pecora, 2000).

Additionally, zeta potential values after each modification step have also been changed significantly indicating successful step-by step formulation of $mSiO_2$ nanoconjugate (Fig. 3D). Zeta potential values of $mSiO_2$ was quite highly positive (38.3 ± 0.707 mV) due to presence of positively charged amine groups. A less positive surface charge (33.6 ± 0.565 mV) of Chr-$mSiO_2$ indicates negatively charged chrysin entrapping and a little probable adsorption. However, fabrication of negatively charged PAA must have musk most of amine groups on Chr-$mSiO_2$ lowering the overall surface charge on Chr-$mSiO_2$@PAA (19.65 ± 2.333 mV). And finally, FA addition to the carboxyl group of PAA through amide bonding were thought to leave the carboxylic group of FA free on Chr-$mSiO_2$@PAA/FA surface leading to negative zeta potential (-24.4 ± 1.272 mV) of Chr-$mSiO_2$@PAA/FA. Thus, the change in overall surface charge in each step also reveals successful modifications step by step.

3.2. Biocompatibility and stability of synthesized nanocarrier

Alongside, hemocompatibility of the final nanocarrier, $mSiO_2$@PAA/FA was checked by hemolysis assay. Fig. 4A illustrates insignificant hemolytic activity of the nanocarrier with respect to the positive control (20 % triton-X-100). Even, at the highest concentration of 500 µg mL^{-1}, the hemolytic activity of $mSiO_2$@PAA/FA is only 7.34 % compared to 32.75 % hemolytic activity of bare $mSiO_2$ nanoparticles, representing exceptional biocompatibility of $mSiO_2$@PAA/FA. The fact of shielding the surface silanol groups of naked $mSiO_2$ by PAA-FA coating may be the reason behind enhanced hemo-compatibility of $mSiO_2$@PAA/FA as this prevents interaction of silanol groups to the RBC membrane rendering RBC membrane less disturbed and damaged (Feng et al., 2013).

Besides, result from BSA adsorption study also demonstrates that PAA and FA modification on $mSiO_2$ has decreased the adsorption of BSA. Fig. 4B illustrates that FA grafting has reduced BSA adsorption upon surface of $mSiO_2$@PAA/FA nanocarrier (1.96 wt%) remarkably with respect to that of the $mSiO_2$ (18.83 wt%) and $mSiO_2$@PAA (10.7 wt%). Such reduction in BSA adsorption not only ensures stability of circulating nano-conjugate but also prolongs blood circulation time of the synthesized nanocarrier.

To check the stability of the final nanohybrid, Chr-$mSiO_2$@PAA/FA was suspended in 1X PBS (pH 7.4) supplemented with 10 % FBS in order to mimic condition similar to human plasma and was further evaluated with DLS for respective average hydrodynamic diameters on 7th and 14th day post-incubation. Comprehensive result mentioned in Table 2 and Fig. 4C, suggests no significant change in hydrodynamic diameter of Chr-$mSiO_2$@PAA/FA over two weeks. Moreover, the PDI values further

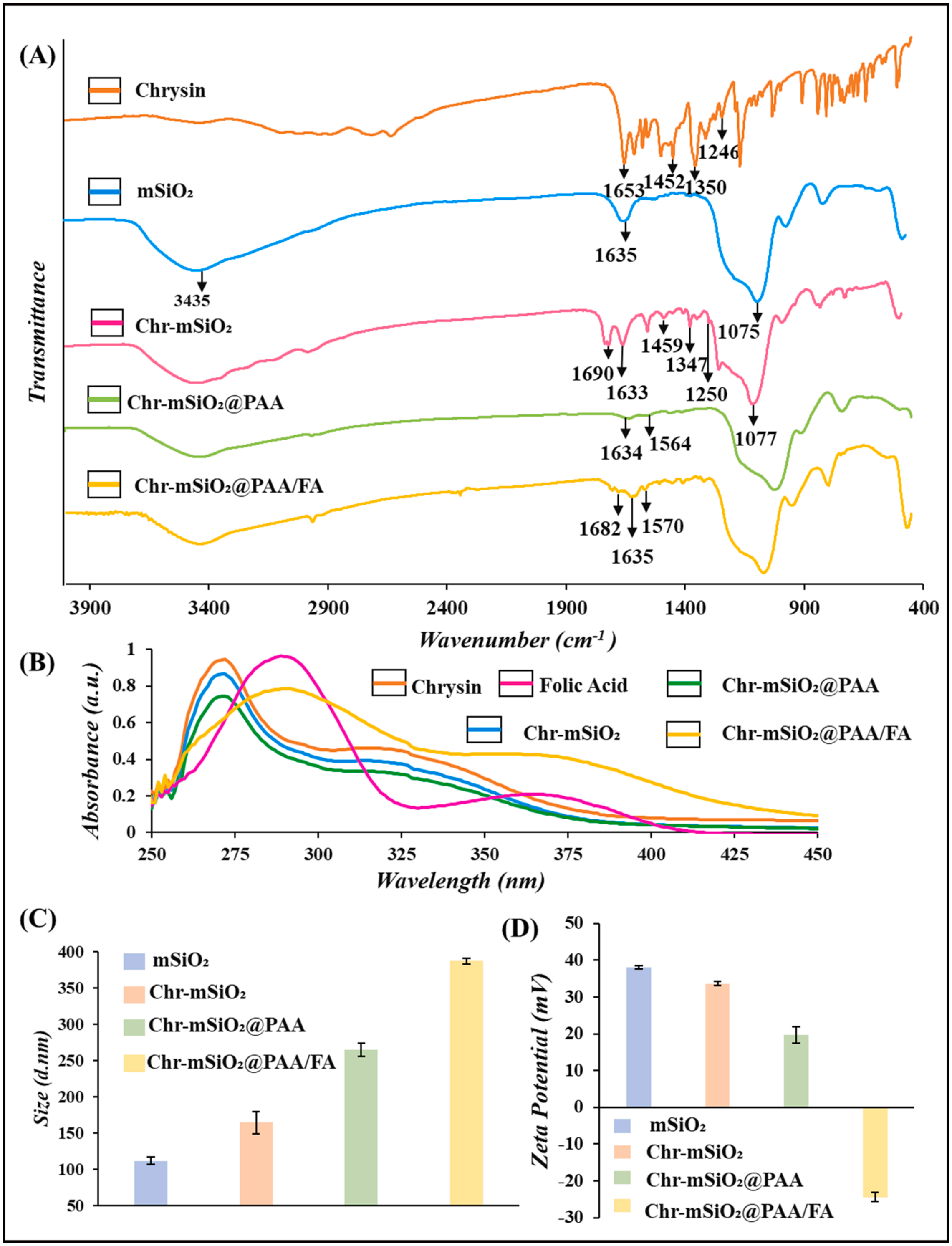

Fig. 3. (A) FTIR spectra of free chrysin, Chr-mSiO$_2$, Chr-mSiO$_2$@PAA, Chr-mSiO$_2$@PAA/FA. (B) UV–vis spectra of free chrysin, Chr-mSiO$_2$, Chr-mSiO$_2$@PAA, Chr-mSiO$_2$@PAA/FA and FA. (C) Hydrodynamic size (d.nm) of mSiO$_2$, Chr-mSiO$_2$, Chr-mSiO$_2$@PAA, Chr-mSiO$_2$@PAA/FA. (D) Zeta potential (mV) of mSiO$_2$, Chr-mSiO$_2$, Chr-mSiO$_2$@PAA and Chr-mSiO$_2$@PAA/FA.

indicate homogeneous size distribution and stability of final nanohybrid and its related advantages for blood circulation.

3.3. PAA-capping enabled pH & time-dependent steady release of chrysin

In order to explore mSiO$_2$-conjugate as potential nano-drug delivery system, release patterns of chrysin in cell-free system were noted from Chr-mSiO$_2$ and Chr-mSiO$_2$@PAA over a period of 48 h. As showed in the Fig. 5A, chrysin release from the Chr-mSiO$_2$ is pH-independent. Within first 6 h, a burst effect is evident which correlates with release of drug adsorbed on the nanocarrier surface (Jabbari et al., 2018). Release increased with over 48 h at the physiological pH (pH 7.4). However, at the lower pH of 5, chrysin release did not change significantly. Such pH-independent behavior of chrysin is probably due to lack of ionic

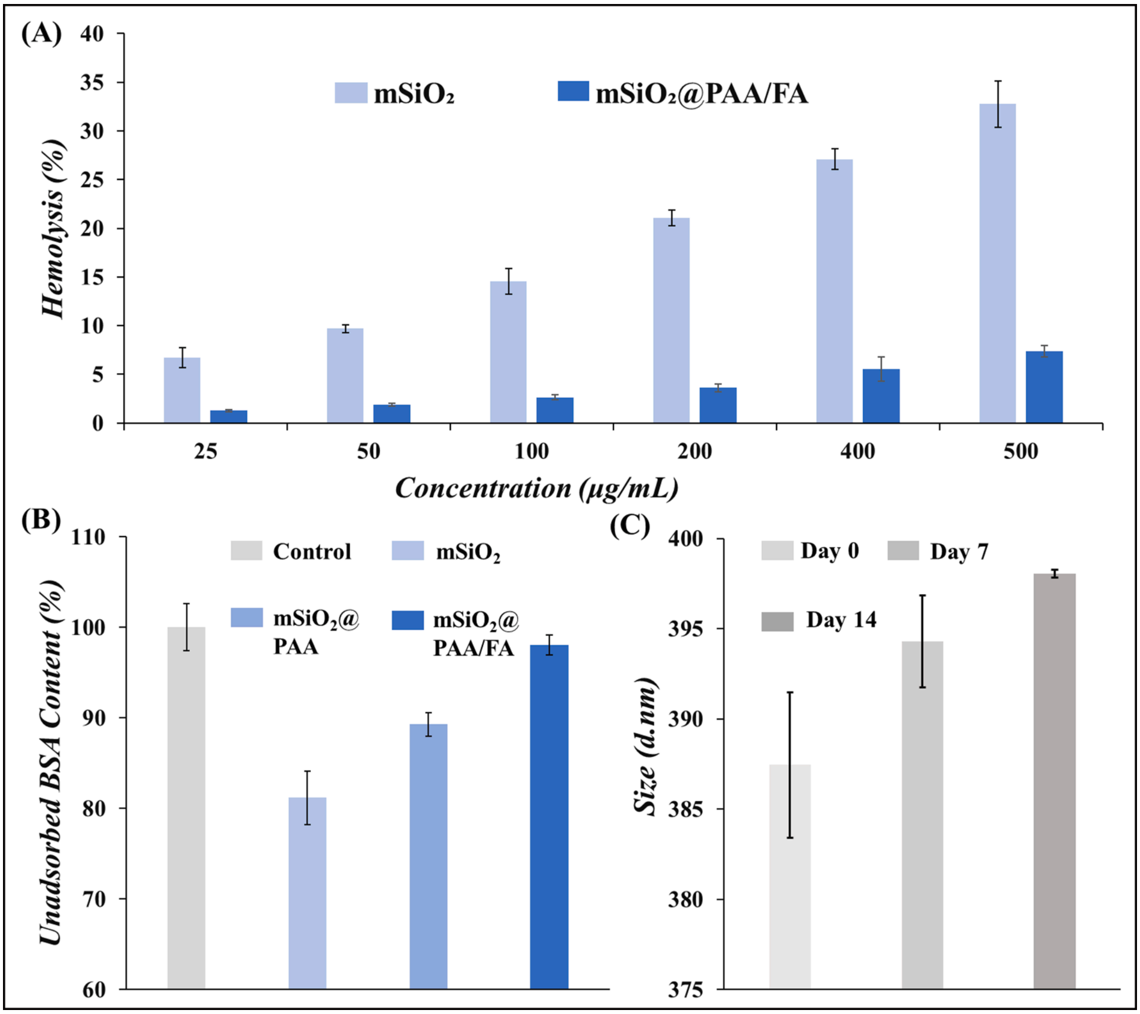

Fig. 4. Assessment of *in vitro* stability and biocompatibility of chrysin nanoconjugate. (A) Hemolysis at different concentrations of $mSiO_2$ and $mSiO_2$@PAA/FA. (B) Unadsorbed amount of BSA of $mSiO_2$, $mSiO_2$@PAA and $mSiO_2$@PAA/FA. Data are represented as mean ± SD (n = 3). (C) Hydrodynamic size (d.nm) of Chr-$mSiO_2$@PAA/FA on 0th, 7th and 14th day after synthesis.

Table 2
Time dependent change in hydrodynamic size of Chr-$mSiO_2$@PAA/FA.

Chr-$mSiO_2$@PAA/FA	Day 0		Day 7		Day 14	
	Size	PDI	Size	PDI	Size	PDI
Average (d.nm)	387.45	0.461	394.30	0.391	398.05	0.543
SD (±d.nm)	4.030	0.169	2.545	0.070	0.212	0.148

interaction with $mSiO_2$ nanocarrier. Chrysin release reaches its peak at 48 h. However, as in Fig. 5B, only about 7.92 ± 0.33 % chrysin was released after 48 h at pH 7.4. While, at pH 6.0 and pH 5.0, total release of chrysin were recorded to rise to 15.62 ± 0.32 % and 53.33 ± 0.76 % respectively. This behavior could be the result of partial detachment and hydrolyzation of PAA layer from the surface of Chr-$mSiO_2$@PAA under acidic condition. PAA possess pKa value of 4.5; thus, around pH 5 it undergoes a reversible coil-to-globule conformational transition due to ionization state of its carboxylic group (Swift et al., 2016). Additionally, over the time of 0–48 h, very little chrysin release can be seen from Chr-$mSiO_2$@PAA at pH 7.4; thus, under normal physiological condition this nanocomposite can be regarded as stable. Also, chrysin release at each distinct pH was higher with time (highest after 48 h), indicating a clear time-dependent nature of chrysin release.

3.4. *FA tagging attributed towards increased cellular uptake of Chr-$mSiO_2$ nanodevices and subsequent cargo release*

When checked flow cytometrically, it was found that fluorescently labeled, FA tagged $mSiO_2$ (Chr-$mSiO_2$@FITC/FA) were taken up superiorly by MCF-7 cells than FA untagged Chr-$mSiO_2$@FITC (Fig. 5C, 5E & Fig. S1). In this context, further intracellular release behavior of chrysin was verified too. Intracellular concentration of chrysin was 5.5-fold higher in $mSiO_2$ bound state than that of the free chrysin treatment. However, there was another 1.8-fold increase in chrysin content in Chr-$mSiO_2$@PAA/FA-treated MCF-7 cells was observed in comparison to Chr-$mSiO_2$@PAA nanoconjugate (Fig. 5D). Therefore, it can be said that entrapping chrysin inside $mSiO_2$, has increased its bioavailability. Additionally, MCF-7 cells with overexpressed folate receptors can uptake FA-labeled Chr-$mSiO_2$ nanohybrids much efficiently than naked $mSiO_2$ due to ligand-receptor recognition and subsequent receptor-mediated endocytosis (Xu et al., 2013).

In comparison to MCF-7 cells, much lesser amount of chrysin uptake occurred in Chr-$mSiO_2$@PAA/FA-treated non-cancerous NKE cells (Fig. 5D). The finding implies folate receptor-oriented tumor cell selectivity of smart Chr-$mSiO_2$@PAA/FA which allows it to differentiate absence of folate receptor overexpression in NKE cells. Thus, all of these observations emphasize the superiority of this nano-formulation with chrysin and its subsequent flagging with FA moieties.

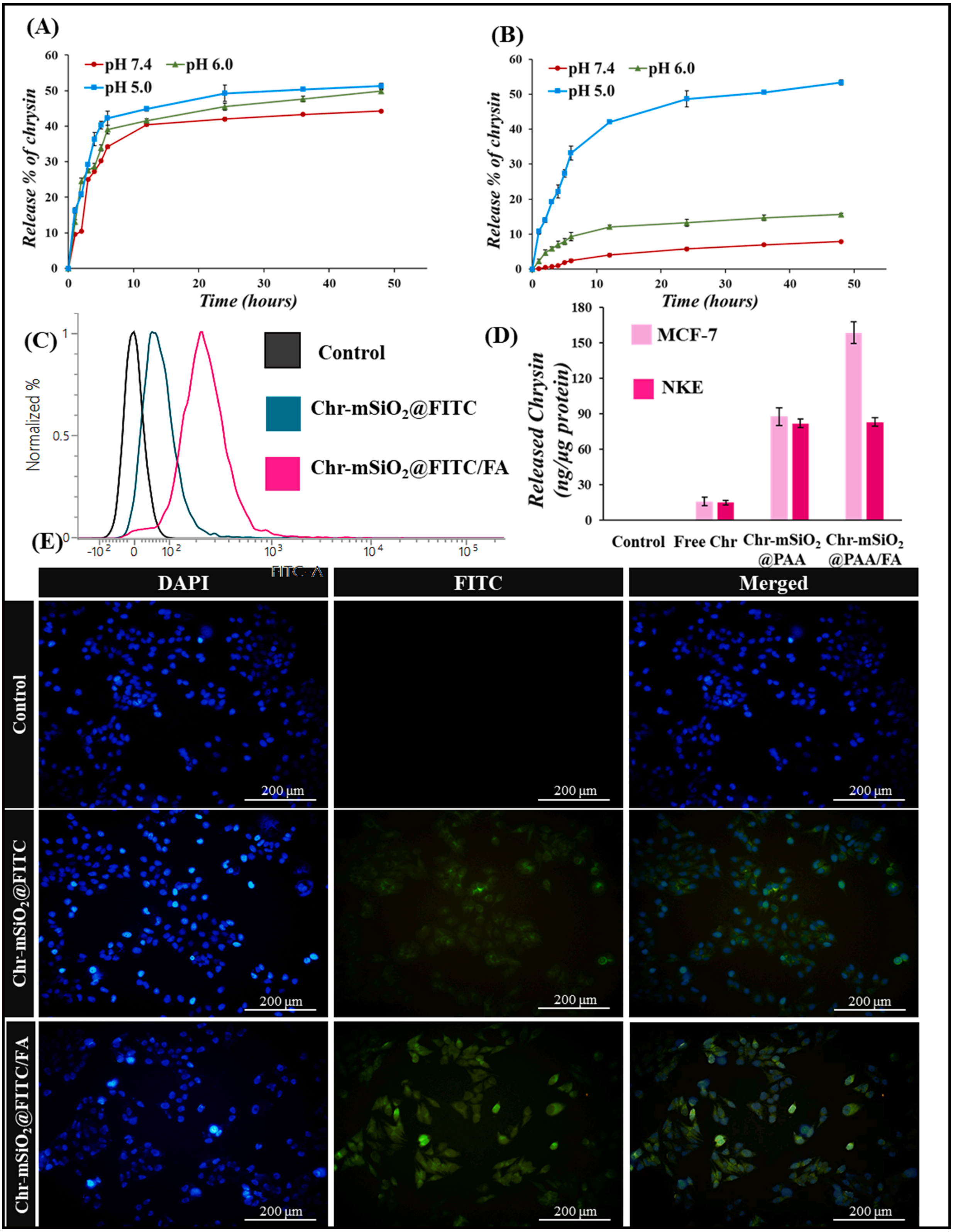

Fig. 5. The release profiles of Chr from (A) Chr-mSiO$_2$ (B) Chr-mSiO$_2$@PAA nanocomposites under different pH conditions (pH 7.4, 6.0 and 5.0) for a time span of 0–48 h. (C) Study of intracellular uptake of FA conjugated mSiO$_2$ nanoparticles in contrast to untagged mSiO$_2$ by FACS. (D) Study of intracellular release of chrysin from Chr-mSiO$_2$@PAA and Chr-mSiO$_2$@PAA/FA in contrast to intracellular availability of free chrysin in MCF-7 and NKE cells. (E) Microscopic images of MCF-7 cells after 3 h incubation with free Chr (control), Chr-mSiO$_2$@FITC, Chr-mSiO$_2$@FITC/FA respectively.

3.5. Chr-mSiO$_2$@PAA/FA showing in vitro cytotoxicity

Inspired by result of cellular uptake study, cytotoxic efficacy of Chr-mSiO$_2$@PAA/FA was evaluated in both MCF-7 and NKE cells. Free chrysin showed a dose-dependent cytotoxicity in a range of 5–40 μg mL^{-1} in MCF-7 cells and 31.426 μg mL^{-1} was recorded as its LC$_{50}$ value. Similar patterns of dose-dependance were noticed in MCF-7 cell line when chrysin was piled up in both Chr-mSiO$_2$@PAA and Chr-mSiO$_2$@PAA/FA. At a particular concentration of chrysin, Chr-mSiO$_2$@PAA/FA (LC$_{50}$ 17.526 μg mL^{-1}) exhibited highest degree of cytotoxicity which must be an attribution to the folate receptor-mediated enhanced endocytosis of Chr-mSiO$_2$@PAA/FA in comparison to Chr-mSiO$_2$@PAA (LC$_{50}$ 24.283 μg mL^{-1}) and free chrysin within MCF-7 cells (Fig. 6A).

Indications of cytotoxicity imposed by the treatments with free chrysin and chrysin nanoconjugates were also studied by optical microscopic images of different experimental groups of MCF-7 cells. Occurrences of cellular shrinkage, membrane blebbing as well as presence of apoptotic bodies gave clear idea about the apoptotic death of treated cells (Fig. 6B).

Furthermore, encouraged by the MTT assessment data, cell killing ability of free chrysin and chrysin-entrapped nanoconjugates were scrutinized by FACS analysis employing Annexin V-FITC staining to the treated MCF-7 cells. At a fixed concentration (10 μg mL^{-1}), Chr-mSiO$_2$@PAA/FA-treated MCF-7 cells exhibited highest percentage of apoptotic MCF-7 cells (37.04 %) compared to free chrysin treated cells (13.06 %), validating the usefulness of FA receptor-oriented drug delivery. Furthermore, increased apoptotic cell population (21.81 %) in Chr-mSiO$_2$@PAA treatment group with respect to free chrysin treated MCF-7 cells also emphasize that chrysin infiltration inside mSiO$_2$ has definitely increased efficiency of chrysin by enhancing its intracellular bioavailability (Fig. 6C). FACS data was further validated by confocal laser scanning microscopy which also suggests increased apoptotic signal via Chr-mSiO$_2$@PAA/FA-treatment with respect to free Chr and Chr-mSiO$_2$@PAA respectively (Fig. S2).

From Fig. 6D, it is also noticed that free chrysin, Chr-mSiO$_2$@PAA and Chr-mSiO$_2$@PAA/FA showed similar pattern of dose-dependency for the mentioned range of doses of chrysin in NKE cell line. But no remarkable cell killing was detected in non-cancerous NKE cells. As expected, due to overexpression of folate receptors in MCF-7 cells, cytotoxic effect of Chr-mSiO$_2$@PAA/FA was way too higher in MCF-7 cells than NKE cells. However, no significant cellular toxicity was noticed for nanocarrier mSiO$_2$@PAA/FA in both cell lines.

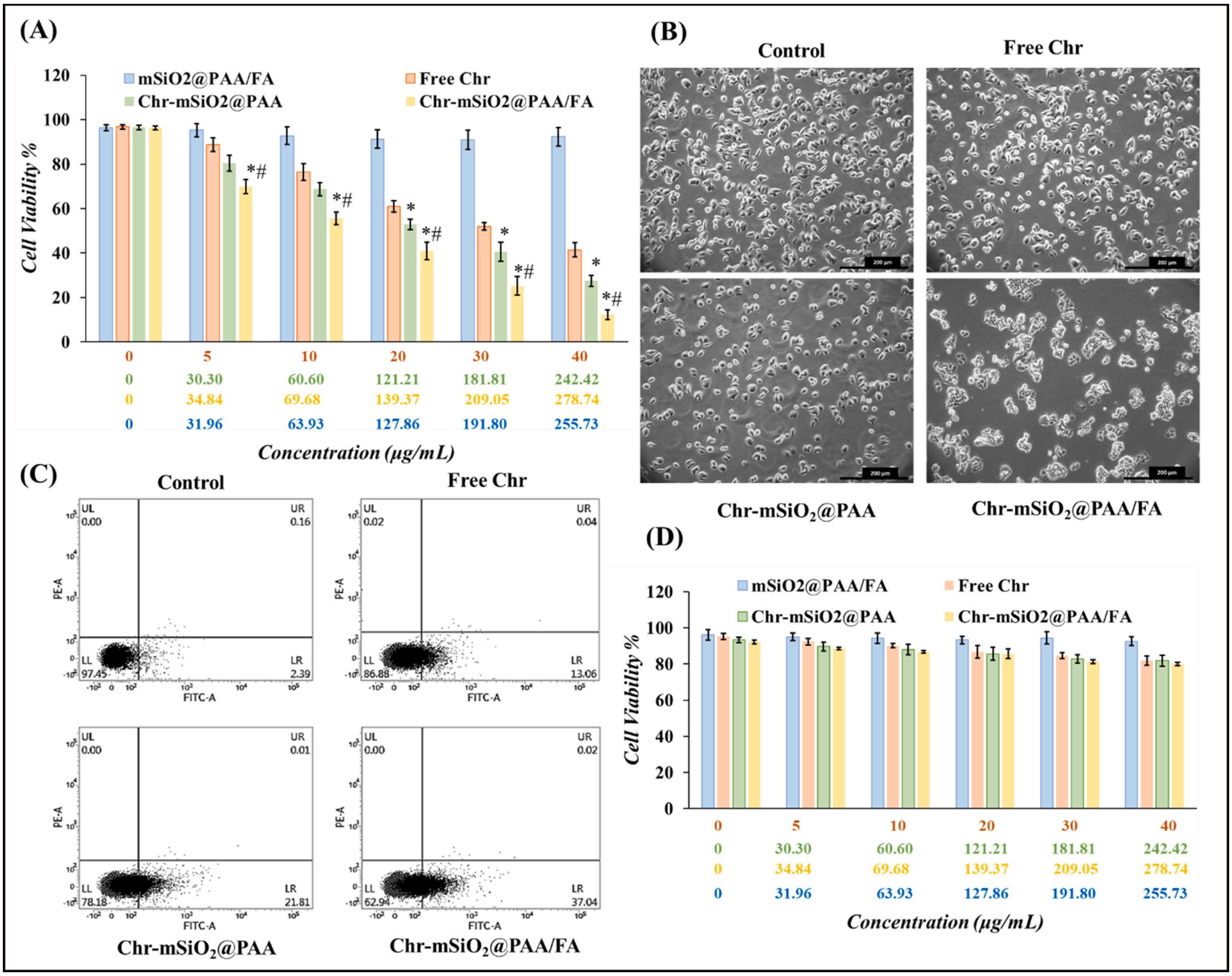

Fig. 6. Comparative study of cytotoxic ability of free Chr, Chr-mSiO$_2$@PAA and Chr-mSiO$_2$@PAA/FA by checking viabilities of (A) MCF-7 cells and (D) NKE cells after incubation with different concentrations of free Chr, Chr-mSiO$_2$@PAA and Chr-mSiO$_2$@PAA/FA for 24 h. Data are represented as mean ± SD (n = 5) where "*" and "#" represent significant differences with respect to chrysin and Chr-mSiO$_2$-PAA-treated groups, respectively, ($P^* < 0.05$, $P\# < 0.05$). (B) Optical microscopic images of MCF-7 cells incubated with free Chr, Chr-mSiO$_2$@PAA and Chr-mSiO$_2$@PAA/FA for 24 h (scale bar: 200 μm). (C) Detection of free Chr, Chr-mSiO$_2$@PAA and Chr-mSiO$_2$@PAA/FA induced apoptosis on MCF-7 cells via Annexin V-FITC staining. Dual parameter dot plot of FITC-labelled Annexin V fluorescence (x-axis) has been shown in logarithmic fluorescence intensity.

3.6. Induction of oxidative stress by chrysin nano-conjugates in MCF-7 cells

In order to study possible mechanism for chrysin-mSiO$_2$ nanodevice-induced selective cytotoxicity against MCF-7 breast carcinoma cell, we were intended to investigate oxidative condition of treated MCF-7 cells. Increased cellular ROS unequivocally exert oxidative stress within the cells, disturbing fine balance in cellular redox system (Ghosh and Sil, 2021; Sun et al., 2022). Thus, flow cytometric study was performed using ROS-sensing cell penetrable dye DCFDA after treating four groups of MCF-7 cells with chrysin and chrysin-trapped nanoconjugates. Relative amount of cumulative ROS generation was studied flow-cytometrically as well as through confocal microscopy. The fluorescence level DCFDA is directly proportional to the amount of cumulative

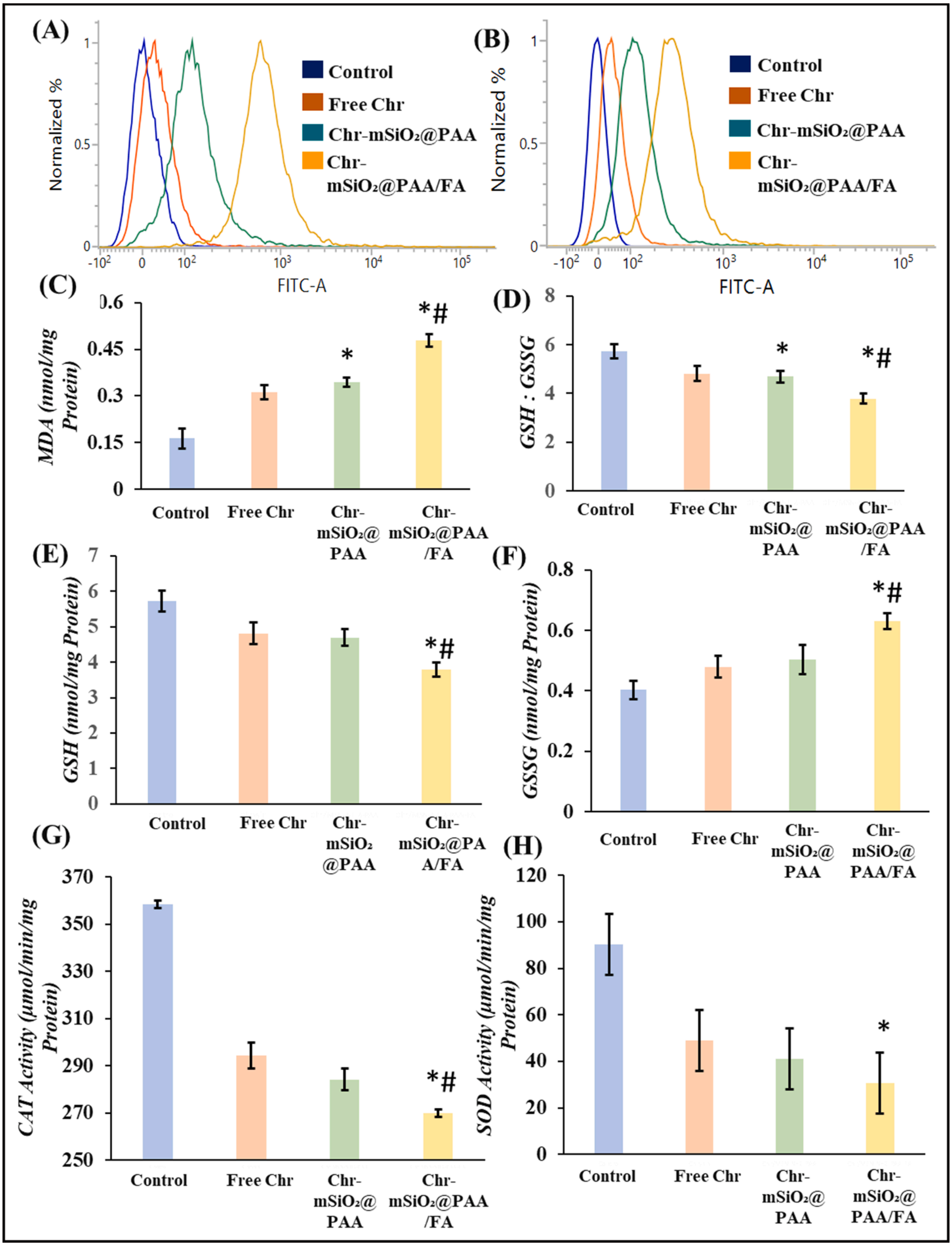

Fig. 7. Oxidative status of MCF-7 cells upon treatment with free Chr, Chr-mSiO$_2$@PAA and Chr-mSiO$_2$@PAA/FA. FACS-assisted detection of (A) intracellular ROS content and (B) change in MMP in MCF-7 cells respectively by DCFDA and JC1 staining. Spectrophotometric detection of (C) intracellular MDA content, (D) GSH to GSSG ratio, (E) GSH content, (F) GSSG content, (G) CAT activity and (H) SOD activity of MCF-7 cells after being treated with free Chr, Chr-mSiO$_2$-PAA and Chr-mSiO$_2$-PAA/FA.

ROS generated in the cell.

Additionally, it has been studied extensively that excessive cellular ROS content can increase mitochondrial membrane porosity reducing cellular MMP. Hence, we also checked the relative MMP of treated cells from separate experimental groups by JC-1-assisted FACS. Similar to DCFDA, green fluorescence level of JC-1 is also directly proportional to loss of MMP.

As depicted in Fig. 7A, S3 & 7B, Chr-mSiO_2@PAA/FA was most potent to induce ROS enhancement and MMP disruption in MCF-7 cells over Chr-mSiO_2@PAA and free chrysin respectively. Hence, at a distinct equivalent dose, green fluorescence intensity (oxidative stress and MMP loss indicator) was highest in the cells, treated with Chr-mSiO_2@PAA/FA and was significantly higher in comparison to cells treated with Chr-mSiO_2@PAA and free chrysin respectively.

Apart from cellular ROS content, control and treated MCF-7 cells were also checked for their relative intracellular MDA content, GSH to GSSH ratio as well as the status of antioxidant enzyme activities for CAT and SOD (Fig. 7C–7H). Among treated cell groups, the MCF-7 cells which were exposed Chr-mSiO_2@PAA/FA, showed lowest GSH:GSSG ratio along with significantly uplifted level of MDA content. Additionally, both CAT and SOD enzyme activities were highly compromised in Chr-mSiO_2@PAA/FA-treated MCF-7 cells ensuring a status of unduly oxidative stress.

3.7. *Chr-mSiO_2@PAA/FA can modulate in vitro cell cycle progression*

Motivated by the observations made from the aforementioned experiments, investigation about the effect of chrysin nanoconjugates upon cell cycle regulation of MCF-7 cells was an obvious incidence. Besides, chrysin has already been assigned to work as a cell cycle arresting agent according to the experiments performed elsewhere (Weng et al., 2005). When treated with Chr-mSiO_2@PAA/FA, MCF-7 cells exhibited marked increase in G_0/G_1-cell population in comparison with control group along with lowered population of MCF-7 cells at G_2/M phase. Thus, like free chrysin, mSiO_2-nanoconjugate of chrysin is also capable of imposing G_0/G_1 arrest. As depicted in Fig. 8A & 8B, it also must be noted that mSiO_2 incorporation and subsequent FA-tagging has remarkably increased the efficiency of free chrysin in terms of cell cycle arrest induction *in vitro*.

3.8. *Chrysin-nanoconjugates induced enhanced apoptotic signal checking cell cycle progression & cellular survival*

One of the prime proteins that regulate cell survival and growth through cell cycle regulation is Akt which often renders at elevated level in several cancer types (Shimura et al., 2012). Thus, we have checked the expression of phosphorylated Akt (p-Akt) protein, passing survival signal to cancer cells. Activated Akt promotes cell cycle progression by enhancing cyclin D1 upregulation through phosphorylation and subsequent inactivation of GSK-3β (Chen et al., 2019b; Saha et al., 2016). In response to growth factors, cyclin D1 is considered as a primary regulator of cell cycle transition from G_1 to S phase for somatic cells (Neganova and Lako, 2008). Thus, inspired by the observation that chrysin-nanoconjugates induct G_0/G_1 arrest *in vitro,* we checked translational expression of p-Akt and its downstream GSK-3β and cyclin D1 (Fig. 8C). Expression of both p-Akt and cyclin D1 were higher enough in untreated MCF-7 cells which were reduced significantly upon chrysin treatment, and even more after Chr-mSiO_2@PAA/FA treatment. Later on, we checked the translational expression of GSK-3β. Expression of GSK-3β was uplifted in treated MCF-7 cells and its expression was highest amongst Chr-mSiO_2@PAA/FA treated cells.

p-Akt as well as increased ROS, both are capable of shifting balance between the antiapoptotic and pro-apoptotic cell machineries (Saha et al., 2016). Hence, we have also checked the expression of proapoptotic protein Bax and that of antiapoptotic protein Bcl-2 (Fig. 8D). It was found that chrysin enhances the ratio of Bax to Bcl-2 protein levels in MCF-7 cells. Following this observation, we have also studied the changes in protein expression of the components of intrinsic apoptosis, cytochrome-C, Apaf-1, cleaved caspase 9 and caspase 3 upon chrysin-nano-formulation treatment. All these proteins showed increased expression after chrysin treatment compared to untreated MCF-7 cells, suggesting possible action of chrysin through intrinsic apoptosis. The result indicated that effectivity of free chrysin was magnified further after nano-encapsulation of chrysin and its FA functionalization. This allowed increased apoptotic activity among MCF-7 cells for equivalent dose of free chrysin.

3.9. *NAC reverses Chr-mSiO_2@PAA/FA-imposed cell death in MCF-7 cells*

NAC pretreatment inhibits intracellular ROS generation in Chr-mSiO_2@PAA/FA treated MCF-7 cells (Fig. 9A). Also, existing reports suggest that ROS can uplift of GSK 3β expression which further capable of decreasing cyclin D1 (Takahashi-Yanaga and Sasaguri, 2008). If so, our motto was to check whether the chrysin-mediated enhanced ROS generation is the key ruler controlling the antineoplastic nature of Chr-mSiO_2@PAA/FA. It was observed that NAC pretreated cells dramatically showed higher viability percentage even after treating with most potent Chr-mSiO_2@PAA/FA (Fig. 9B). So, we hypothesized the obvious outcome would be reduced apoptosis in NAC pretreated MCF-7. Thus, to evaluate our perception, we have also checked the translational expression of key apoptotic proteins of intrinsic pathway (Fig. 9C & 9D). It was found that the expression of antiapoptotic Bcl-2 was significantly higher in NAC pretreated cells accompanied by a decreased expression of Bax and cleaved caspase-3. Alongside, from the study with Annexin V-FITC staining it was found that NAC pretreatment was potent enough to reduce the overall apoptotic MCF-7 cell population significantly even in presence of highly potent Chr-mSiO_2@PAA/FA (Fig. 9E). Altogether, these results suggest that change in redox balance in MCF-7 cells by higher ROS generation is the chief operational hub controlling the antitumor activity of chrysin.

3.10. *PAA-capping and FA-fabrication ensure increased chrysin uptake in tumor tissue*

In HPLC method, linearity of calibration curve for chrysin has been confirmed by $R^2 = 0.9998$. LOD (limit of detection) and LOQ (limit of quantification) were respectively 1.16 % and 3.52 %. The retention time for chrysin was at 3.4 min; whereas, the recovery percentage for chrysin solution at 3, 5, 15, 30 and 50 μg mL^{-1} concentration were calculated respectively as 95.13 %, 102.77 %, 101.89 %, 98.45 % and 100.37 %. Accumulation of chrysin within tumor tissue has been shown to be improved in Chr-mSiO_2@PAA compared to free chrysin (3.08 μg g^{-1} tissue homogenized). Moreover, functionalization of Chr-mSiO_2@PAA with folic acid has further increased tissue accumulation of chrysin from 9.96 μg g^{-1} to 18.27 μg g^{-1} tissue homogenized suggesting FA-guided selective enhanced drug accumulation and release at tumor site (Fig. 10E).

3.11. *mSiO_2@PAA/FA uplifts in-vivo antitumor activity of free chrysin*

Antitumor efficacy of chrysin has been shown to improve with mSiO_2-encapsulation when compared to its non-encapsulated free form which is evident from Fig. 10D. Tumor volume was found to increase gradually in T1 group where the animals were left untreated. Rest of the animals receiving intravenous treatment showed gradual decrease in tumor volume over the treatment period of 14 days where treatment with Chr-mSiO_2@PAA/FA was found to be most effective (Fig. 10C). Additionally, at the day of dissection, the volume and mass of tumors were highest among the animals of untreated group. Rest of animals having chrysin administration either in free form or in mSiO_2-encapsulated form showed significant reduction in both tumor mass and

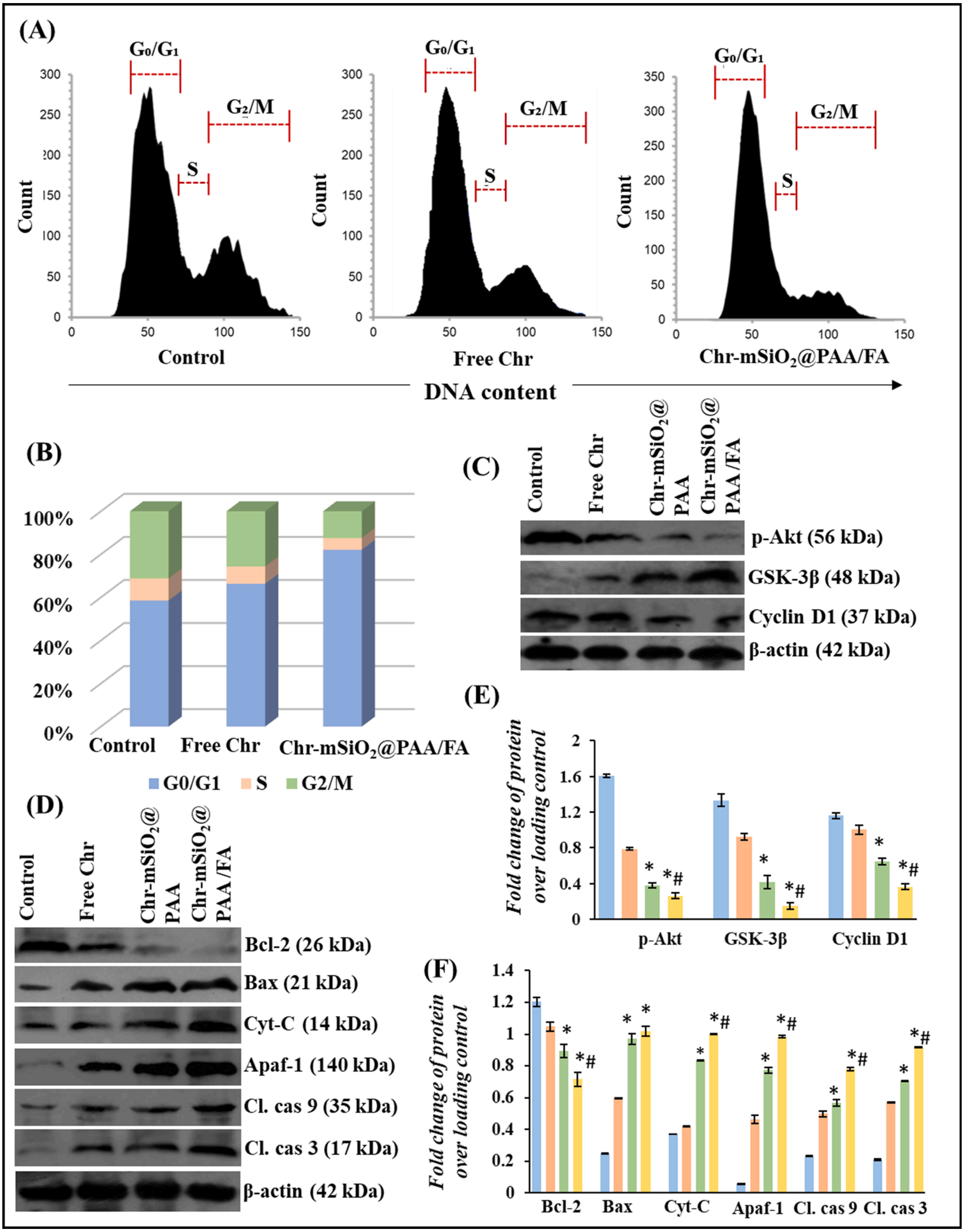

Fig. 8. (A-B) Effect of free chrysin and Chr-mSiO$_2$-PAA/FA upon cell cycle progression of MCF-7 cells. (C-D) Immunoblot analysis of different signaling molecules considered in the study. β-actin was used as an internal control. All the data are representative of three independent experiments. [Here, Cyt-C – cytochrome *C*; Cl. cas 9 – cleaved caspase 9; Cl. cas 3 – cleaved caspase 3.] (E-F) Densitometric analysis of the respective immunoblots. Data are representative of three individual experiments (n = 3). "*" and "#" represent significant differences with respect to chrysin and Chr-mSiO$_2$-PAA-treated groups, respectively, ($P^* < 0.05$, $P\# < 0.05$).

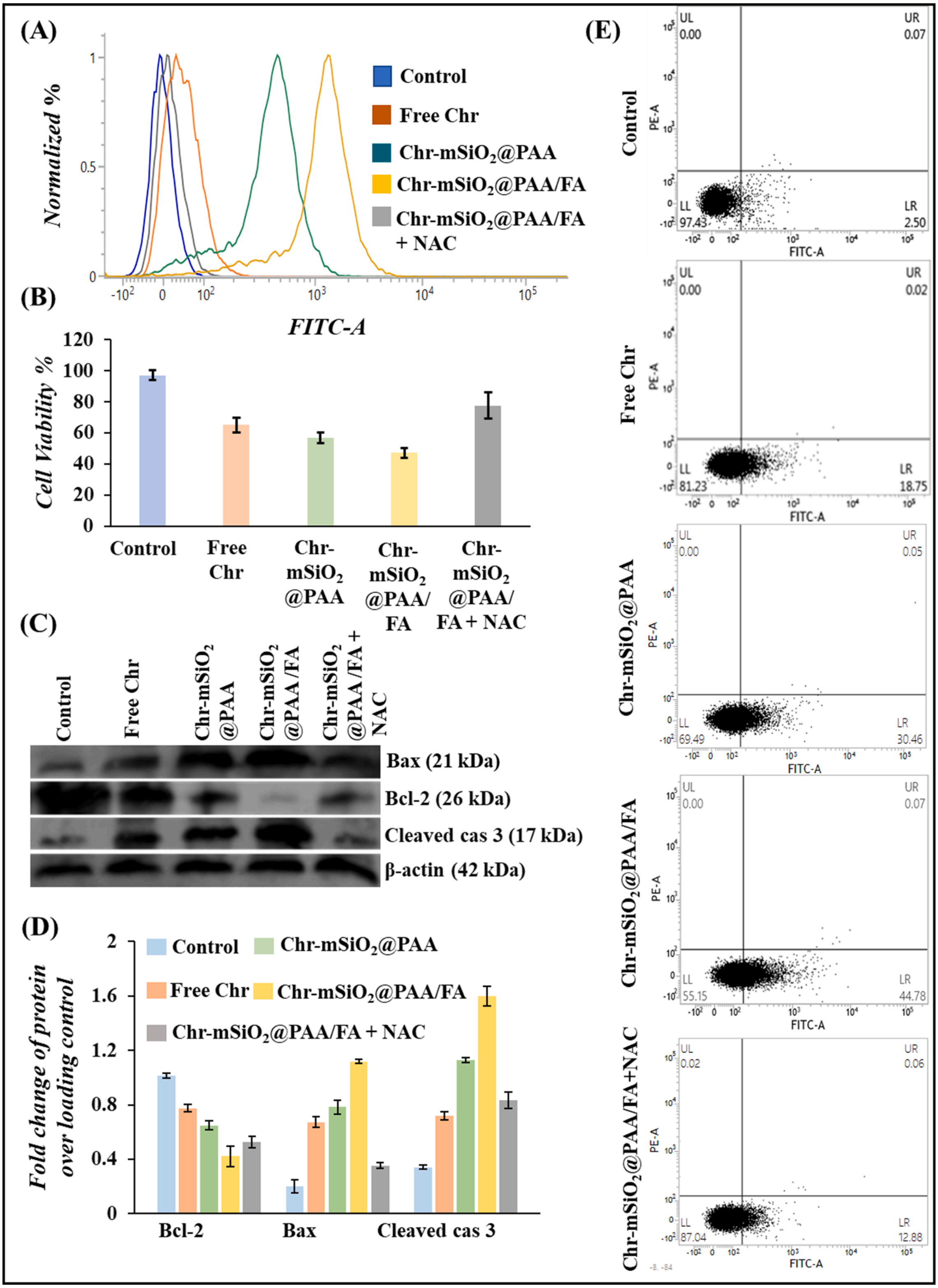

Fig. 9. Effect of NAC pre-treatment: (A) Changes in intracellular ROS content upon NAC pretreatment. (B) Effect of NAC pretreatment upon cell viability of MCF-7 cells. (C) Immunoblot analysis of chief apoptotic molecules upon NAC pretreatment. (D) Densitometric analysis of the NAC pretreatment immunoblots. (E) Effect of cellular apoptosis upon MCF-7 cells upon NAC treatment with or without LC_{50} dose of Chr-mSiO$_2$-PAA/FA. All data are representatives of three individual experiments (n = 3) where “*” and “#” represent significant differences with respect to chrysin and Chr-mSiO$_2$-PAA-treated groups, respectively, ($P^* < 0.05$, $P\# < 0.05$).

volume; which was highest among the animal of T4 group, i.e., those treated with Chr-mSiO$_2$@PAA/FA (Fig. 10A & 10B).

Moreover, the observations from the H & E-stained sections of tumor tissues from all four experimental groups (T1-T4) were also in line (Fig. 11A). Normal skeletal muscle tissue architecture was completely lost in the tumors of group T1. Additionally, numbers of nuclei were too high as seen in Fig. 11A. This condition was slightly improved in the tumor tissues of group T2, where tissue architecture was restored a bit

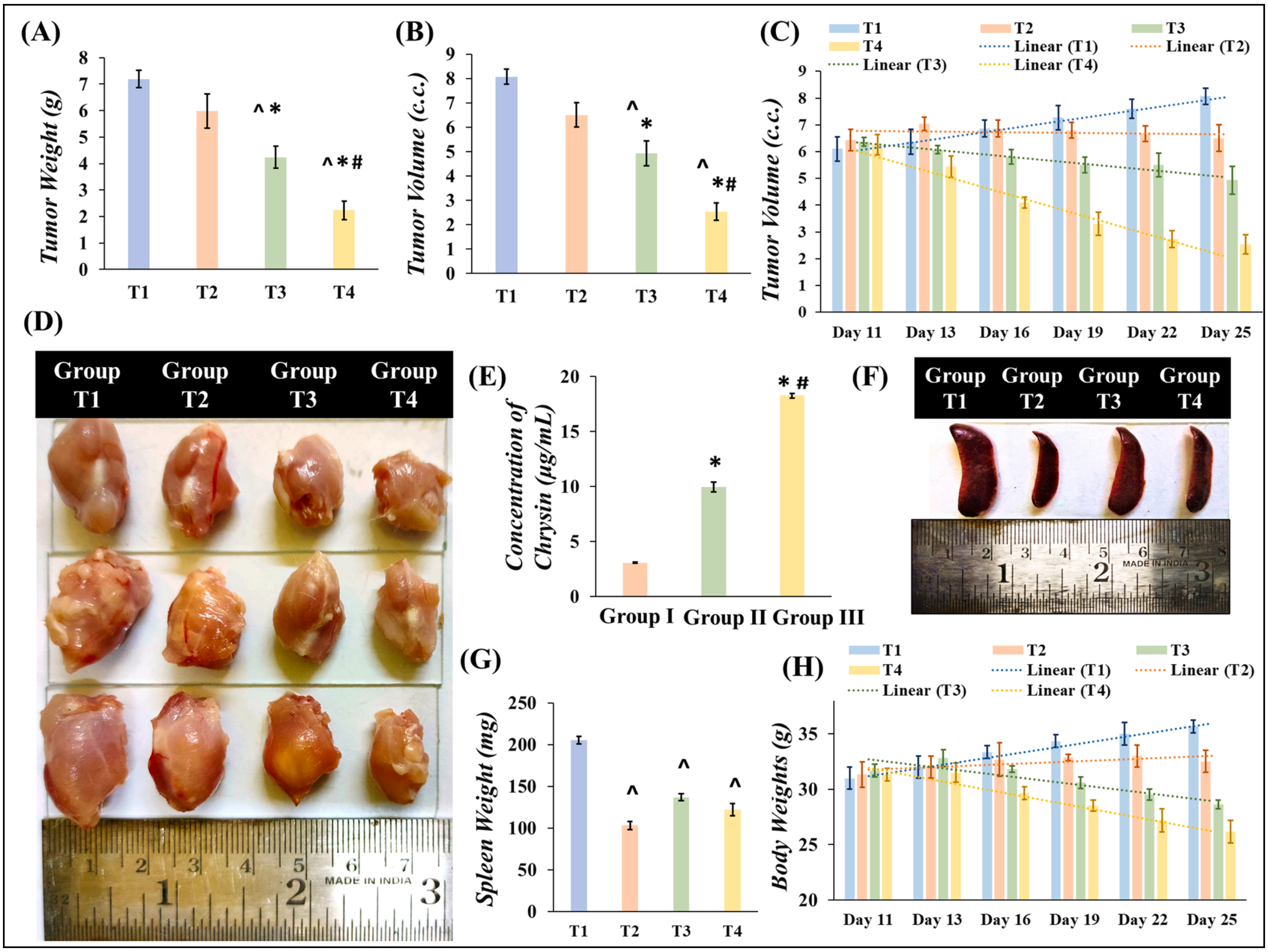

Fig. 10. *In vivo* anti-tumorigenic activity of free Chr, Chr-mSiO$_2$@PAA and Chr-mSiO$_2$@PAA/FA explained through overall reduction in (A) tumor weight and (B) tumor volume. (C) Reduction in tumor volume over the period of treatment. (D) Representative photographs of dissected tumor tissues showing overall reduction in tumor size. (E) Detection of tissue absorption of chrysin in tumor-bearing mice treated with Chr, Chr-mSiO$_2$@PAA and Chr-mSiO$_2$@PAA/FA. "*", "#" and "^" represent significant differences with respect to free Chr treated, Chr-mSiO$_2$-PAA treated and untreated groups respectively ($P^* < 0.05$, $P\# < 0.05$ and $P^\wedge < 0.05$). Changes in splenic profile explained by (F) representative photographs of spleens removed from different experimental mice and change in (G) splenic mass. (H) Changes in overall body weight over the entire treatment period.

but still there were enormous number of nuclei. Reduction in visible nuclei number as well as restoration of muscle tissue architecture can be marked at first in tumors isolated from group T3. However, best condition of recovery can be noted in tumors collected from Chr-mSiO$_2$@PAA/FA-treated mice (T4 group) where tissue architecture was good enough to recognize its muscle tissue origin with much lesser number of nuclei. These observations not only illustrate *in vivo* antitumor activity of chrysin but also suggest uplifted antitumor efficacy of chrysin due to mSiO$_2$-encasing and FA-guided tumor specific routing.

Furthermore, splenic profile of treated animals was also observed (Fig. 10F & 10G). EAC is known to induce splenomegaly and splenic WBC infiltration in induced tumor-bearing mice which can be referred as a marker for existing tumor load *in vivo* (Ghosh et al., 2022a). In free chrysin treated mice, EAC-induced splenomegaly was found to be reduced to great extent probably due to the anti-inflammatory effects of chrysin (Xiao et al., 2016) as well as reduction in tumor load; whereas reduction in splenomegaly and associated distortion in splenic tissue architecture in Chr-mSiO$_2$@PAA and Chr-mSiO$_2$@PAA/FA-treated mice are thought be a result of tumor load reduction (Fig. 11B).

3.12. *Chrysin nanoconjugates capable of inducing intrinsic apoptosis in vivo*

To check whether decrease in tumor size and volume is due to activation of intrinsic apoptosis pathway within tumor tissues, we compared immunohistochemical expression of two key caspases typical to intrinsic apoptosis pathway, i.e., caspase 9 and caspase 3. As depicted in Fig. 11C, 11D & S4, expressions of both caspase 9 and caspase 3 have been increased in treated tumor tissues in comparison with the untreated ones. Expressions of both of these proteins are highest among the tumor tissues collected from group T4. This emphasizes increased efficiency of chrysin nanoconjugates upon FA functionalization for equivalent amount of chrysin. Also, the data suggest that the reduction in tumor size and mass is due to intrinsic apoptosis which lies in line with the findings from the *in vitro* observations.

3.13. *Chrysin nanoconjugates are non-toxic to vital organs*

The aim of any nanohybrid in the field of cancer nano-therapeutics is to gain cancer cell-specificity mostly within *in vivo* physiological condition so that respective preclinical and clinical studies can be performed as well. Hence, a nanohybrid should be smart enough so that it remains capable of exerting cytotoxicity to target cancer cells keeping

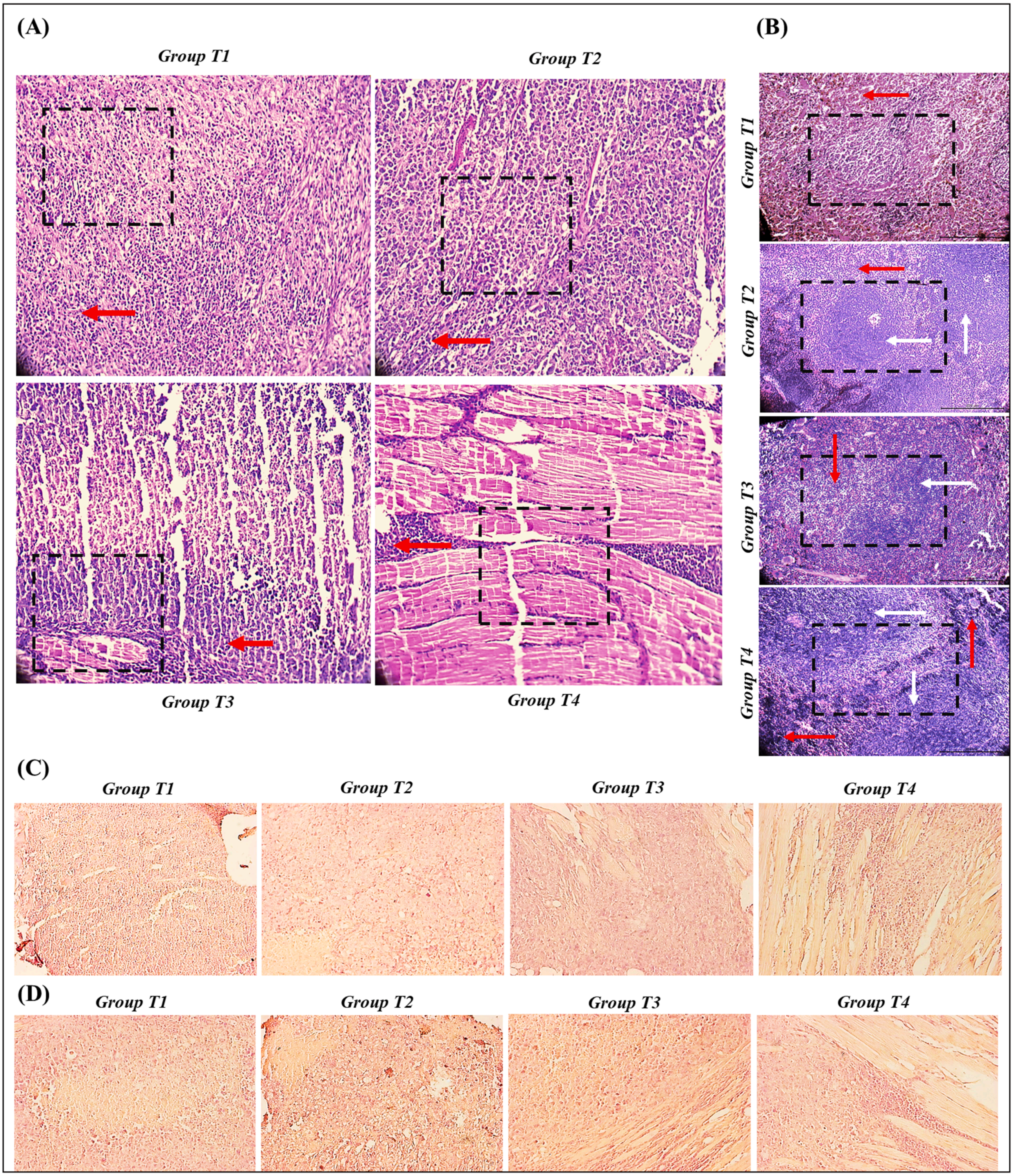

Fig. 11. Representative micrograph of H & E-stained tissue sections of (A) tumor tissues (here, red arrows demarcate multinucleated cells and black-dotted selected areas signify tumor tissue architecture gradually resembling normal muscle architecture with subsequent higher grade of nanohybridization of chrysin) and (B) splenic tissues (here, red and white arrows demarcate red pulp and white pulp of spleen with black-dotted selected areas signifying extent tumor-induced immunological response through enlargement of splenic white pulp) under 20× magnification. Immunohistochemical detection of (C) caspase 9 and (D) caspase 3 in dissected tumor tissue section viewed under 20× magnification of optical light microscope. (For interpretation of the references to colour in this figure legend, the reader is referred to the web version of this article.)

the healthy cells of vital organs safe. Therefore, zero to negligible *in vivo* systemic toxicity is ideal for a nanohybrid to be body hepatic serum markers such as ALP and ALT from animal of group S2-S4 were within normal range, showing no obvious sign of harm in kidney and liver (Ghosh et al., 2019) (Fig. 12A–12D). Additionally, histological evaluation of H & E-stained sections of vital organs such as lung, liver, kidney or heart showed no significant sign of abnormality (Fig. 12E). Thus, Chr-mSiO_2@PAA/FA can be regarded as safe in purpose of *in vivo* treatment-

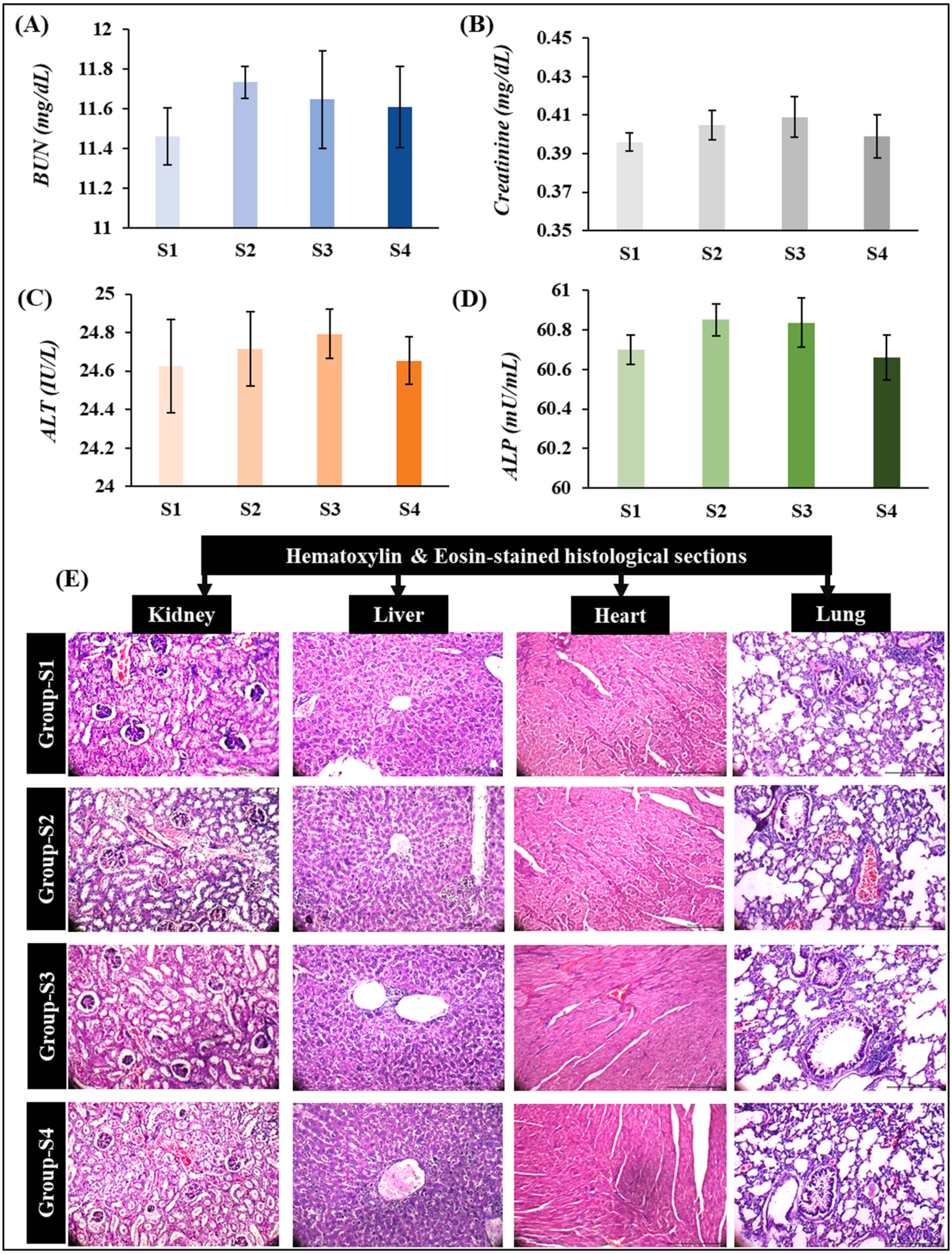

Fig. 12. Analysis of systemic toxicity by assessing serum (A) BUN, (B) Creatinine, (C) ALT and (D) ALP in different experimental groups of mice. Data are represented mean ± SD (n = 3). (E) Histological assessment of H & E-stained microsections of murine kidney, liver, heart and lung from different experimental groups with bright field microscopy under 20× magnification.

related systemic toxicity.

4. Conclusion

In summary, we have demonstrated the prospect of attaching nontoxic PAA as pore blocking agent on $mSiO_2$ to effectively control the release of uploaded cargo according to pH-gradient (Fig. 1B). PAA capping tightly sealed the pores of $mSiO_2$ so that at neutral pH (7.4) negligible premature cargo release can be achieved fulfilling one of the important targets in nanomedicine to prevent uncontrolled drug release and associated side effects. PAA was selected to facilitate the covalent functionalization to the mesoporous silica scaffold through acid-liable amide bond formation. Moreover, the pH-triggered behavior of this hybrid system may bring interesting future applications. Furthermore, this nanostructure with mesoporous silica scaffold core was chemically vectorized with FA offered selective and higher cargo release capacity for chrysin. According to flow cytometry analysis, significant improvement was noticed in cellular uptake of FA-functionalized $mSiO_2$ nanodevice due to receptor-mediated endocytosis in MCF-7 cell lines. *In vivo* experiments in Swiss Albino mice demonstrated higher chrysin accumulation in the tumor tissue following PAA capping and FA functionalization; whereas, healthy cells of vital organs were found unaffected. Hence, FA vectorization allowed increased selectivity and specificity toward cancer cells. Lastly, the issue with chrysin being used as a potent anticancer agent due to its higher hydrophobicity has been smartly overcome by entrapping it inside the pores of $mSiO_2$. Moreover, we have also tried to put our current *in vivo* work in comparison with positive *in vivo* data reported in parallel recent literatures that proves our current chrysin nanoconjugate to be equally potent and comparable (Table S1). Thus, in general the bioavailability and anticancer functionality of chrysin was boosted many folds after its nanoformatting. Therefore, in view of non-toxic nature, an excellent drug release capacity, an enhanced and selective cellular uptake within the tumor tissue of living organisms, effective anticancer activities of such chrysin nanoformulation (Chr-$mSiO_2$@PAA/FA) opens up a highly promising pathway for effective breast cancer treatment.

CRediT authorship contribution statement

Noyel Ghosh: Conceptualization, Methodology, Software, Data curation, Formal analysis, Investigation, Writing – original draft, Visualization, Writing – review & editing. **Mousumi Kundu:** Conceptualization, Methodology, Investigation, Data curation, Formal analysis, Writing – review & editing, Visualization. **Sumit Ghosh:** Conceptualization, Methodology, Data curation, Formal analysis. **Abhishek Kumar Das:** Methodology, Data curation, Formal analysis, Writing – review & editing, Visualization. **Samhita De:** Methodology, Visualization, Formal analysis. **Joydeep Das:** Conceptualization, Data curation, Formal analysis, Visualization, Writing – review & editing. **Parames C. Sil:** Conceptualization, Data curation, Formal analysis, Visualization, Writing – review & editing.

Declaration of Competing Interest

The authors declare that they have no known competing financial interests or personal relationships that could have appeared to influence the work reported in this paper.

Data availability

Data will be made available on request.

Acknowledgement

The authors acknowledge DST, India and UGC, India for proving financial assistance. Authors also extend our sincere gratitude to all of our lab members as well.

Appendix A. Supplementary material

Supplementary data to this article can be found online at https://doi.org/10.1016/j.ijpharm.2022.122555.

References

Azar, L.K., Dadashpour, M., Firouzi-Amandi, A., Zarghami, N., 2021. Design and development of nanostructured co delivery of artemisinin and chrysin for targeting hTERT gene expression in breast cancer cell line: possible clinical application in cancer treatment. Asian Pac. J. Cancer Prev. 23 (3), 919–927.

Bharathi, K., 2019. RP-HPLC method development and validation of Chrysin in bulk and marketed formulation. Int. J. Pharm. Biol. Sci. 9 (1), 602–611.

Bhattacharya, S., Ahir, M., Patra, P., Mukherjee, S., Ghosh, S., Mazumdar, M., Chattopadhyay, S., Das, T., Chattopadhyay, D., Adhikary, A., 2015. PEGylated-thymoquinone-nanoparticle mediated retardation of breast cancer cell migration by deregulation of cytoskeletal actin polymerization through miR-34a. Biomaterials 51, 91–107.

Chen, L., Li, Q., Jiang, Z., Li, C., Hu, H., Wang, T., Gao, Y., Wang, D., 2021. Chrysin induced cell apoptosis through H19/let-7a/COPB2 axis in gastric cancer cells and inhibited tumor growth. Front. Oncol. 11, 651644.

Chen, Y., Liu, X., Wang, H., Liu, S., Hu, N., Li, X., 2019b. Akt regulated phosphorylation of GSK-3β/cyclin D1, p21 and p27 contributes to cell proliferation through cell cycle progression from G1 to S/G2M phase in low-dose arsenite exposed HaCat cells. Front. Pharmacol. 10, 1176.

Chen, C., Tang, W., Jiang, D., Yang, G., Wang, X., Zhou, L., Zhang, W., Wang, P., 2019a. Hyaluronic acid conjugated polydopamine functionalized mesoporous silica nanoparticles for synergistic targeted chemo-photothermal therapy. Nanoscale 11 (22), 11012–11024.

Cheng, W., Nie, J., Xu, L., Liang, C., Peng, Y., Liu, G., Wang, T., Mei, L., Huang, L., Zeng, X., 2017. pH-sensitive delivery vehicle based on folic acid-conjugated polydopamine-modified mesoporous silica nanoparticles for targeted cancer therapy. ACS Appl. Mater. Interfaces 9 (22), 18462–18473.

Chowdhuri, A.R., Singh, T., Ghosh, S.K., Sahu, S.K., 2016. Carbon dots embedded magnetic nanoparticles@ chitosan@ metal organic framework as a nanoprobe for pH sensitive targeted anticancer drug delivery. ACS Appl. Mater. Interfaces 8 (26), 16573–16583.

Chowdhury, S., Ghosh, S., Rashid, K., Sil, P.C., 2016. Deciphering the role of ferulic acid against streptozotocin-induced cellular stress in the cardiac tissue of diabetic rats. Food Chem. Toxicol. 97, 187–198.

Dada, S.N., 2019. Preparation of Folic Acid-Carbon Dots-Doxorubicin Nanoparticles as Targeting Tumor Theranostics. East Tennessee State University. Electronic Theses and Dissertations 3671.

Das, A.K., Ghosh, N., Mandal, A., Sil, P.C., 2022a. Glycobiology of cellular expiry: Decrypting the role of glycan-lectin regulatory complex and therapeutic strategies focusing on cancer. Biochem. Pharmacol. 207, 115367.

Das, A.K., Hossain, U., Ghosh, S., Biswas, S., Mandal, M., Mandal, B., Brahmachari, G., Bagchi, A., Sil, P.C., 2022b. Amelioration of oxidative stress mediated inflammation and apoptosis in pancreatic islets by Lupeol in STZ-induced hyperglycaemic mice. Life Sci. 305, 120769.

Das, J., Sarkar, A., Sil, P.C., 2015. Hexavalent chromium induces apoptosis in human liver (HepG2) cells via redox imbalance. Toxicol. Rep. 2, 600–608.

Deshayes, S., Cabral, H., Ishii, T., Miura, Y., Kobayashi, S., Yamashita, T., Matsumoto, A., Miyahara, Y., Nishiyama, N., Kataoka, K., 2013. Phenylboronic acid-installed polymeric micelles for targeting sialylated epitopes in solid tumors. J. Am. Chem. Soc. 135 (41), 15501–15507.

Evans, B.C., Nelson, C.E., Shann, S.Y., Beavers, K.R., Kim, A.J., Li, H., Nelson, H.M., Giorgio, T.D., Duvall, C.L., 2013. Ex vivo red blood cell hemolysis assay for the evaluation of pH-responsive endosomolytic agents for cytosolic delivery of biomacromolecular drugs. J. Vis. Exp. 73, e50166.

Farokhzad, O.C., Langer, R., 2006. Nanomedicine: developing smarter therapeutic and diagnostic modalities. Adv. Drug Deliv. Rev. 58 (14), 1456–1459.

Feng, W., Zhou, X., He, C., Qiu, K., Nie, W., Chen, L., Wang, H., Mo, X., Zhang, Y., 2013. Polyelectrolyte multilayer functionalized mesoporous silica nanoparticles for pH-responsive drug delivery: layer thickness-dependent release profiles and biocompatibility. J. Mater. Chem. B 1 (43), 5886–5898.

Ganai, S.A., Sheikh, F.A., Baba, Z.A., 2021. Plant flavone Chrysin as an emerging histone deacetylase inhibitor for prosperous epigenetic-based anticancer therapy. Phytother. Res. 35 (2), 823–834.

Garcia-Bennett, A., Nees, M., Fadeel, B., 2011. In search of the Holy Grail: folate-targeted nanoparticles for cancer therapy. Biochem. Pharmacol. 81 (8), 976–984.

Garin-Chesa, P., Campbell, I., Saigo, P., Lewis Jr, J., Old, L., Rettig, W., 1993. Trophoblast and ovarian cancer antigen LK26. Sensitivity and specificity in immunopathology and molecular identification as a folate-binding protein. Am. J. Pathol. 142 (2), 557.

Ghosh, S., Chowdhury, S., Sarkar, P., Sil, P.C., 2018. Ameliorative role of ferulic acid against diabetes associated oxidative stress induced spleen damage. Food Chem. Toxicol. 118, 272–286.

Ghosh, N., Sil, P.C., 2021. Mitochondria and apoptosis. In: Elsevier, pp. 127–149.

Ghosh, N., Hossain, U., Mandal, A., Sil, P.C., 2019. The Wnt signaling pathway: a potential therapeutic target against cancer. Ann. N. Y. Acad. Sci. 1443 (1), 54–74.

Ghosh, N., Chatterjee, S., Biswal, D., Pramanik, N.R., Chakrabarti, S., Sil, P.C., 2022a. Oxidative stress imposed in vivo anticancer therapeutic efficacy of novel imidazole-based oxidovanadium (IV) complex in solid tumor. Life Sci. 301, 120606.

Ghosh, S., Kundu, M., Dutta, S., Mahalanobish, S., Ghosh, N., Das, J., Sil, P.C., 2022b. Enhancement of anti-neoplastic effects of cuminaldehyde against breast cancer via mesoporous silica nanoparticle based targeted drug delivery system. Life Sci. 298, 120525.

Giret, S., Wong Chi Man, M., Carcel, C., 2015. Mesoporous-silica-functionalized nanoparticles for drug delivery. Chem. Eur. J. 21 (40), 13850–13865.

Hakeem, A., Zahid, F., Duan, R., Asif, M., Zhang, T., Zhang, Z., Cheng, Y., Lou, X., Xia, F., 2016. Cellulose conjugated FITC-labelled mesoporous silica nanoparticles: intracellular accumulation and stimuli responsive doxorubicin release. Nanoscale 8 (9), 5089–5097.

Hissin, P.J., Hilf, R., 1976. A fluorometric method for determination of oxidized and reduced glutathione in tissues. Anal. Biochem. 74 (1), 214–226.

Jabbari, S., Ghamkhari, A., Javadzadeh, Y., Salehi, R., Davaran, S., 2018. Doxorubicin and chrysin combination chemotherapy with novel pH-responsive poly [(lactide-co-glycolic acid)-block-methacrylic acid] nanoparticle. J. Drug Deliv. Sci. Technol. 46, 129–137.

Karamipour, S., Sadjadi, M., Farhadyar, N., 2015. Fabrication and spectroscopic studies of folic acid-conjugated Fe3O4@ Au core–shell for targeted drug delivery application. Spectrochim. Acta A Mol. Biomol. Spectrosc. 148, 146–155.

Kundu, M., Sadhukhan, P., Ghosh, N., Chatterjee, S., Manna, P., Das, J., Sil, P.C., 2019. pH-responsive and targeted delivery of curcumin via phenylboronic acid-functionalized ZnO nanoparticles for breast cancer therapy. J. Adv. Res. 18, 161–172.

Kundu, M., Chatterjee, S., Ghosh, N., Manna, P., Das, J., Sil, P.C., 2020. Tumor targeted delivery of umbelliferone via a smart mesoporous silica nanoparticles controlled-release drug delivery system for increased anticancer efficiency. Mater. Sci. Eng. C 116, 111239.

Kundu, M., Sadhukhan, P., Ghosh, N., Ghosh, S., Chatterjee, S., Das, J., Brahmachari, G., Sil, P.C., 2021. In vivo therapeutic evaluation of a novel bis-lawsone derivative against tumor following delivery using mesoporous silica nanoparticle based redox-responsive drug delivery system. Mater. Sci. Eng. C 126, 112142.

Leamon, C.P., Reddy, J.A., 2004. Folate-targeted chemotherapy. Adv. Drug Deliv. Rev. 56 (8), 1127–1141.

Lei, W., Sun, C., Jiang, T., Gao, Y., Yang, Y., Zhao, Q., Wang, S., 2019. Polydopamine-coated mesoporous silica nanoparticles for multi-responsive drug delivery and combined chemo-photothermal therapy. Mater. Sci. Eng. C 105, 110103.

Lu, J., Liong, M., Li, Z., Zink, J.I., Tamanoi, F., 2010. Biocompatibility, biodistribution, and drug-delivery efficiency of mesoporous silica nanoparticles for cancer therapy in animals. Small 6 (16), 1794–1805.

Lungare, S., Hallam, K., Badhan, R.K., 2016. Phytochemical-loaded mesoporous silica nanoparticles for nose-to-brain olfactory drug delivery. Int. J. Pharm. 513 (1–2), 280–293.

Manna, P., Sinha, M., Sil, P.C., 2009. Prophylactic role of arjunolic acid in response to streptozotocin mediated diabetic renal injury: activation of polyol pathway and oxidative stress responsive signaling cascades. Chem. Biol. Interact. 181 (3), 297–308.

Matsumura, Y., Maeda, H., 1986. A new concept for macromolecular therapeutics in cancer chemotherapy: mechanism of tumoritropic accumulation of proteins and the antitumor agent smancs. Cancer Res. 46 (12_Part_1), 6387–6392.

Neganova, I., Lako, M., 2008. G1 to S phase cell cycle transition in somatic and embryonic stem cells. J. Anat. 213 (1), 30–44.

Parker, N., Turk, M.J., Westrick, E., Lewis, J.D., Low, P.S., Leamon, C.P., 2005. Folate receptor expression in carcinomas and normal tissues determined by a quantitative radioligand binding assay. Anal. Biochem. 338 (2), 284–293.

Pecora, R., 2000. Dynamic light scattering measurement of nanometer particles in liquids. J. Nanopart. Res. 2 (2), 123–131.

Peng, H., Dong, R., Wang, S., Zhang, Z., Luo, M., Bai, C., Zhao, Q., Li, J., Chen, L., Xiong, H., 2013. A pH-responsive nano-carrier with mesoporous silica nanoparticles cores and poly (acrylic acid) shell-layers: fabrication, characterization and properties for controlled release of salidroside. Int. J. Pharm. 446 (1–2), 153–159.

Porta, F., Lamers, G.E., Morrhayim, J., Chatzopoulou, A., Schaaf, M., den Dulk, H., Backendorf, C., Zink, J.I., Kros, A., 2013. Folic acid-modified mesoporous silica nanoparticles for cellular and nuclear targeted drug delivery. Adv. Healthc. Mater. 2 (2), 281–286.

Pushpavalli, G., Kalaiarasi, P., Veeramani, C., Pugalendi, K.V., 2010. Effect of chrysin on hepatoprotective and antioxidant status in D-galactosamine-induced hepatitis in rats. Eur. J. Pharmacol. 631 (1–3), 36–41.

Rameli, N., Jumbri, K., Wahab, R., Ramli, A., Huyop, F., 2018. Synthesis and characterization of mesoporous silica nanoparticles using ionic liquids as a template. J. Phys. Conf. Ser. 1123 (1), 012068.

Renner, A.M., Ilyas, S., Schlößer, H.A., Szymura, A., Roitsch, S., Wennhold, K., Mathur, S., 2020. Receptor-mediated in vivo targeting of breast cancer cells with 17α-ethynylestradiol-conjugated silica-coated gold nanoparticles. Langmuir 36 (48), 14819–14828.

Riccardi, C., Nicoletti, I., 2006. Analysis of apoptosis by propidium iodide staining and flow cytometry. Nat. Protoc. 1 (3), 1458–1461.

Sadhukhan, P., Saha, S., Sinha, K., Brahmachari, G., Sil, P.C., 2016. Selective pro-apoptotic activity of novel 3, 3′-(aryl/alkyl-methylene) bis (2-hydroxynaphthalene-1, 4-dione) derivatives on human cancer cells via the induction reactive oxygen species. PLoS ONE 11 (7), e0158694.

Sadhukhan, P., Kundu, M., Chatterjee, S., Ghosh, N., Manna, P., Das, J., Sil, P.C., 2019. Targeted delivery of quercetin via pH-responsive zinc oxide nanoparticles for breast cancer therapy. Mater. Sci. Eng. C 100, 129–140.

Saha, S., Sadhukhan, P., Sinha, K., Agarwal, N., Sil, P.C., 2016. Mangiferin attenuates oxidative stress induced renal cell damage through activation of PI3K induced Akt and Nrf-2 mediated signaling pathways. Biochem. Biophys. Rep. 5, 313–327.

Salama, A.A., Allam, R.M., 2021. Promising targets of chrysin and daidzein in colorectal cancer: amphiregulin, CXCL1, and MMP-9. Eur. J. Pharmacol. 892, 173763.

Salinas, Y., Hoerhager, C., Garcia-Fernandez, A., Resmini, M., Sancenon, F., Matinez-Manez, R., Brueggemann, O., 2018. Biocompatible phenylboronic-acid-capped ZnS nanocrystals designed as caps in mesoporous silica hybrid materials for on-demand pH-triggered release in cancer cells. ACS Appl. Mater. Interfaces 10 (40), 34029–34038.

Salmaso, S., Semenzato, A., Caliceti, P., Hoebeke, J., Sonvico, F., Dubernet, C., Couvreur, P., 2004. Specific antitumor targetable β-cyclodextrin-poly (ethylene glycol)-folic acid drug delivery bioconjugate. Bioconjug. Chem. 15 (5), 997–1004.

Samarghandian, S., Azimi-Nezhad, M., Borji, A., Hasanzadeh, M., Jabbari, F., Farkhondeh, T., Samini, M., 2016. Inhibitory and cytotoxic activities of chrysin on human breast adenocarcinoma cells by induction of apoptosis. Pharmacogn. Mag. 12 (Suppl. 4), S436.

Sarkar, A., Das, J., Manna, P., Sil, P.C., 2011. Nano-copper induces oxidative stress and apoptosis in kidney via both extrinsic and intrinsic pathways. Toxicology 290 (2–3), 208–217.

Sarkar, A., Ghosh, S., Chowdhury, S., Pandey, B., Sil, P.C., 2016. Targeted delivery of quercetin loaded mesoporous silica nanoparticles to the breast cancer cells. Biochim. Biophys. Acta Gen. Subj. 1860 (10), 2065–2075.

Sarkar, A., Sil, P.C., 2014. Iron oxide nanoparticles mediated cytotoxicity via PI3K/AKT pathway: role of quercetin. Food Chem. Toxicol. 71, 106–115.

Sengupta, S., Balla, V.K., 2018. A review on the use of magnetic fields and ultrasound for non-invasive cancer treatment. J. Adv. Res. 14, 97–111.

Shimura, T., Noma, N., Oikawa, T., Ochiai, Y., Kakuda, S., Kuwahara, Y., Takai, Y., Takahashi, A., Fukumoto, M., 2012. Activation of the AKT/cyclin D1/Cdk4 survival signaling pathway in radioresistant cancer stem cells. Oncogenesis 1 (6), e12–e.

Sinha, M., Manna, P., Sil, P.C., 2007. Taurine, a conditionally essential amino acid, ameliorates arsenic-induced cytotoxicity in murine hepatocytes. Toxicol. In Vitro 21 (8), 1419–1428.

Sun, Q., Liu, F., Wen, Z., Xia, J., Li, H., Xu, Y., Sun, S., 2022. Combined effect of heat shock protein inhibitor geldanamycin and free radicals on photodynamic therapy of prostate cancer. J. Mater. Chem. B 10 (9), 1369–1377.

Sung, H., Ferlay, J., Siegel, R.L., Laversanne, M., Soerjomataram, I., Jemal, A., Bray, F., 2021. Global cancer statistics 2020: GLOBOCAN estimates of incidence and mortality worldwide for 36 cancers in 185 countries. CA Cancer J. Clin. 71 (3), 209–249.

Swift, T., Swanson, L., Geoghegan, M., Rimmer, S., 2016. The pH-responsive behaviour of poly (acrylic acid) in aqueous solution is dependent on molar mass. Soft Matter 12 (9), 2542–2549.

Takahashi-Yanaga, F., Sasaguri, T., 2008. GSK-3β regulates cyclin D1 expression: a new target for chemotherapy. Cell. Signal. 20 (4), 581–589.

Tao, W., Zhang, J., Zeng, X., Liu, D., Liu, G., Zhu, X., Liu, Y., Yu, Q., Huang, L., Mei, L., 2015. Blended nanoparticle system based on miscible structurally similar polymers: a safe, simple, targeted, and surprisingly high efficiency vehicle for cancer therapy. Adv. Healthc. Mater. 4 (8), 1203–1214.

Walle, T., Otake, Y., Brubaker, J., Walle, U., Halushka, P., 2001. Disposition and metabolism of the flavonoid chrysin in normal volunteers. Br. J. Pharmacol. 51 (2), 143–146.

Wang, K., Lu, J., Li, J., Gao, Y., Mao, Y., Zhao, Q., Wang, S., 2021a. Current trends in smart mesoporous silica-based nanovehicles for photoactivated cancer therapy. J. Control. Release 339, 445–472.

Wang, L., Zhang, Y., Han, Y., Zhang, Q., Wen, Z., Li, H., Sun, S., Chen, X., Xu, Y., 2021b. Nanoscale photosensitizer with tumor-selective turn-on fluorescence and activatable photodynamic therapy treatment for COX-2 overexpressed cancer cells. J Mater Chem B 9 (8), 2001–2009.

Weng, M.-S., Ho, Y.-S., Lin, J.-K., 2005. Chrysin induces G1 phase cell cycle arrest in C6 glioma cells through inducing p21Waf1/Cip1 expression: involvement of p38 mitogen-activated protein kinase. Biochem. Pharmacol. 69 (12), 1815–1827.

Xiao, X., Liu, Y., Guo, M., Fei, W., Zheng, H., Zhang, R., Zhang, Y., Wei, Y., Zheng, G., Li, F., 2016. pH-triggered sustained release of arsenic trioxide by polyacrylic acid capped mesoporous silica nanoparticles for solid tumor treatment in vitro and in vivo. J. Biomater. Appl. 31 (1), 23–35.

Xiao, J., Zhai, H., Yao, Y., Wang, C., Jiang, W., Zhang, C., Simard, A., Zhang, R., Hao, J., 2014. Chrysin attenuates experimental autoimmune neuritis by suppressing immuno-inflammatory responses. Neuroscience 262, 156–164.

Xu, S., Olenyuk, B.Z., Okamoto, C.T., Hamm-Alvarez, S.F., 2013. Targeting receptor-mediated endocytotic pathways with nanoparticles: rationale and advances. Adv. Drug Deliv. Rev. 65 (1), 121–138.

Xu, Y., Tong, Y., Ying, J., Lei, Z., Wan, L., Zhu, X., Ye, F., Mao, P., Wu, X., Pan, R., 2018. Chrysin induces cell growth arrest, apoptosis, and ER stress and inhibits the activation of STAT3 through the generation of ROS in bladder cancer cells. Oncol. Lett. 15 (6), 9117–9125.

Xu, Q., Yang, Y., Lu, J., Lin, Y., Feng, S., Luo, X., Di, D., Wang, S., Zhao, Q., 2022. Recent trends of mesoporous silica-based nanoplatforms for nanodynamic therapies. Coord. Chem. Rev. 469, 214687.

Yuan, L., Tang, Q., Yang, D., Zhang, J.Z., Zhang, F., Hu, J., 2011. Preparation of pH-responsive mesoporous silica nanoparticles and their application in controlled drug delivery. J. Phys. Chem. C 115 (20), 9926–9932.

Zeng, Y.-B., Yang, N., Liu, W.-S., Tang, N., 2003. Synthesis, characterization and DNA-binding properties of La (III) complex of chrysin. J. Inorg. Biochem. 97 (3), 258–264.

Zhai, W., He, C., Wu, L., Zhou, Y., Chen, H., Chang, J., Zhang, H., 2012. Degradation of hollow mesoporous silica nanoparticles in human umbilical vein endothelial cells. J. Biomed. Mater. Res. Part B Appl. Biomater. 100 (5), 1397–1403.

Zhou, L., Yang, C., Zhong, W., Wang, Q., Zhang, D., Zhang, J., Xie, S., Xu, M., 2021. Chrysin induces autophagy-dependent ferroptosis to increase chemosensitivity to gemcitabine by targeting CBR1 in pancreatic cancer cells. Biochem. Pharmacol. 193, 114813.

Zhu, Y.J., Chen, F., 2015. pH-responsive drug-delivery systems. Chem. Asian J. 10 (2), 284–305.

Zwicke, G.L., Ali Mansoori, G., Jeffery, C.J., 2012. Utilizing the folate receptor for active targeting of cancer nanotherapeutics. Nano Rev. 3 (1), 18496.